

**Study of Jet Quenching in Quark Gluon Plasma Using Jet Charge Measurements**

BY

DHANUSH ANIL HANGAL

M.S., University of Illinois at Chicago, 2018

Integrated MSc. Physics, Indian Institute of Technology Roorkee, 2015

THESIS

Submitted as partial fulfillment of the requirements  
for the degree of Doctor of Philosophy in Physics  
in the Graduate College of the University of Illinois at Chicago, 2020

Chicago, IL

DEFENSE COMMITTEE:

Olga Evdokimov, Chair and Advisor

David Hofman

Zhenyu Ye

Mikhail Stephanov

Camelia Mironov, Massachusetts Institute of Technology

*For Babasaheb Ambedkar, who paved the way for children of lower-caste in India to be able to follow their curiosity and passions. Jai Bhim!*

## ACKNOWLEDGEMENTS

I am immensely thankful to my advisor, Prof. Olga Evdokimov, for mentoring and supporting me through my PhD. I am indebted to her for spending countless hours to discuss and guide me through many intriguing puzzles that I encountered in the course of this thesis work. Special thanks to my dissertation committee members, Dr. Hofman, Dr. Ye, Dr. Stephanov, and Dr. Mironov for their time and flexibility with the remote nature of this thesis defense. I have received valuable guidance from Marta Verweij, Yi Chen, Chris McGinn, and Austin Baty among other members of the CMS Heavy-Ion group, for which I'm very thankful. I am especially grateful to Kurt Jung, for his patience while tutoring me on ROOT and the inner workings of CMS, and for getting me excited about new problems in heavy-ion physics. Particular thanks to Xiao Wang and Jussi Viinikainen for their friendship and lunchtime discussions, which also resulted in key breakthroughs in my analysis work. I wish to thank my parents, Anil Kumar Hangal and Sunita Hangal, for their sacrifices and encouragement to my younger self to not be afraid of tackling big problems; none of this would have been possible without the constant love and support of my parents and sister. Thanks to Aman, Aniket, and Yawar for their continued friendship and for helping me learn that we are all “glorious things made up of star dust”; rest in peace Rohit Vermula. I wish to thank Brian, Alec, and Ram for their friendship and for trivia nights through graduate school. Finally, thanks to my partner Megan McGuire, for including me in her ardent quest of social justice, and for all the positive reinforcements, baked goods, and patience which enabled me to persevere and achieve this milestone.

DAH

## CONTRIBUTION OF AUTHORS

The results reported here are the product of analyses that I carried out as a member of the CMS Collaboration, which have been either previously published in JHEP in Refs. [1, 2], or made public by the CMS Collaboration in Ref. [3, 4, 5, 6]. Following the CMS authorship policy, all members of the CMS Collaboration sign all papers from approximately six months after joining CMS until one year after leaving the collaboration. This policy reflects the fact that each CMS analysis relies heavily on an enormous amount of underlying work on detector and software design, calibration, and maintenance. The details of the CMS detector, track and jet reconstruction, data selection, and Monte Carlo simulation that are used in common by many CMS analyses are summarized in Secs. 5, 6, 8, and 7. I contributed to these as a member of the CMS heavy-ion group, but the work summarized there is not primarily my own. Sections 9 and 10 report the analysis-specific work for which I, with support from my advisor and close collaborators, am primarily responsible; I also personally produced all figures appearing in these sections including those cited to Refs. [1, 2, 3, 4, 5, 6]. In all cases, the analyses was carried out in close collaboration with my advisor Olga Evdokimov, and with the support and helpful scrutiny of other members of CMS, particularly the high- $p_T$  heavy-ion group and the Analysis Review Committees for each paper. In addition, Kurt Jung, Hallie Trauger, Xiao Wang, and Jussi Viinikainen contributed substantially to the analyses documented in Refs. [1, 2].

## TABLE OF CONTENTS

<b>1 INTRODUCTION</b>	<b>1</b>
<b>2 THE QUARK-GLUON PLASMA</b>	<b>3</b>
2.1 Quantum chromodynamics and the quark-gluon plasma . . . . .	3
2.2 Thermodynamics of the quark-gluon plasma . . . . .	5
2.3 Time-evolution of a heavy ion collision . . . . .	7
2.4 Event kinematics and centrality . . . . .	9
2.5 Collectivity in the quark-gluon plasma . . . . .	11
2.6 High- $p_T$ parton suppression . . . . .	14
<b>3 JET TOMOGRAPHY OF THE QUARK-GLUON PLASMA</b>	<b>18</b>
3.1 Jet as a parton proxy . . . . .	18
3.2 Probing the quark-gluon plasma with jets . . . . .	18
3.3 Jet $R_{AA}$ and dijet asymmetry . . . . .	19
3.4 Fragmentation function and jet shapes . . . . .	21
3.5 Flavor dependence of jet energy loss . . . . .	23
<b>4 THEORY OF JET QUENCHING</b>	<b>26</b>
4.1 Theoretical formalisms of jet quenching . . . . .	26
4.2 Comparisons to experimental observables . . . . .	33
4.3 Theoretical motivation for jet charge studies . . . . .	38
<b>5 THE LARGE HADRON COLLIDER AND THE CMS DETECTOR</b>	<b>47</b>
5.1 Large Hadron Collider . . . . .	47
5.2 Compact Muon Solenoid Detector . . . . .	48
5.3 CMS trigger system . . . . .	52
<b>6 DATA AND MONTE-CARLO SAMPLES</b>	<b>54</b>
6.1 Data samples . . . . .	54
6.2 Monte-Carlo simulations and samples . . . . .	54
6.3 Centrality determination . . . . .	58
6.4 Event selection and reweighting . . . . .	58
<b>7 TRACK RECONSTRUCTION</b>	<b>61</b>
7.1 CMS track reconstruction . . . . .	61
7.2 Tracking performance in CMS . . . . .	63
7.3 Primary vertex finding . . . . .	65
<b>8 JET RECONSTRUCTION</b>	<b>67</b>
8.1 Anti- $k_T$ jet algorithm . . . . .	67
8.2 Jet reconstruction in heavy-ion collisions . . . . .	70
8.3 Jet energy corrections . . . . .	73
8.4 Jet flavor identification . . . . .	80
8.5 Jet Spectra and selections . . . . .	81

## TABLE OF CONTENTS (continued)

<b>9 JET CHARGE AND QUARK/GLUON FRACTIONS</b>	<b>83</b>
9.1 Measuring the jet charge . . . . .	83
9.2 Unfolding for detector and background effects . . . . .	87
9.3 Template Fitting for Quark and Gluon fractions . . . . .	96
9.4 Systematic uncertainty studies . . . . .	105
9.5 Results . . . . .	114
<b>10 JET SHAPES FEASIBILITY STUDIES FOR IDENTIFIED HADRONS</b>	<b>122</b>
10.1 Particle Identification with MIP timing detector . . . . .	122
10.2 Jet-track angular correlations . . . . .	123
10.3 Feasibility results of jet shapes . . . . .	128
<b>11 CONCLUSIONS</b>	<b>131</b>
<b>REFERENCES</b>	<b>133</b>
<b>APPENDICES</b>	<b>150</b>
A Open access statements for material adapted from previous publications . . . . .	150
<b>VITA</b>	<b>151</b>

## LIST OF TABLES

Table I	Computational frameworks for jet quenching and description. . . . .	30
Table II	Data samples with triggers used and number of events recorded. . . . .	54
Table III	MC samples with corresponding $\hat{p}_T$ values, cross-sections and number of events.	57
Table IV	Mean and standard deviation of individual flavor jet charge distributions. . . .	97
Table V	Fit parameter values ( $\chi^2$ and NDF) for different track $p_T$ threshold and $\kappa$ bins.	102
Table VI	Systematic uncertainties for extracted jet fractions in different track $p_T$ bins. .	112
Table VII	Systematic uncertainties for extracted jet fractions in different $\kappa$ bins. . . . .	112

## LIST OF FIGURES

1	QCD running coupling . . . . .	4
2	QCD phase space diagram and thermodynamic properties at $\mu_B = 0$ . . . . .	6
3	Time evolution of a heavy-ion collision. . . . .	7
4	Coordinate system and pseudorapidity. . . . .	9
5	Centrality, $N_{\text{part}}$ and $N_{\text{coll}}$ from Glauber model. . . . .	11
6	Ellipticity in PbPb events. . . . .	12
7	Dihadron correlations and $v_n$ measurements . . . . .	13
8	Dihadron correlations in high multiplicity small systems . . . . .	14
9	Illustration of a hard scattering. . . . .	15
10	High- $p_T$ $R_{\text{AA}}$ measurements. . . . .	17
11	Dijets in heavy-ion collisions. . . . .	19
12	Jet $R_{\text{AA}}$ and dijet asymmetry ( $A_J$ ) measurements. . . . .	20
13	Jet fragmentation function in PbPb collisions. . . . .	22
14	Jet shapes in PbPb collisions. . . . .	23
15	Fragmentation function and jet shapes for $\gamma$ -tagged jets. . . . .	24
16	Jet charge measurements in pp collisions from CMS and ATLAS. . . . .	25
17	NLO QCD calculations for jet production. . . . .	26
18	Radiational and collisional energy loss diagrams. . . . .	27
19	Jet transport coefficient as a function of temperature. . . . .	31
20	Cold nuclear modification factors for different flavor partons. . . . .	32
21	Charged-particle $R_{\text{AA}}$ and model comparisons. . . . .	33
22	Jet $R_{\text{AA}}$ measurements with theoretical comparisons. . . . .	34
23	Jet $R_{\text{AA}}$ predictions as a function of jet radius. . . . .	35
24	Jet shapes from coupled jet-fluid model and JEWEL. . . . .	36
25	Jet shapes from SCET <sub>G</sub> and HYBRID. . . . .	37
26	Baryon-to-meson measurements from bulk particles and jet fragments. . . . .	38
27	Flavor dependence of $R_{\text{AA}}$ measurements from DGLV and LBT. . . . .	39
28	Jet flavor composition from SCET <sub>G</sub> and $\hat{q}$ calculation from LBT. . . . .	40
29	Energy loss of quarks vs. gluons from JEWEL and Hybrid. . . . .	41
30	Jet charge distributions for different flavored partons. . . . .	42
31	Jet charge and jet flavor composition in pp collisions. . . . .	43
32	PYQUEN and JEWEL predictions for jet charge modifications. . . . .	45
33	SCET <sub>G</sub> calculations for jet charge modifications. . . . .	45
34	Schematic diagram of Large Hadron Collider. . . . .	47
35	Cut-away and cross-section views of the CMS detector. . . . .	49
36	Schematic diagrams of CMS pixel and strip detectors. . . . .	50
37	Cross-sections of CMS ECAL and HCAL subdetectors. . . . .	51
38	Jet trigger efficiency in pp and PbPb collision datasets recorded in 2015. . . . .	55
39	Schematic diagram of Glauber model interaction. . . . .	57
40	HF energy distribution from PbPb collisions in CMS. . . . .	59
41	Centrality and $v_z$ distributions in data and MC with reweighting. . . . .	60
42	Tracking efficiency and corrections for pp collisions before and after corrections. . . . .	64
43	Tracking efficiency and corrections for PbPb collisions before and after corrections. . . . .	65
44	Track $p_T$ resolution and misreconstruction rate for pp collisions. . . . .	66
45	Illustrations of collinear safety (left) and infrared safety (right) in jet reconstruction	68
46	Comparison of jet algorithm catchment areas. . . . .	69

## LIST OF FIGURES (continued)

47	Area-normalized energy deposited in PbPb events as a function of the event centrality	71
48	Jet energy scale and resolution with PU subtraction.	72
49	Jet energy corrections in CMS.	73
50	Absolute and relative response in $\gamma + jet$ events.	75
51	Post-correction relative response in $\gamma + jet$ events.	76
52	Jet energy scale without fragmentation-dependent corrections.	77
53	Number of jet constituents for quark and gluon jets.	78
54	Jet energy scale as a function of the number of jet constituents.	78
55	Jet energy scale before and after fragmentation-dependent corrections.	79
56	Jet energy resolution before and after fragmentation-dependent corrections.	79
57	Jet flavor composition as a function of jet $p_T$ and $\eta$ .	80
58	Jet spectra in pp collisions vs. $p_T$ , $\eta$ and $\phi$ .	81
59	Jet spectra in PbPb collisions vs. $p_T$ , $\eta$ and $\phi$ .	82
60	Jet charge distributions in signal and background cones.	84
61	Jet charge distributions for inclusive, light quark and gluon jets for different track $p_T$ thresholds.	85
62	Jet charge distributions for inclusive, light quark and gluon jets for different $\kappa$ values.	85
63	Average jet charge in signal and background cones.	86
64	Response matrices for detector inefficiency unfolding in jet charge measurements.	89
65	Response matrices for background unfolding in jet charge measurements.	90
66	Validation of jet charge background modeling in HYDJET.	91
67	Validation of jet charge background modeling in using minimum bias PbPb data.	91
68	Nominal unfolding closure test for jet charge in MC.	92
69	Statistically independent unfolding closure test for jet charge in MC.	93
70	Cross-closure test for unfolding jet charge in MC.	94
71	$\chi^2$ and uncertainty tests for jet charge unfolding iterations.	95
72	Unfolded jet charge distributions compared to raw reconstructed measurements.	95
73	Average jet charge as a function of jet $p_T$ for quark, gluon and inclusive jets in MC.	96
74	Generator-level inclusive jet charge distributions with contribution of different flavors.	97
75	Unfolded data inclusive jet charge distributions with contribution of different flavors.	98
76	Detector-level inclusive jet charge distributions with contribution of different flavors.	98
77	Quark and gluon jet fitting results in MC as a function of track $p_T$ threshold.	99
78	Flavor composition of zero track jets in MC for pp and PbPb collisions.	100
79	Zero-track jets in data and MC for pp and PbPb collisions.	100
80	Corrected quark/gluon jet fitting results in MC as a function of track $p_T$ threshold.	101
81	Corrected quark/gluon jet fitting results in MC as a function of $\kappa$ .	101
82	Distribution of pulls for fitting in all considered bins.	103
83	Jet $p_T$ spectra in data and MC with pre- and post-fitting quark and gluon jet fractions.	104
84	Jet $\eta$ spectra in data and MC with pre- and post-fitting quark and gluon jet fractions.	104
85	Tracking efficiencies for inclusive, positive and negatively charged tracks.	105
86	Relative uncertainties due to tracking inefficiencies in jet charge distributions.	106
87	Validation of extraction of quark and gluon jet fractions using jet charge templates and jet energy resolution effects on jet charge distributions.	108
88	Ratio of zero-track jets in data and MC between PF and Calorimeter jets.	109
89	Track multiplicity in random cones in minimum-bias PbPb data and MC	110
90	Effects of background fluctuations on jet charge measurements.	110

## LIST OF FIGURES (continued)

91	Systematic uncertainties due to limited statistics in MC samples. . . . .	111
92	Summary of systematic uncertainties from various sources for different track $p_T$ thresholds. . . . .	113
93	Summary of systematic uncertainties from various sources for different $\kappa$ values. . . . .	113
94	Unfolded jet charge distributions for $\kappa = 0.5$ along with flavor fractions from fitting results. . . . .	115
95	Unfolded jet charge distributions for a minimum track $p_T$ of 1 GeV along with flavor fractions from fitting results. . . . .	116
96	Unfolded jet charge distributions for a minimum track $p_T$ of 2 GeV along with flavor fractions from fitting results. . . . .	117
97	Standard deviations of unfolded jet charge distributions for pp and PbPb collisions. . . . .	118
98	Jet flavor composition and widths of unfolded jet charge distributions for central PbPb collisions. . . . .	119
99	Fitting results for the extraction of gluon jet fractions in pp and PbPb collisions for different track $p_T$ thresholds. . . . .	119
100	Fitting results for the extraction of gluon jet fractions in pp and PbPb collisions for different $\kappa$ values. . . . .	120
101	Expected performance of inverse velocity ( $1/\beta$ ) vs. total momentum ( $p$ ) from MTD in CMS. . . . .	123
102	Pair-acceptance correction in jet-track correlations using mixed-event technique. . . . .	125
103	Background subtraction in jet-track correlations using large $\Delta\eta$ sidebands. . . . .	126
104	Jet shapes for protons and pions in PYTHIA using MTD information. . . . .	129
105	Integrated particle yields of identified protons and pions correlated to the jet axis as a function of $p_T$ . . . . .	130

## LIST OF ABBREVIATIONS

AdS/CFT	Anti-de Sitter/Conformal Field Theory
AMY	Arnold-Moore-Yaffe
BDMPS-Z	Baier-Dokshitzer-Mueller-Peigné-Schiff-Zakharov
BES	Beam Energy Scan
BNL	Brookhaven National Laboratory
CERN	Conseil Européen pour la Recherche Nucléaire
CMS	Compact Muon Solenoid
CNM	Cold Nuclear Matter
DGLAP	Dokshitzer-Gribov-Lipatov-Altarelli-Parisi
ECAL	Electromagnetic Calorimeter
$E_T$	Transverse Energy
GLV	Gyulassy-Lévai-Vitev
HCAL	Hadronic Calorimeter
HF	Hadron Forward
HLT	High Level Trigger
HT-BW	Higher Twist Berkeley-Wuhan
HT-M	Higher Twist Majumder
IRC	Infrared and Collinear
JEC	Jet Energy Correction
JES	Jet Energy Scale
LBT	Linear Boltzman Transport
LHC	Large Hadron Collider
MC	Monte Carlo
MTD	Mip Timing Detector
PbPb	Lead-lead (collision data)
PDF	Parton Distribution Function
PF	Particle FFlow
pPb	Proton-lead (collision data)
pp	Proton-proton (collision data)
pQCD	Perturbative Quantum Chromodynamics
$p_T$	Transverse Momentum
QCD	Quantum Chromodynamics
QGP	Quark Gluon Plasma
RHIC	Relativistic Heavy Ion Collider
SCET <sub>G</sub>	Soft Collinear Effective Theory with Glauber Gluons
SPS	Super Proton Synchrotron
UE	Underlying Event

## SUMMARY

A deconfined phase of matter, referred to as the quark-gluon plasma (QGP), is generated when a large enough energy density is reached by colliding heavy nuclei at ultra-relativistic energies. The properties of the QGP are studied in this work using jets, which are collimated sprays of hadrons produced from the fragmentation of high transverse momentum ( $p_T$ ) quarks and gluons from hard scatterings occurring at the earliest times of a heavy-ion collision. These hard-scattered quarks and gluons subsequently traverse and interact with the QGP, losing energy in a phenomenon known as “jet quenching.” The jets are thus used as in-situ probes to analyze the rich dynamics of the hot and dense QGP medium. The work presented in this thesis uses lead-lead (PbPb) and proton-proton (pp) collision data recorded at a collision energy of  $\sqrt{s_{\text{NN}}} = 5.02 \text{ TeV}$  per nucleon pair, with the CMS detector at the CERN LHC.

Calibrations to the measured jet energy in both pp and PbPb collisions are derived in this work based on the fragmentation patterns of the jets and also using data-driven techniques. The fragmentation-dependent corrections depend on the reconstructed number of constituents within the jet cone and the data-driven techniques are based on events consisting of jets back-to-back with a photon. These corrections improve the overall jet energy response and also mitigate the biases in quark- and gluon-jet reconstruction performance.

The first measurement of jet charge in heavy-ion collisions is carried out in this work. Jet charge is defined as the momentum-weighted sum of electric charges of particles inside a jet, and its sensitivity to the electric charge of the initiating parton can be leveraged to discriminate between quark- and gluon-jets. A template-fitting method is presented to extract the quark- and gluon-jet fractions in pp and PbPb collisions using jet charge templates from simulations. The results are presented differentially in  $p_T$  of the particles used in the measurement, and additionally, as a function of the event centrality, which parameterizes the degree of overlap between the two colliding nuclei. In these studies, no significant modification of the jet charge is observed in different event centrality bins of PbPb collisions, and with respect to pp results, modulo isospin effects. The quark- and gluon-jet fractions extracted from the template-fitting procedure are observed to be relatively unmodified for a sample of jets with  $p_T > 120 \text{ GeV}$  in central PbPb collisions compared to peripheral PbPb and pp results. These results do not support predictions from weak coupling

## SUMMARY (CONTINUED)

models and other recent interpretations of heavy-ion results showing a significant suppression of gluon jets in central PbPb collisions due to medium effects.

Feasibility studies for jet shape measurements with identified particle species are presented in the latter part of this thesis work. Jet shapes, defined as the momentum-weighted distribution of particles around the jet axis are presented for identified protons and pions using information from the proposed Mip Timing Detector in CMS simulation events. The jet shapes are presented as a function of the distance from the jet axis  $\Delta r = \sqrt{(\Delta\eta)^2 + (\Delta\phi)^2}$ , where  $\Delta\eta$  and  $\Delta\phi$  represent the relative pseudorapidity and azimuthal angle with respect to the jet axis, respectively. The corresponding data measurements can provide key breakthroughs in understanding the possible hydrodynamic medium response to the propagating jet.

## 1 INTRODUCTION

Quantum chromodynamics is the theory of strong interaction between quarks and gluons, the fundamental particles that make up protons, neutrons, and other hadrons, which in turn constitute the majority of everyday matter. Particle accelerators, including the Large Hadron Collider at CERN, have aided us in understanding the strong force by colliding hadrons at speeds very close to that of light. They also provide a glimpse into a novel state of matter known as Quark-Gluon Plasma (QGP), that is predicted to have filled the early universe for a microsecond or so. The QGP, a deconfined phase of quarks and gluons, is produced in heavy-ion collisions at particle colliders and behaves as an almost ideal fluid with remarkably small viscosity. The details of a heavy-ion collision including its initial state effects, how the system attains thermal equilibrium, and the dynamics of Quark-Gluon Plasma are not yet very well understood.

The scales of processes occurring in heavy-ion collisions span many orders, from a bath of strongly interacting soft gluons to highly energetic partons that are produced in hard scatterings. The lifespan of QGP formed in these collisions is of the order of  $10^{-22}$  s, making it challenging to probe the dynamics of the rich QCD matter. Exploring different signatures of the QGP, including via “quarkonium” (bound state of  $q$  and  $\bar{q}$ ) and “flow measurements” (quantifying collective expansion of the QGP) at RHIC and LHC experiments, have contributed immensely to our understanding of its properties. Energetic partons produced in hard scatterings at the earliest time of the collision, serve as valuable tomographic probes of the dense QCD matter. As the droplet of QGP formed in heavy-ion collisions expands hydrodynamically and cools, the hard-scattered quarks and gluons traverse through the deconfined medium while interacting with it. Measurements are performed to characterize the interaction strength of the medium using showers of particles known as “jets”, which are used as final-state proxies for the energetic partons. As the partons penetrate and interact with the QGP, they lose energy and undergo modifications to its shower, a phenomenon is referred to as jet quenching. The properties of QGP can be accessed by studying the modifications, or lack thereof, of a plethora of jet variables in heavy-ion collisions compared to the vacuum reference. The measurements presented in this thesis use pp collisions as a vacuum proxy as no QGP is expected to be formed in hadronic collisions.

Two such observables are jet shapes and jet charge, and their measurements in PbPb and pp collisions form a significant portion of the work presented in this thesis. Jet shapes, defined as the transverse momentum-weighted distribution of particles around the jet axis, show a redistribution of jet energy to softer particles ( $p_T < 3$  GeV) and to large distances from the jet axis in heavy-ion collisions compared to the pp reference [2]. Results from these measurements have successfully constrained the relative contributions of different jet quenching mechanisms [7]. The first measurements of jet charge, defined as the transverse momentum-weighted sum of electric charges of jet constituents, are presented in the thesis for heavy-ion collisions along with the pp results [1]. Jet charge is expected to be sensitive to the electric charge of the initiating parton, and is utilized to discriminate between quark and gluon jets. The jet charge distributions are unfolded for detector- and background-effects and provide experimental input to constrain the flavor (quark/gluon) dependence of jet energy loss. These measurements use PbPb and pp data collected at the CMS detector in 2015 at a center-of-mass energy per nucleon pair ( $\sqrt{s_{\text{NN}}}$ ) of 5.02 TeV.

The various aspects of the research presented in this doctoral thesis are structured as follows. The QGP and its properties along with few basic phenomenological observables are introduced in Sec. 2. Jet measurements in heavy-ion collisions are discussed in Sec. 3, and the theory of jet-QGP interaction is summarized in Sec. 4. The design and performance of the LHC and CMS detector are briefly described in Sec. 5. The details of jet and track reconstruction and calibration are presented in Sec. 8 and Sec. 7, respectively. Section 10 summarizes the measurement procedure of jet shapes and their feasibility in future detector facilities. The details of the first heavy-ion jet charge measurements and the subsequent extraction of quark and gluon jet fractions via a template-fitting method are discussed in Sec. 9. Finally, the results and the underlying physics conveyed through these measurements are summarized in Sec. 11.

## 2 THE QUARK-GLUON PLASMA

### 2.1 Quantum chromodynamics and the quark-gluon plasma

Strong interactions, governed by the theory of quantum chromodynamics, are mediated by the exchange of vector gauge bosons known as gluons that act between quarks and other gluons. The interactions between quarks and gluons, referred together as partons, occur via their color charge, represented by three distinct colors, red, blue, and green. The strength of the interactions is characterized by the running coupling constant  $\alpha_s$ . As shown in Eq. (1),  $\alpha_s$  decreases as the momentum exchanged between two partons  $Q$  increases, and their separation decreases [8].

$$\alpha_s(Q^2) \propto \frac{1}{\ln[\frac{Q^2}{\Lambda_{\text{QCD}}^2}]} . \quad (1)$$

$\Lambda_{\text{QCD}}$  is the fundamental energy scale in quantum chromodynamics. QCD implies that the coupling strength ( $\alpha_s$ ) rapidly increases for low momentum transfer processes as a result of the gluon-gluon interaction, and this dependence is shown in Fig. 1. The weak coupling limit ( $\alpha_s \ll 1$ ) corresponds to large momentum transfer ( $Q^2$ ) processes and extremely high temperatures, and can be handled via perturbative QCD techniques. On the contrary,  $\alpha_s$  is large in the region of large separation, leading to the observed confinement of quarks and gluons in bound states known as hadrons. Consequently, at standard room temperature and density conditions, quarks and gluons are found in bound colorless hadron states, either as color-anticolor ( $q\bar{q}$ ) mesons or color-triplet ( $qqq$ ) baryons.

However, in the regime of large  $Q$ , the so-called running of  $\alpha_s$  results in a property known as “asymptotic freedom” as shown in Fig. 1. For quarks bound within a hadron, the force of containment gets weaker and asymptotically approaches zero. Asymptotic freedom can also be achieved by sufficiently increasing the energy density of a system, allowing for the deconfinement of quarks and gluons. Analogous to a plasma of ions, electrons, and photons in quantum electrodynamics, a phase of deconfined quarks and gluons at extremely high temperature and/or density is known as the quark-gluon plasma (QGP). The necessary conditions of extremely high energy density for QGP formation are believed to have existed for a microsecond or so after the Big Bang. This has

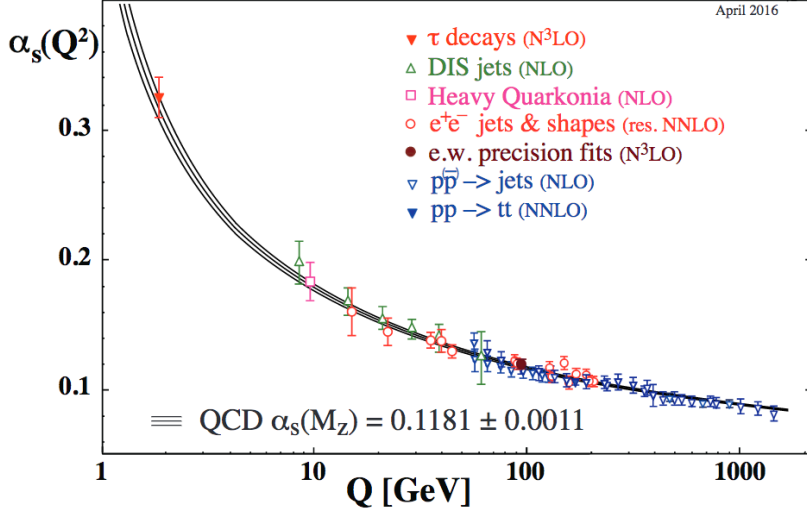


Figure 1. Summary of measurements of  $\alpha_s$  as a function of the energy scale  $Q$ . Figure from [9].

generated a great deal of interest in comprehensively studying the properties and dynamics of QGP in order to better understand the early evolution of the universe.

In the laboratory, relativistic nuclear collisions are currently the only means of achieving high enough energy densities to produce a quark-gluon plasma and probe its transition back into hadronic matter. Exploring QGP dynamics using heavy-ion collisions was first suggested by J. D. Bjorken in the early 1980s [10]. He predicted that the QGP could be generated for a time scale  $\gtrsim 5\text{fm}/c$  at temperatures of  $\gtrsim 200 - 300$  MeV achieved in relativistic nucleus-nucleus collisions. These collisions are achieved by accelerating the electrically-charged heavy nuclei using conventional accelerator facilities and enable the realization of large energy densities of  $\sim 0.5 - 1$  GeV/fm<sup>3</sup>. It was believed that depositing such a large amount of energy into a small volume creates necessary conditions for the hadrons to melt into a gas of weakly interacting quarks and gluons. Studies also laid out key experimental signatures of the short-lived QGP to look out for in heavy-ion collisions, including enhancements of strange (heavy) quarks and higher rates of direct dilepton and photon production compared to collision systems without any QGP effects [11, 12].

The first heavy-ion collisions began in the mid-1980s with fixed-target experiments, in which CERN's Super Proton Synchrotron (SPS) fired very-high-energy beams of lead ions into gold or lead targets. Observations of a suppressed  $J/\psi$  meson (charmonium state) yield from the NA45

experiment among other results from the SPS prompted the announcement of ‘a new state of matter, in which quarks and gluons are “deconfined”’ [13, 14].

Although the earlier claim is debatable, the formation of QGP in relativistic heavy-ion collisions was confirmed shortly thereafter by experiments at the Relativistic Heavy Ion Collider (RHIC) in Brookhaven National Laboratory [15]. However, measurements from these experiments contradicted earlier ideas that the medium produced in these collisions was a weakly coupled plasma of quarks and gluons. Instead, clear signatures of collective behavior (Sec. 2.5) and suppression of energetic particles (Sec. 2.6) were observed, establishing that the QGP behaves more like a strongly coupled near-perfect fluid of quarks and gluons. Since then, experiments at RHIC (BRAHMS, PHENIX, PHOBOS, and STAR) have extensively characterized the medium properties and evolution of the QGP in a wide range of center-of-mass-energies from 7.7 to 200 GeV per nucleon pair [16, 17, 18, 19]. More recently, since heavy-ion collisions began at the Large hadron Collider (LHC) in 2010, results from four collaborations at CERN (CMS, ATLAS, ALICE, and LHCb) have further advanced our understanding of the hot and dense QCD medium by focusing on QGP measurements at much higher center-of-mass-energy scales from 2.76 to 5.02 TeV per nucleon pair [20].

## 2.2 Thermodynamics of the quark-gluon plasma

A phase diagram, as shown in Fig. 2 (right), with temperature on the y-axis and baryochemical potential  $\mu_b$  on the x-axis, is helpful in understanding the features of QCD matter under different conditions. The baryochemical potential of a system ( $\mu_b$ ) parametrizes the excess of quarks over antiquarks in a system. Specifically, it refers to the energy needed to increase the system’s baryon number by one unit. Everyday matter at standard room temperature and density conditions reside within the hadron gas region in the phase space diagram.

Perturbative QCD (pQCD) techniques, which are effective computational tools in studying large  $Q^2$  processes, break down in the phase space of QGP formation. Instead, lattice QCD calculations help explore the behavior of a system of bound state hadrons with increasing temperature [21]. Lattice calculations at  $\mu_b = 0$ , shown in Fig. 2 (left), demonstrate a sharp but continuous rise in the energy density, pressure, and entropy divided by different powers of the temperature at a critical temperature ( $T_c$ ) of around 155 MeV. The rapid increase in the thermodynamic quantities at  $T_c$  is

characteristic of a phase transition with an increase in the number of degrees of freedom due to the deconfinement of quarks and gluons. The condition of  $\mu_b = 0$ , implying no excess of quarks over antiquarks, is a very good approximation for the particles produced in the mid-rapidity region of LHC collisions and an even better approximation for the conditions of the microseconds old universe. The thermodynamic quantities start flattening at a higher temperature, although to a value  $\sim 10\%$  lower than that expected for a non-interacting ideal gas. Owing to the asymptotically free nature of QCD, the thermodynamic quantities are anticipated to eventually reach the Stefan-Boltzmann limit of an ideal gas at much higher temperatures, shown with a dotted line in Fig. 2 (left).

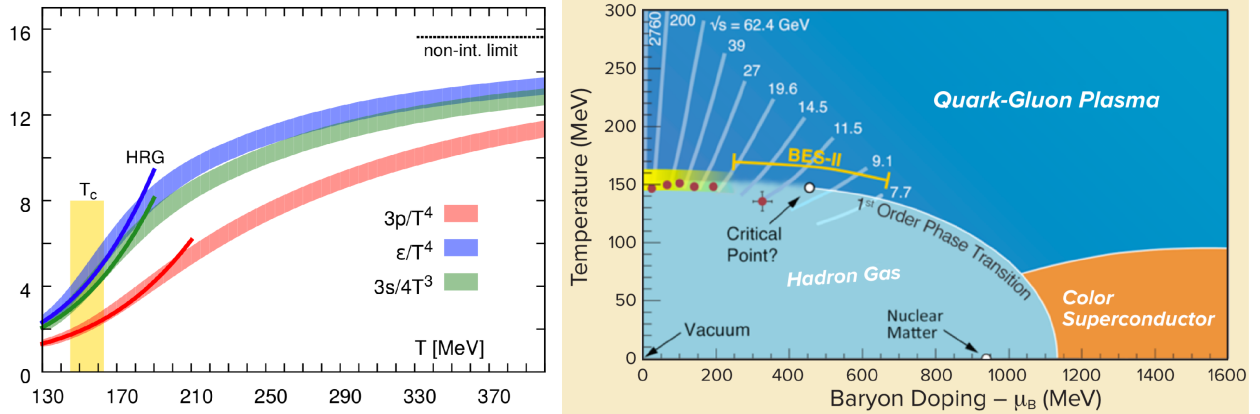


Figure 2. **Left:** Pressure ( $p$ ), energy density ( $\epsilon$ ) and entropy ( $s$ ) divided by different powers of the temperature ( $T$ ), for a QCD system at  $\mu_b = 0$ , showing a smooth transition at  $\sim 155$  MeV. **Right:** QCD phase space diagram as a function of baryochemical potential  $\mu_b$  and temperature  $T$ . The transition between QGP and hadron gas is represented as a continuous crossover at low  $\mu_b$  with a yellow band. Figures from Ref. [22] and Ref. [21].

At low values of  $\mu_b$ , the transition from a hadron gas phase to a deconfined QGP phase, shown with a yellow band in Fig. 2 (right), is a continuous crossover without any discontinuities. The smooth crossover at low  $\mu_b = 0$  values is predicted to turn into a first-order phase transition at sufficiently large  $\mu_b$ , suggesting the existence of a tri-critical point somewhere along the phase boundary [23]. Determining whether such a tri-critical point exists is one of the primary goals of the RHIC Beam Energy Scan (BES) program, where collisions are studied at varying center-of-mass energies ranging from 7.2 to 200 GeV to probe temperatures surrounding  $T_c$  [24]. QCD matter at high  $\mu_b$  and low temperatures are predicted to be found in the center of neutron stars, in the form of a new phase called color superconductors. Very little is currently known about color

superconductors and accessing this phase space region directly via experiments in the laboratory is presently unfeasible.

Heavy-ion collisions at RHIC and LHC energies present a unique opportunity to study the evolution of QCD matter from deconfined QGP to hadrons. An immense amount of energy is deposited in the region between the colliding nuclei, very quickly creating a hot QGP in thermal equilibrium between them. The QGP then expands and cools for an effective lifetime of the order of  $10^{-22}$  s before transitioning into a hadron gas. The estimated evolution trajectories of the hot QCD matter produced in LHC and RHIC collisions are shown on the phase space diagram in Fig. 2 (right).

### 2.3 Time-evolution of a heavy ion collision

A summary of our understanding of the different stages of a heavy-ion collision is presented below and the corresponding graphic depiction at different time scales is shown in Fig 3 [25].

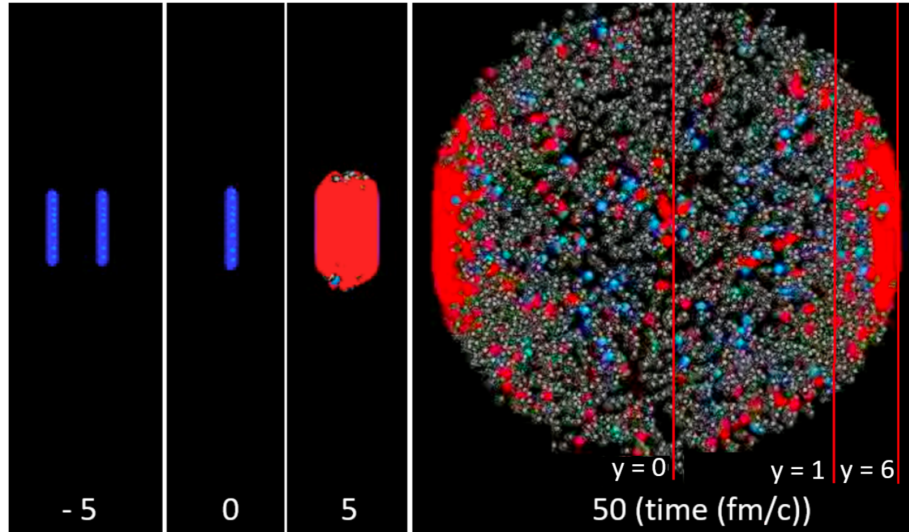


Figure 3. An illustration of the evolution of a heavy ion collision at different timestamps. The red regions represent the QGP formed in the collision. Silver and blue particles in the right frame represent mesons and baryons, respectively, free-streaming towards the detector. Figure from Ref. [26].

**1. Initial state :** Two nuclei (diameter  $\sim 14$  fm in case of Pb nuclei) are accelerated close to the speed of light, and are consequently extremely Lorentz contracted into flat-discs along the beam axis to a thickness of  $14/\gamma$ . The relativistic  $\gamma$  factor is 2500 corresponding to a LHC center-of-mass

energy of 5.02 TeV per nucleon pair. The approaching Pb discs each have 208 nucleons, with every nucleon containing three excess quarks than antiquarks, along with gluons. The momentum of each nucleon is a superposition of the momentum of each of its constituents. The two nuclei approach each other with an impact parameter  $b$ , and this decides the degree of overlap between the nuclei.

**2. Thermalization :** An immense amount of energy is deposited between the discs once they collide. A majority of the interactions between the two nuclei are low  $Q$  processes and only a very small fraction of the incident partons undergo hard scatterings. After a time period of 1 fm/c following a head-on collision, the average energy density between the nuclei is calculated to be around 12 GeV/fm<sup>3</sup>, far above that of a hadron ( $\sim 500$  MeV/fm<sup>3</sup>). The system equilibrates and thermalizes very quickly into a strongly coupled liquid of QGP within a time scale of 1 fm/c. The mechanism of how a far-from-equilibrium system thermalizes rapidly is not very well understood [27].

**3. Hydrodynamization :** The resulting thermalized QGP consists of deconfined quarks and gluons, strongly coupled to its neighbors, and behaves as a near-perfect liquid with extremely low specific viscosity ( $\eta/s \approx 0.16$ ) [28]. The specific viscosity is defined as the ratio of a liquid's shear viscosity  $\eta$  to its entropy density  $s$ , and is used to characterize how well it can be described by ideal fluid dynamics. The QGP continues to cool and expand hydrodynamically in all directions for a time scale of 10 fm/c in the lab frame. The energy density profile of the dilating QGP is also observed to be very sensitive to the initial shape of the nuclear collision overlap region [29].

**4. Hadronization :** The QGP continues to expand and cool until the energy density at a given point falls below that of a hadron. Following this, quarks and gluons combine to form a gas of hadrons and this process is known as “chemical freeze-out”. Based on the relative abundance of the different final particle species near mid-rapidity, in RHIC and LHC central heavy-ion collisions, the chemical freeze-out has been measured to occur at a temperature of about 155 MeV [30, 31]. The system of hadrons in a state of chemical-freeze out continues to interact elastically, expanding and cooling further until it reaches a point of “kinetic freeze-out”. The hadrons cease to interact with each other following the kinetic freeze-out, and the momenta of the final state particles are fixed [30].

**5. Free-streaming :** The final state hadrons then stream outwards freely, eventually reaching the detectors. The full event is reconstructed using the spatial and momentum distribution information of the final state particles as measured by the detector.

Fig. 3 represents the different stages of a heavy-ion collision, and the right frame shows the final state hadrons streaming towards the detector. A plethora of experimental signatures can be used to probe the rich dynamics of QGP at different stages of its evolution. A few basic phenomenological observables in a heavy-ion collision are briefly described below before jumping into signatures of the QGP.

## 2.4 Event kinematics and centrality

Following the convention in high-energy physics, results and measurements in this thesis are presented in natural units, i.e., with  $\hbar = c = 1$ . This implies that different quantities including energy, mass, momenta, and temperature are all measured in units of eV. The relativistic energy–momentum equation, relating a particle’s rest mass, total energy, and momentum is shown below in Eq. (2):

$$E^2 = p_x^2 + p_y^2 + p_z^2 + M^2 . \quad (2)$$

Conventionally, in high energy collider physics, the direction along the colliding beam is assigned the z-axis with the azimuthal ( $\phi$ ) axis spanning a transverse plane perpendicular to the beam. Instead of directly using the polar angle, we define rapidity ( $y$ ) as shown in Eq. (3) due to the relativistic nature of the collisions.

$$y = \frac{1}{2} \ln \left( \frac{E + p_z}{E - p_z} \right) . \quad (3)$$

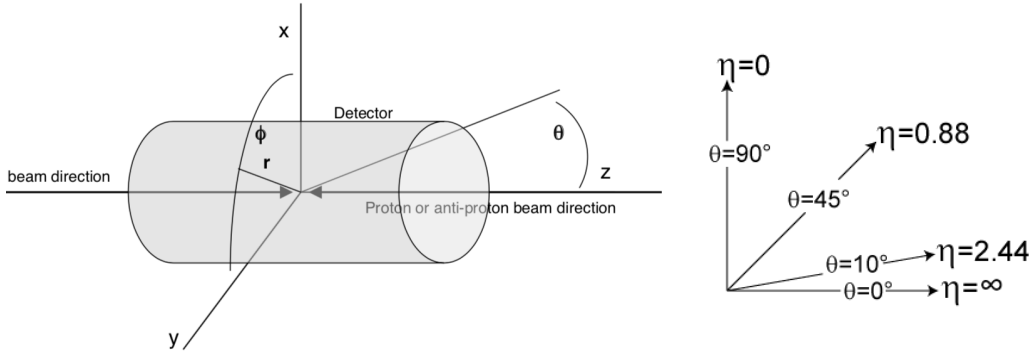


Figure 4. **Left:** Cylindrical coordinate system used in high-energy collider physics measurements. **Right:** Relation between polar angle  $\theta$  and pseudorapidity  $\eta$ . Figures from Ref. [32] and Ref. [33].

Rapidity is a Lorentz-invariant quantity and varies between 0 and  $\infty$  for transverse and parallel orientations relative to the beam axis, respectively. However, in practice, the mass and energy of the detected particles are not directly measurable. We, therefore, turn to a quantity known as 'pseudorapidity' ( $\eta$ ), defined in Eq. (4) as:

$$\eta = \ln \left( \frac{|\vec{p}| + p_z}{|\vec{p}| - p_z} \right) . \quad (4)$$

Pseudorapidity is Lorentz-invariant for particles with zero rest mass. This is a very good approximation for particles produced in relativistic collisions, given their rest mass is negligible compared to their total energy. It can also be calculated directly from the polar angle  $\theta$  of an outgoing particle as shown in Eq. (5):

$$\eta = -\ln \left[ \tan \left( \frac{\theta}{2} \right) \right] . \quad (5)$$

The relation between different values of the polar angle ( $\theta$ ) and pseudorapidity ( $\eta$ ) are shown in Fig. 4 for clarity. For a given z position, pseudorapidity ( $\eta$ ) from 0 to  $\infty$  and the azimuth ( $\phi$ ) from 0 to  $2\pi$  in radians can be used to describe the entire spatial configuration of a system.

In heavy-ion collisions, the impact parameter  $b$  of the approaching nuclei significantly affects the physics of the ensuing processes. The fraction of overlap between the discs decides the initial geometry and size of the QGP, including whether QGP is formed in the first place. Collisions can vary from being entirely head-on to barely grazing as they pass each other, and anything in between corresponds to a lenticular shaped nuclei overlap region as illustrated in Figs. 5 (left) and 6. The initial geometry of the colliding nuclei overlap region and the energy density fluctuations in the nuclei influence the shape of the resulting QGP. The degree of overlap or the "centrality" of a collision is expressed as a percentage quantile, ranging from 0% (most central) to 100% (most peripheral). For example, the 0 – 10% centrality class refers to the 10% events with the smallest impact parameter in a given sample, while 90 – 100% centrality refers to the 10% events having the least degree of overlap.

The impact parameter cannot be measured directly for a given collision, however, reliable control has been achieved in inferring it on an event-by-event basis from other experimental

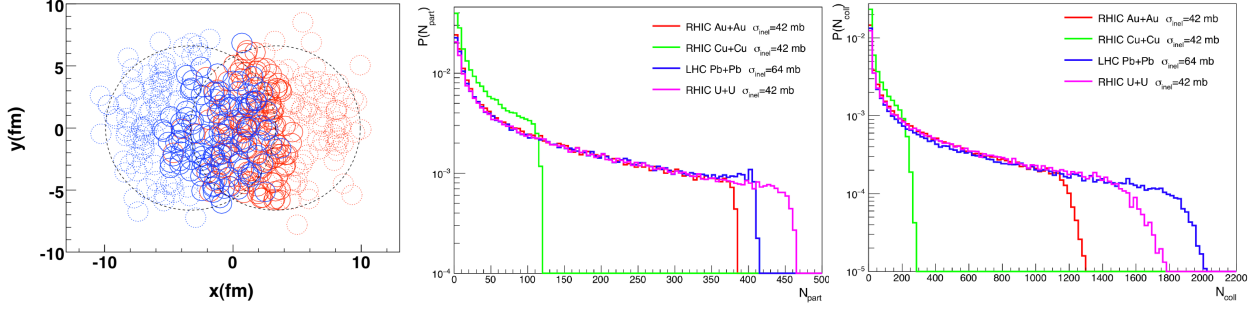


Figure 5. **Left:** Simulation of a PbPb collision at LHC with an impact parameter  $b \approx 7$  fm. Participant nucleons ( $N_{\text{part}}$ ) are shown with solid circles and spectators with dotted circles. **Middle and Right:** Distributions of  $N_{\text{part}}$  and  $N_{\text{coll}}$  in different collision systems at RHIC and LHC according to Glauber calculations. Figures from Ref. [34].

observables. In a collision event, the number of participating nucleons ( $N_{\text{part}}$ ) and the number of binary collisions ( $N_{\text{coll}}$ ) aid us in interpreting the degree of overlap of the discs. It is assumed that the  $N_{\text{part}}$  and  $N_{\text{coll}}$ , and by extension  $b$ , are monotonically related to the number of particles produced and/or the total energy deposited in a collision. Theoretical models known as “Glauber model calculations” [35] characterize the relations between these quantities and the collision centrality, and are discussed further in Sec. 6.2.1.

## 2.5 Collectivity in the quark-gluon plasma

The strongly coupled nature of an almost hydrodynamically ideal QGP liquid implies that any initial spatial anisotropies in the azimuthal plane could manifest in the form of anisotropies in the final momentum configuration. These anisotropies could arise from either the lenticular shape of the nuclei overlap region or from local energy density fluctuations in the incoming nuclei. If the QGP were a weakly interacting gas of quarks and gluons in random motion or a highly viscous liquid, the initial azimuthal anisotropies produced in the collision would be washed out and would result in an isotropic expansion. Instead, the non-circular geometry of the QGP formed in off-central collisions translates into a faster hydrodynamic expansion in the direction of larger gradients (Fig 6). The anisotropies, referred to as “collective flow”, are only minimally dampened in the thermalization and hydrodynamization phases of the evolution and survive through hadronization and free-streaming stages as well [36]. The azimuthal anisotropy in the spatial momentum distribution can be directly

observed in a sample reconstructed PbPb collision event display from the CMS detector as shown in Fig 6.

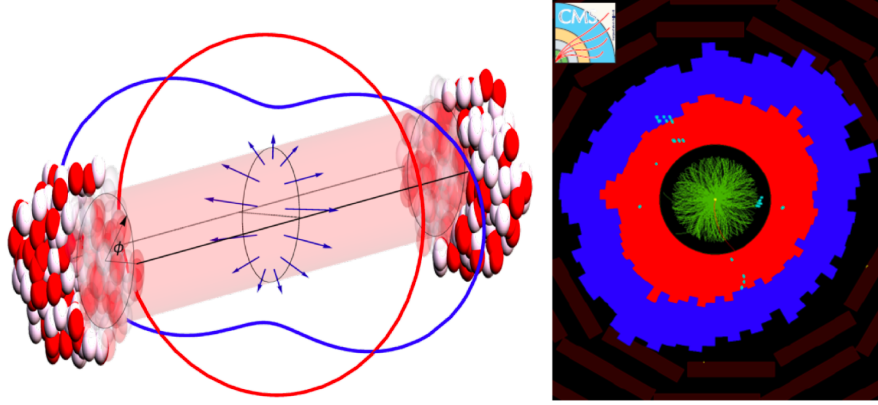


Figure 6. **Left:** Illustration of an off-central heavy-ion collision with a lenticular overlap region resulting in anisotropic gradients in the azimuthal plane. **Right:** Cross-section of a PbPb event reconstructed in the CMS detector. The azimuthal anisotropy is evident from the distribution of charged tracks (green) and energy deposited in the electromagnetic and hadronic calorimeters (red and blue respectively). Figures from Ref. [37]

The angular distribution of the hadrons with respect to the reaction plane ( $\psi_{RP}$ , the plane spanned by the impact parameter  $\vec{b}$  and the direction of the beam  $\vec{z}$ ) of an event can be factorized via a Fourier transformation to quantify its momentum anisotropy. The factorization into the different order flow harmonics is shown below in Eq. (6).

$$\frac{dN}{d\phi} = \frac{N}{2\pi} \left( 1 + 2 \sum_n v_n \cos(n(\phi - \psi_{RP})) \right), \quad (6)$$

where  $\phi$  is the azimuthal angle,  $N$  is the total number of particles in the event, and  $v_n$ 's are referred to as the “harmonic flow coefficients”. The different  $v_n$  coefficients, shown in Fig. 7 (right) for PbPb collisions, carry information about the corresponding order anisotropies in the initial state and constrain the specific viscosity of the QGP liquid. The flow of particles in the plane transverse to the colliding beams, known as “directed flow”, is quantified by the first-order coefficient,  $v_1$ . The second-order coefficient,  $v_2$ , relates to the elliptic flow component of the anisotropy originating from the lenticular overlap of the colliding nuclei. The higher-order coefficients like  $v_3$  (triangular flow) and so on are a result of the fluctuations or lumpiness in the initial nuclei energy density.

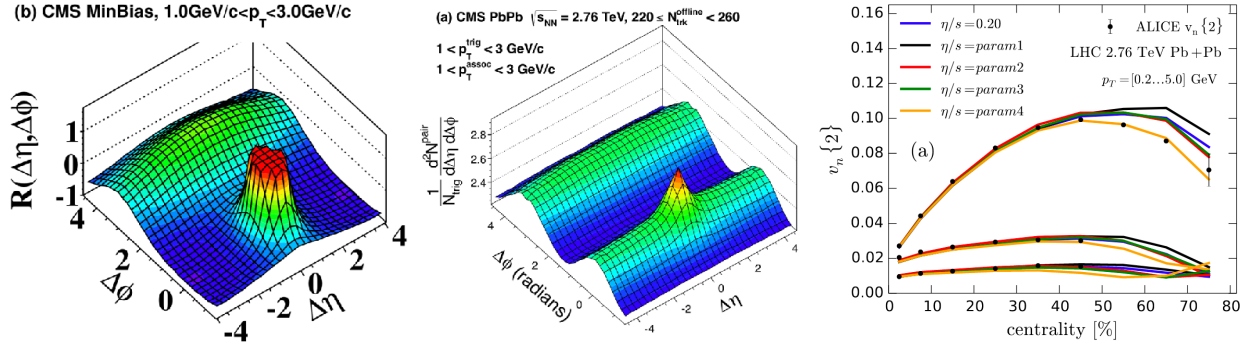


Figure 7. **Left and Middle:** 2D maps of dihadron correlations from pp (left) and PbPb (middle) collisions by the CMS experiment. The near side ridge at large  $\Delta\eta$  is observed in PbPb but is absent in pp collisions. **Right:** Predictions for  $\eta/s$  from a hydrodynamic model for different temperature conditions compared with ALICE measurements of the  $v_n$  coefficients ( $n = 2$  to  $4$  from top to bottom). Figures from Ref. [38], [39] and [40].

Two- and multi-particle correlations are also utilized to measure the azimuthal anisotropies and harmonic flow coefficients. In two-particle correlation studies, the relative pseudorapidity ( $\Delta\eta$ ) and relative azimuth ( $\Delta\phi$ ) are measured between a particle in a specified momentum range (trigger particle) and all other particles in the same event (associated particles). Two-dimensional histograms showing  $\Delta\eta$  and  $\Delta\phi$  between the triggered and associated particles are shown in Fig. 7 (left and middle) for pp and PbPb collisions as measured by the CMS detector. An away-side (referring to  $\Delta\phi \approx \pi$ ) peak, is expected due to the conservation of momentum. The away-side peak is smeared as a function of  $\eta$  because of the different momentum fraction carried by the different partons of a nucleon. The shower originating from a high-transverse momentum ( $p_T$ ) parton contributes to a jet-like peak at  $(\Delta\eta, \Delta\phi = 0, 0)$ . Finally, the observed ridge at large  $\Delta\eta (> 1)$  on the near-side of the triggered particle is a consequence of the predicted elliptic ( $v_2$ ) and higher-order ( $v_3, v_4$ , etc.) flow coefficients. The 2D map is projected over large  $\Delta\eta$  region ( $\Delta\eta > 1$ ), onto the  $\Delta\phi$  axis and is fit with Fourier functions to extract the  $v_n$ 's [38, 39].

The resulting  $v_n$ 's from two-particle correlation measurements are shown in Fig. 7 (right) as a function of the collision centrality. The elliptic flow, parametrized by  $v_2$ , is roughly independent of  $\eta$  and is observed to be the strongest in mid-central collisions (40 – 50%) due to the lenticular nature of the initial nuclear overlap region. The  $v_n$  measurements, in comparison to calculations

from a hydrodynamic model with temperature-dependent parametrization of  $\eta/s$ , constrain the specific viscosity of the medium.

The possibility of QGP formation in smaller collision systems was sparked by non-zero  $v_n$  measurements in high-multiplicity pPb and pp collisions. Fig. 8 shows the ridge at large  $\Delta\eta$  is still present in high-multiplicity pPb and pp collisions, but disappears for high-multiplicity  $e^+e^-$  collisions. These results have prompted questions regarding how small of a collision system can still produce QGP [41].

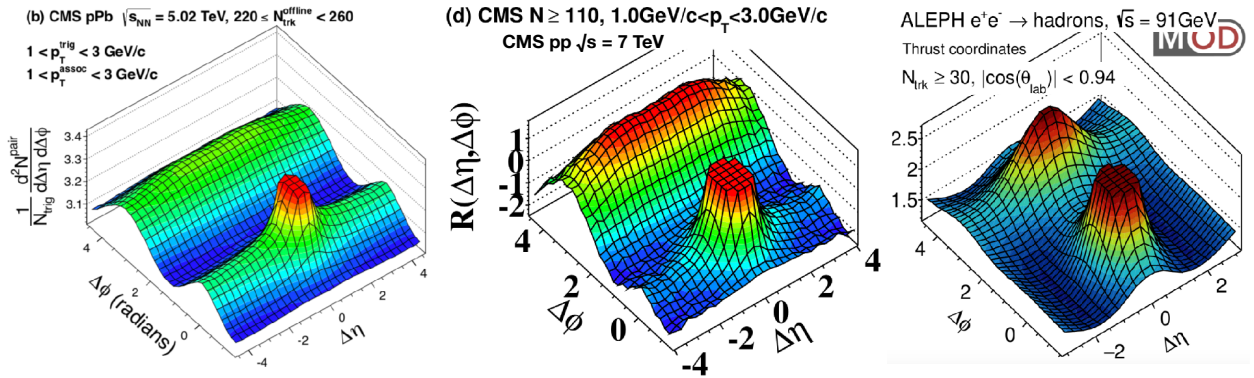


Figure 8. 2D maps of dihadron correlations from high-multiplicity pPb (left), pp (middle) and  $e^+e^-$  (right) collisions by the CMS and ALEPH experiments. The near side ridge at large  $\Delta\eta$  is observed in pPb and pp collisions but is absent in  $e^+e^-$  collisions. Figures from Ref. [38], [39] and [42].

## 2.6 High- $p_T$ parton suppression

While most of the interactions in relativistic collisions are soft (low- $Q$ ) processes, very rarely two partons from the colliding nuclei undergo a hard scattering at the earliest time of the collision. The hard scatterings produce a pair of back-to-back high- $p_T$  partons or electroweak bosons at large angles relative to the beam axis. The pair of energetic quarks or gluons, produced in the large-angle scattering, undergo fragmentation and hadronization before reaching the detector. The large momentum transfer scales (or low  $\alpha_s$ ) involved in the hard scatterings imply that the production of high- $p_T$  partons,  $\gamma$ , and W/Z bosons could be well described by perturbative QCD (pQCD) calculations. The total cross-section of the final-state high- $p_T$  hadrons in pp collisions can be factorized into its different stages with varying  $Q$  scales as shown in Eq. (7):

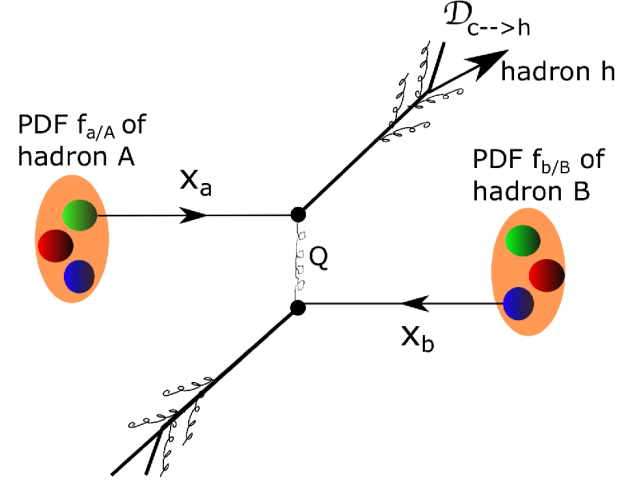


Figure 9. Illustration of a hard scattering process involving large momentum transfer. ( $A + B \rightarrow \text{hadron}$ )

$$\sigma_{AB \rightarrow \text{hadron}}^{\text{hard}} = f_{a/A}(x_a, Q^2) \otimes f_{b/B}(x_b, Q^2) \otimes \sigma_{AB \rightarrow C}^{\text{hard}} \otimes D_{C \rightarrow \text{hadron}}(z, Q^2). \quad (7)$$

Here,  $\sigma_{AB \rightarrow C}^{\text{hard}}$  is the hard-scattering cross-section and for low enough values of  $\alpha_s$ , it can be calculated fairly precisely from perturbative QCD calculations. The parton distribution functions (PDFs) of the incoming nucleons are represented by  $f_{a/A}(x_a, Q^2)$  and  $f_{b/B}(x_b, Q^2)$ , and are modified compared to those constructed from free-proton PDFs (Fig. 20). The last term,  $D_{C \rightarrow \text{hadron}}(z, Q^2)$  represents the final state parton branching and its hadronization, known as “fragmentation function”. The low  $Q^2$  processes involved in PDFs and fragmentation functions call for a non-pQCD approach to its measurement. Global fitting to various experimental measurements form  $e^+e^-$  collisions at the LEP and other DIS experiments have successfully constrained the PDF and fragmentation function quantities. Finally, Dokshitzer-Gribov-Lipatov-Altarelli-Parisi (DGLAP) equations [43, 44, 45] can be used to extrapolate the measurements from global fits to different  $\alpha_s$  scales. Along with PDF and  $D(z, Q^2)$  measurements, QCD factorization has proven to be a remarkable tool in comprehensively describing the production, fragmentation, and hadronization of hard partons in pp collisions.

In heavy-ion collisions, the well-calibrated high- $p_T$  partons provide a unique window into understanding the properties of the QGP, as the hard-scattered objects are produced even before the QGP thermalizes. The energetic quarks and gluons traverse the entire evolving QGP while interacting with the hot medium, resulting in the parton’s energy loss and a modification in the

fragmentation function, collectively referred to as “jet quenching” [46]. The partons lose energy while penetrating the QGP due to elastic scatterings with the medium constituents and also from a medium-induced gluon Bremsstrahlung radiation [47, 48]. The parton shower could also be modified by possible medium-induced changes to fragmentation functions, represented in the above Eq. 7 by  $D_{C \rightarrow \text{hadron}}(z, Q^2)$ . The modifications to the parton energy and shower in the medium are explored using various phenomenological high- $p_T$  observables.

The emerging high- $p_T$  hadrons from heavy-ion collisions carry a wealth of information regarding the medium’s properties, including its temperature and viscosity. Firstly, due to the color interactions with the medium, an overall decrease in the average energy of high- $p_T$  partons is expected in the QGP compared to the vacuum reference. Consequently, the yield of high- $p_T$  hadrons is suppressed in heavy-ion collisions compared to pp events, and the corresponding energy loss is parametrized using  $R_{\text{AA}}$  measurements.  $R_{\text{AA}}$ , or the nuclear modification factor as shown in Eq. (8), is defined as the ratio of yield in nuclear collisions scaled by the number of binary collisions ( $N_{\text{coll}}$ ) to that in pp [49].

$$R_{\text{AA}}(p_T) = \frac{1}{\langle N_{\text{coll}} \rangle} \frac{dN^{\text{AA}}/dp_T}{dN^{\text{pp}}/dp_T} = \frac{1}{T_{\text{AA}}} \frac{dN^{\text{AA}}/dp_T}{d\sigma^{\text{pp}}/dp_T}, \quad (8)$$

$$\text{and } T_{\text{AA}} = N_{\text{coll}}/\sigma_{\text{inel}}^{\text{pp}}. \quad (9)$$

The nuclear overlap function ( $T_{\text{AA}}$ ) is defined as the ratio of  $\langle N_{\text{coll}} \rangle$  with the total inelastic cross-section of pp collisions ( $\sigma_{\text{inel}}^{\text{pp}}$ ), and can be calculated from a Glauber model as elaborated in Sec. 6.2.1 [35]. The variable  $T_{\text{AA}}$  is generally used in place of  $N_{\text{coll}}$  in  $R_{\text{AA}}$  measurements as it can be calculated more accurately. The variable  $\sigma$  is the total inelastic proton-proton cross-section for the sample used in the measurement. The  $R_{\text{AA}}$  measurements from different experiments, and for different particles, are shown in Fig. 10 as a function of the transverse momentum ( $p_T$ ) and a significant suppression is observed in the yield of high- $p_T$  charged hadrons [50, 51]. Charged hadron  $R_{\text{AA}}$  measurements shown in Fig. 10 (right) exhibit a continuous rise with increasing  $p_T$  and indicate very little suppression for hadrons with  $p_T > 200$  GeV. No suppression is observed for high- $p_T$  charged hadron yield in pPb collisions in Fig. 10 (left) indicating the lack of QGP formation in smaller collision systems. Measurements are also shown for particles with no color charge, like

$\gamma$ , W and Z bosons which are not expected to interact with the QGP. The  $R_{AA}$  for the colorless probes is observed to be consistent with unity as expected, which also serves as a check for the  $N_{coll}$  and  $T_{AA}$  scaling.

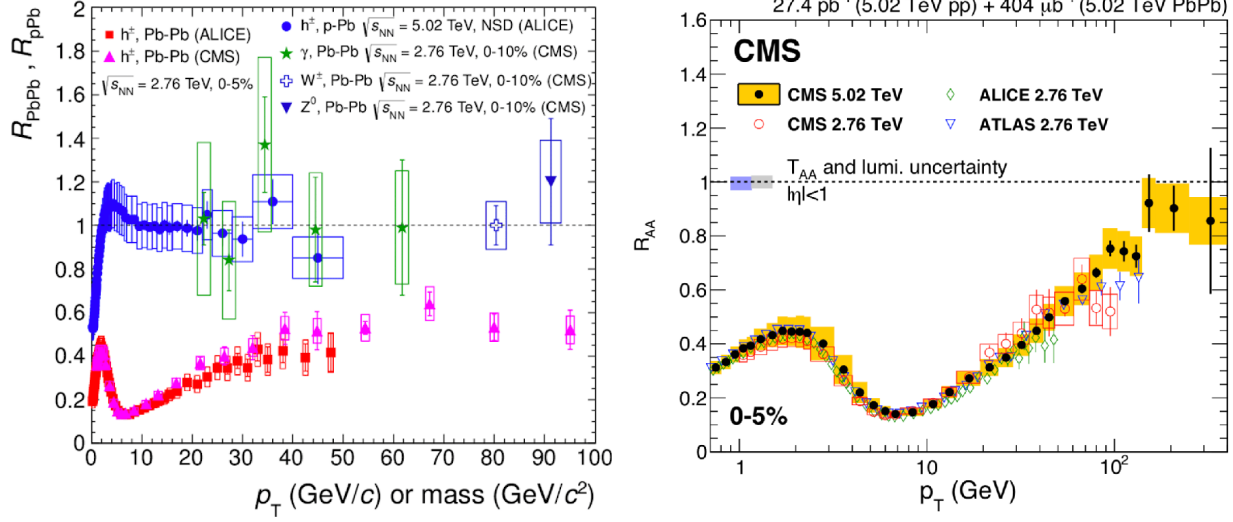


Figure 10. **Left:**  $R_{AA}$  measurements for charged particles,  $\gamma$  and electroweak bosons in PbPb and for charged particles in pPb collisions as measured by the ALICE Collaboration. **Right:**  $R_{AA}$  measurements from CMS for charged particles with  $p_T$  up to 400 GeV and at collision energies of 2.76 and 5.02 TeV per nucleon pair. Both measurements are shown for the 0 – 5% centrality bin in PbPb collisions. Figures from Ref. [51] and Ref. [50]

High- $p_T$   $R_{AA}$  measurements in CMS are carried out using collision events recorded by triggering on an energetic hadron. This biases the  $R_{AA}$  towards partons with a narrow fragmentation shower, consisting of one very hard hadron, which are more likely to be quarks than gluons. This bias of systematically rejecting wider partonic showers, with softer particles, becomes stronger at higher  $p_T$  resulting in an upward trend for the charged particle  $R_{AA}$ . Instead, topological clusters known as “jets” are used as parton proxies to mitigate this bias and increase the sensitivity towards the initial hard parton. This is discussed in detail in the following chapter.

### 3 JET TOMOGRAPHY OF THE QUARK-GLUON PLASMA

#### 3.1 Jet as a parton proxy

Hard perturbative scatterings in relativistic collisions produce energetic quarks, antiquarks, and gluons, which fragment, radiate, hadronize, producing a collimated cone-shaped spray of particles, referred to as a jet. Fully reconstructed jets are observed to connect better to the energy and direction of the initial hard-scattered parton compared to measuring high- $p_T$  hadrons. Total cross-sections for jets can be calculated similarly to that of high- $p_T$  hadrons, within the framework of the QCD factorization paradigm due to the large momentum transfer involved in its production. The formation and evolution of jets in vacuum have been studied extensively at  $e^+e^-$  (LEP, SLC),  $ep$  (HERA), and  $pp$  (Tevatron, RHIC, LHC) colliders and is currently very well understood [43, 45, 44]. Various jet clustering algorithms, which are infrared and collinear (IRC) safe, have been developed iteratively for different measurements and this is elaborated in Sec. 8.1.

#### 3.2 Probing the quark-gluon plasma with jets

Jets produced in ultra-relativistic heavy-ion collisions have to traverse and interact with the QGP, and can provide crucial insight into the internal structure and properties of the dense QCD matter [47, 52]. As a parton passes through the strongly coupled QGP liquid, it loses energy and longitudinal momentum (quenching), gains momentum transverse to its original direction (momentum broadening), and deposits energy into the thermal medium (wake). The theory regarding different quenching mechanisms and quark/gluon flavor-dependent energy loss models is discussed in Sec. 4.

The presence of a large background in heavy-ion collisions due to the enormous initial entropy creates non-trivial obstacles in the course of heavy-ion jet reconstruction. This background, or the “underlying event” (UE), is produced from unrelated parton interactions among other sources. The contribution of the underlying event to the jet needs to be properly subtracted to obtain the true momentum of the jet and this is elaborated further in Sec 3.2.

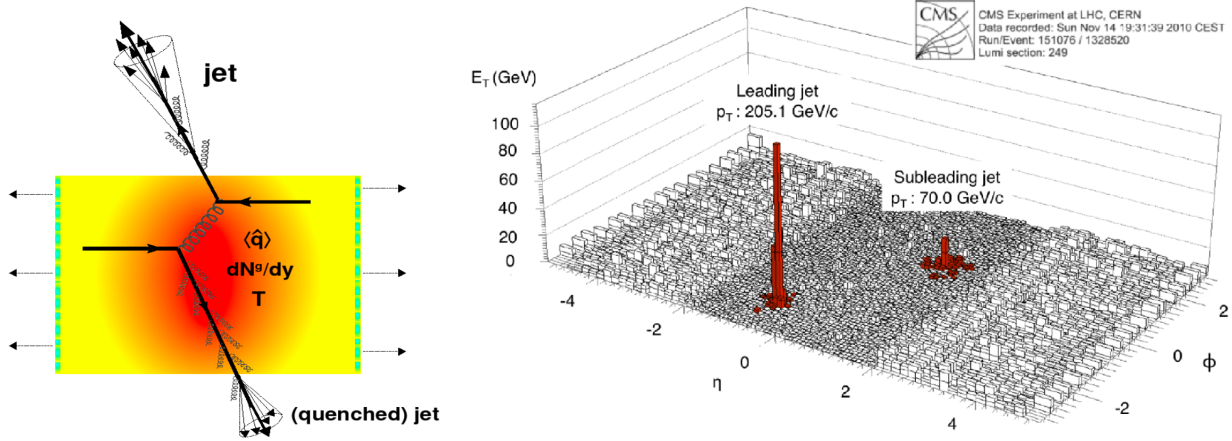


Figure 11. **Left:** An illustration of a dijet produced in a hard scattering close to the surface of QGP in a heavy-ion collision. One of the partons has to traverse through a substantially longer path length in the QGP leading to an asymmetric dijet in the final state. **Right:** PbPb collision event with an asymmetric dijet recorded by the CMS detector. Figures from Ref. [47] and Ref. [53].

### 3.3 Jet $R_{AA}$ and dijet asymmetry

A wide variety of jet measurements have been performed in heavy-ion collisions and in a vacuum reference, to obtain a detailed picture of the full jet evolution in QGP. Extensive  $R_{AA}$  measurements have been performed for jets to parametrize parton energy loss. Inclusive jet  $R_{AA}$  results are shown in Fig. 12 (left) for two different centrality classes. A significant suppression is observed in the jet yield, with a strong dependence on the collision centrality. Jet  $R_{AA}$  measurements include contributions from partons with softer and wider fragmentation showers, which are systematically missed in high- $p_T$  hadron measurements. The jet  $R_{AA}$  for central collisions thereby remains relatively suppressed even at very high energies (1 TeV) unlike the biased charged particle  $R_{AA}$  [54, 55].

The energy loss experienced by a propagating parton depends on its initial energy, the width of its shower and path length in the QGP among other factors. This is evident from dijet asymmetry results, which were the first jet quenching measurements performed with fully reconstructed jets. CMS and ATLAS Collaborations jointly confirmed a strong modification of energy balance in back-to-back dijets produced in PbPb collisions relative to the pp reference and embedded Monte Carlo (MC) simulations. Compelling differences in the measured energies of azimuthally opposite jets can also be observed in individual reconstructed PbPb events shown in Fig. 11(right). Figure 12

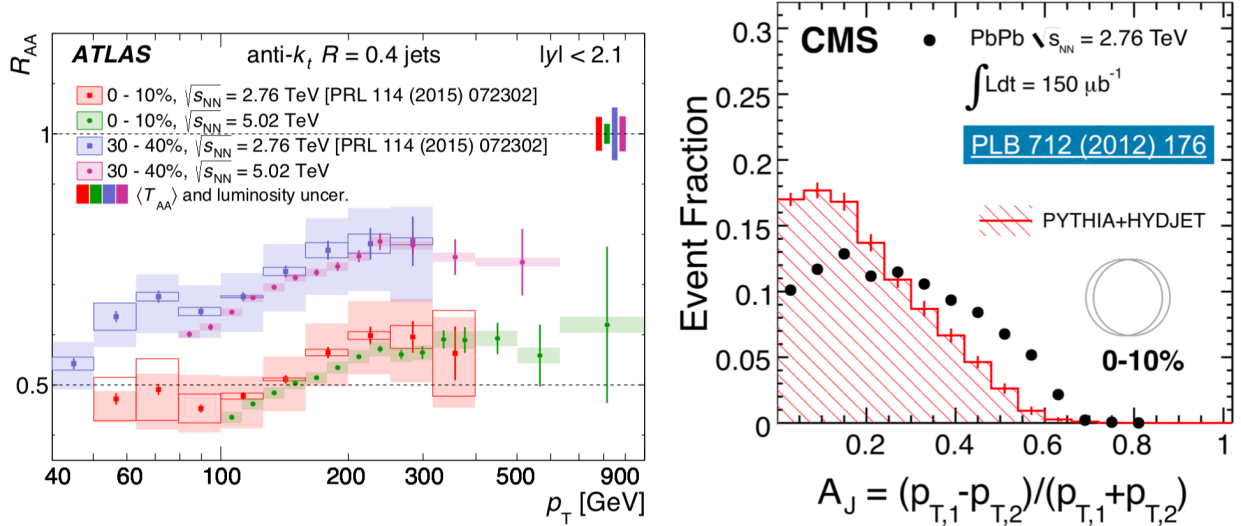


Figure 12. **Left:** Jet  $R_{AA}$  measurements by ATLAS for PbPb collisions in two centrality bins and recorded at different collision energies. **Right:** Dijet asymmetry ( $A_J$ ) measurements by CMS shown for the 0 – 10% centrality bin in PbPb collisions, compared to predictions from PYTHIA+HYDJET. Figures from Ref. [54] and Ref. [53].

(right) shows measurements of the dijet asymmetry ( $A_J$ ), as defined in Eq. (10), for central PbPb collisions, compared to predictions simulations without any quenching effects.

$$A_J = \frac{p_{T,1} - p_{T,2}}{p_{T,1} + p_{T,2}} , \quad (10)$$

In Eq. 10,  $p_{T,1}$  and  $p_{T,2}$  are the measured transverse momenta of the pair of recoiling jets under consideration. If the back-to-back partons produced in the hard scattering were to undergo either approximately equal energy loss (i.e. similar jets traversing roughly equal path-lengths through the QGP) or negligible energy loss (as in vacuum), the  $A_J$  distribution would peak at 0. However, if the hard scattering occurs near the surface of the QGP, as depicted in Fig. 11 (left), the pair of dijets produced could each pass through different lengths of the hot QCD matter. This results in the jet with the longer path-length suffering a substantially higher energy loss, resulting in a smaller measured  $p_T$ . The differential energy loss in the QGP for a recoiling pair of high- $p_T$  partons having similar initial transverse momentum leads to an asymmetric dijet. Measurements of  $A_J$  from CMS shown in Fig. 12 (right) show that asymmetric dijets occur more frequently in central PbPb collisions compared to unquenched simulation results [56, 53]. The peak of the  $A_J$  distribution for

unquenched PbPb simulations is close to zero as expected and any deviation from zero is caused by three-jet events and jet energy resolution effects. Simulations are performed by embedding hard scattering events from PYTHIA [57] (Sec. 6.2) into a heavy-ion collision background simulated with the HYDJET event generator [58] (Sec. 6.2), without accounting for any parton energy loss effects in the QGP.

### 3.4 Fragmentation function and jet shapes

The energy lost by partons passing through the QGP is observed to be recovered by soft hadrons at large angular distances from the jet axis [59, 2]. Observables like jet fragmentation function and jet shapes help examine the details of jet fragmentation and its modification in the QGP. The jet fragmentation function captures the partitioning of the jet energy into its constituent particles (tracks) and is measured via the variables  $z$  and  $\xi$ , defined in Eq (11).

$$z = \frac{p_{||}^{\text{track}}}{p^{\text{jet}}}, \quad \xi = \ln \frac{1}{z}, \quad (11)$$

where  $p_{||}^{\text{track}}$  is the momentum component of the track along the jet axis and  $p^{\text{jet}}$  is the magnitude of the jet momentum. Low values of  $\xi$  correspond to high- $p_T$  particles within the jet cone and vice versa. Jet fragmentation function results are shown for pp collisions and in different centrality classes of PbPb events in Fig. 13 as measured by the CMS experiment [60]. The results from peripheral PbPb collisions are in agreement with pp within systematic uncertainties, implying no modification. However, for more central PbPb events, a significant excess at high  $\xi$  (track  $p_T < 3$  GeV) is observed, compensated by a depletion in the intermediate  $\xi$  region (track  $p_T \approx 6$  GeV). From these results, an enhancement of the soft particle contribution to the jet energy is observed in PbPb collisions offset by a suppression of high- $p_T$  particles, compared to the pp reference.

The redistribution mechanisms of jet energy to softer particles in heavy-ion collisions and its dependence on the distance from the jet axis ( $\Delta r$ ) can be further constrained using jet shapes[61, 2, 59]. Measurement of jet shapes including their dependence on particle species forms the latter portion of the work presented in this thesis (Sec. 10). The distance  $\Delta r$  is given by  $\Delta r = \sqrt{(\Delta\eta)^2 + (\Delta\phi)^2}$ , where  $\Delta\eta$  and  $\Delta\phi$  represent the relative pseudorapidity and azimuthal angle of charged hadrons with respect to the jet axis, respectively. Jet shape is defined as the

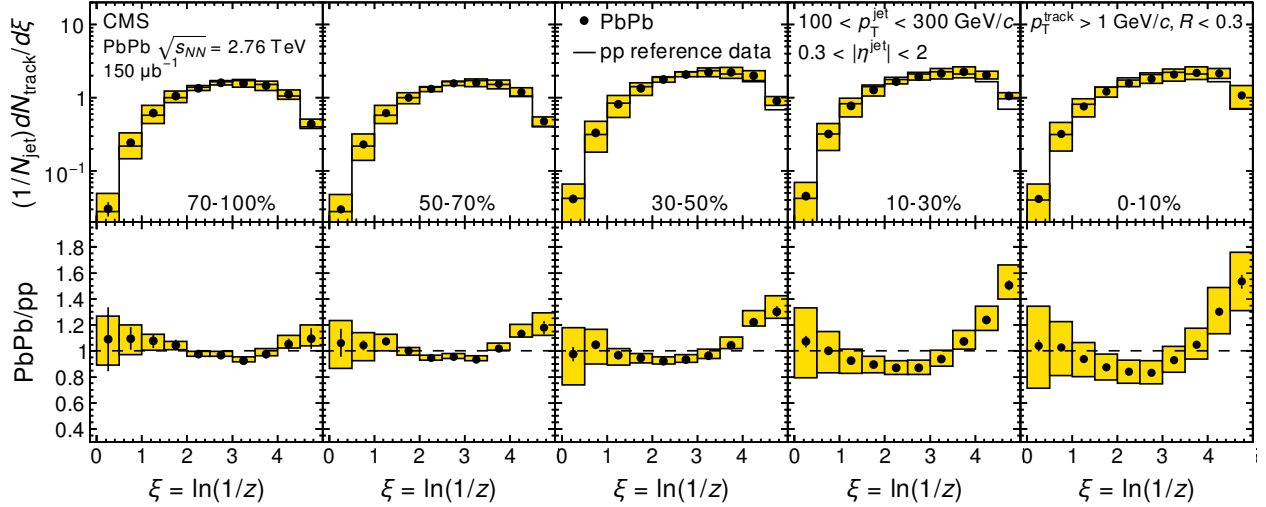


Figure 13. **Upper:** Jet fragmentation function distributions in pp and in different centrality classes of PbPb collisions. **Lower:** Ratio of the fragmentation function distributions in PbPb collisions to that in pp. Figure from Ref. [60].

distribution of particles in annular rings (of width  $\delta r$ ) around the jet axis, with each particle weighted by its  $p_T$  (Eq. (12)).

$$P(\Delta r) = \frac{1}{\delta r} \frac{1}{N_{\text{jets}}} \sum_{\text{jets}} \sum_{\text{tracks} \in \delta r} p_T^{\text{trk}}, \quad (12)$$

Results from the CMS experiment for jet shape measurements are shown in Fig. 14 for pp and PbPb collisions. These measurements characterize the radial distribution of energy up to large angular distances from the jet axis ( $\Delta r = 1$  or  $60^\circ$ ). In line with the fragmentation function results, jet shapes also show a strong suppression of high- $p_T$  particles correlated with the jet axis in PbPb collisions relative to pp events. A hint of depletion is also observed for low  $p_T$  particles at small distances from the jet axis ( $\Delta r \sim 0.1$ ). The ‘‘lost’’ energy is recovered in PbPb events at mid to large angles from the jet axis ( $\Delta r > 0.3$ ), with a strong enhancement of soft particles with  $p_T < 3$  GeV (Fig. 14). The mechanisms by which the medium interaction causes the redistribution of jet energy to softer particles extending to large angles from the jet axis is discussed further in Sec. 4.

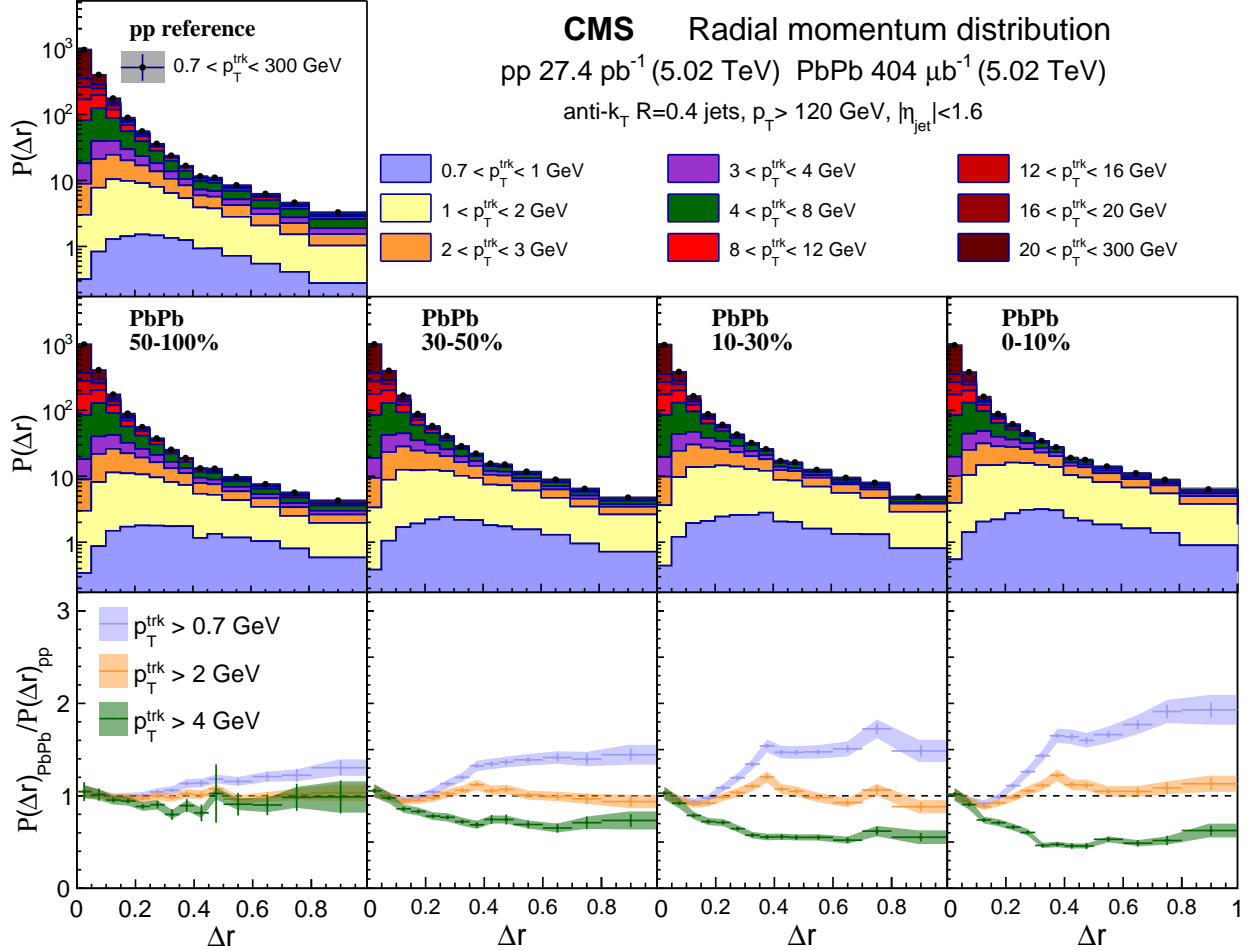


Figure 14. **Top and Middle:** Jet shapes distributions in pp and different centrality classes of PbPb collisions as measured by the CMS experiment. **Bottom:** The ratio between PbPb and pp data for the indicated intervals of track  $p_T$ . Figure from Ref. [2].

### 3.5 Flavor dependence of jet energy loss

The energy loss suffered by a jet in the medium has long been theorized to depend strongly on whether it is initiated by a quark or a gluon due to their distinct color charges. Jets initiated by different flavored partons (quark vs. gluon) cannot be directly discriminated in their final state after full jet reconstruction. Events in which jets are produced back-to-back with photons or other electroweak bosons have an advantage of better control on the precision of jet  $p_T$  measurements. Colorless probes remain unperturbed by the medium and help constrain the  $p_T$  of the recoiling parton. Photon-tagged jet samples are also expected to have an enhanced fraction of quark jets at

LHC energies compared to inclusive dijets. Measurements for photon-tagged jets, shown in Fig. 15, help throw light on the evolution of a quark-dominated jet sample in the medium [62, 63]. It should be noted that the jet  $p_T$  range of the two jet shape measurements (photon-tagged vs. inclusive) are quite different, and no conclusive comparisons can be drawn from these results.

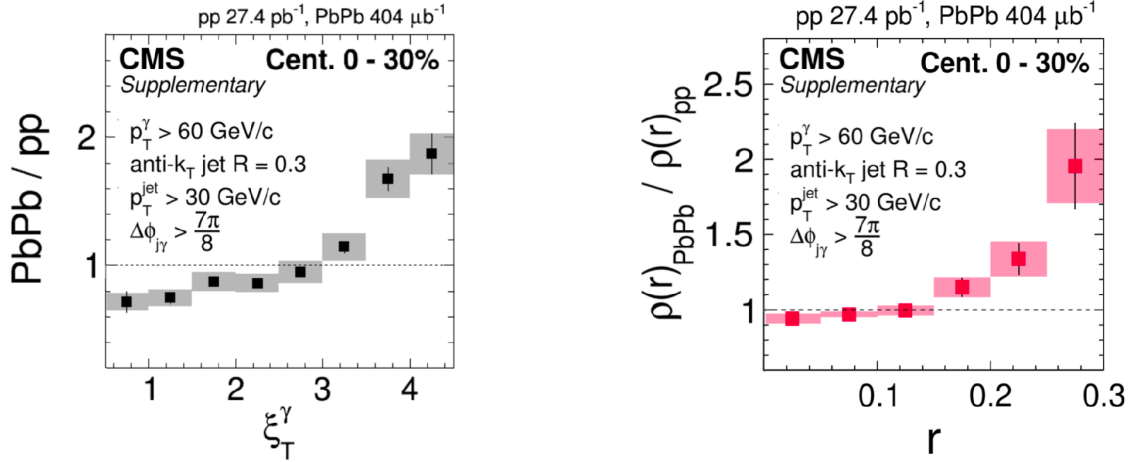


Figure 15. Ratio between central PbPb and pp data for jet fragmentation function (left) and jet shapes (right) for photon-tagged jets. Figures from Ref. [62] and Ref. [63]

However, other properties of a jet can be used to robustly differentiate between quark and gluon jets, and study their respective quenching patterns. Jet charge is one such variable, and its first measurements in heavy-ion collisions along with its applications for jet flavor tagging is a major portion of the work presented in this thesis. Jet charge, defined as the  $p_T$ -weighted sum of all the electric charges of particles inside a jet cone, is expected to be sensitive to the electric charge of the initiating parton [64]. Jet charge distributions are observed to be distinct for gluons and quarks and have been previously measured in pp collisions by CMS and ATLAS as shown in Fig. 16. The first jet charge measurements in PbPb collisions along with the pp results at the same collision energy are presented in Sec. 9. Jet charge is also employed to extract the fraction of quark and gluon jets in pp and PbPb collisions (Sec. 9), providing insight into the differential quenching for different flavor jets in heavy-ion collisions.

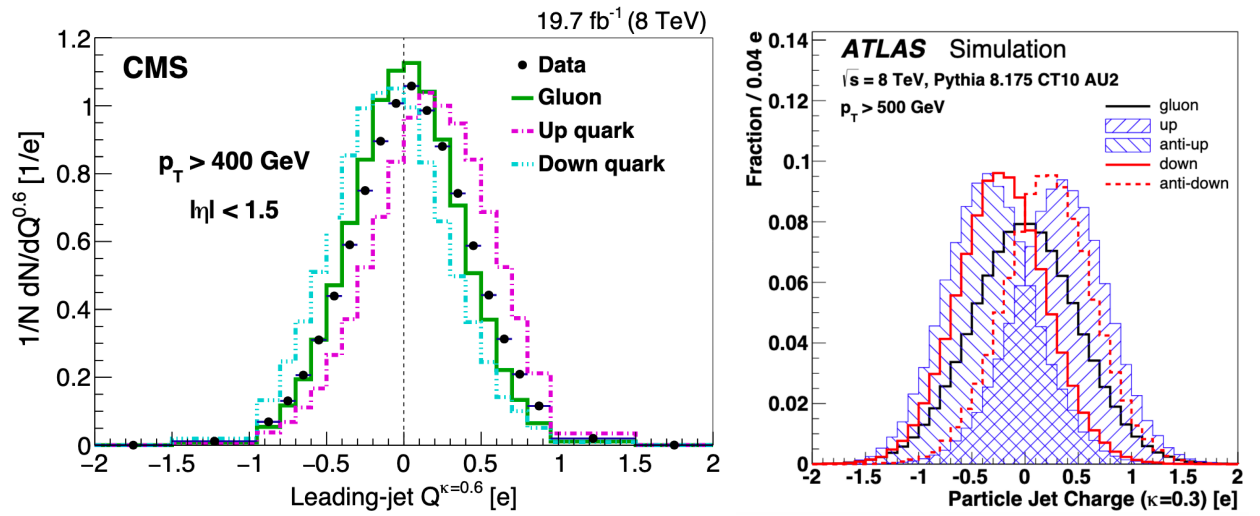


Figure 16. Jet charge measurements in data and for different flavor jets in simulation from CMS and ATLAS for pp collisions. Figures from Ref. [65] and Ref. [66].

## 4 THEORY OF JET QUENCHING

The large scales involved in the production of high  $p_T$  jets in hadronic collisions enables the use of perturbative QCD techniques to study them. The production cross-section of jets in pp collisions can be obtained via QCD factorization as shown in Eq. (7). Predictions for high  $p_T$  jet production from next-to-leading order perturbative QCD calculations are shown in Fig. 17 for pp collisions at RHIC and LHC for collision energies of  $\sqrt{s_{NN}} = 200$  GeV and 8 TeV, respectively. Good agreement is observed between the NLO pQCD calculations and experimental measurements for the inclusive jet production [67, 68, 69] over orders of magnitude in  $p_T$  and  $\sqrt{s}$ . The reliable theoretical control of jet production in vacuum serves as a baseline to study its modifications in high-energy heavy-ion collisions.

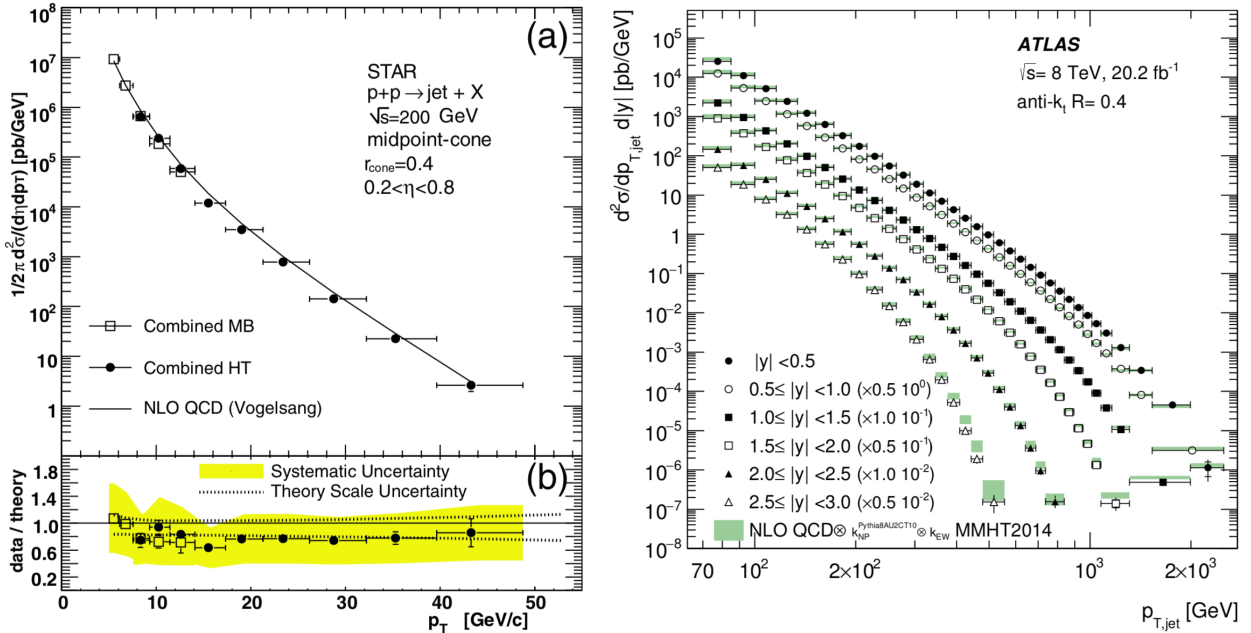


Figure 17. Production cross-section for inclusive jets in pp collisions at RHIC at  $\sqrt{s_{NN}} = 200$  GeV (left) and at LHC at  $\sqrt{s_{NN}} = 8$  TeV (right) compared to results from NLO pQCD calculations. Figures from Refs. [68, 69].

### 4.1 Theoretical formalisms of jet quenching

Achieving a comprehensive understanding of the dynamics of QGP and its effects on hard probes is challenging due to the low  $Q^2$  (non-perturbative) nature of the processes involved. Different

approaches have been adopted to study the jet-medium interactions including analyzing the extent of strong/weak coupling of the jet with the medium at different times [47, 52, 48, 70]. In the weak coupling limit, hard partons are expected to lose energy in the medium via radiative and collisional processes shown in Fig. 18.

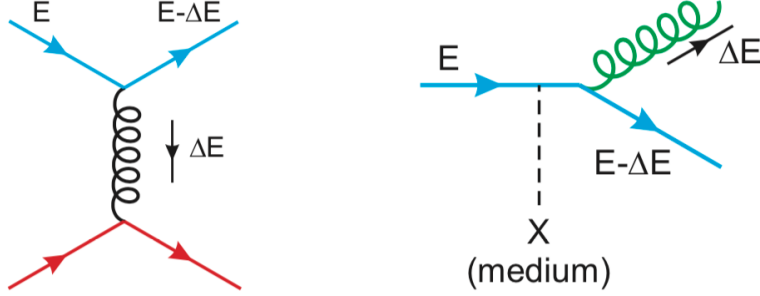


Figure 18. Diagrams showing collisional (left) and radiative (right) energy losses of a quark of energy  $E$  traversing the QGP. Figure from Ref. [47].

Even in the absence of a hot and dense medium, energetic partons produced in hard scatterings are highly virtual and they emit gluons and/or split into quark-antiquark pairs in order to reduce their virtuality. DGLAP equations describe the evolution of a high- $p_T$  parton in vacuum until the parton virtuality drops to  $\mathcal{O}(1\text{GeV}^2)$  and undergoes hadronization [43]. However, in the presence of QGP, partons additionally suffer elastic and inelastic scatterings with the medium constituents. The inelastic scatterings modify the gluon radiation and parton splitting probabilities of the partons compared to the vacuum scenario. Medium-induced gluon radiations are theorized to be the dominant mode of energy loss for light quarks and gluons in QGP. Energy loss via elastic scatterings with the medium, referred to as collisional energy loss, is also an essential ingredient while studying the full jet evolution in the medium. Collisional effects are expected to play an important role particularly for heavy quarks due to a reduction in the phase-space of medium-induced gluon radiations, known as the “dead-cone effect” [71].

However, the weak coupling limit of parton-medium interactions only applies fully at experimentally unrealizable temperatures. Strong coupling effects between the parton and QGP need to be taken into consideration at temperatures explored in heavy-ion collisions at RHIC and LHC ( $T \sim 150 - 600$  MeV) [72]. Various models have been developed to study the multiple aspects of jet quenching via analytical calculations and phenomenological studies. A brief synopsis of the

formalisms describing the parton shower evolution in a strongly coupled QCD medium, including the relative significance of the proposed mechanisms in the different  $p_T$  regions and parton flavors, is discussed below.

- **BDMPS-Z** : The Baier-Dokshitzer-Mueller-Peigne-Schiff-Zakharov formalism [73, 74, 75] is based on modeling the QGP medium as a collection of static colored scattering centers and capturing the emitted gluon spectra. The propagating partons are modeled to lose energy through multiple soft scatterings with the medium constituents, and can only be used to describe the radiational aspect of the energy loss due to the static nature of the scattering centers. Predictions from this formalism are related to the jet energy loss measurements ( $R_{AA}$ ) via quenching weights that can be calculated from the BDMPS gluon spectrum. Models like BDMPS-Z, which describe energy loss using multiple soft scattering processes can fully characterize the medium through the jet transport coefficient  $\hat{q}$ , defined in Eq. 13.

$$\hat{q} = d(p_\perp^2)/dL , \quad (13)$$

$\hat{q}$  measures the square of the momentum transferred to the medium per unit path length, in the direction transverse to that of jet propagation.

- **GLV** : The Gyulassy-Lévai-Vitev model [76, 77] describes the gluon radiation spectra via the concept of opacity expansion, in terms of the number of parton scatterings in the medium. Almost all implementations of this model expand only up to one term ( $N = 1$ ), known as the single hard scattering limit. Unlike the BDMPS-Z formalism, this model accounts for the interference between the medium-induced and vacuum gluon radiations. The medium was initially described using static scattering centers but was later updated in the DGLV formalism to dynamical scattering centers to accommodate collisional energy loss as well [78]. The expanded DGLV model also accounts for the effects of heavy quarks but does not account for any energy flow into the medium. radiative effects are expanded in terms of the number of scatterings a parton experiences.
- **Higher-Twist** : The HT formalism [79, 80] models the QGP as a combination of single-parton-exchange ‘twist-2’ matrix elements and those arising from the parton-QGP interactions, referred to as ‘higher-twist’ processes. The exchange of multiple partons in the medium is described as power

corrections to the leading-twist cross-section, depending on the exchanged  $Q^2$  and medium length. The initial model, HT-BW, was developed only for a single scattering per gluon emission and was later expanded to incorporate multiple scatterings in HT-M [81]. Unlike GLV, Higher-Twist is based on the leading moment of  $Q^2$  distribution and can consequently fully characterize the medium using  $\hat{q}$ .

- **AMY** : The Arnold-Moore-Yaffe approach [82, 83] is a finite temperature field theory that models the QGP as a weakly interacting medium in thermal equilibrium. This model treats the traversing partons as having very small initial virtuality (offshellness) and hence do not account for vacuum radiations. AMY formalism is only applicable at very high temperatures or at early times of the collision due to the perturbative QCD treatment of the QGP medium.
- **Soft Collinear Effective Theory** : SCET [84] was initially developed to deal with the infrared divergences while analyzing the interaction between a parton and soft collinear gluon modes. SCET factorizes the energy scales into 'soft' and 'ultrasoft' gluon fields based on the momentum scale of the collinear gluons. This model is expanded to the SCET<sub>G</sub> formalism by adding another gluon mode (Glauber Gluons) to account for the QGP medium effects [85]. Glauber gluons are soft gluons that have a momentum predominantly in a direction transverse to that of the propagating parton, and lead to momentum broadening. Unlike BDMPS and GLV, SCET<sub>G</sub> is also able to account for hard scatterings resulting in a large momentum transfer to another parton. Along with the Glauber gluons, modified DGLAP equations can be used to calculate the in-medium fragmentation functions for heavy-ion collisions in this model [86].
- **Linear Boltzmann Transport** : The LBT model [87, 88] keeps track of both the jet shower evolution and the medium recoil partons via a Boltzmann equation. The collision kernels for elastic scatterings are given by pQCD parton scattering processes while the medium-induced gluon radiation is implemented according to the HT formalism. This model also monitors the medium excitations resulting from the propagating parton via a hydrodynamic simulation and is thereby able to account for the "back-reaction" effects. The jet shower is allowed to evolve over a series of time steps, with the collisional, radiational and back-reaction effects being included at each step.

- **Hybrid Strong/Weak Coupling model with AdS/CFT** : The Hybrid model [89, 90] interprets the evolution of a parton traversing a strongly-coupled QGP on par with a string falling into a 4 + 1-dimensional anti-deSitter (AdS) space-times containing a black hole horizon. Holographic calculations, from modeling QCD as a  $N = 4$  supersymmetric Yang-Mills theory, are used to analyze the modifications to a high- $p_T$  parton in the medium, including non-perturbative calculation of medium-induced gluon radiation. The gauge/gravity duality has been implemented to solve for the energy loss of a parton traversing unit length of the medium ( $dE/dx$ ), and is dependent on the initial parton energy and medium temperature. The Hybrid model has successfully described various heavy-ion results by combining strongly-coupled calculations and perturbative QCD techniques and also accounting for the hydrodynamic medium response (“back-reaction”) [72].

A list of event generators and frameworks used in the implementation of each/combination of the above quenching formalisms is presented in Table I, along with a brief description.

MC Framework	Description
PYQUEN [91]	Event generator with BDMPS-Z model for radiative energy loss and accounts for collisional energy loss in the high momentum transfer limit.
MARTINI [92]	Event generator with radiative energy loss according to AMY formalism; includes collisional energy losses.
HYBRID [90]	Only event generator based on the strong coupling approach; models in-medium parton as a dragging string in a black hole.
MATTER [93]	Vacuum-like shower generator implementing a medium modified DGLAP evolution based on a modified Sudakov form factor.
JEWEL [94]	Bottom-up approach event generator with full implementation of BDMPS-Z, also includes elastic interactions with the medium.
YAJEM [95]	Event generator with a full implementation of the BDMPS-Z model, without explicitly model the medium.
CUJET [96]	Implements DGLV formalism to compute opacity contributions to the medium-induced radiation; includes elastic interactions.
Q-PYTHIA [97]	Event generator based on a medium modified Sudakov form factor, but includes the BDMPS kernel in the factor construction.
JETSCAPE [98]	Computational framework for developing complete event generators and permits modular incorporation of different aspects of a heavy-ion collision.

TABLE I. A list of computational frameworks invoking different formalisms of jet quenching in the QGP. The table includes both standalone event generators and modular frameworks.

A cumulative plot, with the temperature-scaled  $\hat{q}$  values extracted from the different models discussed above, is shown as a function of the temperature T in Fig. 19 [99]. The  $\hat{q}$  value is also

shown for cold nuclei from DIS and is observed to be an order of magnitude smaller than that measured in LHC and RHIC energies. In the limit of strong coupling, the specific viscosity  $\eta/s$  is predicted to saturate while the temperature-scaled jet transport parameter  $\hat{q}/T^3$  continues to decrease, making it a better quantity to characterize the medium on a broader scale [100].

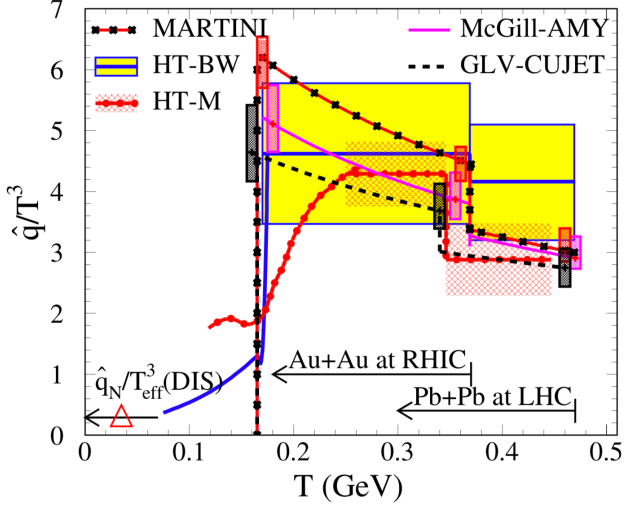


Figure 19. Temperature dependence of the temperature-scaled jet transport parameter  $\hat{q}/T^3$  extracted from various models for an initial quark jet. The range of temperatures in central heavy-ion collisions at RHIC and LHC are shown with arrows. Figure from Ref. [99].

#### 4.1.1 Cold nuclear matter effects

The comparison of heavy-ion measurements to the vacuum baseline (pp collisions) also needs to account for the effects of different nuclear parton distribution functions, referred to as the “cold nuclear matter effects”. Factoring out the cold nuclear matter effects is imperative while attempting to characterize the properties of the QGP medium based on modifications observed in heavy-ion collisions. The nPDFs are usually calculated using DIS structure function data from HERA, which explores high- $p_T$  particle and/or jet production in a wide kinematic range of  $(x, Q^2)$  [101, 102]. Fig 20 shows the cold nuclear modification factors for different flavor partons, defined as the ratio of lead PDFs to that constructed from free-proton PDFs. CNM effects manifest in final-state measurements intertwined with those of the hot QCD medium in heavy-ion collisions, and require careful consideration while analyzing the observables. No significant modifications are expected to the jet charge results presented in this thesis due to CNM effects [103].

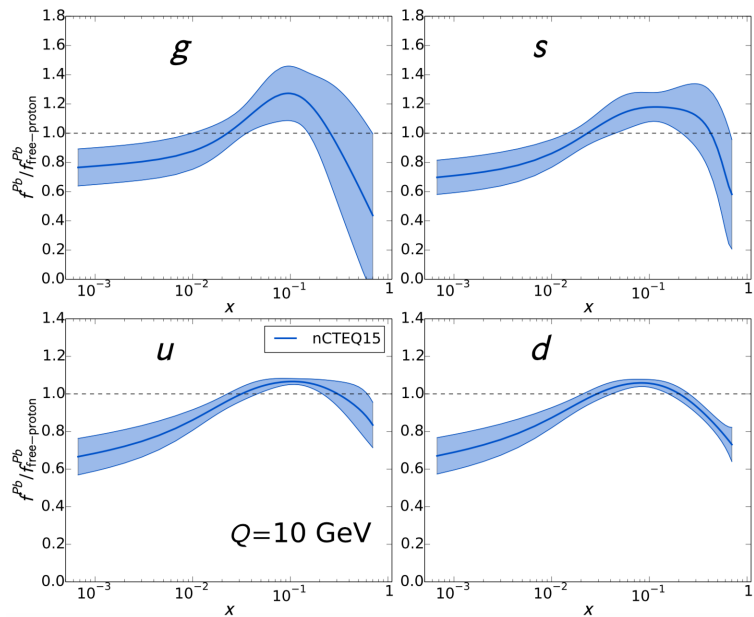


Figure 20. Cold nuclear modification factors defined as ratios of lead PDFs to those constructed from free-proton PDFs, with a scale of  $Q = 10$  GeV for different flavor partons. Figure from Ref. [101].

## 4.2 Comparisons to experimental observables

### 4.2.1 Charged-particle $R_{AA}$

Energy loss models often tune free parameters in the formalism to match  $R_{AA}$  or other experimental measurements in the most central collisions. Further comparisons to the non-central bins and other experimental observables, discussed below, serve to constrain the validity of the different approaches. Charged-particle  $R_{AA}$  measurements from CMS are shown in Fig. 21 along with results from other experiments and predictions from various models [50]. The general trends of the  $R_{AA}$  curve as a function of  $p_T$  is captured by all the models shown for  $p_T > 10$  GeV. As justified earlier, better control is expected over the quenching mechanism while comparing model predictions with full jet  $R_{AA}$  measurements and is discussed in the next section.

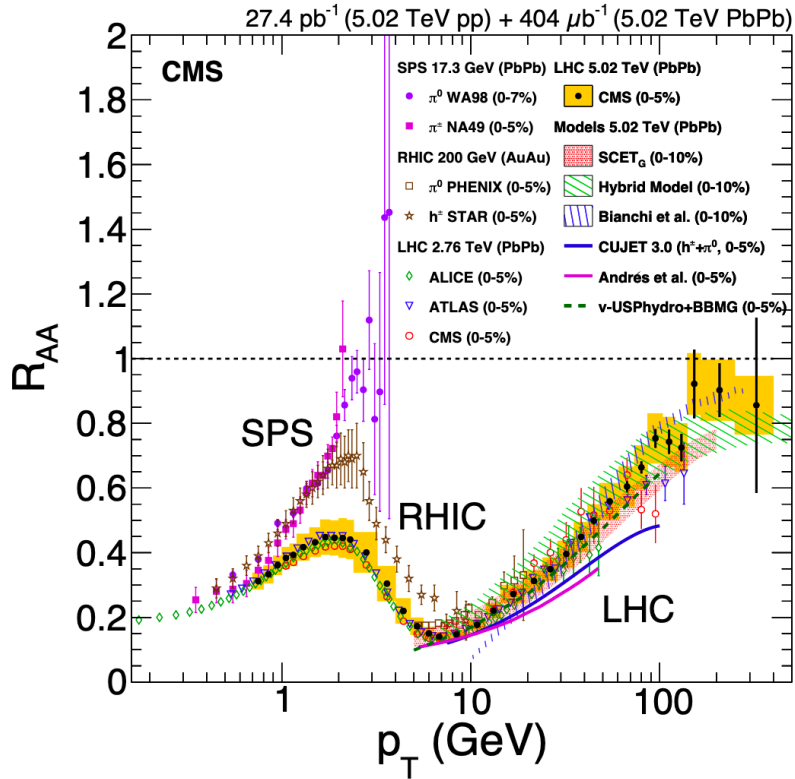


Figure 21. Charged-particle  $R_{AA}$  measurements from CMS in the 0-5% centrality bin in PbPb collisions at 5.02 TeV. Predictions from various models for the  $R_{AA}$  are also shown. Figure from Ref. [50].

### 4.2.2 Jet $R_{AA}$

Predictions for jet  $R_{AA}$  from LBT and  $\text{SCET}_G$  are shown in Fig. 22 together with experimental measurements from ATLAS in the 0-10% centrality bin [54]. The predictions from  $\text{SCET}_G$  are shown for different coupling parameters of the medium  $g$ , both of which underestimate the suppression at large  $p_T$ . Predictions from LBT model, which additionally keeps track of medium recoil partons along with the shower evolution, describes the data much better at  $p_T > 250$  GeV. Fig 22 shows the comparison of CMS jet  $R_{AA}$  measurements to results from LBT, MARTINI and AdS/CFT, all coupled with MATTER, a vacuum-like shower generator based on a medium-modified DGLAP evolution. They are observed to generally capture the trend of the CMS jet  $R_{AA}$  results for jets with radius parameter  $R = 0.4$  in the most central bin [98].

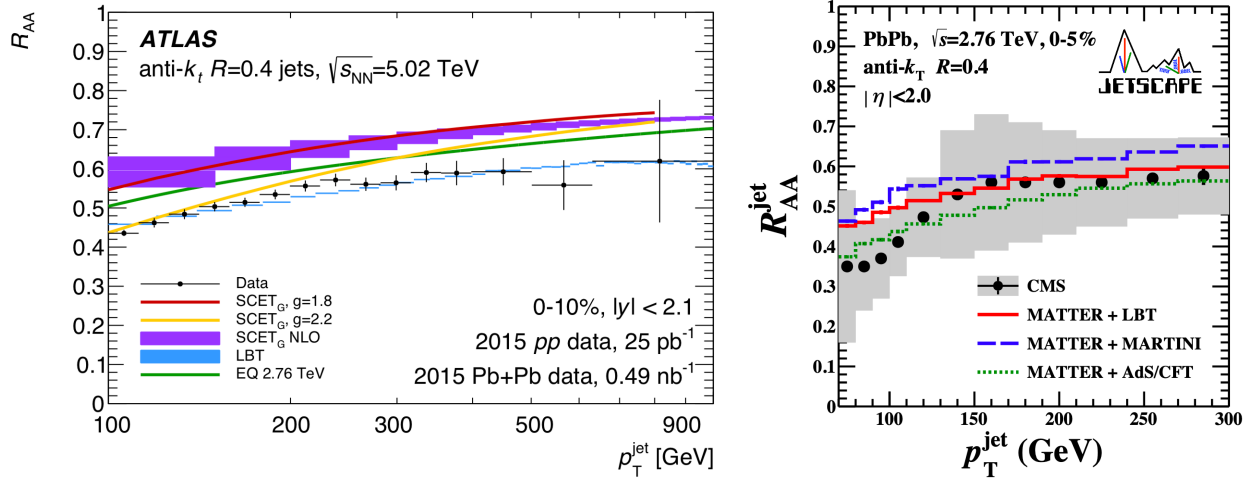


Figure 22. Jet  $R_{AA}$  from ATLAS (left) and CMS (right) as a function of  $p_T$  for the most central collisions, along with results from various models. Figures from Ref. [54] and Ref. [98].

The jet  $R_{AA}$  predictions from different models are shown in Fig. 23 for different jet cone sizes, which all show some dependence on the radius parameter [104]. Varying the size of the jet, as discussed in Sec. 8, is expected to include different fractions of contribution from the quenched jet and medium response, thereby providing insight into the parton-QGP interactions. CMS results show a strong suppression of jets at all measured radii in central collisions. The results from various models generally describe the  $R_{AA}$  trends for smaller radius jets as measured by CMS, but show very distinct predictions for large radius ( $R = 1$ ) jets.

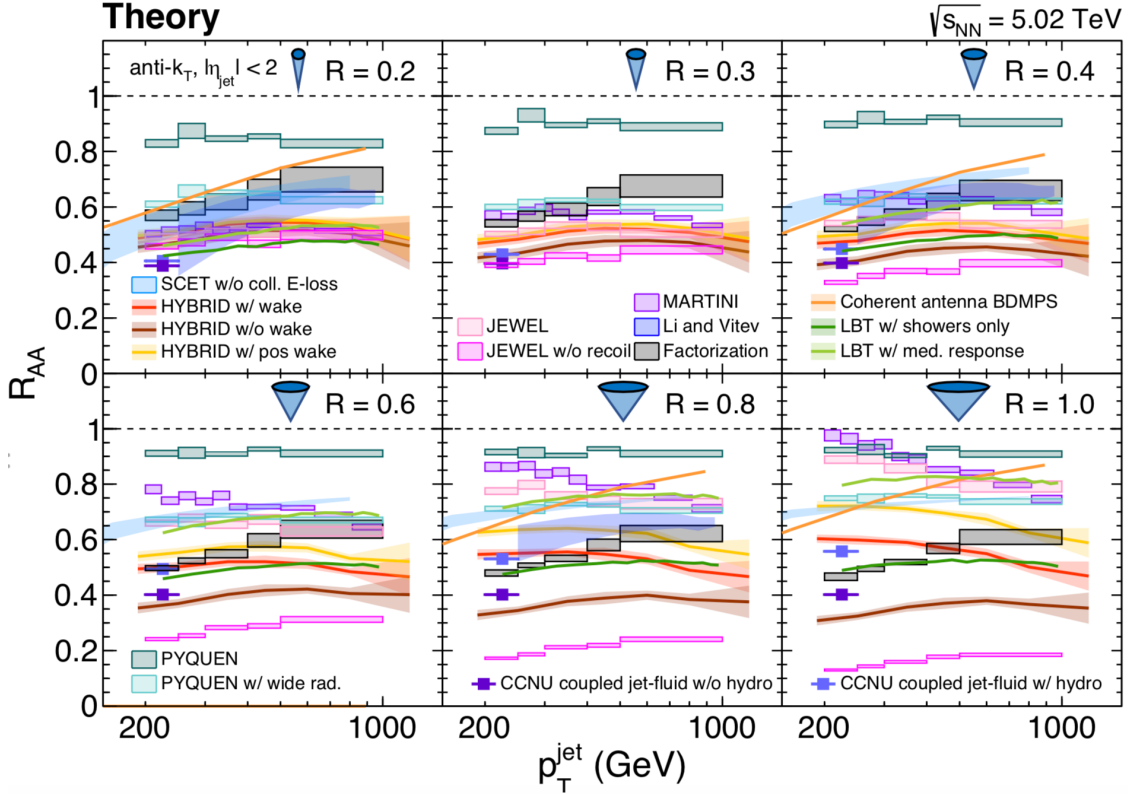


Figure 23. Jet  $R_{AA}$  predictions from different formalisms for the most central collisions. Results are shown for different jet radius parameters, from  $R= 0.2$  to  $R= 1$ . Figure from Ref. [104].

#### 4.2.3 Jet shapes

Jet shapes have been measured up to large angular distances from the jet axis ( $\Delta r = 1$ ) and provide valuable insight into jet energy loss mechanisms and its recovery [61, 2]. The latest results for jet shapes from CMS are shown in Fig. 14 and the features are discussed in Sec. 3.4. A significant redistribution of energy to large radii and softer fragments is observed from central PbPb jet shapes compared to pp measurements. PYTHIA describes the observed jet shapes in pp collisions up to  $\Delta r = 0.4$  generally well, but underestimate the energy distribution at large angular distances, where non-perturbative contributions dominate [105].

The calculations for jet shapes in central PbPb collisions are shown in Fig. 24 (left) from the coupled jet-fluid model [7] along with the CMS measurements. It is evident that the parton shower modification alone cannot describe the jet shapes at large angular distances, but needs to account for the hydrodynamic medium response effects. Medium excitations induced from the energy lost by the jet are shown to carry the energy to large distances from the axis, while the inner hard core of

the jet becomes more collimated. Similar predictions are also shown from JEWEL in Fig. 24 (right), which captures the redistribution of energy to large angles only after the inclusion of medium recoil effects [106].

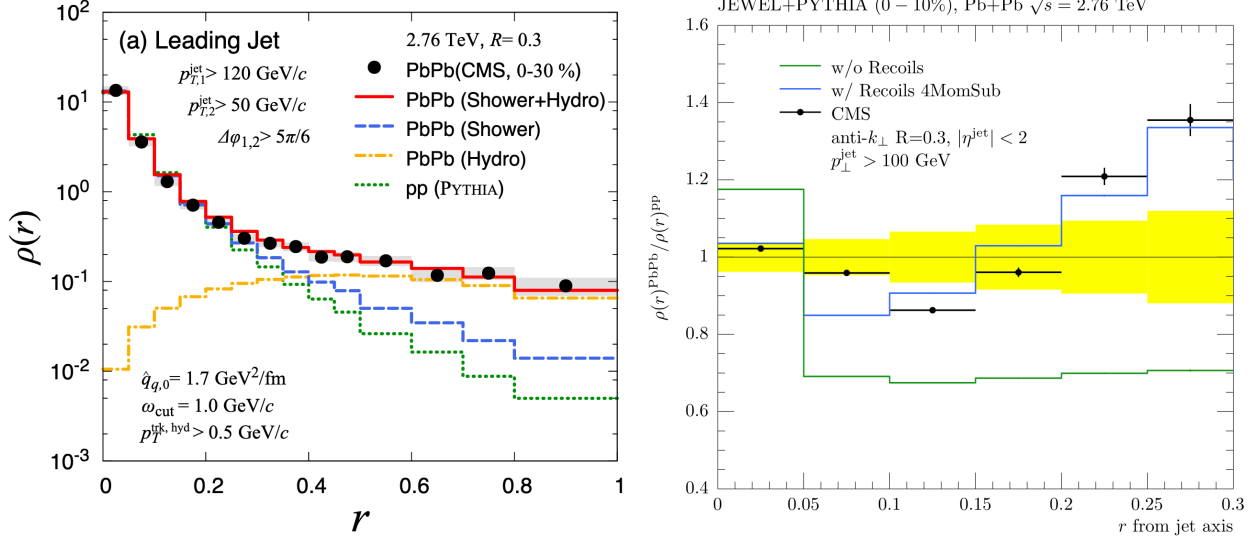


Figure 24. Jet shapes predictions for central PbPb collisions from the coupled jet-fluid model (left) and JEWEL (right). Figures from Ref. [7] and Ref. [106].

Theoretical calculations from the SCET<sub>G</sub> for the modifications in central PbPb jet shapes compared to pp are shown in Fig. 25 (left), with the coupling between the collinear partons and the medium  $g = 2$  [107]. The blue band in Fig. 25 (left) shows the modification in jet shapes due to CNM effects and is observed to be very small, unlike in jet  $R_{AA}$  measurements. SCET<sub>G</sub> calculations account for possible modifications in jet shapes due to the differential quenching of quark and gluon jets in the QGP, which have significantly distinct jet shapes. The resulting narrowing of the jet shapes is shown with the red band in Fig. 25 (left), by keeping the jet-by-jet shapes same while increasing the quark jet fractions in the sample. The green band shows the final SCET<sub>G</sub> calculations by including the in-medium parton shower broadening along with all the above effects, and describes the data trends well up to  $\Delta r = 0.3$ .

The Hybrid model introduces strong coupling effects to study the propagation of the parton in the QGP [72]. A theory dependent free parameter,  $K (= \hat{q}/T^3)$ , is used to quantify the transverse momentum broadening in this model. Jet shapes are measured with respect to the final reconstructed jet axis and are shown to be insensitive to the original parton direction or whether the parton

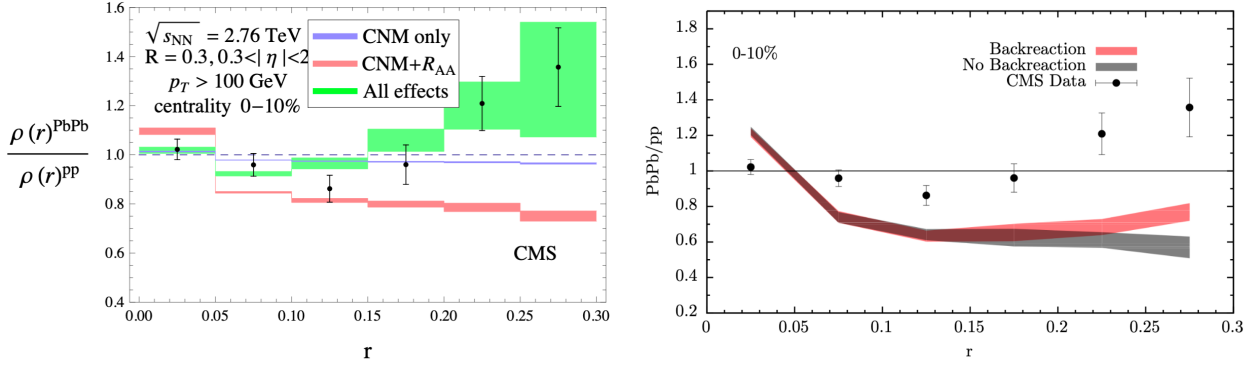


Figure 25. Predictions for ratio of jet shapes between central PbPb and pp collisions from SCET<sub>G</sub> (left) and HYBRID (right) model, along with CMS measurements. Figures from Ref. [107] and Ref. [72].

suffered any transverse momentum kicks. This in turn implies that the jet shape ratio between PbPb and pp has very little dependence on the transverse momentum broadening parameter  $K$ . Predictions for jet shapes from the Hybrid model are shown in Fig. 25 (right) for  $K = 0$ , and a narrowing of the jet cone is observed without accounting for any medium response effects. The medium response or "back-reaction" in PbPb collisions is included in the calculations as a plasma wake and/or a Mach cone in the direction of jet propagation, and the resulting jet shapes show a slight enhancement at large values of  $\Delta r$ . However, the reversal in the trend of the predicted jet shapes ratio by including back-reaction effects does not nearly capture the magnitude of the enhancement observed at large  $\Delta r$  in data. This could result from the underestimation of energy deposited in the medium, overestimation of the hydrodynamization of the deposited energy, or undermining back-reaction effects by over-subtracting the "background" compared to the CMS approach.

An observation of a strong enhancement of soft particles at large angular distances from the jet axis in heavy-ion collisions suggests two possible mechanisms for the jet-medium interaction. The first scenario involves jet fragments propagating through and interacting with the medium constituents resulting in a broadening of the jet profile. However, there is also a second possibility of the jet energy being absorbed and thermalized into the medium, which then appears as a shock wave at large angles. In the former case, the enhanced particle yields at large angles would reflect particle

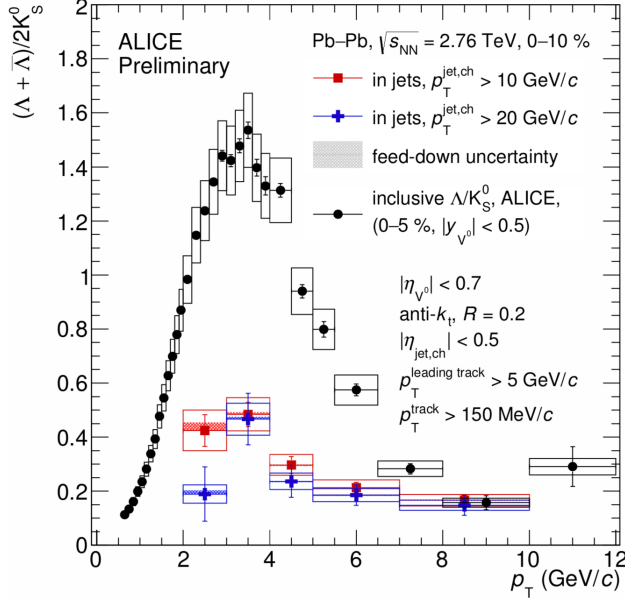


Figure 26. Measurements of baryon-to-meson ( $\Lambda$  to  $K_S^0$ ) particle yields ratio as a function of  $p_T$  in 0–10% central PbPb collisions, for bulk particles (black) and for those inside the jet cone (colored). Figure from Ref. [108].

species composition similar to those of a hard parton shower, whereas, in the latter picture, a bulk medium-like particle production is expected due to the thermalization of the deposited energy.

An enhanced ratio of baryons to mesons in the intermediate  $p_T$  regions has been established as a key signature of QGP due to radial flow and parton recombination [109]. The enhancement is however not observed for particles inside a jet cone, where the baryon to meson ratio is suppressed by a factor of 4 – 5 compared to the bulk medium results as shown in Fig 26 [108]. Performing large  $\Delta r$  jet shapes measurements with identified particle species of charged pions, kaons and protons would, therefore, be a key breakthrough in understanding the role of medium response in parton energy loss mechanisms. The work included in the latter part of the thesis summarizes the jet shapes measurements up to large angular distances and the feasibility of these measurements for different identified particle species (Sec. 10).

### 4.3 Theoretical motivation for jet charge studies

The parton flavor dependence of energy loss and jet modifications in the QGP has long been of great interest in order to better understand the parton-medium interactions. According to many early perturbative QCD calculations of jet quenching, gluons are expected to lose significantly more

energy while traversing the QGP compared to quarks due to their larger color factor [110, 111, 112]. The pQCD calculations predict the ratio of medium-induced fractional energy losses for quarks and gluons to follow the vacuum ratio of gluon radiation (Casimir Scaling), given by Eq. 14:

$$\frac{\Delta E_q}{\Delta E_g} = \frac{C_F}{C_A} = \frac{4}{9}, \quad (14)$$

where  $C_F/C_A$  is the ratio of the Casimir color factors for quarks and gluons according to QCD and is given by  $C_A = N$  and  $C_F = (N^2 - 1)/2N$  for a general  $SU(N)$  group ( $N = 3$  for QCD). The stronger quenching predictions for gluons are shown via  $R_{AA}$  calculations for the different flavor partons from GLV and LBT models in Fig. 27.

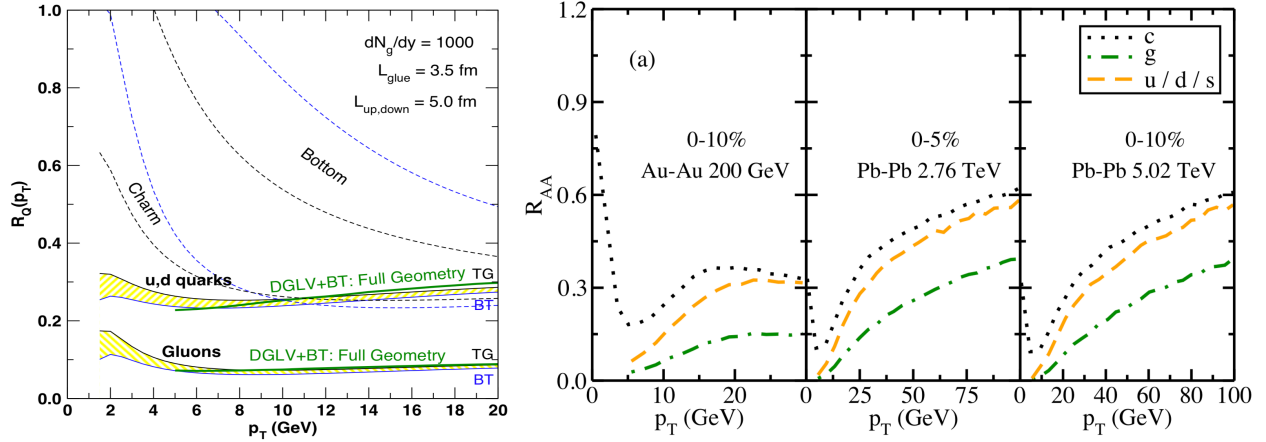


Figure 27. Flavor dependence calculations of  $R_{AA}$  measurements for partons in heavy-ion collisions from DGLV (left) and LBT (right) models. Figures from Ref. [110] and Ref. [111].

Gluons are predicted to undergo significantly larger suppression than quarks due to medium effects in all  $p_T$  ranges according to predictions from both DGLV and LBT. Light quarks are expected to undergo higher energy loss compared to heavy quarks due to the "dead-cone effect", which is outside the scope of this thesis work [71]. Fig. 28 (left) shows the expected flavor compositions (light quarks and gluons) of the jet spectra as a function of  $p_T$  according to SCET<sub>G</sub>, indicating a clear suppression of gluon jets in central PbPb collisions compared to pp [112]. Calculations of the jet transport coefficient from the LBT model are also shown in Fig. 28 (right) and it is observed to be significantly larger for gluons compared to quarks [111].

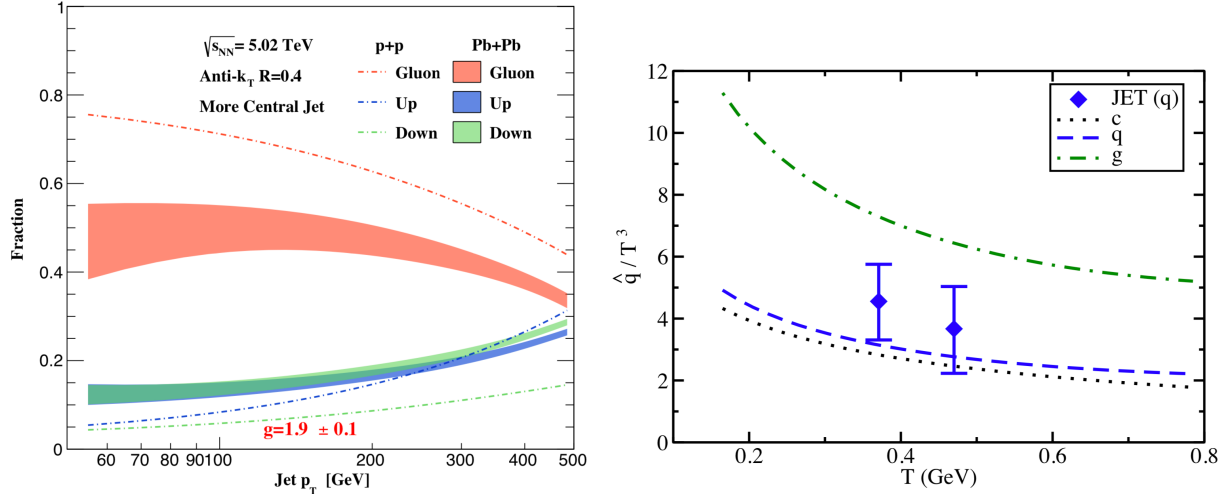


Figure 28. **Left:** SCET<sub>G</sub> calculations for fractions of up quark, down quark and gluon-initiated jets in pp and central PbPb collisions. **Right:** Predictions from the LBT model for the temperature-scaled jet transport coefficient for quarks and gluons as a function of parton  $p_T$ . Figures from Ref. [112] and Ref. [111].

However, a large discrepancy is observed in the proton over pion yield ratios observed in Au+Au collisions at RHIC and those expected from pQCD calculations from the weak coupling model [113, 114]. Results from the Hybrid Strong/Weak coupling approach based on holographic calculations also predict a smaller difference in the rate of energy loss for quarks and gluons in QGP, compared to the weakly coupled case. The results from the Hybrid model are shown in Fig. 29 (left), as a ratio of the number of quark jets to the number of gluon jets for different centrality bins in PbPb collisions [90]. A significantly weaker centrality dependence of the ratio is predicted in the case of strongly coupled model compared to either radiational or collisional models. Compared to the weakly coupled scenario, the Hybrid strongly coupled model predicts a modified ratio of the energy lost by quarks and gluons given by Eq. 15:

$$\frac{\Delta E_q}{\Delta E_g} = \left( \frac{C_F}{C_A} \right)^{1/3} = \left( \frac{4}{9} \right)^{1/3}, \quad (15)$$

These results have challenged our current understanding of the flavor dependence of parton energy loss and prompted a more comprehensive study of the phenomenon. Recent theoretical and phenomenological studies have predicted a breaking of the Casimir scaling when applied to the rate of energy loss ratio of quarks and gluons in QGP [115]. This is shown in Fig. 29 (right), in the form

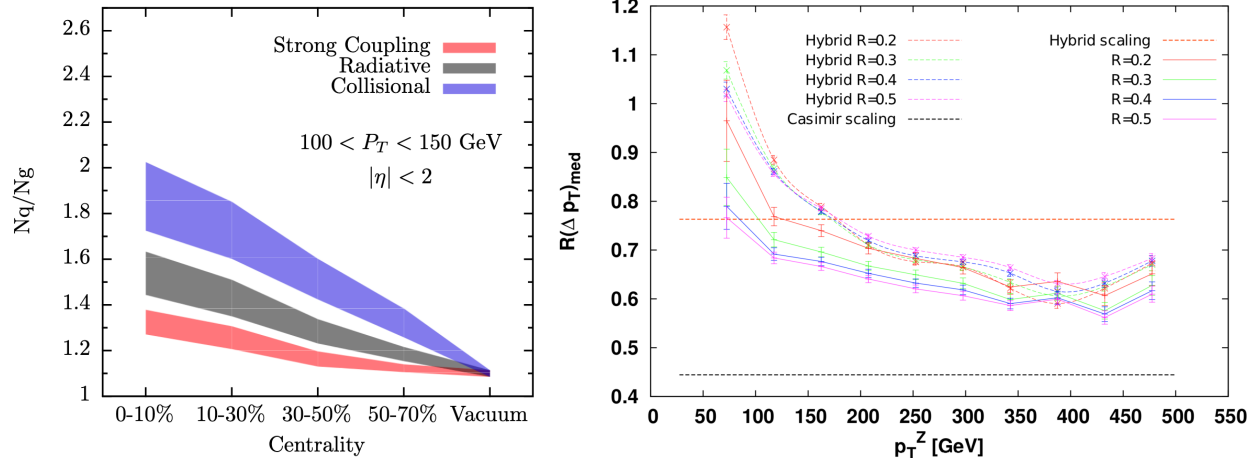


Figure 29. **Left:** Predictions from the Hybrid model for the ratio of number of quark to gluon jets via three different energy loss mechanisms as a function of centrality in PbPb collisions. **Right:** Ratio of quark to gluon energy loss as a function of the initial parton  $p_T$  in central PbPb collisions. The calculations from JEWEL and Hybrid models are shown with solid and spline lines, respectively. Figures from Ref. [90] and Ref. [115].

of purely medium-induced quark to gluon energy loss ratio ( $R(\Delta p_T)_{\text{med}}$ ) as a function of the initial parton  $p_T$ , from JEWEL and Hybrid simulations. The Casimir scaling from the weak coupling model ( $= 4/9$ ) and the Hybrid model strong coupling scaling ( $= (4/9)^{1/3}$ ) are shown with the black and red dotted lines, respectively. Results of  $R(\Delta p_T)_{\text{med}}$  from JEWEL and Hybrid for different jet radii depart significantly from the Casimir scaling, and moreover, exhibit a quark vs. gluon energy loss ratio consistent with unity at lower  $p_T$ . The Casimir scaling violation when applied to in-medium energy loss is also predicted in other theoretical studies [116], and depict quark and gluon jets as being more similar in the hot QCD medium than in vacuum.

To further understand the quenching and modifications of individual flavor jets in the hot QCD medium, we turn to the experimental discrimination of quark- and gluon-initiated jets. Although some progress has been achieved in differentiating quark and gluon jets in pp collisions, applying these techniques to heavy-ion collisions remains a considerable challenge [117, 118, 119, 120, 121, 122, 123]. One such distinguishing variable between quarks, antiquarks, and gluons is their electric charge ( $+ \frac{2}{3}$  for up quarks,  $- \frac{1}{3}$  for down quarks and 0 for gluons). The electric charge of a hard parton cannot be directly experimentally measured, however, it can be estimated by measuring the charge of the jet reconstructed from its final-state hadron shower.

Jet charge, defined in Eq. 16 as the transverse momentum-weighted sum of the electric charges of the jet constituents, is expected to be sensitive to the electric charge of the initiating parton.

$$Q^\kappa = \frac{1}{(p_T^{\text{jet}})^\kappa} \sum_{i \in \text{jet}} q_i p_{T,i}^\kappa . \quad (16)$$

In Eq. 16,  $p_T^{\text{jet}}$  represents the transverse momentum of the jet,  $q_i$  and  $p_{T,i}$  depict the electric charge and transverse momentum of the jet constituents, respectively, and  $\kappa$  is a free parameter (with the requirement that  $\kappa > 0$ ) that controls the sensitivity of the jet charge to low- and high- $p_T$  particles. Jet charge was initially introduced by Field and Feynman to estimate the quark electric charge [64] and has since been used to understand quark and hadron models, measure the electric charge of the bottom and top quarks, and to tag W bosons [124, 125, 126, 127, 128].

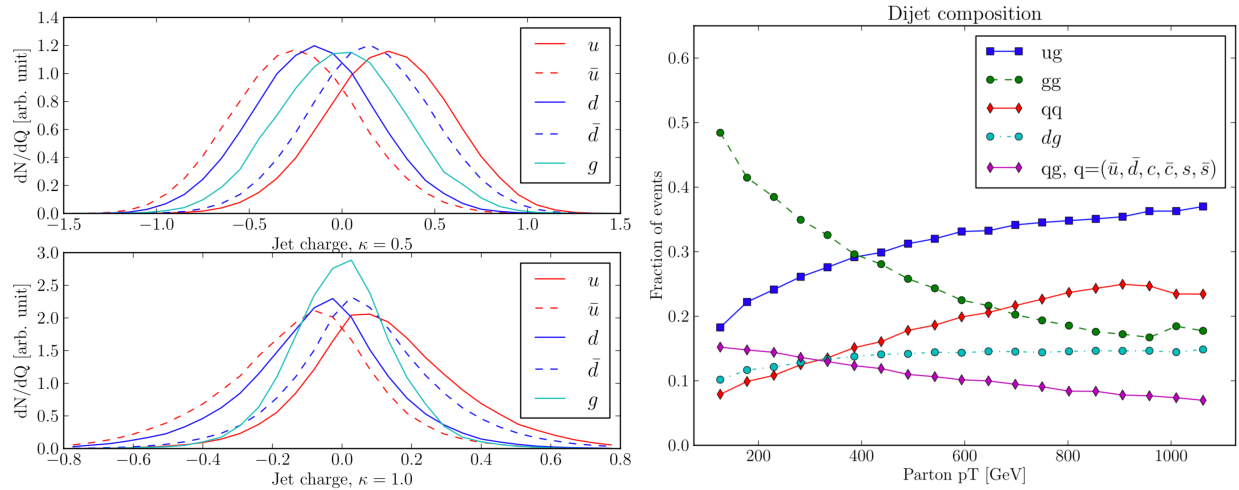


Figure 30. **Left:** Calculations of jet charge distributions for different flavored jets in pp collisions and for  $\kappa = (0.5, 1.0)$  **Right:** Contributions of different hard scattering processes to inclusive dijet production in pp collisions at LHC energies as a function of the parton  $p_T$ . Figures from Ref. [120].

Calculations of the jet charge distributions for different flavored partons and for two values of  $\kappa$  are shown in Fig. 30 (left). It is observed that the  $Q^\kappa$  distribution of gluons is centered at zero while those of positively charged up-quark and negatively charged down-quark jets sit on opposite sides of zero. Inclusive jet charge distributions are thereby sensitive to the fraction of quark and gluon jets in the sample, providing a unique opportunity to study the flavor-dependent jet quenching in heavy-ion collisions. The contributions of different hard scattering processes to the

dijet cross-section are shown in Fig. 30 (right) for pp collisions and an increased light-quark fraction ( $u,d$ ) is observed at higher  $p_T$  due to valence quark effects [120].

The average and standard deviation of the jet charge distributions have been measured in pp collisions (Fig. 31) and are reasonably well described by leading-order Monte-Carlo event generators for all measured  $\kappa$  values [66]. The increasing fraction of light quarks from valence contributions, particularly up quarks, at higher  $p_T$  results in a larger average jet charge.

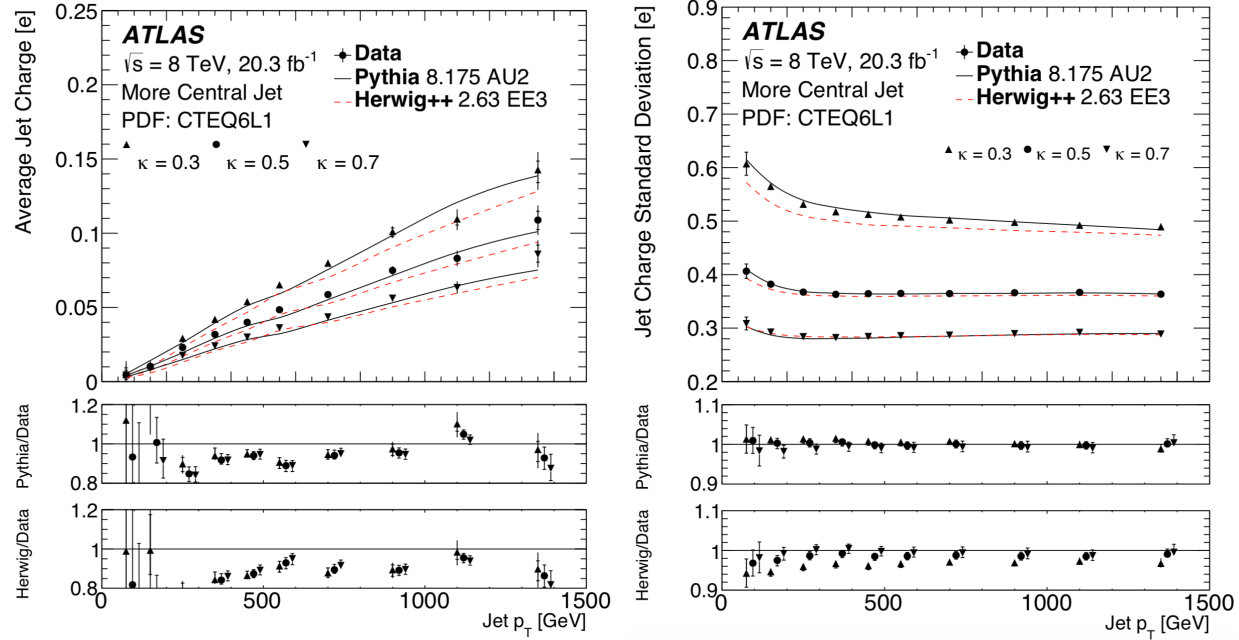


Figure 31. The measured average (left) and standard deviation (right) of inclusive jet charge distributions from pp collisions shown as a function of jet  $p_T$  and for different values of  $\kappa = (0.3, 0.5, 0.7)$ . Results are compared to predictions from PYTHIA8 and HERWIG++. Figures from Ref. [66].

Jet charge is expected to be independent of the hard scattering process for narrow and well-separated energetic jets [112]. Moreover, jet charge is relatively unaffected by gluon splitting as the resulting quark and antiquark effects are expected to cancel out leading to a jet charge of 0, modulo soft radiations [112]. The emission of soft collinear radiations from a high- $p_T$  parton is expected to affect the measured jet charge for  $\kappa > 0$  making it an infrared unsafe quantity. Initial-state radiation (ISR), final-state radiation (FSR) and hadronization effects must, therefore, be taken into account for model comparisons of jet charge distributions [120]. However, in spite of large experimental uncertainties on jet fragmentation functions, it has been demonstrated that

the dependence of the average and width of jet charge distributions on energy and jet size can be calculated using pQCD techniques [120].

In PbPb collisions, an enhanced contribution of down quarks from neutrons modifies the jet charge distributions significantly compared to pp collisions. The average jet charge is plotted for pp, pn and nn collisions in Fig. 32 (left), all of which contribute to Pb (82 protons and 126 neutrons) collisions and result in significantly different average  $Q^\kappa$  values [103]. Additionally, jet charge measurements in heavy-ion collisions are expected to be sensitive to the distinct suppression of quark and gluon jets and medium-modified jet fragmentation functions. An increased quark jet fraction in a sample is expected to result in a widening of the jet charge distributions due to a reduced contribution from zero-charge gluons. Furthermore, the observed excess of soft particles within the jet cone in central PbPb collisions compared to peripheral PbPb and pp results from jet shapes and fragmentation function measurements could play a non-trivial role in modifying the jet charge distributions.

The effects of the hot QCD on the propagating parton can be interpreted via  $R_{CP}$  (Eq. 17) or the ratio of average jet charge in central heavy-ion collisions (with QGP effects) to that in peripheral collisions (assumed as the vacuum reference).

$$R_{CP} = \frac{\langle Q_{\text{central}}^\kappa \rangle}{\langle Q_{\text{peripheral}}^\kappa \rangle}. \quad (17)$$

The CNM effects cancel out in  $R_{CP}$  measurements due to the identical nPDFs for the colliding systems, thus providing insight into the medium modification of the jet charge.  $R_{CP}$  calculations are shown in Fig. 32 (right) from JEWEL and PYQUEN for two values of the energy loss scaling, 4/9 (pQCD Casimir limit), and 1. As expected, no modification is observed in  $R_{CP}$  for a scaling value of 1 which implies similar energy loss for quarks and gluons. In contrast, the pQCD limit Casimir scaling leads to markedly distinct quenching for different flavored partons resulting in a modified  $R_{CP}$ , due to a much larger fraction of quark jets surviving the QGP interaction compared to gluon jets in central collisions [103].

Calculations from SCET<sub>G</sub>, which includes QGP effects via medium-induced splitting functions, are shown in Fig. 33 for the ratio of average jet charge between central PbPb and pp collisions for different values of  $\kappa$ . A strong shift in the averaged jet charge is predicted in PbPb collisions

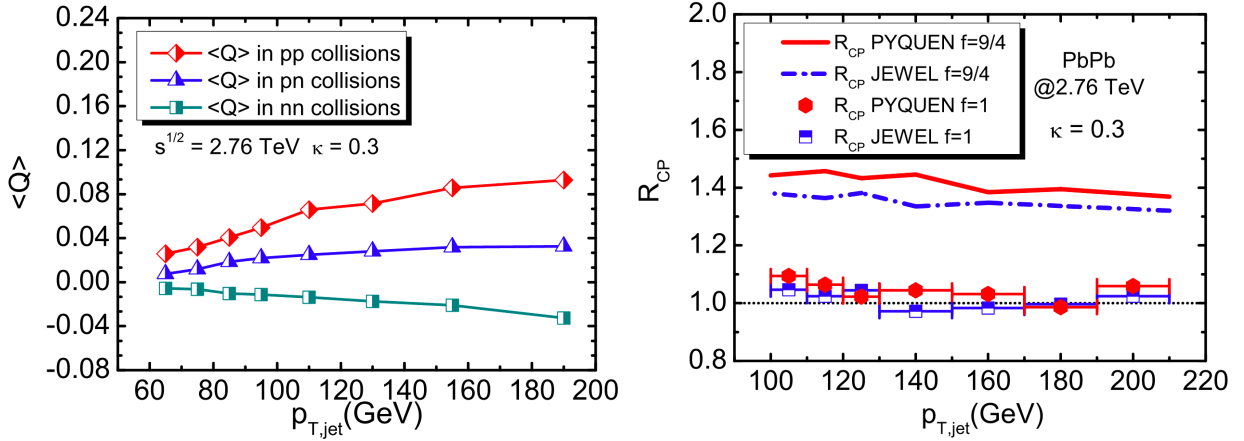


Figure 32. **Left:** Predictions of average jet charge as a function of jet  $p_T$  in hard-scattering events in pp, pn and nn collisions from PYTHIA8. **Right:**  $R_{CP}$  predictions from JEWEL and PYQUEN for the average jet charge in PbPb collisions with different values of energy loss scaling parameters. Figures from Ref. [103].

compared to pp primarily due to isospin effects from the enhanced down quark contribution in heavy-ion collisions, with the medium-modified parton showers resulting in next-to-leading order effects on the ratio [112].

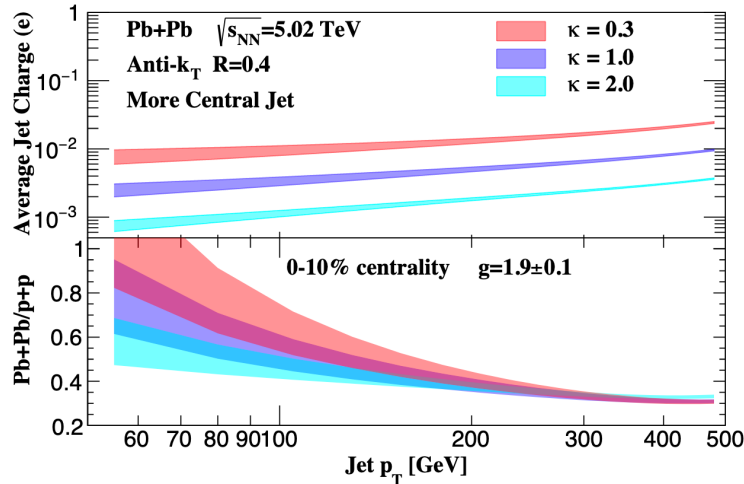


Figure 33. Calculations of averaged jet charge in central PbPb collisions from SCET<sub>G</sub> model for different values of  $\kappa$  as a function of the jet  $p_T$ . The ratio of the averaged jet charge calculations in central PbPb to pp collisions is shown in the bottom panel. Figure from Ref. [112].

Recent theoretical studies and calculations discussed above have established the suitability of using jet charge to explore the flavor-dependence of parton energy loss in QGP among other applications [115, 112, 103]. The work included in this thesis describes the first efforts of measuring jet

charge in heavy-ion collisions, and unfolding them for detector and background effects. Furthermore, a fitting procedure has been implemented using templates of jet charge from simulations to extract the fractions of quark- and gluon-initiated jet in pp and PbPb collisions. Results from these studies help throw light on the significance of color charge in the interaction of a propagating parton with the hot QCD medium.

## 5 THE LARGE HADRON COLLIDER AND THE CMS DETECTOR

### 5.1 Large Hadron Collider

The Large Hadron Collider (LHC), located in CERN, is the world's largest and most powerful particle collider in the world. It consists of a 27-kilometer ring of superconducting magnets and an accelerating framework placed inside a tunnel at an average depth of 100 m below the ground. Inside the ring, particles are accelerated in opposite directions to speeds close to that of light, in two separate beam pipes maintained at ultrahigh vacuum conditions. A complex combination of superconducting magnets (cooled to below 2 K using liquid helium) focuses and directs the high-energy particle beams around the accelerator. The particle beams are then made to collide at four locations around the accelerator, with particle detectors positioned at each of the four crossing points (CMS, ATLAS, ALICE, and LHCb). A complete description of the LHC can be found in Ref. [129].

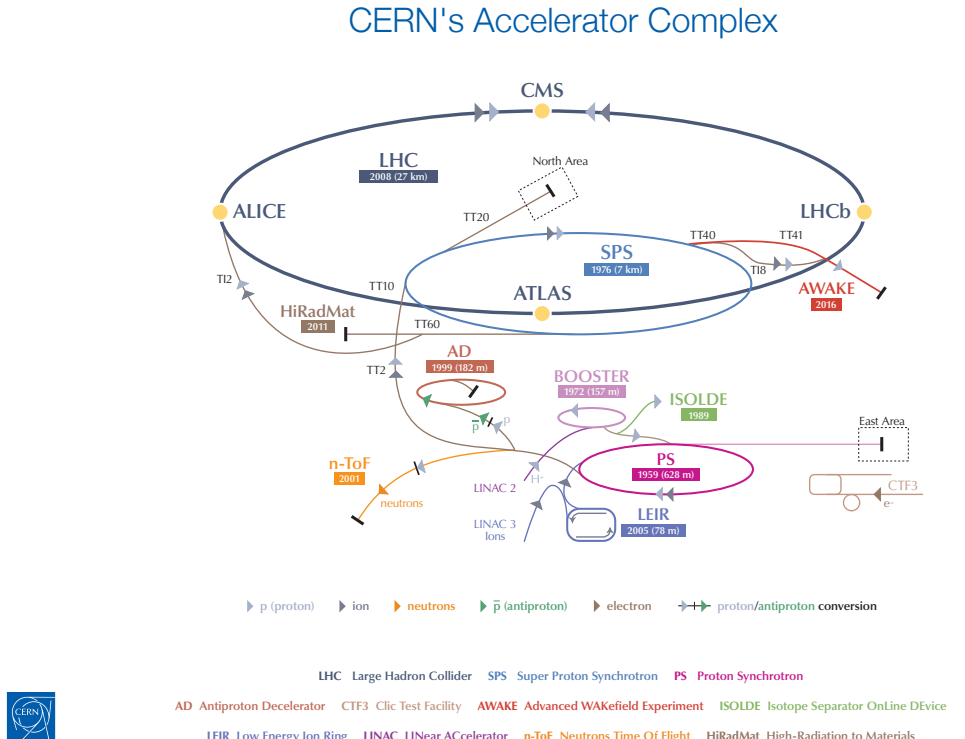


Figure 34. Schematic diagram of the Large Hadron Collider accelerator complex, consisting of various accelerators and particle detectors. Figure from CERN-Poster-2013-377.

The bulk of the data recorded at the LHC includes proton-proton (pp) collisions at center-of-mass energies  $\sqrt{s_{\text{NN}}} = 7, 8$  and  $13$  TeV. The LHC also accelerates and collides heavy ions (e.g.  $^{206}\text{Pb}^{82+}$ ) to deliver collision data for lead-lead (PbPb), proton-lead (pPb) and more recently, xenon-xenon (XeXe) collisions. Reference runs with pp collisions at energies similar to that of heavy-ion collisions have also been recorded for vacuum baseline measurements. The work presented in this thesis uses PbPb and pp collision data recorded in 2015 at a center-of-mass energy  $\sqrt{s_{\text{NN}}} = 5.02$  TeV per nucleon pair.

At peak performance in Run 2, the LHC collided 2,808 bunches of protons (each bunch containing  $\sim 1.2 \times 10^{11}$  protons) every second with a bunch spacing of 25 nanoseconds. This corresponds to a peak instantaneous luminosity of  $2.1 \times 10^{34} \text{ cm}^{-2} \text{ s}^{-1}$  delivered to the all-purpose high-luminosity detectors (CMS and ATLAS). LHCb and ALICE experiments aimed for a low number of collisions per bunch crossing and their luminosity was therefore maintained at a much lower value. The lead collisions recorded in 2015, correspond to a bunch spacing of 100 nanoseconds and a peak instantaneous luminosity of  $2.7 \times 10^{27} \text{ cm}^{-2} \text{ s}^{-1}$ . In high luminosity pp collisions, multiple distinct proton-proton collisions (up to 60) occur frequently within a single recording, referred to as “pile-up.” [130]. In contrast, pile-up is rarely observed in PbPb collisions due to larger bunch spacing. Any pile-up contributions could be eliminated via background subtraction techniques in both pp and PbPb collision measurements.

## 5.2 Compact Muon Solenoid Detector

The central feature of the Compact Muon Solenoid (CMS) detector is a superconducting solenoid providing a magnetic field of 3.8 T and measures 6 m in internal diameter, 13 m in length, and 14,000 tons in weight. Within the solenoid volume are enclosed a silicon pixel and strip trackers, and electromagnetic and hadron calorimeters (ECAL and HCAL, respectively). The calorimeters each consists of a barrel and two endcap sections, and together with the hadron forward (HF) calorimeter, they provide extensive coverage up to  $|\eta| < 5.2$ . The CASTOR and Zero Degree calorimeters further extend the detector coverage to the very-forward regions and close to the beamline. Outside of the solenoid, the CMS comprises a muon tracking system that uses gas-ionization chambers and the entire setup is embedded in a steel flux-return yoke. A detailed

description of the CMS detector can be found in Ref. [131], and a cut-away diagram of the CMS detector, along with a detector cross section in the mid-rapidity region is shown in Fig. 35.

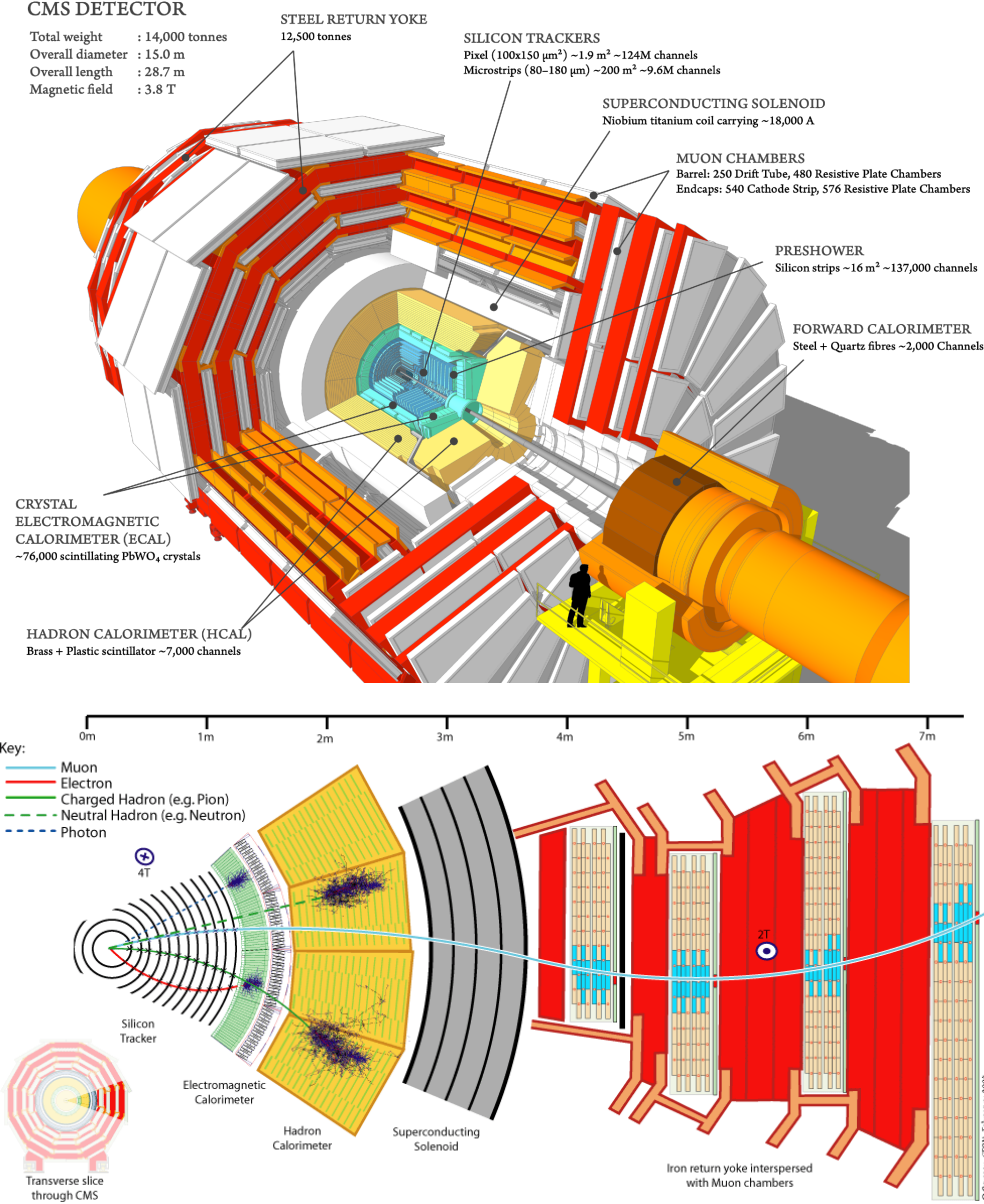


Figure 35. Cut-away (top) and cross-section (bottom) views of the CMS detector, showing all sub-detectors and particle trajectories for different particle species. Figures from Refs. [132, 133].

### 5.2.1 Tracking in the CMS detector

The tracking system is the innermost subdetector component of CMS due to its non-destructive nature and consists of a combination of silicon pixel and strip detectors. The silicon pixel detector (with three layers of radii 4.4 cm to 10.2 cm) is positioned closest to the beamline, where the particle fluxes per unit detector area are highest. This is surrounded by a larger silicon strip detector with layers extending up to a radius of 110 cm. The tracker system further includes “barrel” and “endcap” sections, and measures charged particles in the full  $\phi$  range and up to  $|\eta| < 2.5$ . During the period when the data used in this thesis work were recorded, the pixel and strip detectors consisted of 66 million silicon pixels in 1440 modules and 9.3 million strips in 15,148 modules, respectively.

The pixel detector provides three-dimensional position measurements of the “hits” arising from the interaction of charged particles with the tracker. The resolution on the hit position is  $\sim 10 \mu\text{m}$  in the transverse direction and  $20 - 40 \mu\text{m}$  in the longitudinal direction, with the third coordinate given by the pixel plane position. The strip detector further consists of four components : Tracker Inner Barrel (TIB), Tracker Inner Disk (TID), Tracker Outer Barrel (TOB) and Tracker Endcap (TEC). The relative positions of all the subdetector systems within the tracker are shown in Fig. 36. The measurement resolution and reconstruction efficiency of the tracker system is further discussed in Sec. 7, and a full description can be found in Ref. [134].

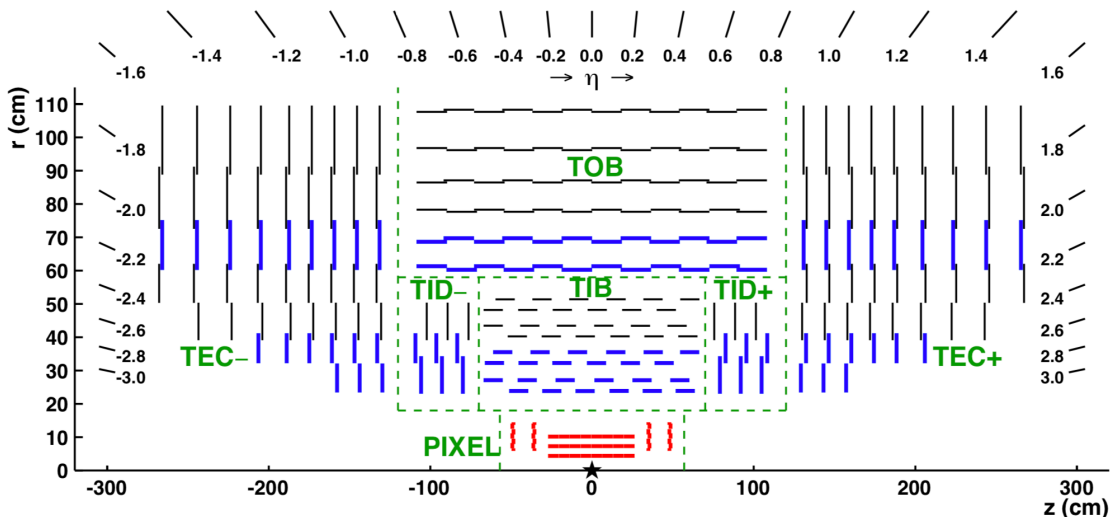


Figure 36. Longitudinal cross-section of the CMS pixel and silicon strip detectors in the  $r$ - $z$  plane. Figure from Ref. [134].

### 5.2.2 Calorimetry in the CMS detector

Calorimeters measure the energy of incident particles including that of high- $p_T$  particles produced in hard scatterings and are an essential component of a collider physics program. The calorimeter setup in CMS consists of two detectors in the mid-rapidity region, ECAL as the inner-layer and HCAL as the outer-layer, as shown in Fig. 35. The energy measured from the calorimeters is a vital input for reconstructing jets used extensively in this thesis.

The Electromagnetic Calorimeter is made up of 75,848 lead tungstate scintillator crystals and provides excellent spatial and energy resolution for particles interacting electromagnetically. The ECAL is made up of a barrel (EB) and two endcap (EE) regions, which provide pseudorapidity coverage of  $|\eta| < 1.48$  and  $1.48 < |\eta| < 3.0$ , respectively (Fig. 37). Preshower detectors consisting of two planes of silicon sensors are placed in front of each ECAL endcap and are used in the identification of pions and electrons. The spatial granularity of the ECAL in the mid-rapidity region corresponds to  $0.0174 \times 0.0174$  in the  $\Delta\eta - \Delta\phi$  space. The ECAL provides a photon energy resolution of  $1 - 2.5\%$  in the barrel region for different  $\eta$  regions and probabilities of photon conversion, and  $2.5 - 3.5\%$  in the endcaps [135]. The measured energy resolution for electrons in the ECAL lies between  $1.7 - 4.5\%$  in the barrel and endcap regions [136].

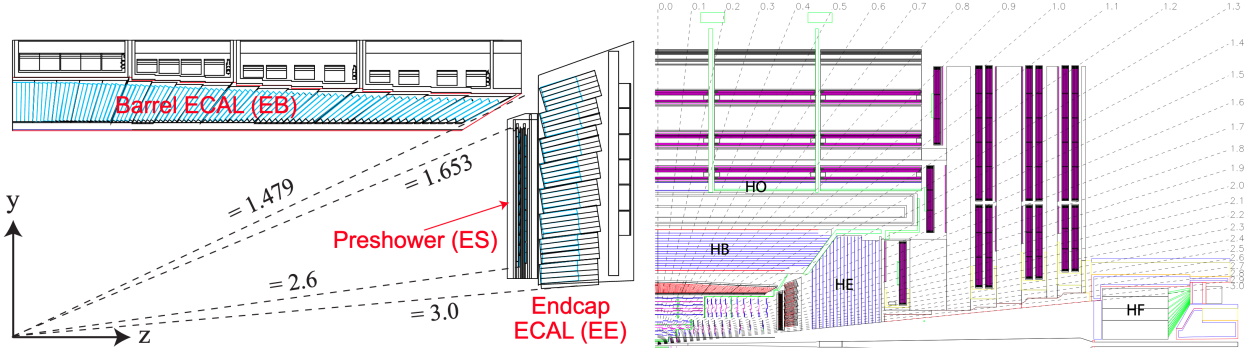


Figure 37. Cross-section of the CMS electromagnetic calorimeter (ECAL) (left) and hadron calorimeter (HCAL) (right), consisting of barrel and endcap sections. Figures from Ref. [137] and Ref. [131].

The Hadron Calorimeter consists of a barrel (HB) and endcap (HE) regions, corresponding to a pseudorapidity coverage of  $|\eta| < 1.3$  and  $1.3 < |\eta| < 3.0$ , respectively. Additionally, it also consists of an outer region (HO), outside of the solenoid as shown in Fig. 37 (right) due to volume

restrictions. The HCAL is a hermetic detector and measures the energy of hadrons, i.e., particles made of quarks and gluons (e.g. protons, neutrons, pions, and kaons) using a system of scintillator tiles embedded with wavelength-shifting fibers. Within the barrel region, HCAL cells map on to  $5 \times 5$  grids of ECAL crystals to form calorimeter towers projecting radially outwards and provides a spatial  $\Delta\eta - \Delta\phi$  granularity of  $0.087 \times 0.087$ . The energy deposited in each calorimeter tower (combination of ECAL and HCAL) and its position are then used in determining the location, energy and axis of reconstructed jet objects with the appropriate calibrations.

The Hadron Forward (HF) Calorimeter is made up of two halves, each of which is placed at a distance of 11.2 m on either side of the nominal interaction point and provide a coverage of  $3.0 < |\eta| < 5.2$ . The HF calorimeter is an essential component of heavy-ion experimental studies as it is used in the event centrality determination as explained in Sec. 6.2.1.

### 5.3 CMS trigger system

At peak performance in Run 2, the LHC delivered a peak instantaneous luminosity of  $\sim 2.1 \times 10^{34} \text{ cm}^{-2}\text{s}^{-1}$  corresponding to about 1 billion pp collisions per second at  $\sqrt{s_{\text{NN}}} = 13 \text{ TeV}$ . PbPb collisions were delivered with a much larger bunch spacing at a peak instantaneous luminosity of  $\sim 2.7 \times 10^{27} \text{ cm}^{-2}\text{s}^{-1}$  in 2015. The size of each recorded PbPb event is also much larger than in pp collisions. In order to store all these events, CMS would need to read, process, and store tens of terabytes every second which is currently unfeasible, thereby necessitating a sophisticated triggering system to select only events of interest. A two-level online trigger system is employed in CMS, composed of hardware-based level one trigger (L1) and a software-based high-level trigger (HLT), to quickly select events that meet certain criteria and to not introduce any biases in the measurements. For the work presented in this thesis, triggering is implemented to primarily select pp and PbPb events with energetic jets while also recording “minimum bias” events meeting minimal requirements with a prescale factor (e.g., a prescale of ten implies only one in every ten events of interest are recorded while the other nine are discarded). The minimum-bias dataset needs to be prescaled in order to discard a fraction of events while being recorded based on the physics need, whereas high- $p_T$  jet-triggered events are quite rare and typically require no prescaling.

The hardware-based L1 trigger system eliminates events failing to meet certain loose requirements within a timespan of  $\sim 3.2 \mu\text{s}$ . This system scans for energy cluster deposits in the

calorimeter towers or hits in the muon chambers and does not take into input any information from the tracker. Once an event is accepted in the L1 triggering system, the event data is forwarded to the HLT trigger system at the rate of  $\mathcal{O}(10^5)$  Hz in pp collisions.

The second level of triggering, or the HLT system, consists of a farm of computing nodes running sophisticated event filtering algorithms based on reconstructed physics objects. The event reconstruction running in the HLT is very similar to that performed in the offline full event reconstruction, with steps implemented to minimize the processing time. The decisions at this level can be performed with full physics objects reconstructed using information from all the subdetectors including the tracker. The events used in this research work are recorded using HLT jet-triggers ( $p_T$  above 100 GeV) with background subtraction implemented at the HLT level in PbPb collisions. The L1 and HLT triggers together reduce the number of events being recorded for offline analysis down to  $\mathcal{O}(10^2)$  Hz from an initial rate of  $\mathcal{O}(10^9)$  every second. A full description of the CMS trigger system can be found in Ref. [138].

## 6 DATA AND MONTE-CARLO SAMPLES

### 6.1 Data samples

The data samples used in this analysis were collected with the CMS detector at a center-of-mass collision energy  $\sqrt{s_{\text{NN}}} = 5.02$  TeV per nucleon pair, during Run 2 at the CERN LHC in 2015. The total data recorded during this period and used in the work presented in this thesis corresponds to an integrated luminosity  $\mathcal{L}_{\text{int}}$  of  $404 \mu\text{b}^{-1}$  for PbPb and  $27.4 \text{ pb}^{-1}$  for pp collisions. Collision events relevant to the work in this thesis are selected using a combination of L1 and HLT triggers as discussed in Sec. 5.3. HLT triggers are employed to select and record events with at least one jet having  $p_T > 100$  GeV in PbPb and pp collisions, referred to as jet-triggered events. Another set of events, referred to as minimum-bias events, are also recorded using an extremely loose set of selection criteria in order to confirm the presence of a collision event. The total number of recorded jet-triggered and minimum-bias events used in these studies from good data blocks, i.e., events passing a validation procedure confirming that all subdetectors were operational and behaving as expected is summarized in Table. II for pp and PbPb collisions. The HLT jet triggers requiring a 100 GeV jet are fully efficient for offline-reconstructed jets with  $p_T > 120$  GeV for pp and PbPb collisions as shown in Fig. 38. The online HLT jet triggers used in PbPb data collection accounts for the background in the jet reconstruction using a "Pedestal Subtraction" technique, discussed in Sec. 8.2.

Dataset	Trigger	Number of selected events
PbPb	Minimum-Bias	764k events
PbPb	HLT Jet100	3.35M events
pp	HLT Jet100	2.66M events

TABLE II. Summary of data samples used in this work along with the triggeres used and the total number of recorded events passing the trigger requirements.

### 6.2 Monte-Carlo simulations and samples

A comprehensive understanding of detector response and basic kinematic distributions is imperative in the process of extracting physics results from experiments. For this purpose, collisions and the ensuing detector responses are simulated using Monte-Carlo (MC) generators by modeling

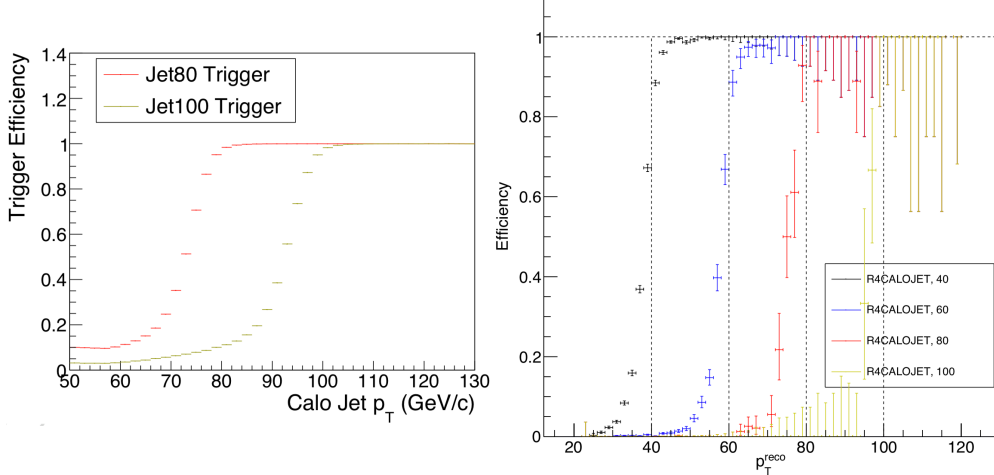


Figure 38. Efficiency of different  $p_T$  jet triggers used in pp and PbPb collision datasets recorded in 2015. Figures from Ref. [5].

known features of the collisions and the subdetector systems. The MC samples are utilized in studying detector responses, deriving efficiency corrections, analyzing the feasibility of measurements, and template-based fitting procedures. MC simulation samples are used extensively in this thesis work in the calibration of jet energy, understanding background effects in jet reconstruction, and for templates in fitting procedures. The different MC generators used in this work are discussed below:

- **PYTHIA** is the most widely-used event generator in high-energy collider physics and is able to reproduce the various features of pp collisions across a wide range of energies. It is currently available in two versions, PYTHIA6 [57] and PYTHIA8 [139], which are both different implementations of the same underlying physics model. It is a leading order generator and can be used to create a sample of rare hard-scattering events producing energetic partons. The fragmentation of the leading parton are handled via Sudakov form factors [140] and the hadronization of the parton shower is implemented using the Lund string hadronization model [141]. PYTHIA also accounts for initial- and final-state radiations, and multi-parton interactions which play an important role in understanding the soft component of pp collisions. **The hard-scattering processes are governed by a variable  $\hat{p}_T$  in PYTHIA, which refers to the initial transverse momentum produced in the hard process.** Samples of PYTHIA6, tune Z2 [142] are used in this thesis and are observed to successfully capture the various features of pp collision data recorded with the CMS detector in

2015. Samples of PYTHIA8 V212 [139] tune CUETP8M1 [143] are also used in this work for cross-checks and systematic uncertainty studies.

- **HYDJET** is used in the full simulation of PbPb collisions along with PYTHIA in CMS heavy-ion jet-related studies [58]. The PbPb collisions are modeled in HYDJET as a hydrodynamically evolving soft background that expands until the temperature drops below a given freeze-out threshold. HYDJET has been tuned to match particle multiplicities and background densities observed in PbPb collisions from the CMS detector and accounts for the expected anisotropic flow effects and the resulting long-range correlations in heavy-ion collisions. To study PbPb events with jets in CMS, PYTHIA hard-scattering signal events are embedded into the HYDJET background and are referred to as PYTHIA+HYDJET.
- **GEANT** is used to simulate the CMS detector and to study the signals induced by the final-state particles interacting with different components of the detector. The detector response modeled by GEANT4 package [144] is a crucial part of studying the resolution, inefficiencies, and other aspects of final-state particle measurements.

The simulation samples used in this work are generated from PYTHIA and PYTHIA+HYDJET for pp and PbPb collisions, respectively. Staggered MC samples with different starting  $\hat{p}_T$  values are generated and used with the appropriate weights, in order to correctly reproduce the observed cross-sections in pp collisions. The MC datasets employed in this thesis studies are summarized in Table III, along with the respective  $\hat{p}_T$  values, cross-sections used in combining the samples, and the number of generated events.

### 6.2.1 Glauber model

Calculations from the Monte-Carlo Glauber model help characterize the number of participating nucleons ( $N_{\text{part}}$ ) or the number of binary collisions ( $N_{\text{coll}}$ ) in an event [35, 34]. Glauber measurements in the CMS operate in the "optical limit", i.e., analyzing a heavy-ion collision in terms of the individual interactions of the constituent nucleons. The model assumes that at sufficiently large energies, the participating nucleons carry enough momentum for their trajectory to remain essentially undisturbed as the nuclei interact and pass through each other.

Generator	Process	Cross section (mb)	Number of events
PYTHIA	$\hat{p}_T > 50 \text{ GeV}/c$	$3.778 \times 10^{-3}$	486k
	$\hat{p}_T > 80 \text{ GeV}/c$	$4.412 \times 10^{-4}$	485k
	$\hat{p}_T > 120 \text{ GeV}/c$	$6.147 \times 10^{-5}$	480k
	$\hat{p}_T > 170 \text{ GeV}/c$	$1.018 \times 10^{-5}$	449k
	$\hat{p}_T > 220 \text{ GeV}/c$	$2.477 \times 10^{-6}$	259k
	$\hat{p}_T > 280 \text{ GeV}/c$	$6.160 \times 10^{-7}$	235k
PYTHIA+HYDJET	$\hat{p}_T > 50 \text{ GeV}/c$	$3.778 \times 10^{-3}$	2M
	$\hat{p}_T > 80 \text{ GeV}/c$	$4.412 \times 10^{-4}$	2.99M
	$\hat{p}_T > 120 \text{ GeV}/c$	$6.147 \times 10^{-5}$	3M
	$\hat{p}_T > 170 \text{ GeV}/c$	$1.018 \times 10^{-5}$	2.99M
	$\hat{p}_T > 220 \text{ GeV}/c$	$2.477 \times 10^{-6}$	3M
	$\hat{p}_T > 280 \text{ GeV}/c$	$6.160 \times 10^{-7}$	3M

TABLE III. Summary of MC samples used in this work along with the corresponding  $\hat{p}_T$  values, cross-sections and the number of generated events.

In this model, the two initial nuclei are treated as non-uniform quantum objects with spatial density variations described by a modified Fermi distribution. For a given pair of colliding nuclei,  $A$  and  $B$ , with the radial nucleon density in each nucleus denoted by  $\rho_A(r)$  and  $\rho_B(r)$ , the "nuclear overlap function"  $T_{AB}$  is defined in Eq. 18 as:

$$T_{AB} = \int d^2\vec{s} \int dz_A \rho_A(\vec{s}, z_A) \int dz_B \rho_B(\vec{s} - \vec{b}, z_B), \quad (18)$$

where  $\int dz_A \rho_A(\vec{s}, z_A)$  and  $\int dz_B \rho_B(\vec{s} - \vec{b}, z_B)$  describe the nucleon probability density at  $(\vec{s}, z_A)$  and  $(\vec{s} - \vec{b}, z_B)$ , respectively, as shown in Fig. 39.

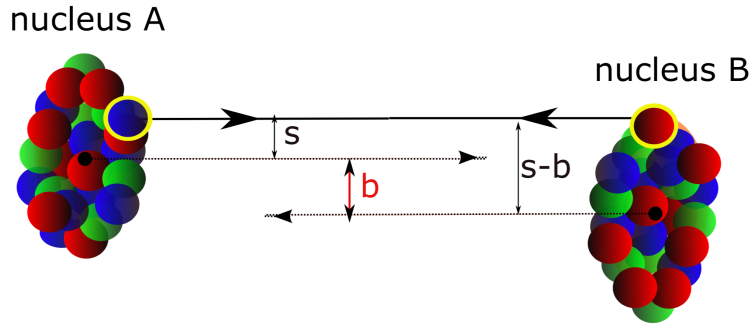


Figure 39. Schematic diagram of Glauber model interaction for a nucleus-nucleus collision, with impact parameter  $b$  between the two nuclei.

The total number of binary collisions for a given nuclear overlap function is given by:

$$N_{\text{coll}}(b) = \sigma_{NN}^{\text{inel}} T_{AB}, \quad (19)$$

where  $\sigma_{NN}^{\text{inel}}$  is the nucleon-nucleon inelastic cross-section at a given center of mass energy, and is constrained using inputs from the proton-proton inelastic cross-section. The probability of a hard scattering increases with  $N_{\text{coll}}$  leading to a larger jet production cross-section in head-on collisions (Fig. 40), thereby requiring an appropriate normalization in observables such as  $R_{AA}$ . The Glauber MC model is implemented using the TGLAUBERMC v3.2 software package and the average values of  $N_{\text{part}}$ ,  $N_{\text{coll}}$  and  $T_{AA}$  for PbPb collisions at 5.02 TeV can be found in Ref. [34].

### 6.3 Centrality determination

In CMS, the event centrality, related to initial nuclear overlap in PbPb events, is defined based on the transverse energy deposited in the Hadron Forward (HF) Calorimeter towers ( $3.0 < |\eta| < 5.2$ ). The HF energy is used to divide the event sample into centrality classes, each representing a percentage of the total inelastic hadronic cross-section [53]. For the results presented in this work, events in PbPb collisions are divided into four centrality intervals corresponding to 0–10% (most central), 10–30%, 30–50%, and 50–100% (most peripheral). Since most variables of physics interest are measured in mid-rapidity, short-range correlation biases are reduced by using information from the forward sections of the CMS detector (i.e., the HF calorimeter) to define event centrality. The measured HF energy distribution is shown in Fig. 40 for PbPb collisions recorded at 2.76 TeV for minimum-bias and jet triggered events, with the largest energy deposited for events corresponding to the smallest impact parameter (0% centrality). It is also evident from Fig. 40 that triggering on events consisting of energetic jets heavily biases the event selection towards more central PbPb collisions.

### 6.4 Event selection and reweighting

Various quality criteria are applied in both data and MC to optimize detector performance and to reduce contamination from non-collision events and effects (< 1% of the total events), potentially arising from detector noise backgrounds, ultra-peripheral collisions and beam gas events.

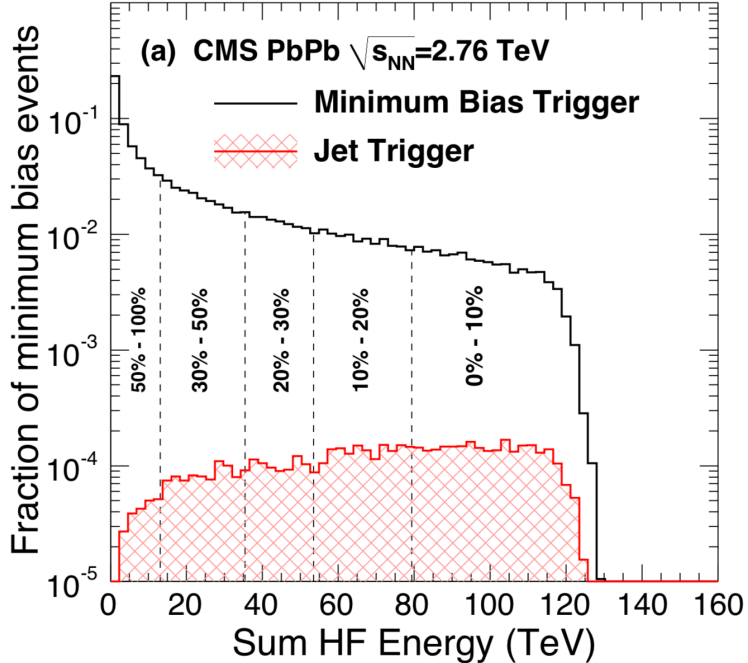


Figure 40. Distribution of transverse energy in the HF calorimeter from PbPb collisions recorded at 2.76 TeV for minimum-bias and jet-triggered events. Figure from Ref. [53].

The standard set of event selection criteria used in CMS jet-related studies are applied in this work as well and are listed below:

- The vertex-z position required to be within 15 cm of the nominal beam spot position
- A primary vertex filter is applied to exclude the contribution from beam-gas events and ultra-peripheral collisions by requiring events to have a reconstructed primary vertex constructed from at least two tracks.
- A HB/HE noise filter is applied to remove events featuring uncharacteristic calorimeter noise based on studies in Ref. [145].
- A beam-scraping filter is applied only in pp collisions, requiring at least 25% of tracks in the event to pass the high purity selection to remove erroneously reconstructed events.
- A filter is applied to PbPb events, requiring that the shapes of clusters in the pixel detector be compatible with those expected from a PbPb collision event.
- The PbPb events are also required to have energy deposits of more than 3 GeV per tower in at least three towers in each of the HF calorimeters.

The distribution of z position of the primary vertices ( $v_z$ ) and centrality for jet-triggered events in PbPb collision data and MC (PYTHIA+HYDJET) are shown in Fig. 41. The  $v_z$  distribution in data is centered about the nominal beam spot and although beam parameters are provided as an input for the simulations, residual differences are observed between the data and MC distributions. A  $v_z$ -based reweighting procedure is therefore applied to events in MC (both pp and PbPb) to match the distribution in data as illustrated in Fig. 41 (right). The centrality distribution is biased towards more central events in PbPb data as events with a higher number of binary collisions are more likely to produce hard scatterings. Samples of HYDJET events are produced as a constant function of centrality, with one PYTHIA signal event embedded in each HYDJET event. The resulting sample of PYTHIA+HYDJET events is therefore required to be reweighted to match the centrality distributions observed in PbPb data as shown in Fig. 41 (left).

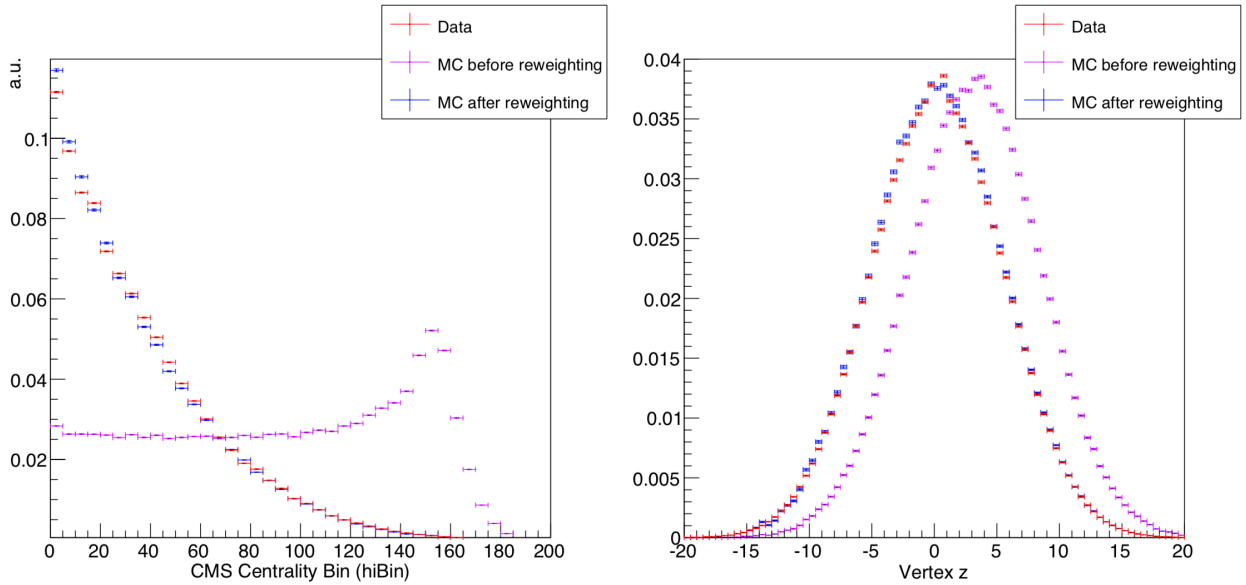


Figure 41. Distributions of primary vertex z-positions and centrality in PbPb data and PYTHIA+HYDJET MC samples for jet-triggered events, along with the reweighted MC distributions. Figures from Ref. [5].

## 7 TRACK RECONSTRUCTION

### 7.1 CMS track reconstruction

In high-energy physics, a track refers to the trail left behind by particles produced in a collision as they traverse through and interact with the detector material. In CMS, charged particles produced in collisions deposit electric charge, referred to as hits, in different layers of the silicon tracker which can be used to reconstruct the particle’s trajectory. In the presence of a large magnetic field near the center of CMS ( $\sim 3.8$  T), trajectories of charged particles having transverse momentum  $p_T$  trace the shape of a helix. Track finding from the pixel detector in CMS is also used in the reconstruction of primary collision vertex in both pp and PbPb collision events. The task of precisely finding charged tracks in PbPb collisions is much more complicated and challenging due to a drastic increase in the number of charged particles by an order of magnitude in heavy-ion collisions compared to pp. The procedure of tracking charged particles in CMS can be found in detail in Ref. [146] and the different steps are discussed below briefly for pp and PbPb collisions:

- **Hit Reconstruction:** Reconstructing hits from the charge deposited in the different layers of the tracker is the first step in the tracking procedure. In the inner pixel detector, adjacent pixels recording a charge signal above a certain threshold are bunched together as clusters. The true position of a hit is determined by comparing the voltages recorded in the pixel clusters to templates from simulations. Similarly, in the outer strip detector, adjacent strips recording a charge signal above a threshold are also combined into a strip cluster. The positions of hits in the strip tracker is determined from a charge-weighted average of all the strip positions in the cluster. An average hit reconstruction efficiency of  $> 99\%$  is observed in the hit reconstruction procedure at CMS, which also corrects for the Lorentz drift inside the pixels and sensor inefficiencies. Hit reconstruction is performed similarly in both pp and PbPb collisions.
- **Track seeding:** The trajectories of potential tracks of charged particles in an event are initially estimated using “seeding layers” and “tracking regions.” The trajectory of a track is constrained using hits corresponding to sets of three-dimensional hits with a helical path in the pixel detector. Sets of three hits in the pixel detector are therefore used in seeding iterations, with the addition of an extra pixel layer in 2016 facilitating the use of four pixel hits. The beamspot is also provided

as an input in the initial seeding iterations but more precise information from the reconstructed primary vertex and silicon strip detector is also included in the later iterations. The other parameter used in the seeding procedure is the tracking region, a three-dimensional region in space that the helical path of a track must emanate from, and helps constrain the  $p_T$  of the tracks identified from the seeding algorithm. In PbPb collisions, pile-up rate is very low and hence the tracking region is restricted to a region of 2 mm around the primary vertex to reduce the contribution from the underlying event.

- **Track finding and fitting:** The initial seeds generated from the previous step are propagated to the entire tracker volume using a Kalman filter algorithm [147, 148, 149] to further reduce the uncertainty on the track trajectory. As a charged particle traverses through the tracker, its initial estimated trajectory is updated continuously using the algorithm as more tracker layer hits are supplied to the measurement. The track candidate is extrapolated to the next layer by assuming a perfectly helical track path in an ideal magnetic field, ignoring any energy loss and multiple scatterings. The next step includes a search for tracker modules (up to two) which are compatible with the estimated trajectory from the previous step. The clusters in the identified modules are then compared and attached to the track trajectory based on a  $\chi^2$  test and "ghost" hits are added in cases where particles failed to generate a hit due to module inefficiency. In the last step, multiple track candidates and trajectories are formed and updated by adding hits from the compatible modules in the layer before extrapolating it to the next layer. The finalized track trajectories are then smoothed using a Kalman filter fit method to reduce biases resulting from either a low resolution in beam spot measurement or from anomalous hits erroneously appended to a track. A similar procedure is also followed for propagating tracks through the entire tracker in PbPb collisions. The entire tracking procedure is performed iteratively by initially searching for tracks that are easiest to find. The hits associated with the tracks found in an earlier iteration are removed in the following iterations, thereby decreasing the combinatorial complexity in the subsequent search for more difficult low- $p_T$  tracks. A total of five iterations are performed in the tracking procedure in both pp and PbPb collisions from identified seeds.
- **Track selection and Merging:** A selection is applied on the output of the Kalman Filter step to reduce contribution of fake tracks using a Boosted Decision Tree (BDT) implemented with

the ROOT multivariate toolkit (TMVA). The BDT is trained on simulations for track quality classification and when applied to data, it returns a single number (-1 to 1) based on the average output of many trees. Based on the BDT output, only charged tracks passing the most stringent set of quality criteria (referred to as "high purity" tracks) are used in the work presented in this thesis. The criteria are based on the parameters listed below and are discussed in detail in Ref. [146].

- An upper threshold on relative track- $p_T$  uncertainty ( $\Delta p_T/p_T$ ),
- Number of hits associated with the track trajectory ( $N_{\text{hits}}$ ),
- Number of layers containing hits associated with the track ( $N_{\text{layers}}$ ) and number of intercepting layers with no hits on the trajectory,
- A minimum requirement on the goodness-of-fit of the track ( $\chi^2/N_{\text{dof}}/N_{\text{layers}}$ ),
- Thresholds on longitudinal and transverse impact parameters (dz and dxy) with respect to the primary vertex position referred to as distances of closest approach (DCA) variables.

Multiple tracks can be identified from different iterations in the above tracking procedure corresponding to the same charged particle and it is necessary to merge them in the final step. Once the duplicate tracks are identified and merged as discussed in Ref. [146], the final track information is stored for further use in the reconstruction of various physics objects and in analyses.

## 7.2 Tracking performance in CMS

The performance of tracking is analyzed based on the efficiency of finding tracks, resolution on measured properties of the tracks, and misreconstruction rate of identifying fake tracks. The efficiency is defined as the probability of correctly identifying and reconstructing tracks corresponding to charged particles. The efficiency varies significantly for pp and PbPb collisions, and also as a function of  $p_T$  and different regions of the detector ( $\eta$  and  $\phi$ ). The tracking efficiency in CMS is observed to be 80 – 90% and mostly uniform in  $p_T$ ,  $\eta$ , and  $\phi$  for pp collisions as shown in Fig. 42. In PbPb collisions, the tracking efficiency is 60 – 70% in the majority of the  $p_T$  region and irrespective of the event centrality and reduces drastically for particles with  $p_T < 1$  GeV (Fig. 43). The efficiencies

are calculated using Monte-Carlo simulation samples from PYTHIA and PYTHIA+HYDJET which are reconstructed after passing through the full GEANT detector simulation and CMS tracking algorithm setup. The reconstructed tracking distributions are compared to those generated in the simulations without any detector effects and the ratios are shown in the bottom panel.

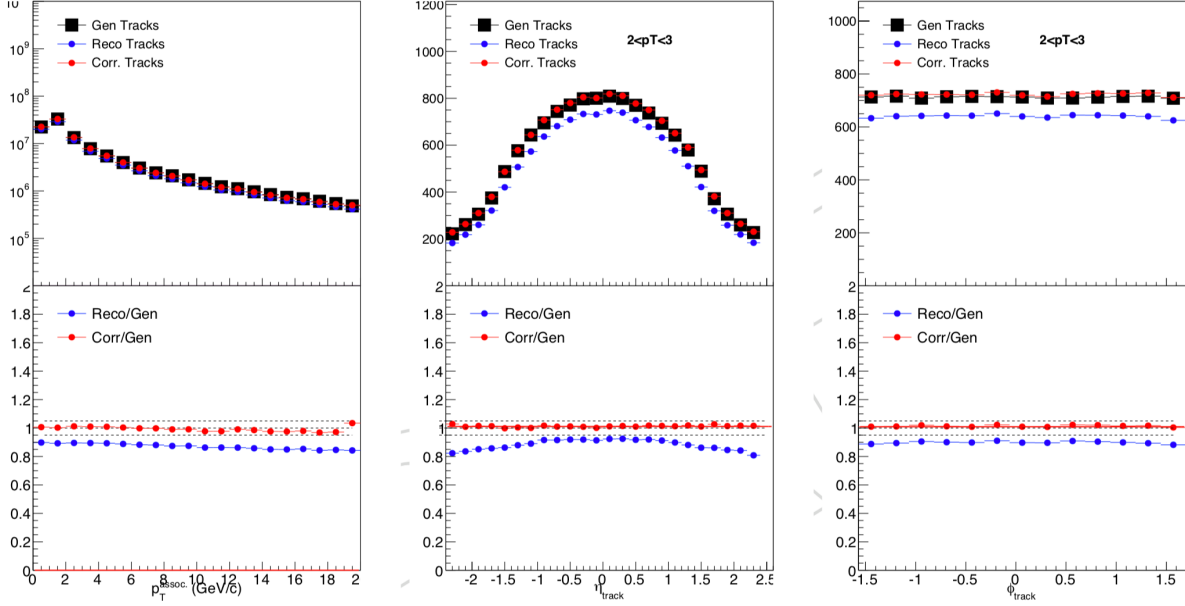


Figure 42. The tracking efficiency for pp collisions in CMS before and after corrections. Figure from Ref. [5].

The inverse of the efficiencies are applied as corrections as a function of  $p_T$ ,  $\eta$ ,  $\phi$ , and local charged particle density and additionally as a function of centrality in PbPb collisions. The response of the tracker in pp and PbPb collisions is shown in Figs. 42 and 43 for pp and PbPb collisions, respectively, before and after the corrections. The reconstructed track distributions are observed to be in agreement with the generated ones after applying the corrections and a systematic uncertainty of 3.9% (5%) is assigned to the measured track  $p_T$  in pp (PbPb) collisions to account for possible differences between data and MC [50].

The resolution on the measured  $p_T$  is shown in Fig. 44 (left) for pp collisions and is  $\sim 1\%$  between 1 and 10 GeV in the barrel region. Even in PbPb collisions, the  $p_T$  resolution is observed to be  $< 2\%$  for  $p_T < 100$  GeV in all centrality bins. The excellent resolution in the  $p_T$  region of interest is made possible due to the strong magnetic field at the center of CMS.

The misreconstruction rate is defined as the probability of finding and building a fake track which does not correspond to a real charged particle. Fake tracks arise from random combinations

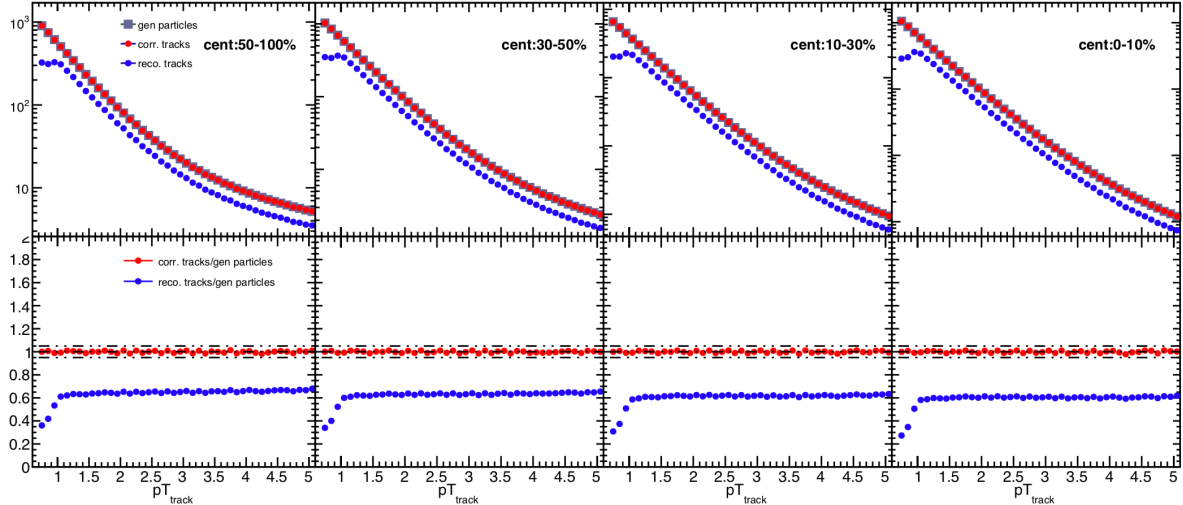


Figure 43. The tracking efficiency for PbPb collisions in CMS before and after corrections. Figure from Ref. [5].

of hits in the tracker and the probability of finding one increases with track multiplicity and is, therefore, higher for more central PbPb collisions. The rate of track misreconstruction is observed to be  $< 3\%$  for pp collisions as shown in Fig. 44 (right), and a similar rate is observed for central PbPb collisions due to stringent track quality selection criteria applied at the cost of efficiency.

### 7.3 Primary vertex finding

The spatial position of the initial interaction between the protons or heavy nuclei inside the detector referred to as the "primary vertex" of the collision is measured using the CMS tracking system [146]. The primary vertex is found to be the point of the common origin of a collection of tracks corresponding to a single collision event. The reconstruction of the event primary vertex is crucial to mitigate the effects of pile-up in pp collisions and in heavy-flavor tagging mechanisms. The reconstruction of primary vertices in CMS is performed in three main steps listed below, and the details of the algorithms involved in the CMS vertexing procedure can be found in Ref. [53].:

- Input tracks passing certain quality thresholds are selected by requiring them to be originating from the beam spot center.
- The selected input tracks are then clustered together and are used to produce a list of vertices attached to the tracks, with the Deterministic Annealing (DA) algorithm as discussed in Ref. [150].

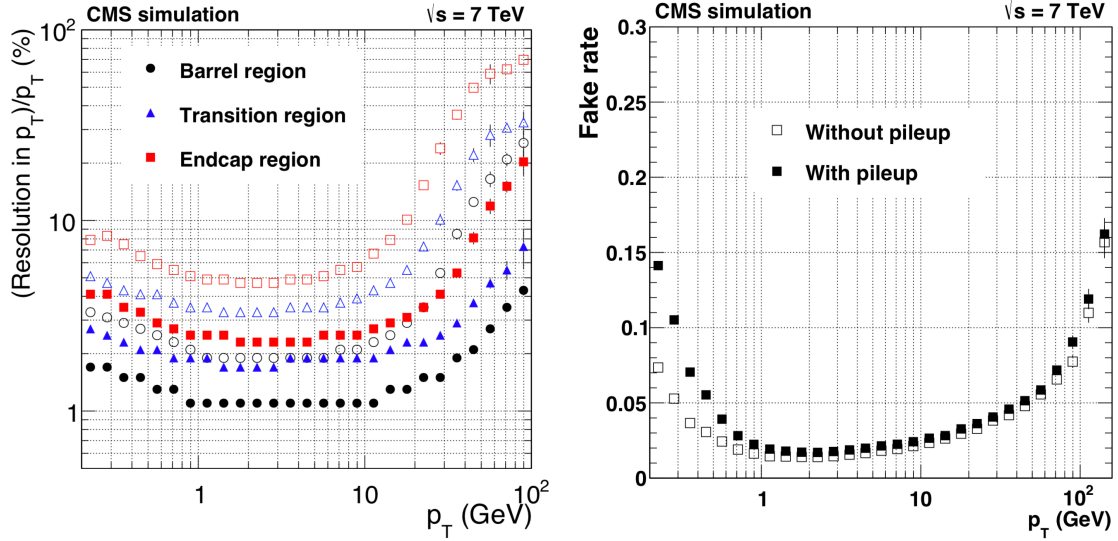


Figure 44. The track  $p_T$  resolution (left) and misreconstruction rate (right) for pp collisions in CMS at 7 TeV. For the resolution, the solid (open) symbols correspond to the half-width of the 68%(90%) intervals centered on the mode of the distribution in residuals. Figures from Ref. [146].

- A fitting procedure is performed on the tracks in each cluster to reconstruct x, y, and z positions of the event primary vertex with a resolution on the measurement.

## 8 JET RECONSTRUCTION

*Portions of the material in this chapter, which is my own work, were published in Ref. [2, 4, 6]*

Jets are topological objects reconstructed using clusters of cells in the detector that are used to group together collimated sprays of hadrons fragmenting from an energetic parton. Reconstructed full jets are used as probes to connect better to the original hard scattering partons, and could provide insights into QCD and hot medium effects. However, the definition of a jet, including its energy and boundary, is ambiguous and depends on the jet algorithm and the physics objects used for clustering. In general, jet algorithms are required to have good control over experimental reconstruction, while being theoretically calculable [151, 152]. In view of these requirements, the following properties are desired in any jet clustering algorithm:

- Simple to implement in experimental analyses and theoretical calculations;
- Defined and yields finite cross sections at any order of perturbation theory;
- Invariant under the radiation of infinitesimally soft particles;
- Insensitive to collinear splittings into hard fragments.

The last two items are together referred to as Infrared and Collinear (IRC) safety and are prerequisites to making jet results theoretically calculable. For example, if the number of jets being reconstructed in an event is sensitive to soft radiations or collinear splittings from a hard parton, it significantly biases the jet spectra and introduces divergences in theoretical calculations. This is illustrated in Fig. 45 from Ref. [153], where the number of jets being reconstructed is modified by a collinear splitting (left) or soft radiation (right). Initial jet algorithms such as the iterative cone [154], which define jets within specific conical regions around a seed do not satisfy the IRC safety requirements. Extensive work has been performed towards improving jet reconstruction algorithms which satisfy the above conditions and are easily implementable [152, 153].

### 8.1 Anti- $k_T$ jet algorithm

High-energy hadron colliders currently employ a class of jet clustering algorithms known as sequential recombination algorithms, which iteratively identify and combine pairs of calorimeter towers or particles with the smallest distance to reconstruct jets. Jets formed through these

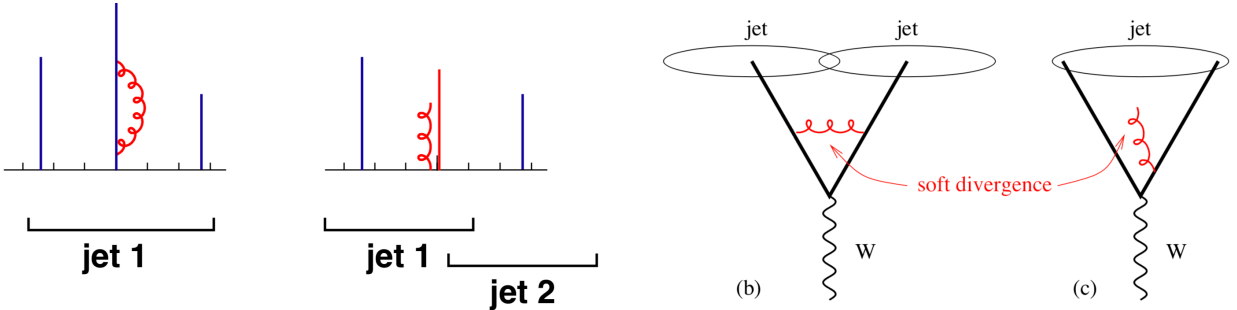


Figure 45. Illustrations of collinear safety (left) and infrared safety (right) in jet reconstruction. Figure from [153].

algorithms are not necessarily circular and the iterations are performed until all the available constituents (towers or particles) are exhausted or a terminating condition is reached. The distance parameter between the constituent pairs  $(i, j)$  for the proximity matching is defined in sequential clustering algorithms (Eq. 20) as:

$$d_{i,j} = \min(k_{t,i}^{2p}, k_{t,j}^{2p}) \frac{\Delta_{i,j}^2}{R^2}, \quad (20)$$

for all potential pairs  $(i, j)$  of particles/towers/intermediate jets (referred to as pseudojets).  $k_{t,i}$  refers to the transverse momentum of the constituent  $i$ ,  $\Delta_{i,j}$  denotes the angular distance between two constituents and  $R$  represents the radius parameter for jet reconstruction. Varying values of the jet radius parameter  $R$  is a trade-off between including more of the fragmenting signal hadrons and including effects from the background particles.  $R$  is chosen to be 0.4 in the work presented in this thesis which is typical for light quark and gluon jets, and larger values of  $R$  are usually chosen for boosted heavy boson or top quark jets. The variable  $d_{i,B}$  is also calculated for every constituent  $i$  with respect to the beamline  $B$ , and is defined in Eq. 21 as:

$$d_{i,B} = k_{t,i}^{2p}, \quad (21)$$

The exponent  $p$  in Eqs. 20 and 21 can be varied and setting it to  $(-1)$  is the (anti-) $k_T$  algorithm [155, 156], while setting it to 0 is the Cambridge/Aachen algorithm [157]. The  $k_T$  algorithm clusters via a  $p_T$ -ordering, starting from clustering the softest constituents first and eventually combining the harder fragments into the jet. The Cambridge/Aachen algorithm, however,

is independent of the  $p_T$  of the constituents and follows a pure angular ordering to cluster the closest constituents first. Jets reconstructed using kT and C/A algorithms are shown in the  $\eta$ - $\phi$  space in Fig. 46 and are observed to be quite irregular compared to the iterative cone algorithms.

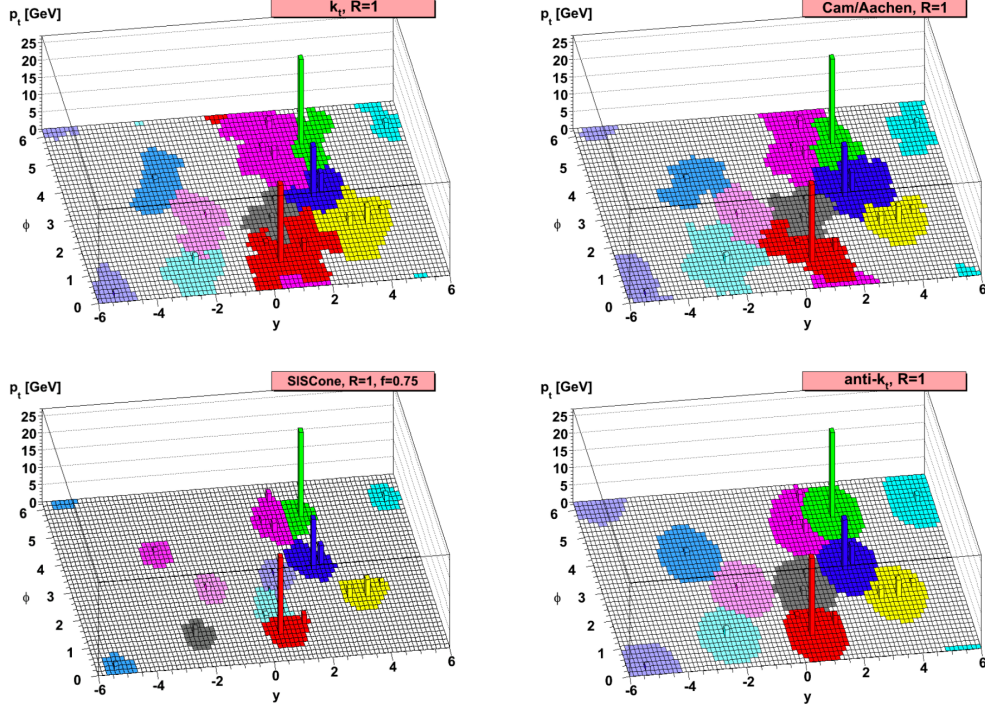


Figure 46. Jets reconstructed at the parton-level clustered with four different jets algorithms, showing the active catchment areas of the resulting hard jets. Figure from [156].

Setting the exponent  $p = -1$  is referred to as the anti- $k_T$  algorithm [156], and is currently the most commonly employed algorithm in high-energy experimental measurements. The negative exponent used in determining the distance parameter in anti- $k_T$  algorithm reproduces the circular regular shapes of jets observed in iterative cone algorithms as shown in Fig. 46. All the sequential clustering algorithms described above are observed to be IRC safe and are implemented in experimental measurements using the FASTJET [158] framework to improve timing performances.

CMS analyses use two types of inputs to jet reconstruction algorithms, referred to as “calorimeter” and “particle-flow” (PF) jets. For calorimeter jets, energy deposits from mapped grids of ECAL and HCAL (referred together as calorimeter towers) are used as input in the clustering algorithms. In the PF jet reconstruction method, particle candidates reconstructed using information from the full detector is used in the clustering. Identifying the particles in the PF method, referred

to as particle-flow candidates, involves a complex procedure implemented in CMS by including and matching the information from the tracker, calorimeters, and the muon chamber [159]. The jet energy resolution is observed to be better when reconstructed with PF candidates compared to calorimeter towers, especially at very low  $p_T$  ( $< 50$  GeV). However, the difference in the resolution is negligible at jet energies relevant to the work presented in this thesis. Additionally, calorimeter jets provide an advantage of being insensitive to auto-correlation tracking biases in jet-track correlation studies, as information from the tracker is not used in calorimeter jet reconstruction. The measurements presented in this thesis use calorimeter jets reconstructed using the anti- $k_T$  jet algorithm with a radius parameter of 0.4 (jointly referred to as “ak4Calo” jets) in pp collisions. Additional background subtraction is applied for jet reconstruction in PbPb collisions to account for the underlying event activity.

## 8.2 Jet reconstruction in heavy-ion collisions

An enormous amount of energy and entropy is produced in heavy-ion collisions, higher than ever observed in pp collisions. Up to 1600 particles and  $1.65 \pm 0.1$  TeV can be produced in the midrapidity region ( $|\eta| < 0.45$ ) of a single central PbPb collision at LHC energies. This poses a challenge in accessing the “true” information carried by a fragmenting parton while plowing through the QGP formed in these collisions. While accessing the information of an energetic parton produced in a hard scattering via jets in PbPb collisions, the particles produced in unrelated nucleon interactions in the same collision are treated as background, referred to as the underlying event (UE). The UE is observed to fluctuate from event-to-event and also as a function of eta and phi and has to be accurately removed via background subtraction techniques to obtain the true momentum of the original jet. There is a growing need for accurately estimating and subtracting background contribution to jets even in pp collisions as we enter the era of high-luminosity collisions, with large pile-up effects.

Various background estimation and subtraction techniques have been proposed and studied and different methods are chosen based on the jet observable and physics phenomena being studied. The noise/pedestal subtraction technique (PU) [160] is typically used in measurements where the jet is viewed as a macroscopic object [53, 60, 61, 55, 2, 63], including the jet shapes and jet charge measurements presented here. However, in analyses probing the jet substructure (e.g. jet mass and

splitting function measurements [161, 162]), the constituent subtraction method (CS) [163] is viewed to be advantageous. The implementation of the PU subtraction technique is briefly discussed below:

- The average energy deposited in the calorimeter towers is measured along with its dispersion in different  $\eta$  strips for a given event. The  $\eta$ -dependent average “pedestal” energy ( $\rho(\eta)$ ) is normalized to the  $\eta\text{-}\phi$  area and shown in Fig. 47.

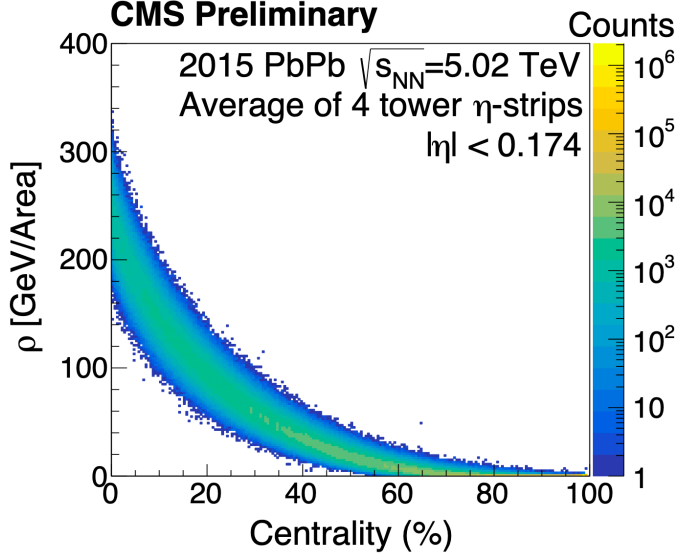


Figure 47. The area-normalized energy deposited in the calorimeter towers in PbPb events as a function of the event centrality. Figure from [164].

- The  $\rho(\eta)+\sigma(\eta)$  is subtracted from all the towers in the corresponding rapidity regions and any towers with resulting negative energies are set to zero.
- The subtracted towers are then clustered using the anti- $k_T$  jet algorithm, and the resulting jet energies are oversubtracted due to the inclusion of the jets in estimating  $\rho(\eta)$ .
- Once anti- $k_T$  jets are identified in the event, another iteration of  $\rho(\eta)$  and  $\sigma(\eta)$  estimation is performed after excluding the identified jet regions.
- The updated  $\rho(\eta)+\sigma(\eta)$  is subtracted from all the towers, in the respective rapidity regions, similar to the first iteration with a reduced effect of jet signal on UE energy estimation.
- The newly subtracted towers are then clustered again into anti- $k_T$  jets, referred to as “akPu4Calo” jets used in the work presented in this thesis.

The average background contribution to jets in central PbPb collisions at LHC energies is observed to be  $\sim 200$  GeV/Area in the mid-rapidity region, as seen in Fig. 47. The precise estimation and subtraction of this contribution without introducing any biases are essential to obtain meaningful physics results regarding the QGP properties. The performance of the PU subtraction technique can be quantified via closure and resolution plots on the measured jet energy shown in Fig. 48, from CMS PYTHIA and PYTHIA+HYDJET simulation studies.

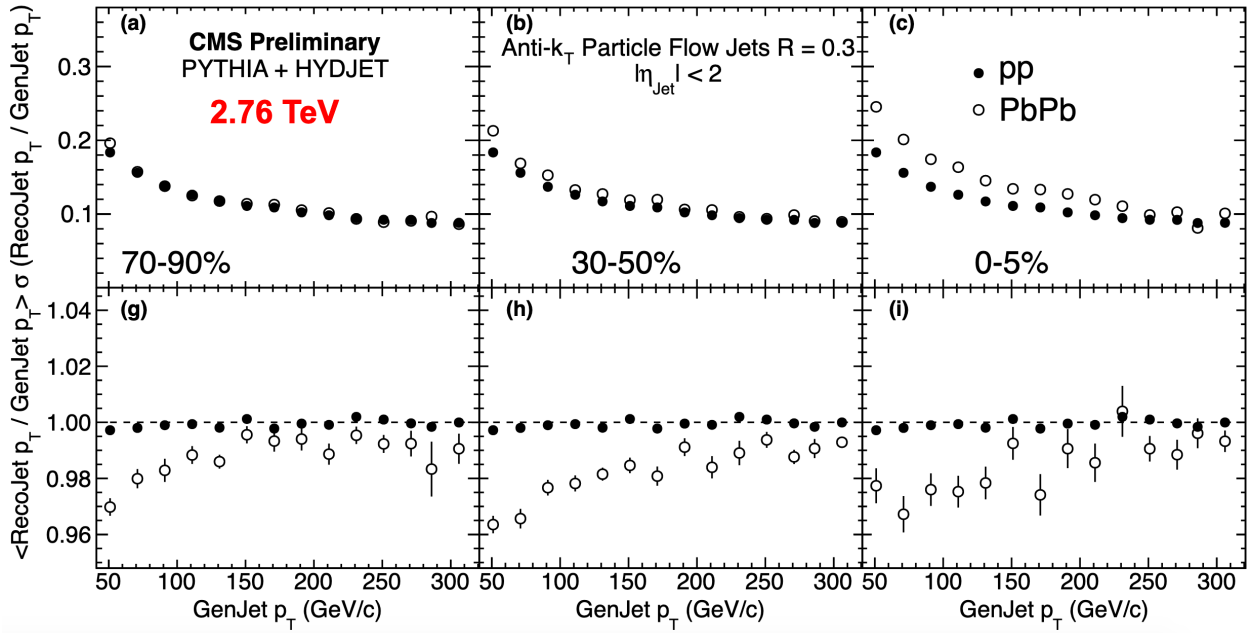


Figure 48. Jet energy scale and resolution for akPu4Calo jets in PbPb collisions as a function of jet  $p_T$  compared to results from pp. Figure from [164].

The jet energy closures are shown in Fig. 48, with all the corrections applied (Sec. 8.3) and are consistent with unity within 3% in both pp and PbPb collisions. The resolution is similar between pp and peripheral PbPb collisions and is worse in central PbPb collisions, where it is  $\sim 18\%$  at 120 GeV, which is the lower threshold used in the studies presented here. The PU subtraction algorithm is also implemented in CMS jet reconstruction with very efficient timing performances using the FASTJET framework [158].

Further improvements are necessary and ongoing with respect to heavy-ion jet reconstruction to deal with biases and shortcomings of the current subtraction techniques. For example, the PU subtraction does not account for any azimuthal dependency of the background which is a prominent feature of mid-central PbPb collisions (Sec. 2.5). The long-range azimuthal correlations observed in

heavy-ion collisions arising from flow effects result in an anisotropic distribution of soft particles in  $\phi$ . Novel methods are currently being explored to account for the background flow modulation and to preserve the constituent resolution, which are essential in order to measure a whole range of jet substructure observables in heavy-ion collisions [164, 165].

### 8.3 Jet energy corrections

The energy of the jets reconstructed in pp and PbPb collisions at the CMS detector need to be corrected for detector inefficiencies and non-linear response of the calorimeters. A detailed description of the jet energy correction procedure in CMS can be found in Ref. [166]. The corrections are applied in a series of factorized steps, with the largest correction factors applied first followed by the final fine-tuning corrections, with each correction being applied on top of the previous one. A flow chart of the series of jet corrections applied to reconstructed jets in data and MC is shown in Fig. 49, and are discussed below:

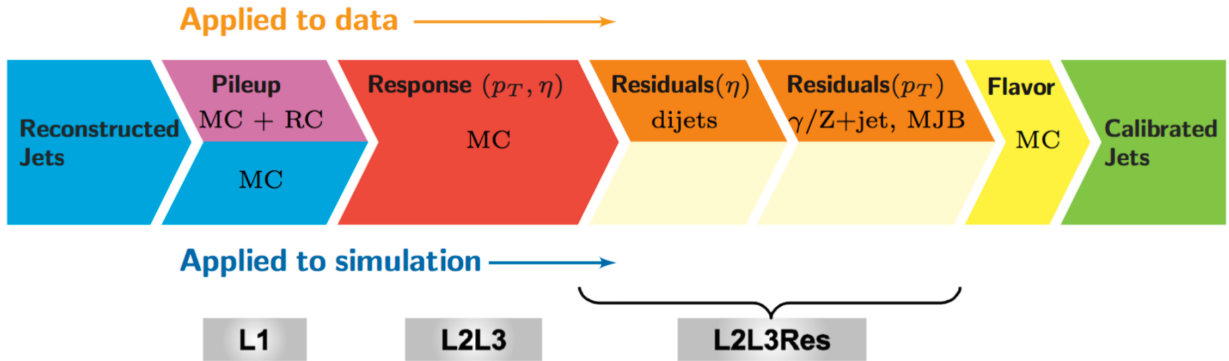


Figure 49. Schematic diagram of the jet energy corrections applied in CMS.

#### 8.3.1 Monte-Carlo corrections

The first and largest correction factor is derived from Monte Carlo simulations based on the observed jet energy response. The hard scattering partons from a QCD dijet MC sample undergo fragmentation and hadronization and are reconstructed as full jets based on their interaction with the detector simulation. The final reconstructed jets are then matched to the initial generated jets and the distributions of the ratio of their  $p_T$  are fit with Gaussian functions in jet  $p_T$  intervals. The

means of the fits are analyzed as a function of the jet  $p_T$  and  $\eta$ , and their inverse are applied as corrections (vary from 5% to 20% based on the jet  $p_T$  and  $\eta$ ).

### 8.3.2 Data-driven corrections

Following the MC-based corrections, data-driven jet energy corrections are applied to further improve the jet energy measurements. These corrections are applied only to jets in data as the residual non-closures corrected for in this step are not observed in MC. The first of the data-driven corrections are based on dijets reconstructed in an event, which are expected to be back-to-back in azimuthal and roughly carry the same amount of energy, modulo multi-jet events. The jets reconstructed in the barrel region are expected to be well-calibrated in the first step of the correction procedure and are used as reference objects for the recoiling probe jet outside of the barrel region. Corrections are derived as a function of the jet  $\eta$  based on the ratio of response functions in MC and data in dijet events, after removing contributions from three-jet events. It should be noted that jets produced in central (head-on) heavy-ion collisions are expected to be quenched due to QGP medium effects, and a significant imbalance of jet energy is observed in dijets in central heavy-ion collisions [56, 53]. Therefore, only the most peripheral events are used to derive the data-driven jet energy corrections for PbPb collisions, where no jet quenching effects have been observed.

Once the jets are corrected using both simulation samples and the recoiling jets, colorless reference objects such as photons or Z bosons are used to further correct for any remaining non-closures in the overall scale factors. Photons and Z-bosons reconstructed with very good control in CMS and rare events containing a hard jet recoiling off of either of these well-calibrated objects are used in this procedure. These corrections are derived as a part of this thesis work with  $\gamma + jet$  events for jets with  $|\eta| < 1.3$  from a  $p_T$  of 30 GeV to 500 GeV, and have been included in the official CMS framework for use by all relevant measurements.

In this procedure, the jet energy response is studied using the  $p_T$  balance and MPF (missing transverse momentum projection fraction) methods [166]. The jet response in the  $p_T$  balance method, defined in Eq. 22, is analyzed by comparing the reconstructed jet transverse momentum ( $p_{T,jet}$ ) to that of the recoiling photon ( $p_{T,ref}$ ). The response in the MPF method, defined in Eq. 23,

takes into consideration the total hadronic activity in the collision event recoiling versus the photon.

$$R_{\text{jet},p_T} = \frac{p_{T,\text{jet}}}{p_{T,\text{ref}}} , \quad (22)$$

$$R_{\text{jet,MPF}} = 1 + \frac{\vec{p}_{T,\text{miss}} \cdot \vec{p}_{T,\text{ref}}}{(p_{T,\text{ref}})^2} . \quad (23)$$

The difference and complementarity of the two response determinations is used to propagate the systematic uncertainties in the corrections. The  $p_T$  imbalance between the jet and the recoiling photon can also arise from the presence of additional jets in an event and this should be accounted for while deriving the corrections. The additional jet activity is parameterized by the variable  $\alpha$ , defined as the “ratio of the most energetic jet that does not originate from the event topology under study, divided by the typical momentum scale of the event” [166]. The responses are evaluated as a function of  $\alpha$ , defined in Eq. 24 for  $\gamma + \text{jet}$  events, and the corrections are extrapolated to  $\alpha = 0$  to address only jet energy response effects.

$$\alpha = \frac{p_{T,2\text{nd jet}}}{p_{T\gamma}} , \quad (24)$$

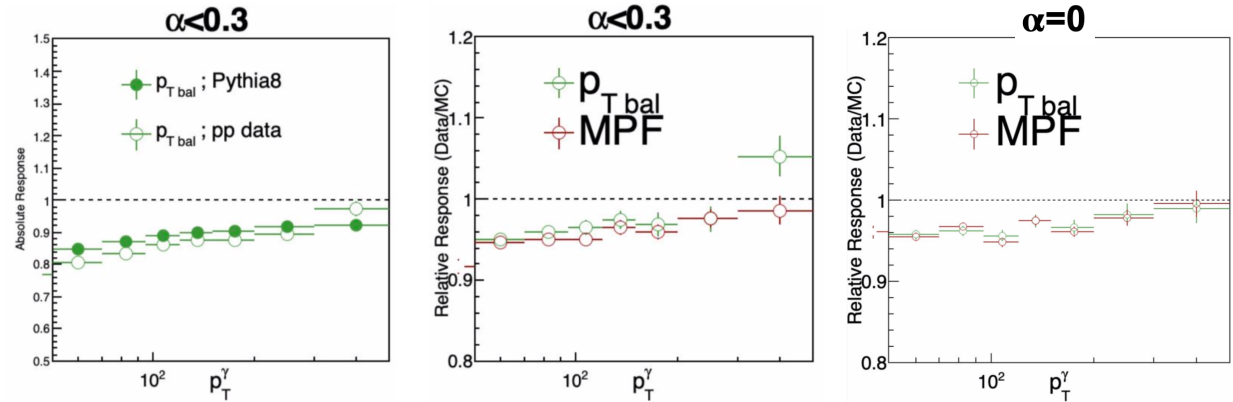


Figure 50. **Left:** Absolute response in  $\gamma + \text{jet}$  events from pp data and PYTHIA. **Middle:** Relative response in  $\gamma + \text{jet}$  events from the two methods. **Right:** Relative response extrapolated to  $\alpha = 0$ . Figure from Ref. [6].

The absolute response, determined using Eqs. 22 and 23, are shown in the left panel of Fig. 50 for a sample bin of  $\alpha < 0.3$  for both data and MC. The relative response is plotted in

the middle panel of Fig. 50 for the same  $\alpha$  bin, showing the ratio of the absolute response curves between data and MC using the two methods. The relative response is then extrapolated to  $\alpha = 0$  and shown in the right panel of Fig. 50, the inverse of which are applied as the absolute corrections. The final jet energy response after applying the data-driven corrections are shown in Fig. 51, and is observed to be consistent with unity within  $\sim 2\%$ .

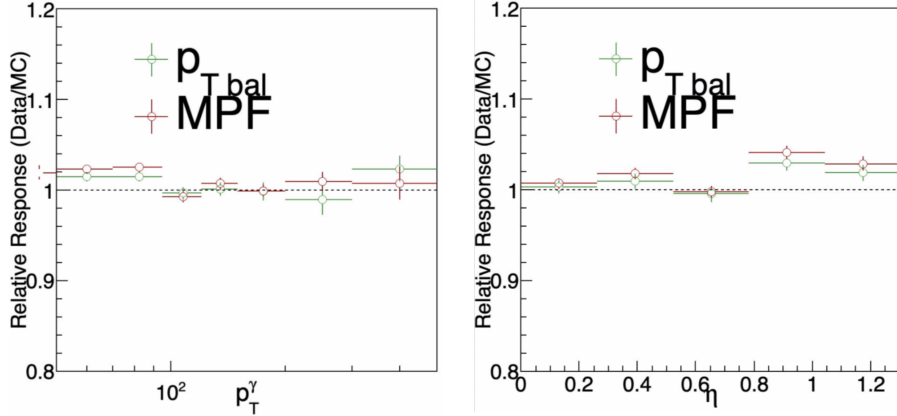


Figure 51. Relative response in  $\gamma + \text{jet}$  events from the two methods after applying the residual data-driven corrections. Figure from Ref. [6].

The data-driven corrections are expected to be biased in PbPb collisions due to a strong suppression of jets observed in central events from jet quenching effects (Sec. 3.3). Therefore, only the most peripheral events are used to derive these corrections in PbPb collisions, where only cold nuclear matter and minimal quenching effects are expected, and are applied to the whole sample.

### 8.3.3 Fragmentation-dependent corrections

The calibrations derived in the previous sections correct for the overall scale factor in a given sample, and provide access to the “true”  $p_T$  of the jet on an average. The resulting jet energy scale after the previous corrections depends on  $p_T$  and, to a lesser extent, centrality, as shown in Fig. 52 for pp and PbPb collisions. The closures are also shown separately for quark and gluon-initiated jets with blue and red markers respectively in the figures, and it is evident that quark-initiated jets are constantly overcorrected and gluon-initiated jets undercorrected in all centrality bins after the initial corrections.

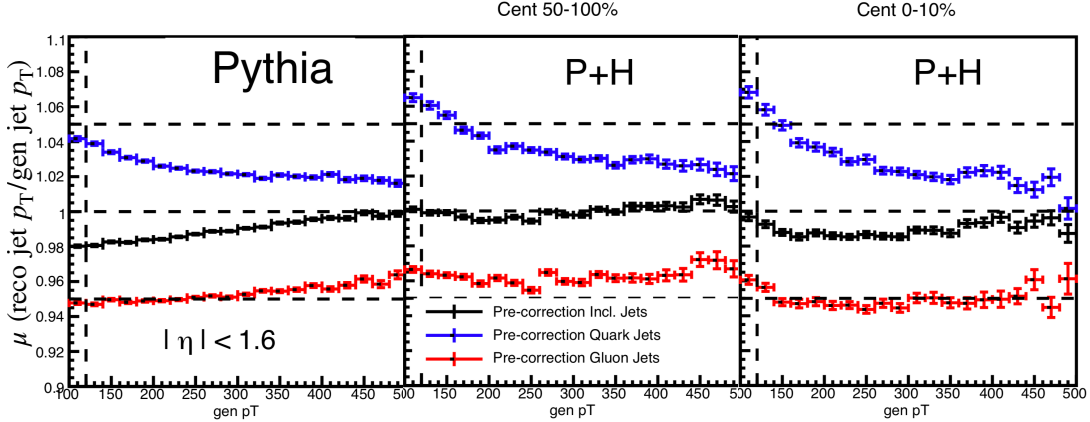


Figure 52. Jet energy scale as a function of jet  $p_T$  for pp and PbPb collisions from simulations, shown separately for inclusive, quark and gluon jets. Figure from Ref. [4].

Due to observed detector non-linearities for calorimeter jets reconstructed in CMS, the detector response depends on the number of particles in the jet. Energy corrections are therefore derived based on the reconstructed number of particle flow candidates within the jet cone, which corresponds to  $N_{PF}$  for pp and the number of background-subtracted PF candidates or  $N_{CS}$  for PbPb collisions. The distribution of the number of constituents in the jet cone is shown for a sample of reconstructed jets with  $130 < p_{T,\text{reco}} < 140$  GeV, separately for quark and gluon jets in Fig. 53. It is evident from these figures that, on an average, quark jets have a fewer number of constituents in the jet cone compared to gluon jets. This observation that gluon jets consistently tend to fragment softer than quark jets allows improving quark and gluon jet energy closures by utilizing the information about the number of particles in the jet cone to derive and apply corrections.

The dependence of the jet energy scale on the number of particles in the jet cone (with  $p_T > 2$  GeV) for a sample jet  $p_T$  bin is shown in Fig. 54 with blue markers. Only PF candidates with  $p_T > 2$  GeV are used in these corrections to reduce the effects of the underlying event. The jets with a higher number of constituents are observed to be undercorrected and vice versa after applying the initial corrections, and the scale decreases linearly with increasing  $N_{PF}$  or  $N_{CS}$  for inclusive jets. The difference in the response for quark and gluon jets is mainly because gluon jets have a higher number of particles compared to quark jets on an average. Flattening the scale as a function of the number of jet constituents would, therefore, reduce this bias.

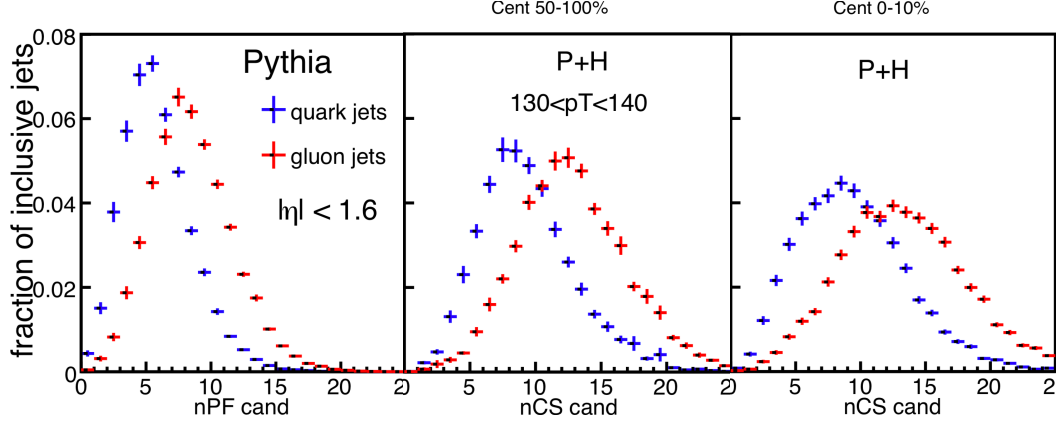


Figure 53. The number of constituents with  $p_T > 2$  GeV within the jet cone for quark and gluon jets having  $130 < p_{T,\text{reco}} < 140$  GeV. Figure from Ref. [4].

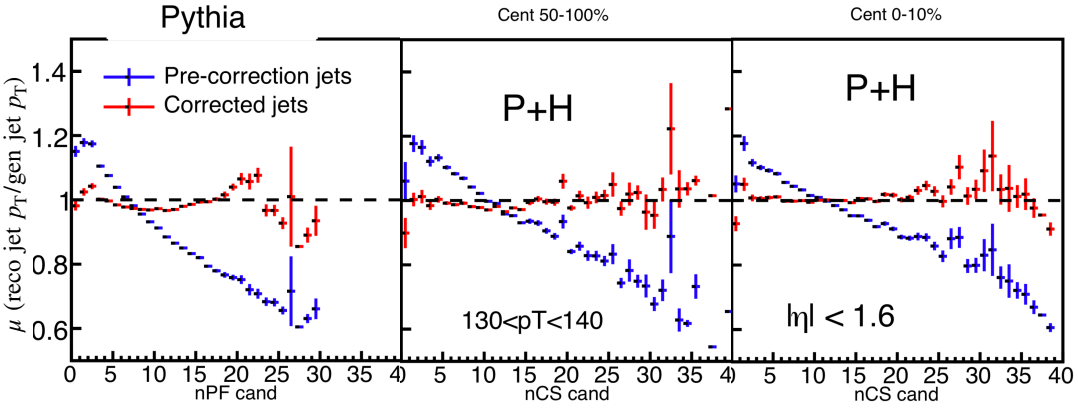


Figure 54. Jet energy scale shown as a function of the number of jet constituents from simulation studies before and after corrections. Figure from Ref. [4].

A correction factor that accounts for the scale non-closure as a function of both the number of jet constituents and the reconstructed jet  $p_T$  is applied as a two-dimensional correction. To achieve this, linear fits are applied to the jet energy scale as a function of  $N_{PF}$  or  $N_{CS}$  for each of the reconstructed jet  $p_T$  bins. The resulting linear fit parameters are then further smoothed as a function of jet  $p_T$  using higher-order fitting functions to eliminate any fitting or statistical outliers. The correction factors are finally extracted for any given  $N_{PF}$  or  $N_{CS}$  and reconstructed jet  $p_T$  based on the higher-order fits.

The jet energy closures after applying the two-dimensional corrections are shown with red markers as a function of the jet constituent multiplicity in Fig. 54 and are observed to be relatively

flat and consistent with unity. The closures for quark, gluon, and inclusive jets after applying the fragmentation dependent corrections are shown in Fig. 55 as a function of the generated jet  $p_T$ .

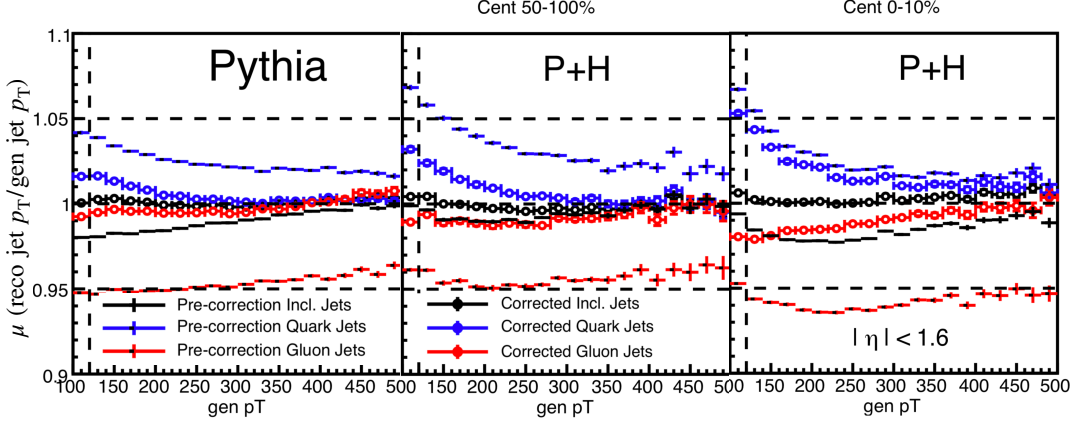


Figure 55. Jet energy scale before and after the corrections as a function of jet  $p_T$  for pp and PbPb collisions from simulation studies, shown separately for inclusive, quark and gluon jets. Figure from Ref. [4].

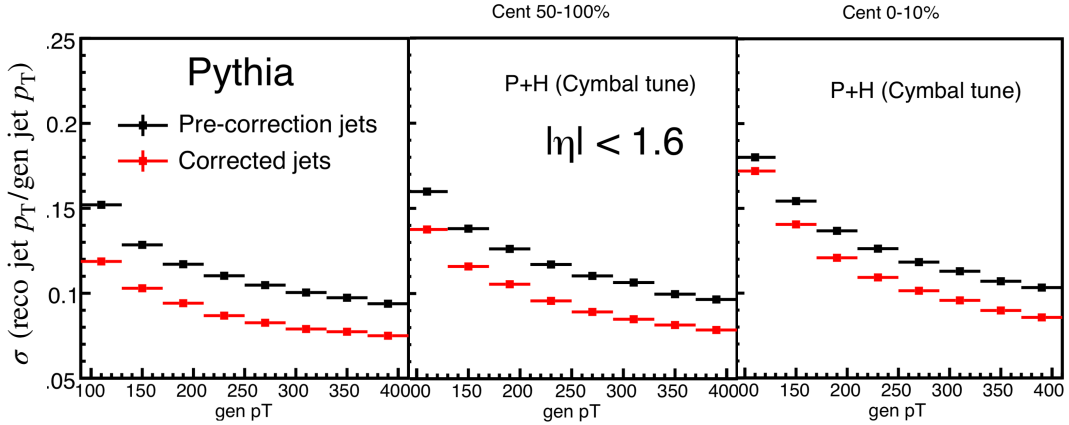


Figure 56. Jet energy resolution shown as a function of jet  $p_T$  for pp and PbPb collisions from simulation studies before and after the corrections. Figure from Ref. [4].

It is observed from Fig. 55 that the fragmentation-based corrections derived as discussed above results in a significant decrease in the energy response bias between quark and gluon calorimeter jets. These corrections reduce the difference in the energy response between quark and gluon jets from 12% (9%) to 6% (2%) in central PbPb (pp) collisions. The jet energy resolution, shown in Fig. 56, is observed to improve in pp and in all centrality bins in PbPb collisions by 2 – 3% as a result of these corrections. These corrections have been standardized and implemented in various

CMS jet analyses, and lead to a significant reduction in the systematic uncertainties on various measurements [2, 1] as discussed in Sec. 10.2.4.

## 8.4 Jet flavor identification

The measurements presented in this thesis rely on precisely identifying the flavor of the parton (quark vs. gluon) initiating the jet in MC simulations. For the jet flavor assignment, all initial-state partons in a given event are scanned through and the most energetic partons are selected. Angular distances ( $\Delta r$ ) are calculated between all combinations of the selected high- $p_T$  partons and the axes of jets reconstructed in the event. The jets, reconstructed with a radius parameter  $R$ , are then assigned a flavor based on the highest  $p_T$  parton that lies within the jet cone ( $\Delta r < R$ ).

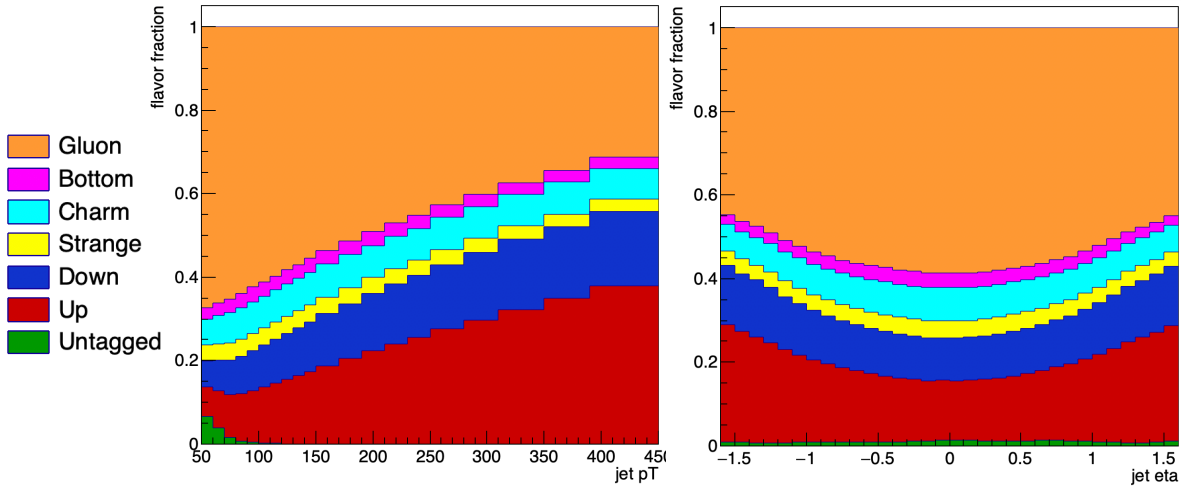


Figure 57. Jet flavor composition as a function of jet  $p_T$  and  $\eta$  from simulation studies. The antiquark contributions are grouped with the respective quark fractions. Figure from Ref. [5].

The flavor composition of the jets produced in CMS assigned via the above-described tagging algorithm is shown in Fig. 57 as a function of jet  $p_T$  and  $\eta$ . From these studies, gluon jets are expected to constitute about 59% of the inclusive sample of jets with  $p_T$  above 120 GeV. Similarly, up and down (anti)quark jets are predicted to make up about 32% of the sample with the other 9% arising from charm, strange, and bottom (anti)quark jet contributions. The low  $p_T$  and midrapidity regions are observed to be dominated by gluon-initiated jets, and the valence light quark contributions increase at higher  $p_T$  and more forward regions. The quark and antiquark contributions of each flavor have been clubbed together in Fig. 57. Reconstructed jets corresponding to no initial energetic

partons in the event are classified as untagged jets and are observed predominantly at low  $p_T$ . Untagged jets could result from either UE fluctuations or other resolution effects, and are not found above the jet  $p_T$  threshold (120 GeV) used in these studies.

## 8.5 Jet Spectra and selections

The distributions of corrected jets as a function of  $p_T$ ,  $\eta$ , and  $\phi$  are shown below for pp collisions in Fig. 58 and for various centrality bins in PbPb collisions in Fig. 59. To reduce contamination from fake jets and single photons, the jets are selected such that the highest- $p_T$  track inside the jet contains no less than 1% and no more than 98% of the total jet energy. The number of jets in the sample is also shown in the figures and a reasonable agreement is observed in the spectra between data and simulation.

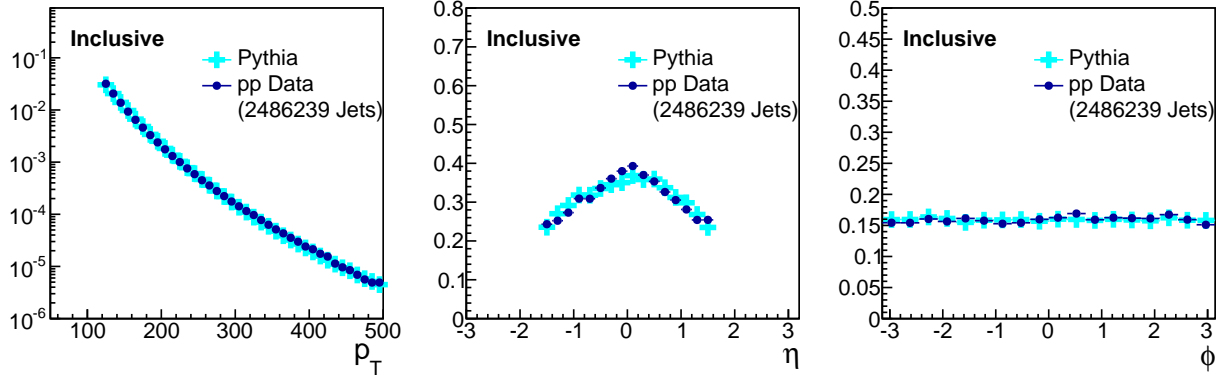


Figure 58. Jet spectra and statistics as a function of  $p_T$ ,  $\eta$  and  $\phi$  in pp data and PYTHIA. Figure from Ref. [5].

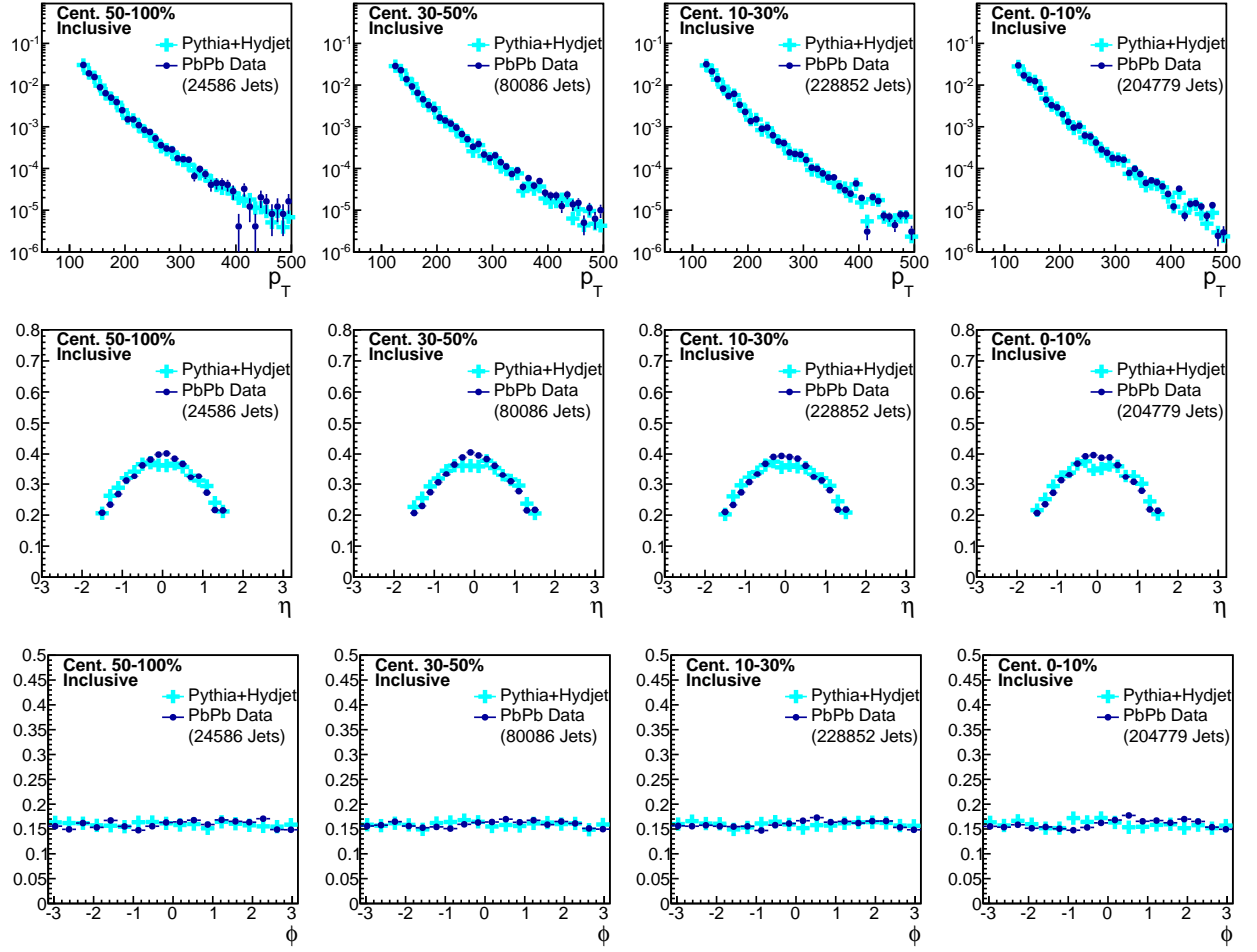


Figure 59. Jet spectra and statistics as a function of  $p_T$ ,  $\eta$  and  $\phi$  in various centrality bins in PbPb data and PYTHIA+HYDJET. Figure from Ref. [5].

## 9 JET CHARGE AND QUARK/GLUON FRACTIONS

*Portions of the material in this chapter, which is my own work, was published in Ref. [1, 5]*

### 9.1 Measuring the jet charge

Jet charge refers to the  $p_T$ -weighted sum of the electric charges of the particles in a jet. It is defined as:

$$Q^\kappa = \frac{1}{(p_T^{\text{jet}})^\kappa} \sum_{i \in \text{jet}} q_i p_{T,i}^\kappa. \quad (25)$$

The variable  $p_T^{\text{jet}}$  is the transverse momentum of the jet,  $q_i$  and  $p_{T,i}$  are the electric charge and the transverse momentum of the  $i$ -th particle, respectively. The  $\kappa$  parameter in the exponent of the particle momenta controls the relative weight given to low and high momentum particles. Low values of  $\kappa$  enhance the contribution to the jet charge measurements from low  $p_T$  particles while high  $\kappa$  highlight the high  $p_T$  contributions.

Measurements of jet charge are performed in pp and PbPb collisions by considering angular correlations of high- $p_T$  jets and tracks. Jets are reconstructed using the anti- $k_T$  algorithm with a radius parameter  $R = 0.4$  and are selected to have  $p_T > 120$  GeV and to be found within the pseudorapidity range  $|\eta| < 1.5$ . In this inclusive jet selection, multiple jets can be selected from the same event, provided that each satisfies the jet selection criteria. Reconstructed charged tracks with  $p_T$  above 1 GeV within the jet cone (relative angular distance from the jet axis  $\Delta r = \sqrt{(\Delta\eta)^2 + (\Delta\phi)^2} < 0.4$ ) are used in the measurement of the jet charge. Theoretical predictions suggest that  $\kappa \sim 0.5$  is the most sensitive to the charge of the parton initiating a jet in pp collisions [167]. In this analysis, measurements are shown for  $\kappa$  values of 0.3, 0.5 and 0.7, and with different thresholds on the track  $p_T$  of 1, 2, 4, and 5 GeV to maintain a broad sensitivity to both hard and soft particles inside jets. The jet charge distributions presented in this analysis are normalized to the number of jets selected in the sample.

In heavy-ion collisions, particles from the underlying event that happen to fall inside the jet cone affect the jet charge measurements and are treated as background. The track  $p_T$  cutoff of 1 GeV reduces the heavy-ion underlying event contribution to the jet charge measurement but does not eliminate it. To estimate the background contribution, the jet charge is measured with jets from

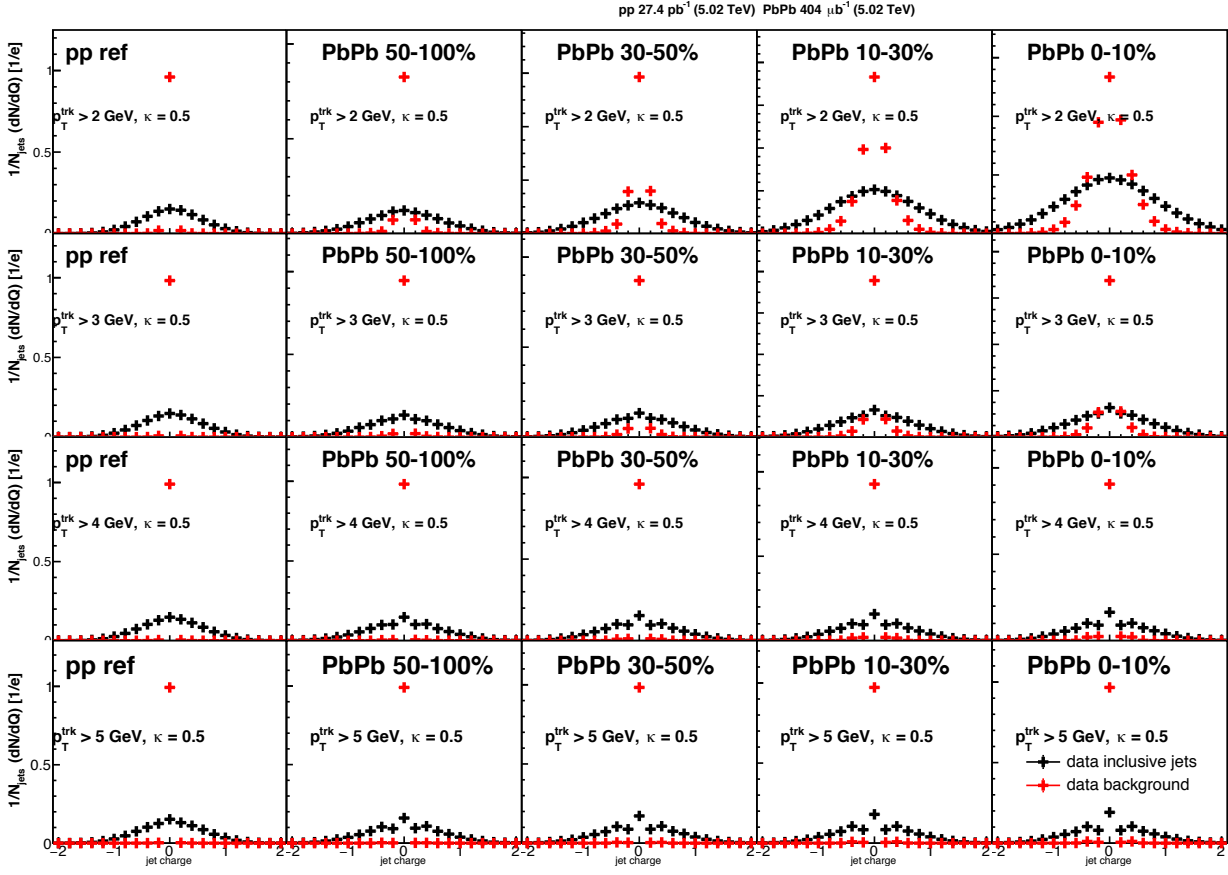


Figure 60. Jet charge distributions in the signal and background cones for pp and PbPb collisions. The distributions are shown for increasing track  $p_T$  thresholds from top to bottom rows. Figure from Ref. [5].

the jet-triggered signal event and tracks in a matched minimum-bias event, required to have a vertex position within 1 cm and collision centrality within 2.5% of the signal event. The reconstructed signal and the background jet charge distributions in pp and PbPb data are shown in Fig. 60 for different values of track  $p_T$  threshold and  $\kappa = 0.5$ . The reconstructed jet charge distributions in pp and PbPb data, including detector and background effects, are well modeled by PYTHIA and PYTHIA+HYDJET, respectively, as shown in Figs. 61 and 62.

The background contributions from the soft underlying event to the jet charge, shown in Fig. 60, is higher for selections of lower track  $p_T$  thresholds and  $\kappa$  values, as expected. It is also considerably larger in more central PbPb collisions compared to peripheral and pp collisions. The dips in the signal distributions on either side of zero observed in higher track  $p_T$  threshold bins are due to the tracking inefficiency of the detector [66]. The jet charge distributions from MC at the

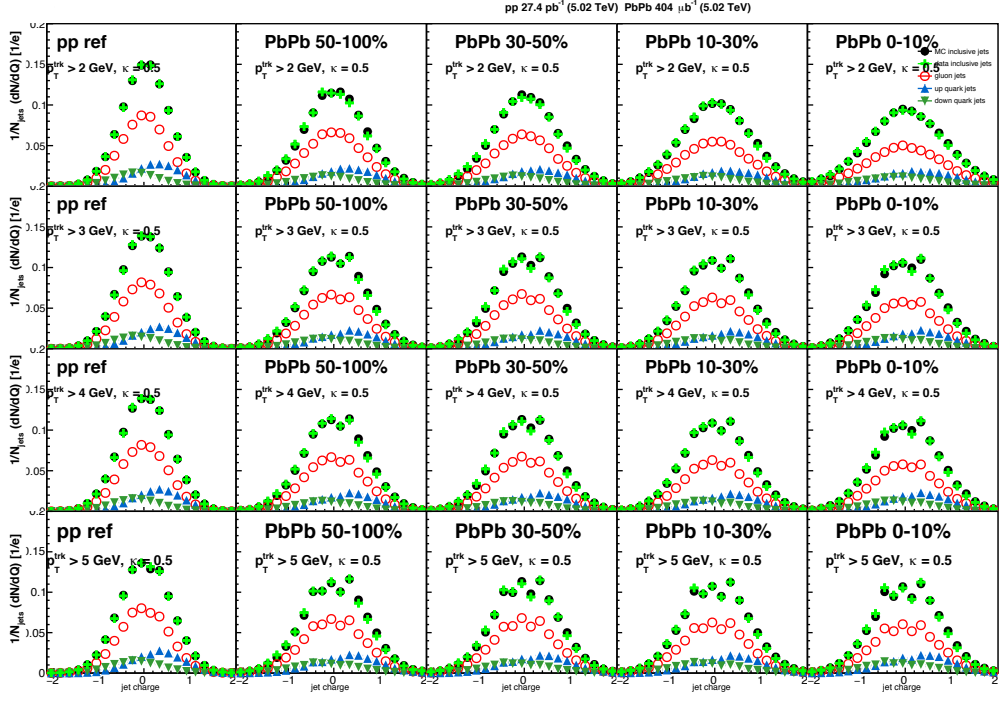


Figure 61. Jet charge distributions in the jet cone shown for data inclusive jets (green), MC inclusive jets (black), up and down quark jets (up and down blue markers) and gluon jets(red) with different  $p_T$  thresholds for the tracks. Figure from Ref. [5].

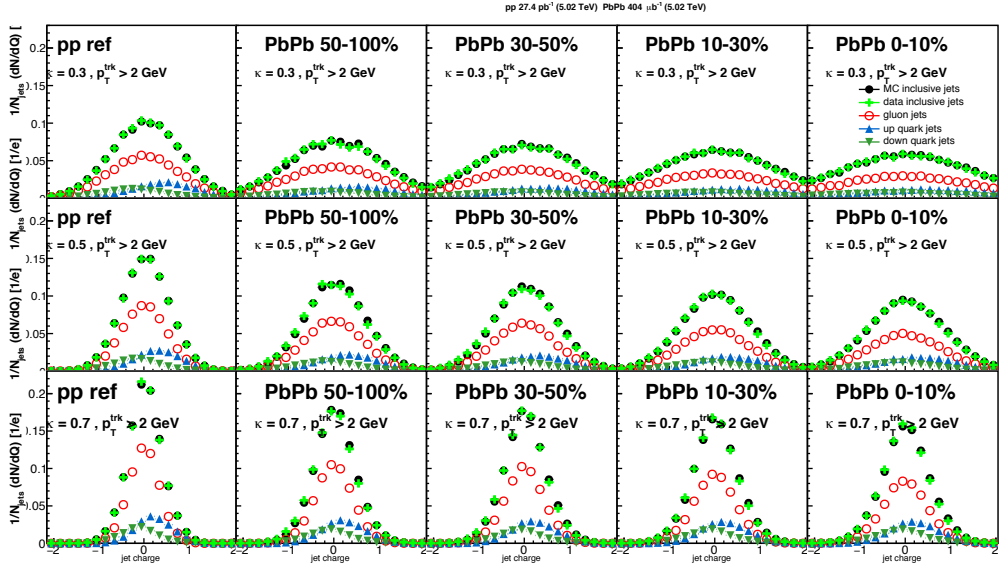


Figure 62. Jet charge distributions in the jet cone shown in data inclusive jets (green), MC inclusive jets (black), up and down quark jets (up and down blue markers) and gluon jets(red) with different  $\kappa$  values. Figure from Ref. [5].

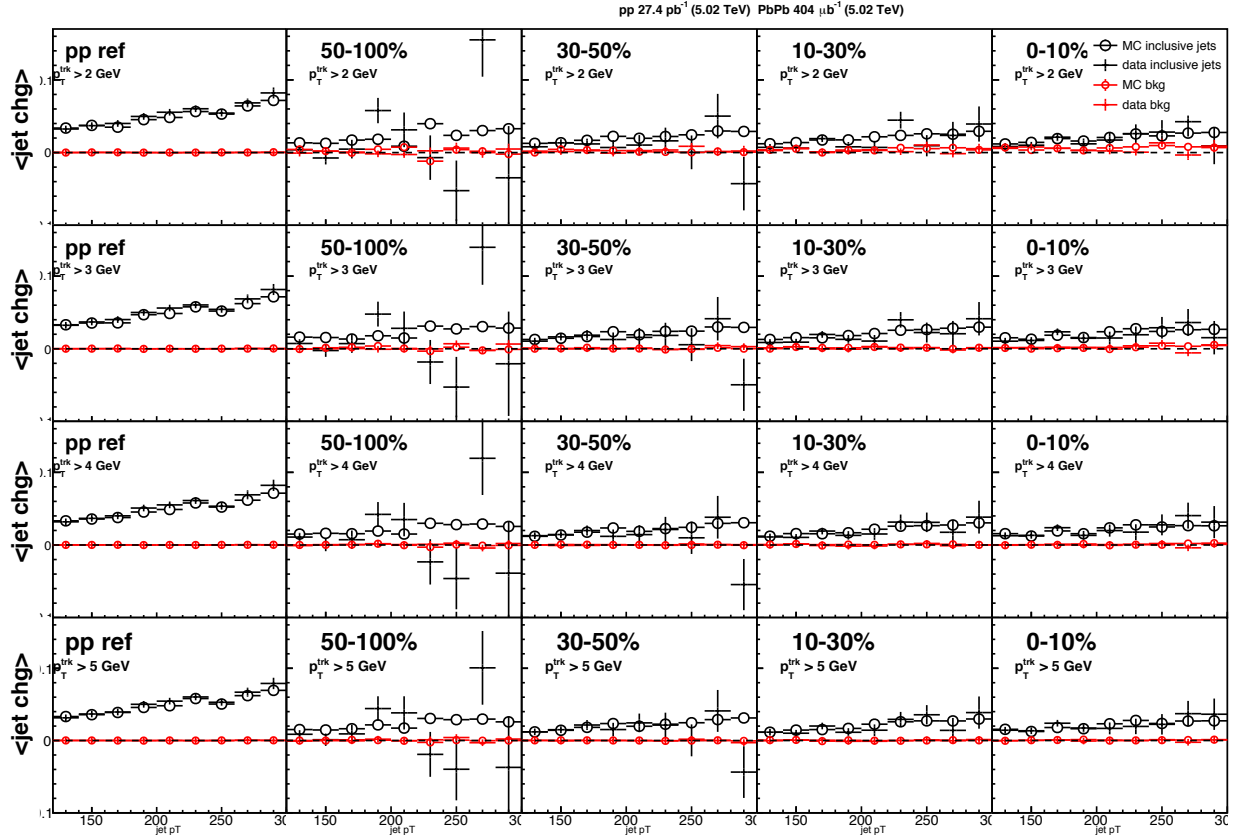


Figure 63. Average of the jet charge distributions as a function of jet  $p_T$  in the signal and background cones for pp and PbPb collisions in data and simulations. The distributions are shown for increasing track  $p_T$  thresholds from top to bottom rows. Figure from Ref. [5].

detector and generator levels are shown in Fig. 68 for a sample track  $p_T$  threshold and  $\kappa$  bin. The reconstructed distributions are observed to be smeared compared to the generator level jet charge due to detector inefficiencies and resolution, and additionally due to background in PbPb collisions.

The average of the reconstructed signal and background jet charge distributions is plotted as a function of the jet  $p_T$  in Fig. 63 for pp and PbPb data, and is observed to be well modeled by PYTHIA and PYTHIA+HYDJET, respectively. The average of the jet charge in PbPb data is observed to be smaller than in pp due to an enhanced contribution of negatively charged down quarks from neutron interactions in PbPb collisions. The average of the background jet charge distributions is observed to be consistent with zero as expected. The background contribution to jet charge observed in data is well modeled by HYDJET, which is used to unfold the reconstructed jet charge distributions for background effects.

## 9.2 Unfolding for detector and background effects

In order to compare with other experiments or theoretical predictions, jet charge measurements are unfolded from the detector-level with background effects into the signal distributions at the final-state particle level. The jet charge distributions in MC simulations at the detector level are smeared compared to those constructed using generator level information because of detector resolution and efficiency effects, and additionally due to background effects in PbPb collisions. Unfolding is performed using D'Agostini iterative Bayesian method [168, 169, 170], as implemented in the RooUnfold software package [171]. Response matrices are derived from PYTHIA for pp and from PYTHIA+HYDJET for different centrality bins in PbPb collisions.

### 9.2.1 Response matrices

The jet charge measurements at the detector-level in pp and PbPb collisions are smeared by tracking efficiency effects, and this smearing increases with decreasing  $\kappa$  values [146]. In PbPb collisions, there is additional smearing that is caused by the background from the underlying event and long-range correlations [38, 39]. The unfolding is performed to account for these effects using the D'Agostini iterative method, as implemented in the ROOUNFOLD software package. Response matrices are derived from PYTHIA and PYTHIA+HYDJET simulation samples for pp and PbPb collisions, respectively.

The unfolding approach utilizes a response matrix that maps the true generator-level distribution of a variable onto the reconstructed distribution of the same variable from MC samples. To unfold for the tracking efficiency effects in pp (90%) and PbPb (65%) collisions, response matrices are built from MC jet charge measurements made using reconstructed level charged tracks mapped onto the measurements made using generator level charged tracks. Only tracks arising from the hard scattering are used in both the detector level and generator level measurements while building the response matrices for PbPb tracking efficiency unfolding using PYTHIA+HYDJET samples. These response matrices are shown in Figs. 64 for different values of track  $p_T$  threshold and  $\kappa$ .

To account for the background effects in PbPb collisions, response matrices are built from PYTHIA+HYDJET jet charge measurements made with all reconstructed charged tracks, including the contribution from the underlying event, mapped onto the measurements using reconstructed

charged tracks arising from the hard scattering only. The response matrices for background unfolding in various centrality bins are shown in Figs. 65 for different values of track  $p_T$  threshold and  $\kappa$ .

As a cross-check for this method, the contribution from the underlying event is estimated using a data-driven method from minimum bias PbPb events added to the MC signal jet charge. In this method, the minimum-bias PbPb event is required to have a similar  $v_z$  (within 1 cm) and centrality (within 2.5%) as the signal event. The MC signal jet charge, smeared for background effects from both HYDJET and the data-driven method, is compared to the reconstructed jet charge distributions (including the background) in Figs. 66 and 67, respectively, showing good agreement. As expected, the background effect is negligible in the peripheral events and its significance increases in more central PbPb collisions.

The response matrices used in unfolding for the two effects are combined and are constructed using jet charge distributions measured with all reconstructed tracks (arising from both hard scattering and UE) mapped onto those measured with generated tracks from the hard scattering only. The resulting unfolding matrices are then used to unfold the detector level jet charge measurements to the final state particle-level in a single step.

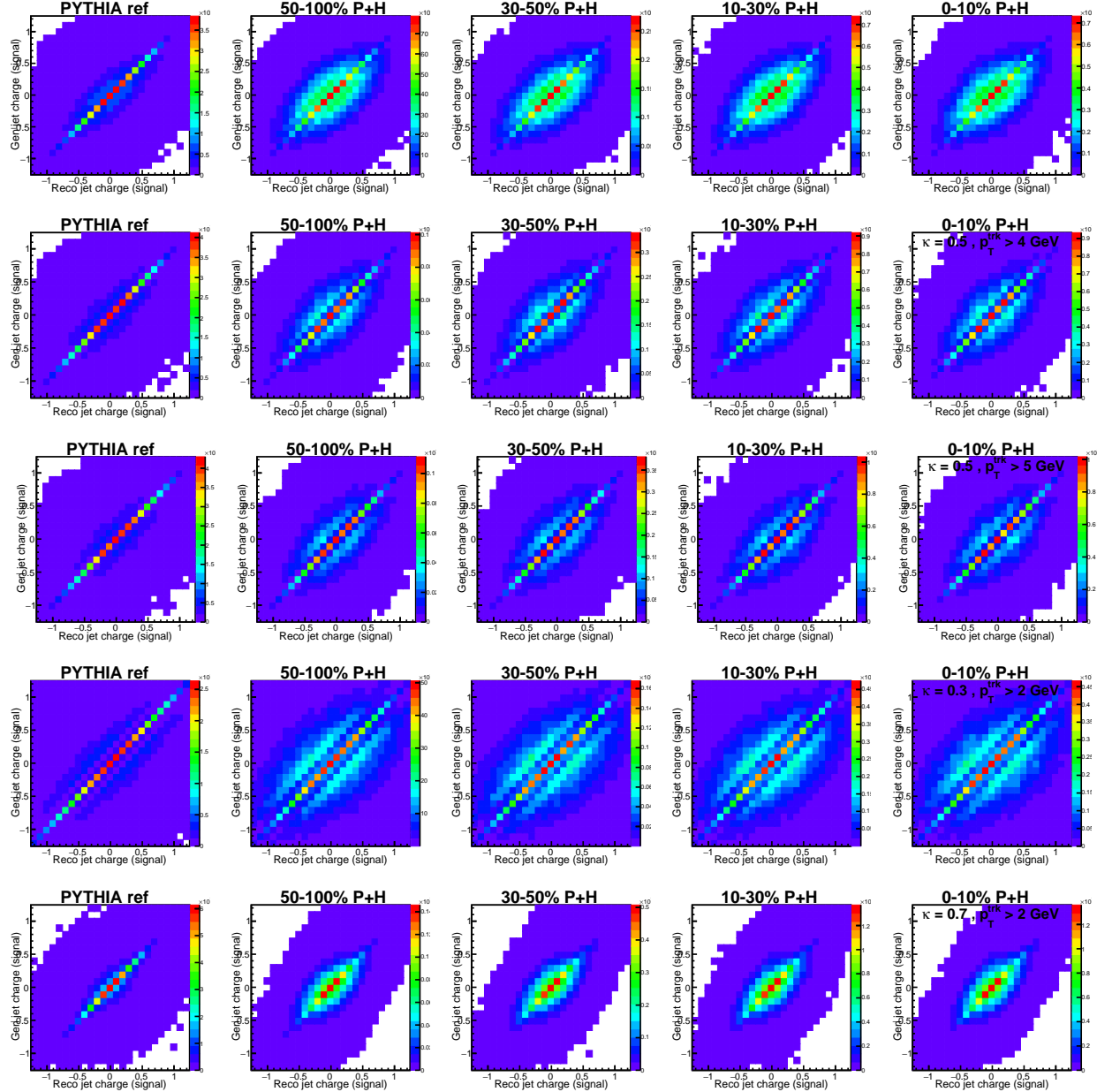


Figure 64. Response matrices for “detector effects unfolding” obtained using PYTHIA. The response matrices are shown for pp (first column) and in different PbPb event centrality bins (second to fifth columns), and for different values of track  $p_T$  thresholds and  $\kappa$  in different rows. Figure from Ref. [5].

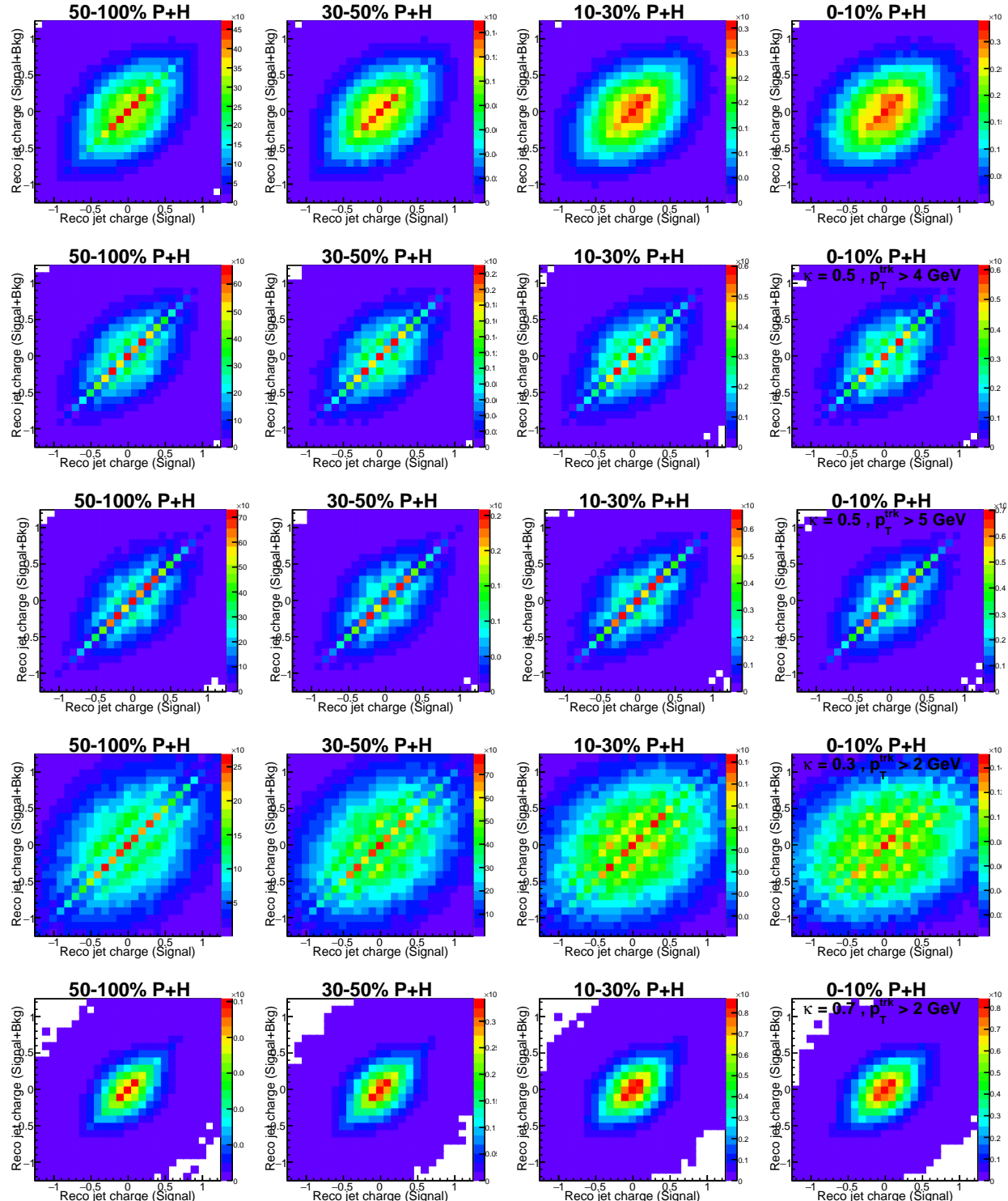


Figure 65. Response matrices for “background unfolding” in PbPb collisions obtained using PYTHIA+HYDJET in different event centrality bins shown in different columns, and for different values of track  $p_T$  thresholds and  $\kappa$  in different rows. Figure from Ref. [5].

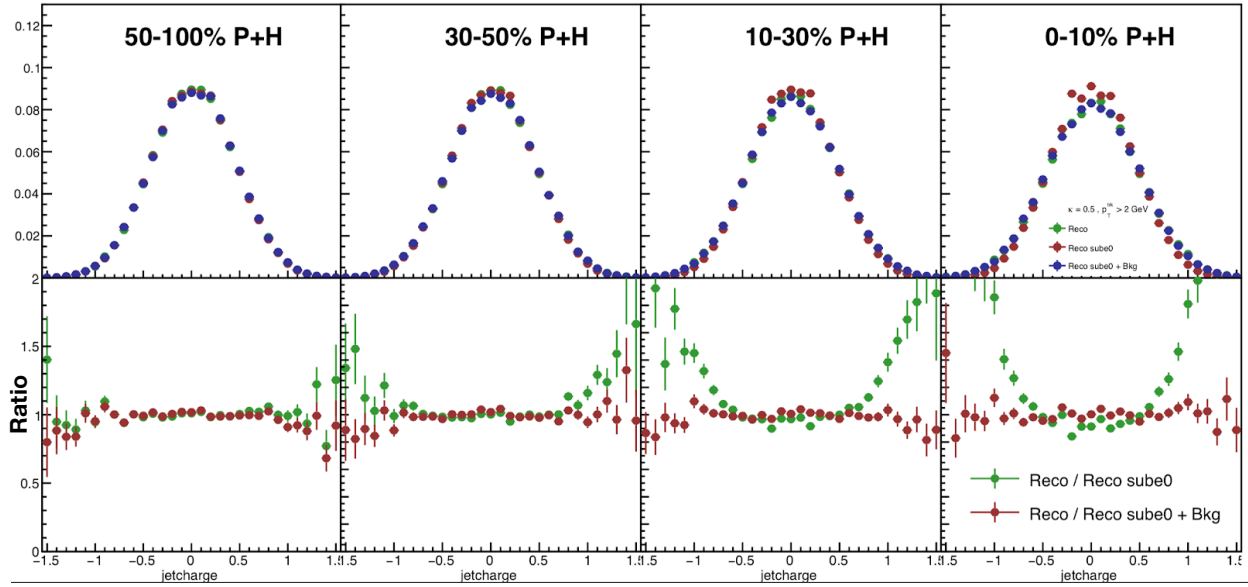


Figure 66. Top : PbPb MC jet charge measurements (including background) in green, PbPb MC jet charge distributions constructed using reconstructed tracks arising from the hard scattering only (red), and smeared for background using HYDJET (blue). Bottom : Ratio of the reconstructed MC (signal+background) to unsmeared and smeared MC jet charge distributions. Figure from Ref. [5].

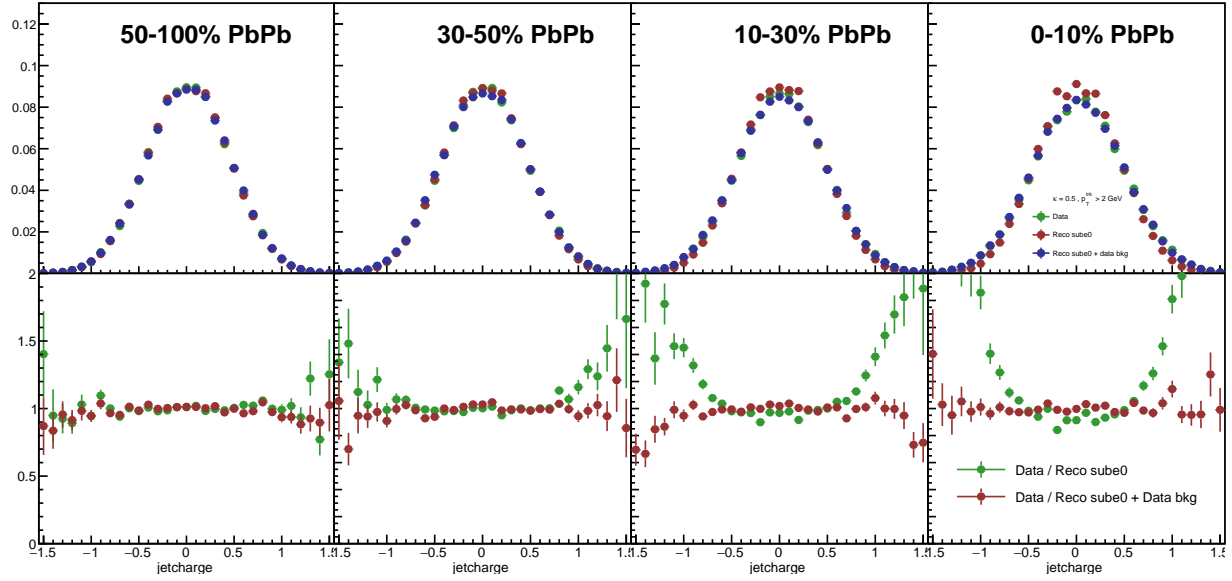


Figure 67. Top : PbPb data jet charge measurements (including background) in green, MC jet charge distributions constructed using reconstructed tracks arising from the hard scattering only (red), and smeared for background using data driven methods (blue). Bottom : Ratio of the reconstructed data (signal+background) to unsmeared and smeared MC jet charge distributions. Figure from Ref. [5].

### 9.2.2 Closure tests and effects of unfolding

To validate the unfolding implementation, closure tests are performed using the Monte Carlo samples. The detector-level reconstructed jet charge distributions obtained using PYTHIA and PYTHIA+HYDJET are unfolded using the corresponding response matrices from the same MC sample and are compared with the generator level distributions. These sanity tests return the expected results and the unfolded distributions are in perfect agreement with the generator level distributions by definition (Fig. 68).

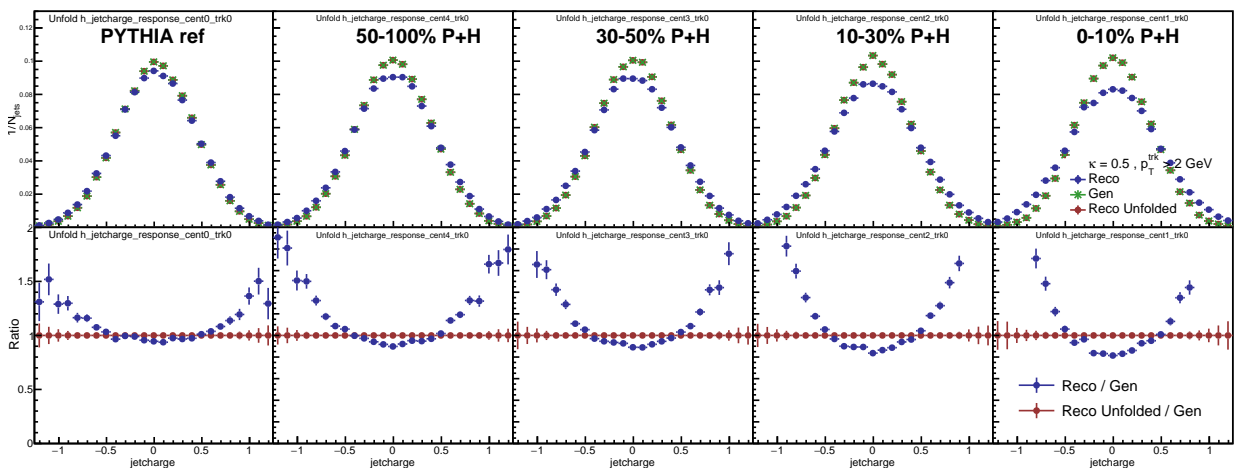


Figure 68. Ratio of unfolded MC jet charge distributions with generator-level after one iteration in PYTHIA and in different event centrality bins in PYTHIA+HYDJET for track  $p_T > 2$  GeV and  $\kappa = 0.5$ . Figure from Ref. [5].

Next, a detector level jet charge distribution is constructed using 50% of the full available sample and is unfolded using a statistically independent response matrix constructed using the other half of the sample, and the ratios are shown in Fig. 69, showing good closure. The final unfolded distributions shown here for PYTHIA+HYDJET are unfolded for both tracking efficiency and background effects.

In the second set of tests, known as the cross-closure test, detector level distributions from the inclusive sample of PYTHIA and PYTHIA+HYDJET are unfolded using modified response matrices populated using dominant gluon and quark jet samples from the same MC. These modified samples correspond to 80% gluon and 40% gluon jets, respectively, compared to the nominal value of 60% gluon jets. The unfolded distributions (Fig. 70) show good agreement with the generator level

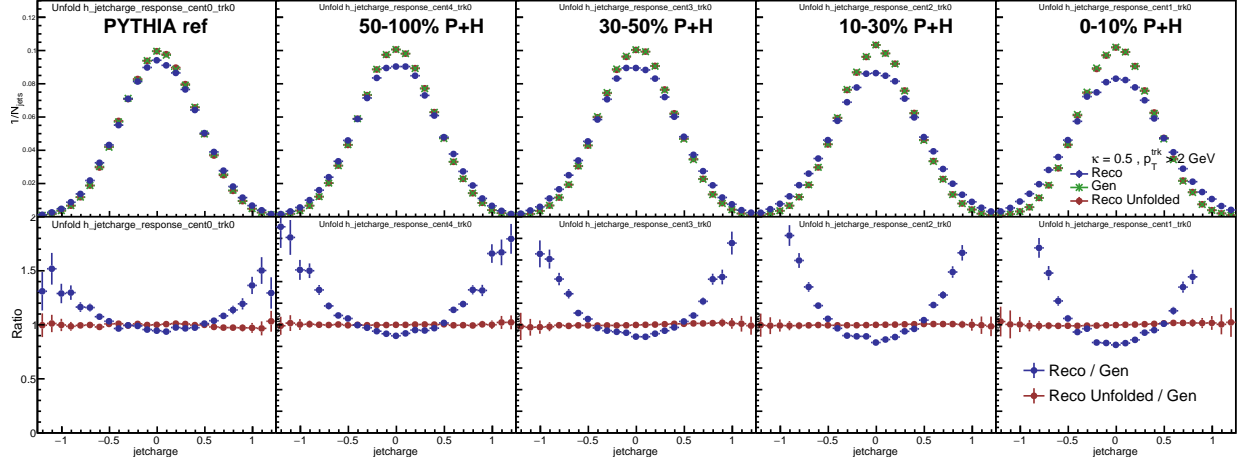


Figure 69. Ratio of unfolded jet charge distributions with generator-level after one iteration in PYTHIA and in different event centrality bins in PYTHIA+HYDJET for track  $p_T > 2$  GeV and  $\kappa = 0.5$ . In this figure, the MC sample is split and one half is used to construct the response matrix and the other half is used to test the unfolding. Figure from Ref. [5].

distributions, with the differences being included as a systematic uncertainty due to the choice of MC generator (Sec. 9.4). The jet charge observable is sensitive to the fragmentation and hadronization of an energetic parton and the quark/gluon jet fractions in a sample. Quark and gluon jets are observed to have distinctive fragmentation functions and hence varying their relative fractions by 50% gives a good bound on systematic uncertainty due to the choice of the MC for unfolding. The slope observed in the ratio in Fig. 70 is due to the fact that the inclusive jet charge distribution, which is asymmetric about zero is being unfolded using a dominant gluon and quark jet samples in this test, which are less and more asymmetric about zero compared to the nominal sample, respectively.

For background unfolding in PbPb, the cross closure tests are performed by unfolding the detector level jet charge distributions with response matrices constructed using background estimated from matched PbPb data minimum bias samples as discussed above. The results from this method are observed to be in good agreement with the nominal results.

Following the strategy of previous results [66], pseudo-data, in this case, jet charge distributions from modified PYTHIA samples ( $q/g$  fractions varied by 50%) are unfolded using the nominal response matrix as a test of the unfolding methodology. Quark and gluon jet fractions are varied by 50% in the modified simulation samples, which is expected to give a good bound on

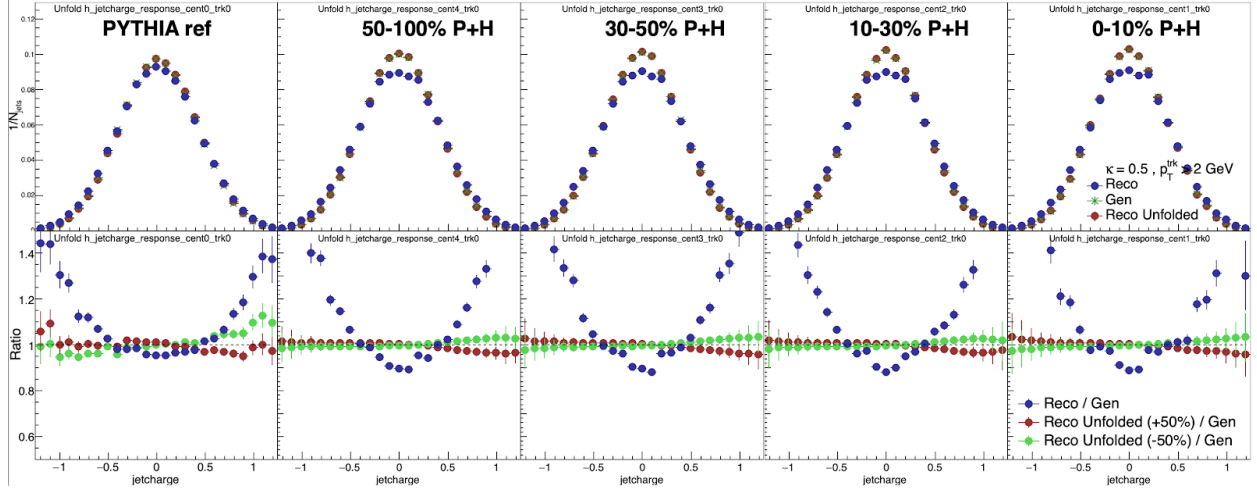


Figure 70. Ratio of unfolded jet charge distributions with truth after two iterations in PYTHIA and in different event centrality bins in PYTHIA+HYDJET for track  $p_T > 2$  GeV and  $\kappa = 0.5$ . In this figure, separate MC samples of dominant and reduced gluon jet fractions are used to construct the response matrices and the nominal inclusive MC sample is used to test the unfolding. Figure from Ref. [5].

the potential modification of the jet charge distribution in data. The number of iterations in the unfolding procedure trades off unfolding bias towards MC distributions with statistical fluctuations. After three to four iterations, it is observed that the relative statistical uncertainties (including bin-to-bin correlations) exceed 10% compared to the relatively flat systematic uncertainties (based on the differences between unfolded and generated distributions in the pseudo-data) (Fig. 71). Based on these results, the optimal number of iterations of 3-4 is obtained to balance the unfolding bias and statistical fluctuations. The systematic uncertainty here refers to the non-closure between the pseudo-data unfolded distributions (unfolded using nominal response matrices) and the generator-level distributions of the same pseudo-data.

The unfolding is performed using the response matrices constructed as described above, and the unfolded data is shown in Fig. 72 for a sample selection of track  $p_T$  threshold and  $\kappa$ . For this selection, the unfolding process is terminated after three iterations as it is observed that the points tend to oscillate around the same set of values. The rest of the final unfolded data jet charge distributions, along with the systematic uncertainties, can be found in Sec. 9.5.

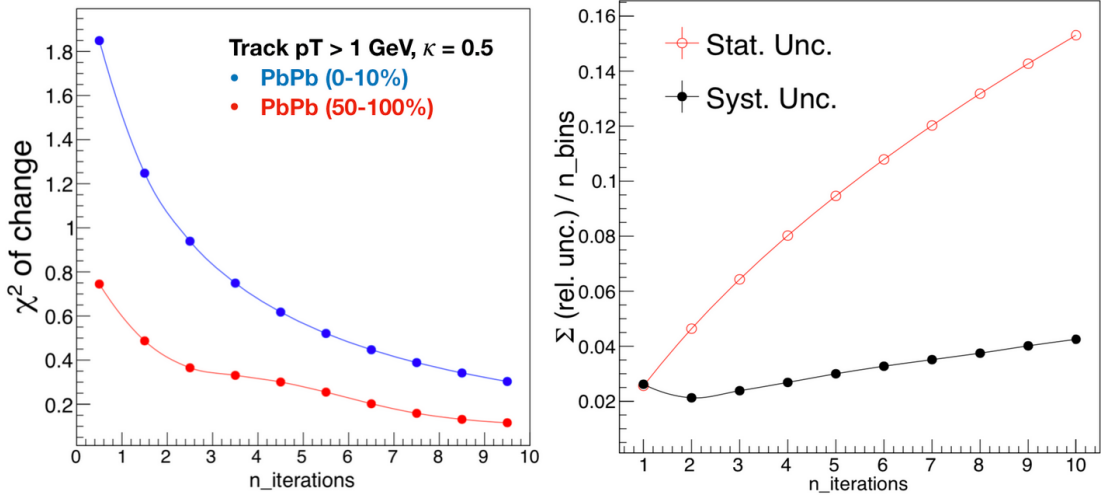


Figure 71. (Left) The  $\chi^2$  of change in the unfolding procedure between two successive iterations. (Right) Comparison of the relative statistical and systematic uncertainties in the unfolded jet charge distributions as a function of the number of iterations used in the unfolding procedure. Figure from Ref. [5].

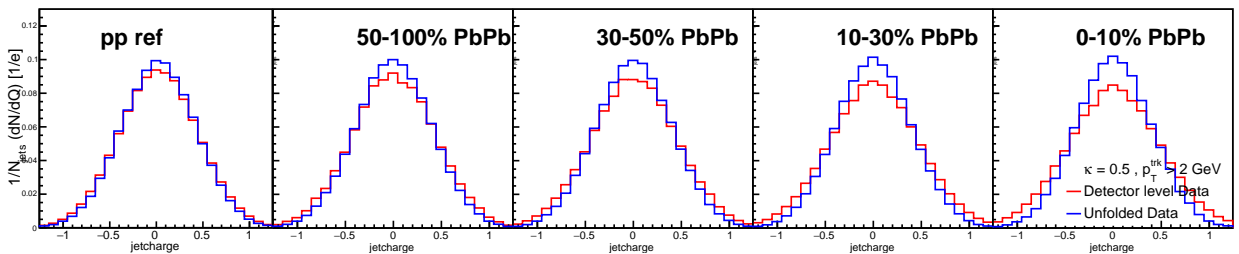


Figure 72. Detector level and unfolded data jet charge distributions shown for pp and in different event centrality bins in PbPb collisions for track  $p_T > 2 \text{ GeV}$  and  $\kappa = 0.5$ . Figure from Ref. [5].

### 9.3 Template Fitting for Quark and Gluon fractions

The generator level jet charge measurements for different flavored jets from PYTHIA and PYTHIA+HYDJET are used as templates in fitting the unfolded jet charge distributions from data to estimate the fractions of quark and gluon jets in the sample. The average jet charge for jets initiated by gluons and light quarks are well separated (Figs. 61 and 62 and Table IV) and have little dependence on the jet  $p_T$  (Fig. 73). The average jet charge predictions for gluon jets from PYTHIA, and cross-checked with other MC generators, are consistently zero while that for up and down quark jets are positive and negative, respectively [66, 120]. This enables the stable extraction of quark and gluon jet fractions in the inclusive jet  $p_T$  region. Light antiquarks ( $\bar{u}$  and  $\bar{d}$ ) are varied with the respective light quark fractions in the fitting procedure. To reduce the number of degrees of freedom, separate templates are not used for the extraction of the fractions of all the “other” quarks and anti-quarks ( $c$ ,  $\bar{c}$ ,  $s$ ,  $\bar{s}$ ,  $b$ , and  $\bar{b}$ ). The “other” quark fractions are kept fixed in the fitting procedure and are considered in the systematic uncertainty studies in Sec. 9.4.

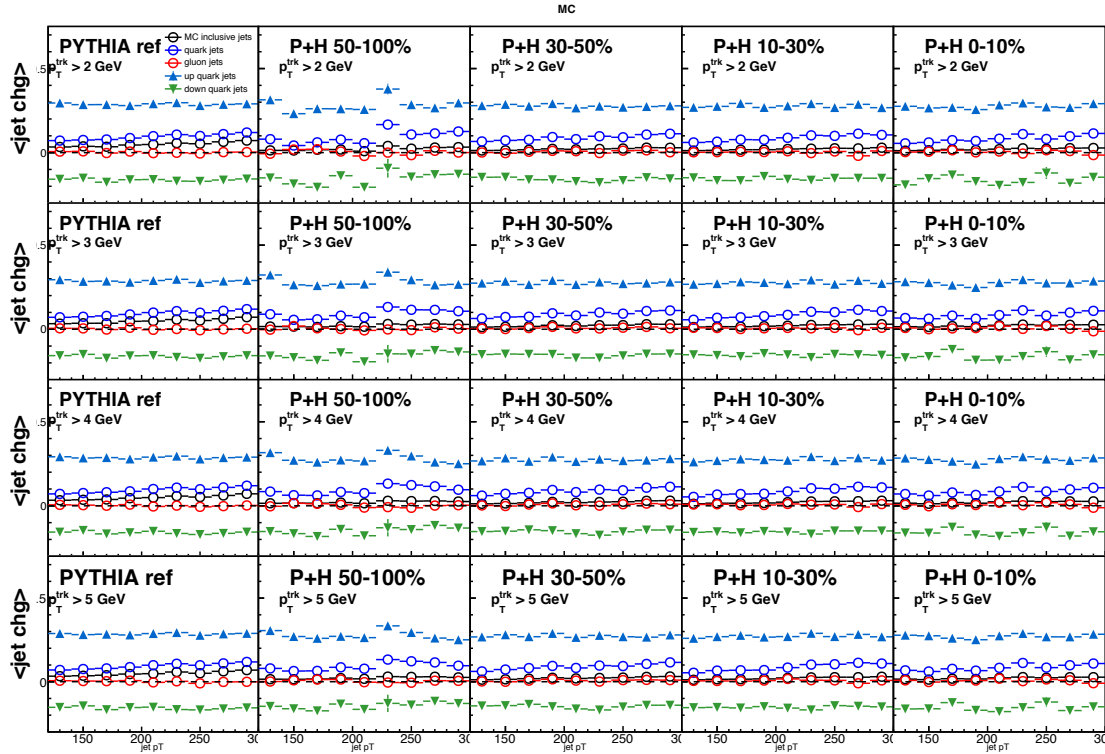


Figure 73. Average jet charge for inclusive jets (black), up and down quark (up and down blue markers) and gluon jets(red) in MC with different  $p_T$  thresholds for the tracks. Figure from Ref. [5].

Jet flavor	Mean [e]	Standard deviation [e]
Up quark	0.254	0.341
Down quark	-0.15	0.335
Gluon	0.001	0.364

TABLE IV. Mean and standard deviation of jet charge distributions for individual flavor jets from PYTHIA. The statistical uncertainties on the quoted values is less than 0.1%

### 9.3.1 Fitting results

Jet charge is measured using reconstructed jets and tracks in pp and PbPb collisions and unfolded for detector and background effects. The unfolded distributions are fitted using jet charge templates for different flavors from generator-level MC using a  $\chi^2$  minimization method. Jets with zero tracks above the threshold  $p_T$  used in the measurements are excluded in the fitting procedure and considered in the systematic uncertainty studies. The fraction of jets with no tracks above a certain track  $p_T$  inside the jet cone is shown in Fig. 79 for data and MC as a function of the lower threshold of the track  $p_T$ .

The fitting is shown for a sample track  $p_T$  bin with  $\kappa = 0.5$  in Fig. 74 at the generator-level for MC (PYTHIA) and in Fig. 75 for pp and different centrality bins of PbPb data. The rest of the fitting results are shown in Sec. 9.5. Fig. 74 in MC serves as validation and closure test that the templates work as expected for the flavor fraction extraction, as the fraction of the different flavors of quark and gluon jets extracted from the fits matches the direct measurement from MC.

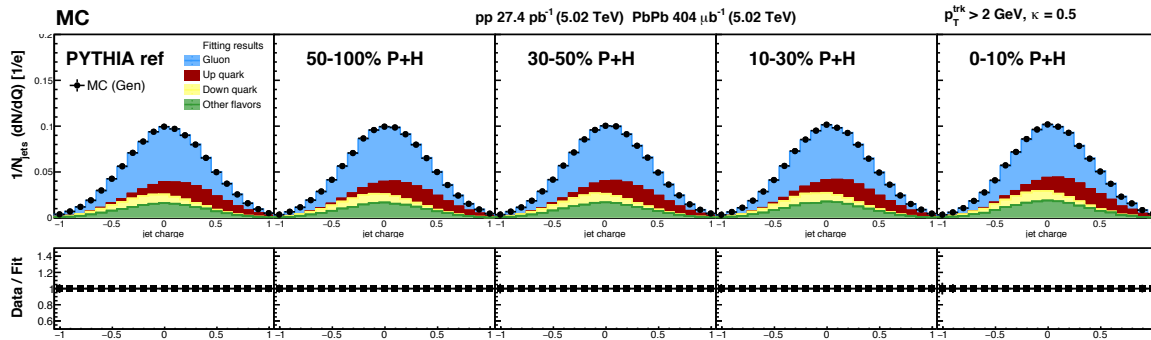


Figure 74. **Top panel:** Inclusive jet charge distributions (generator level) shown with black points along with gluon jets, up and down quark jets and “other” quark jets shown as stacked plots scaled to their respective fit fractions. **Bottom panel:** Ratio of the inclusive jet charge measurement to the fit. Figure from Ref. [5].

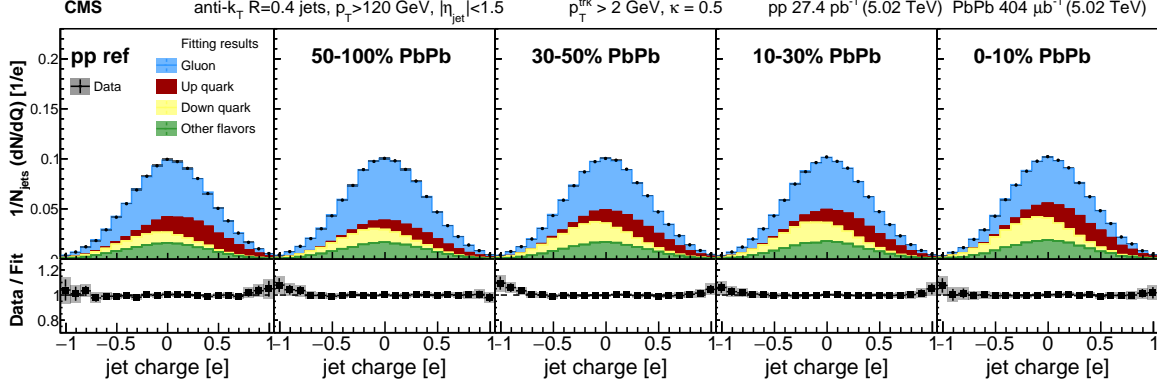


Figure 75. **Top panel:** Unfolded data inclusive jet charge distributions shown with black points along with gluon jets, up and down quark jets and “other” quark jets shown as stacked plots scaled to their respective fit fractions. **Bottom panel:** Ratio of the inclusive jet charge measurement to the fit. Figure from Ref. [5].

The fitting is also shown for a sample track  $p_T$  bin with  $\kappa = 0.5$  in Fig. 76 at the reconstructed level with background and detector effects in MC (PYTHIA and PYTHIA+HYDJET). This is a closure test that the templates work as expected for the flavor fraction extraction after accounting for the detector and background effects.

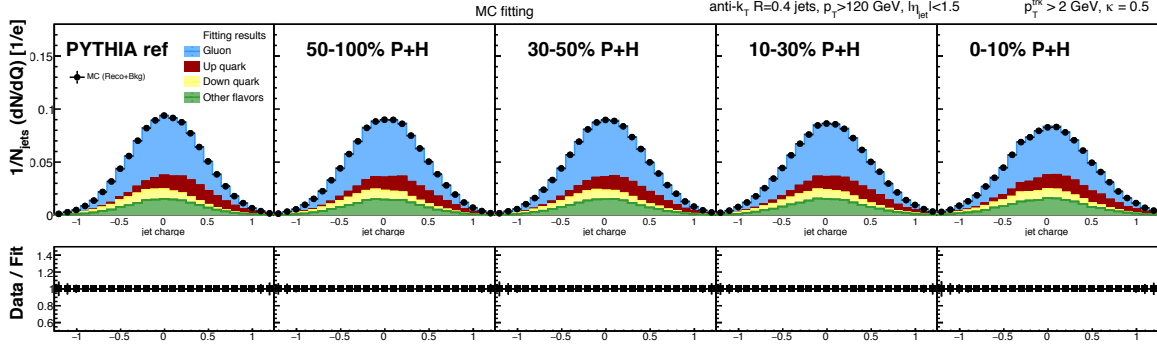


Figure 76. **Top panel:** Inclusive jet charge distributions (detector level) shown with black points along with gluon jets, up and down quark jets and “other” quark jets shown as stacked plots scaled to their respective fit fractions **Bottom panel:** Ratio of the inclusive jet charge measurement to the fit. Figure from Ref. [5].

### 9.3.2 Correction factors

A correction factor is applied to the extracted quark/gluon fractions to account for the non-linear detector bias towards selecting jets which fragment harder as discussed in Sec. 8.3. Jets with a harder constituent  $p_T$  spectrum are more likely to be successfully reconstructed as the calorimeter response does not scale linearly with incident particle energy, resulting in a bias toward the selection of jets with fewer associated tracks. This results in a systematic preferential reconstruction of quark jets as they fragment harder on average compared to the gluon jets (Fig. 53). This bias is reduced, but not eliminated, by applying the jet energy corrections described in Sec. 8.3 based on the number of jet constituents, as shown in Fig. 55. To compensate for the residual effect observed in Fig. 77, an extra correction factor is applied to the extracted fractions of quark and gluon jets to account for the jet energy scale (JES) difference between them.

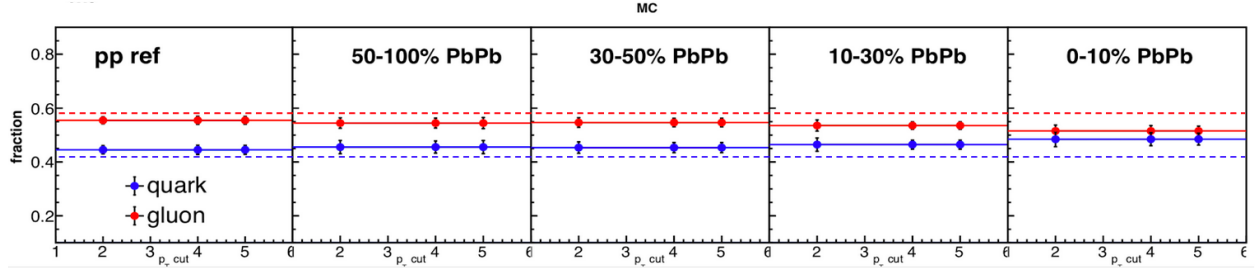


Figure 77. Fitting results at the detector-level for the extraction of quark and gluon jet fractions in MC shown in solid points as a function of the track  $p_T$  threshold along with dotted lines for the direct measurement of the fractions from generator level MC. Figure from Ref. [5].

The PYTHIA+HYDJET templates in the fitting procedure in PbPb collisions are constructed by including the proportional cross-sections of pp, pn, and nn interactions and cross-checking with EPPS16 nPDFs [91]. As expected, down quark fraction increases in PbPb collisions as a result of an enhanced contribution of valence down quarks in lead nuclei (having 126 neutrons and 82 protons in each nucleus).

The contribution from jets with zero tracks in the jet cone above the  $p_T$  threshold, which were excluded in the fitting procedure, to the quark/gluon ratio measurements, is assigned from MC with proper uncertainties attached to it described in the later section Sec. 9.4. The flavor composition of the jets with no tracks reconstructed above the  $p_T$  threshold is shown in Fig. 78 and are observed to be predominantly quark jets. It is observed that the fraction of jets with no tracks

above a certain  $p_T$  threshold is higher in data compared to MC, shown in Fig. 79. This difference increases with increasing track  $p_T$  threshold due to observed depletion of high  $p_T$  tracks in the jet cone in central PbPb collisions [2] due to medium-induced modifications to the fragmentation functions, which is not captured in PYTHIA+HYDJET.

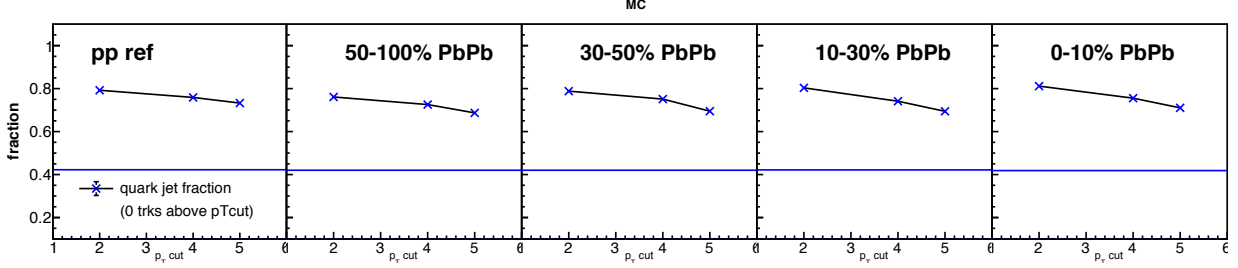


Figure 78. Quark jet fraction in a sample of jets with zero tracks in the jet cone above a threshold  $p_T$  in MC, with the rest being made up by gluon jets. The quark fraction of jets in the inclusive jet sample is shown in solid line for reference. Figure from Ref. [5].

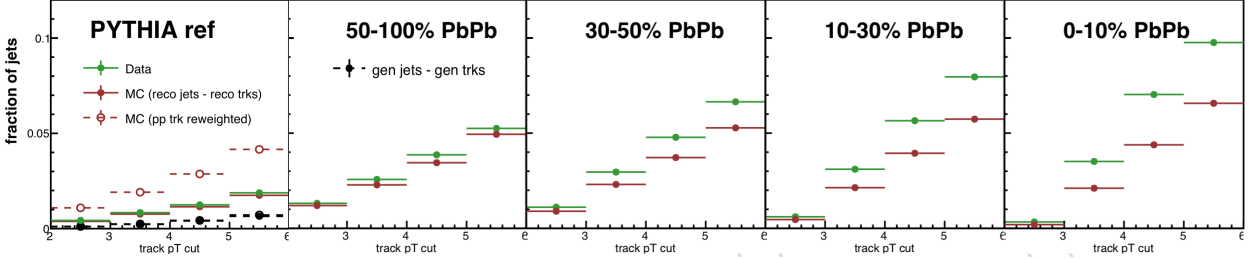


Figure 79. Fraction of jets in the inclusive jet sample with no tracks above a given threshold  $p_T$  in data and MC for pp and PbPb collisions.

The fraction of “other” quarks, kept fixed in the fitting procedure, are added to the light quark fit results for the total quark fraction. The fit results, after applying the correction factors are consolidated and shown as a function of the  $p_T$  threshold of the tracks in Fig. 80 and as a function of the  $\kappa$  in Fig. 81 for MC along with the fractions from direct MC measurements shown in dotted lines. These plots validate the fitting methodology and correction procedures by reproducing the quark/gluon jet fractions observed directly from MC simulations.

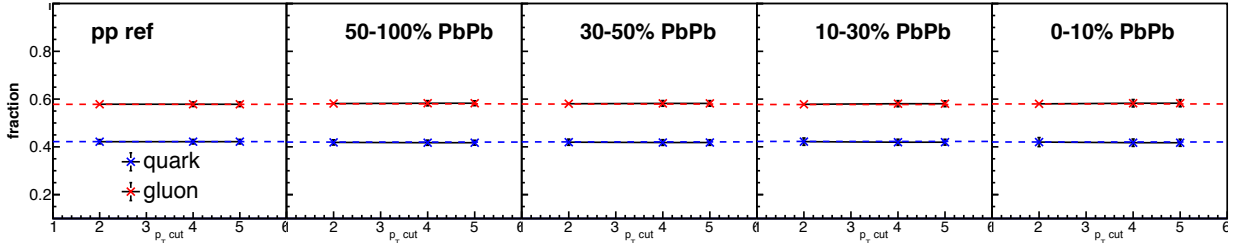


Figure 80. Fitting results for the extraction of quark and gluon fractions along with corrections in MC (detector level) shown in solid points as a function of the track  $p_T$  threshold along with dotted lines for the direct measurement of the fractions from generator level MC. Figure from Ref. [5].

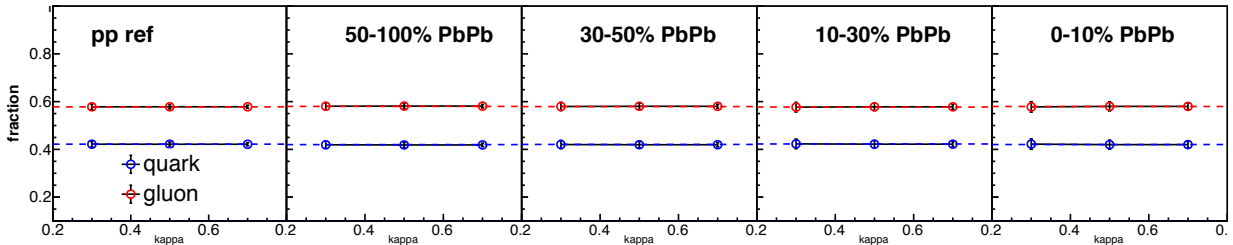


Figure 81. Fitting results for the extraction of quark and gluon fractions in MC shown in solid points as a function of the lower  $p_T$  threshold of tracks along with dotted lines for the direct measurement of the fractions from MC for jet  $p_T > 120$ . Figure from Ref. [5].

### 9.3.3 $\chi^2/NDF$ for the fits

The goodness of the fit is checked using the  $\chi^2$  and NDF for the fits for pp and different centrality bins in PbPb data, and the corresponding table is shown below in Table V. The systematic uncertainties on the data jet charge measurements are considered in the fitting procedure along with the statistical uncertainties.

### 9.3.4 Pull distributions for the fits

Pseudo experiments are performed to check the bias of the fit and the coverage of the uncertainties. Toy samples are generated using the extracted fit parameters and the corresponding pull distributions are shown below in Fig. 82 for the fits in different track  $p_T$  and  $\kappa$  bins.

<b>Track <math>p_T</math> thresh.</b>	$\kappa$	<b>pp / PbPb centrality</b>	$\chi^2$	<b>NDF</b>
1 GeV	0.5	pp	9.56797	21
		50-100% PbPb	2.63625	21
		30-50% PbPb	9.32342	21
		10-30% PbPb	5.45709	21
		0-10% PbPb	0.70967	21
2 GeV	0.3	pp	28.8533	29
		50-100% PbPb	10.8662	29
		30-50% PbPb	14.5302	29
		10-30% PbPb	24.5728	29
		0-10% PbPb	35.2548	29
2 GeV	0.5	pp	7.22425	21
		50-100% PbPb	5.56617	21
		30-50% PbPb	24.3116	21
		10-30% PbPb	13.5924	21
		0-10% PbPb	11.609	21
2 GeV	0.7	pp	32.7128	17
		50-100% PbPb	13.4214	17
		30-50% PbPb	10.6294	17
		10-30% PbPb	6.37745	17
		0-10% PbPb	6.41058	17
4 GeV	0.5	pp	21.4862	21
		50-100% PbPb	9.82929	21
		30-50% PbPb	5.75445	21
		10-30% PbPb	15.8561	21
		0-10% PbPb	4.40084	21
5 GeV	0.5	pp	36.4978	21
		50-100% PbPb	7.66993	21
		30-50% PbPb	7.43026	21
		10-30% PbPb	15.9253	21
		0-10% PbPb	7.24748	21

TABLE V. The  $\chi^2$  and NDF values shown for the fits for different selections of  $\kappa$  and threshold values of track  $p_T$ .

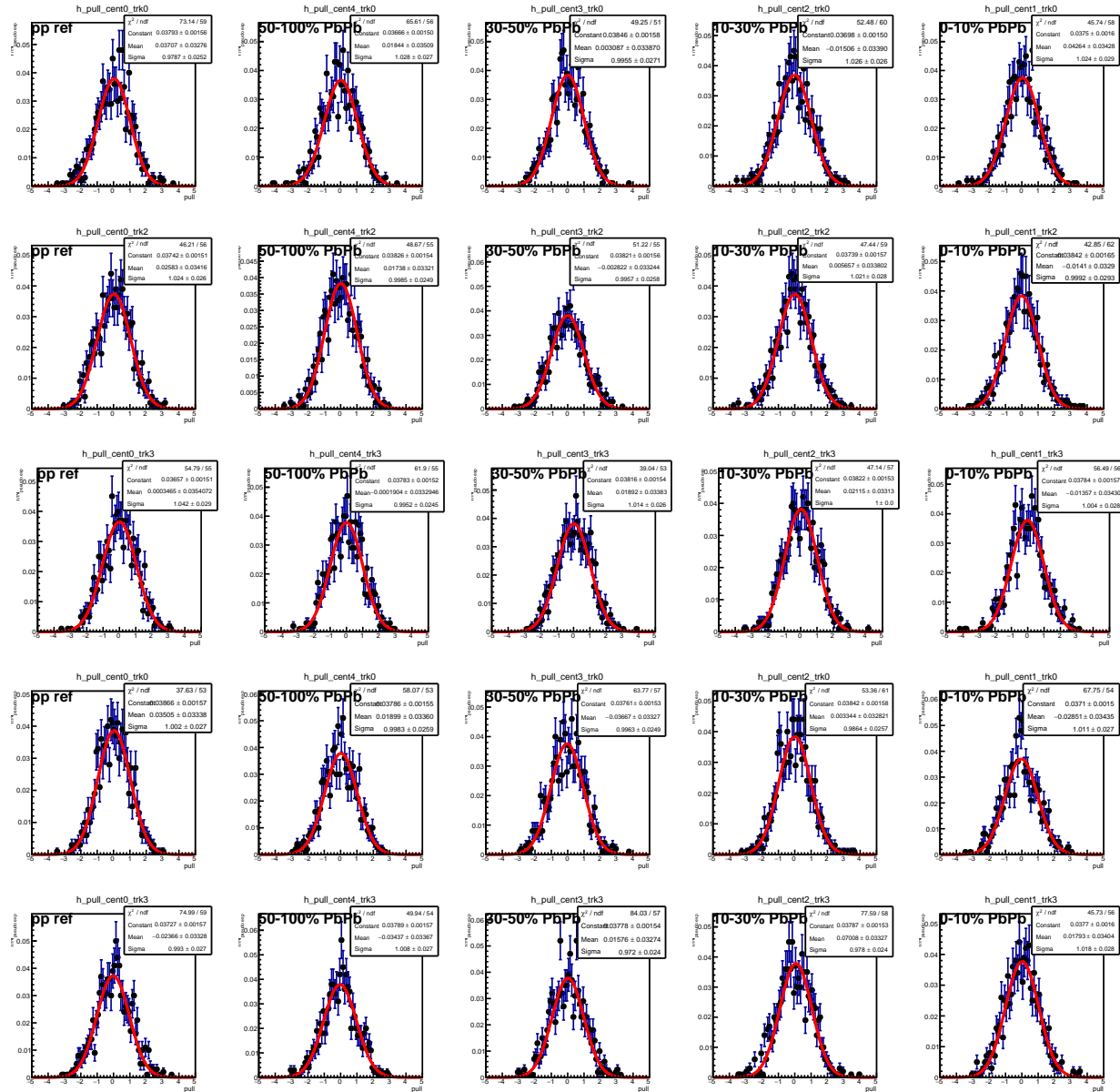


Figure 82. Distribution of pulls for the fitting in different event centrality bins for various values of track  $p_T$  thresholds and  $\kappa$ . Figure from Ref. [5].

### 9.3.5 Jet kinematics in data and MC

The jet kinematic distributions in data are compared to MC with pre-fit and post-fit quark/gluon fractions in Fig. 83 and Fig. 84 and a good agreement is observed as seen in Sec. 8.5.

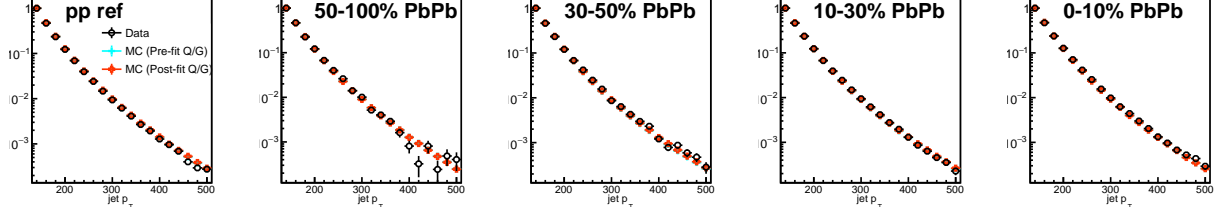


Figure 83. Transverse momentum distributions for pp and PbPb data compared to simulations (with nominal and fit values of quark/gluon jet fractions) for each collision centrality bin. Figure from Ref. [5].

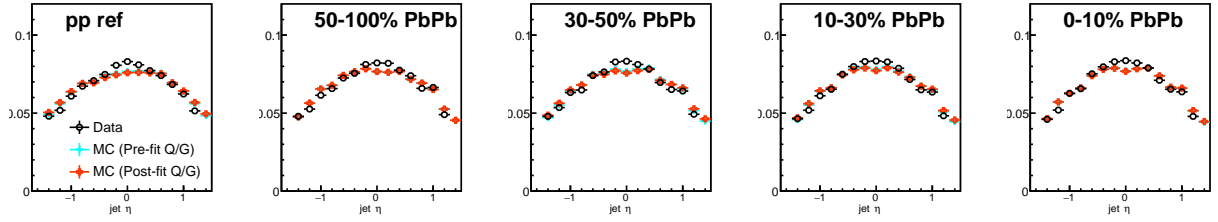


Figure 84. Jet  $\eta$  distributions for pp and PbPb data compared to simulations (with nominal and fit values of quark/gluon jet fractions) for each collision centrality bin. Figure from Ref. [5].

## 9.4 Systematic uncertainty studies

Several sources of systematic uncertainty are considered for the jet charge measurements and fitting results, including effects from unfolding, tracking efficiencies, background correction, jet reconstruction and MC statistics.

### 9.4.1 Tracking efficiencies

The uncertainty related to the tracking efficiency is estimated from simulation by taking the ratio between the reconstructed and generated yields. The effect of differences in tracking efficiencies between positive and negative particles in the tracker is analyzed and is propagated as a systematic uncertainty. The tracking efficiencies are shown below in MC (Fig. 85) for both pp and PbPb collisions, and are different for positive (negative) particles from the nominal value by 0.25%(-0.25%) independent of the track  $p_T$ . The reconstruction efficiency of the positive (negative) particles is varied by these values in populating the response matrices used in the data unfolding. The resulting modified unfolded data jet charge distributions are fit with the generator-level templates and the differences in the extracted fractions of quarks and gluon jets are quoted as a source of systematic uncertainty (Fig. 92 and Fig. 93).

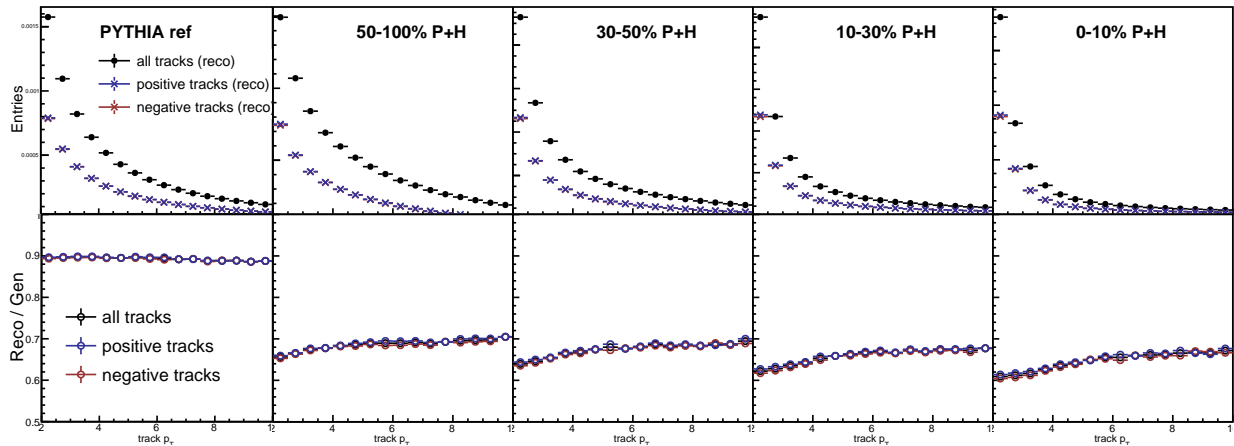


Figure 85. Tracking efficiency closures comparing generated tracks to reconstructed tracks for nominal, positive tracks and negative tracks shown as a function of the track  $p_T$ . Figure from Ref. [5].

Systematic uncertainties arising from possible differences in track reconstruction between data and simulation, including the erroneous reconstruction of tracks, are also evaluated. The relative fraction of reconstructed  $D^*$  mesons in the  $D^* \rightarrow D\pi \rightarrow K\pi\pi$  and  $D^* \rightarrow D\pi \rightarrow K\pi\pi\pi\pi$  decay channels in simulated and data events are compared to study the difference in the track reconstruction efficiency in pp data and simulation. [172]. Track quality variables before track selections are also compared in both pp and PbPb data and simulation [50], and based on these studies, a  $p_T$ -independent uncertainty of 4% (5%) is assigned on the measured track  $p_T$  in pp (PbPb) collisions. The uncertainties are propagated into the response matrices by varying the track  $p_T$  reconstruction efficiency by the above values. The resulting deviations in the fitting fractions from the nominal results are included as systematic uncertainties. The relative uncertainties on the unfolded jet charge distributions from the data/MC tracking differences are shown in Fig. 86, and for the fitting fractions in Fig. 92 and Fig. 93.

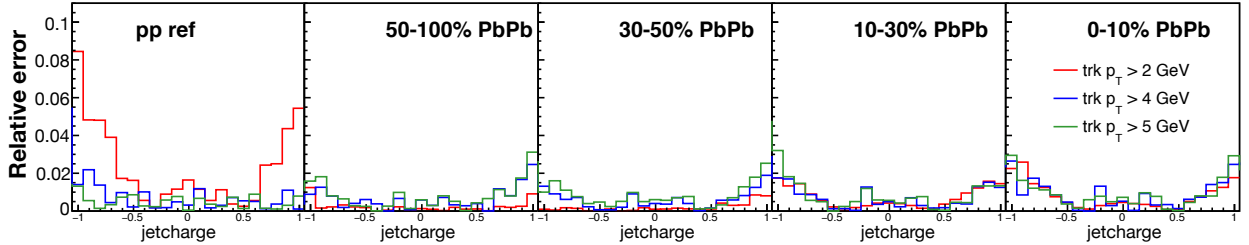


Figure 86. Relative uncertainties in jet charge distributions due to tracking reconstruction differences between data and MC. Figure from Ref. [5].

#### 9.4.2 Unfolding uncertainties

Cross closure tests are performed to study the systematic effects due to the response matrix populated from a particular MC event generator. In this study, the detector level distributions from the inclusive sample of PYTHIA and PYTHIA+HYDJET are unfolded using the response matrix populated using a dominant gluon and quark jet samples from the same MC sample as discussed in Sec. 9.2.2. The resulting deviations from the nominal unfolded distributions are included as systematic uncertainties.

For background unfolding in PbPb, the cross closure tests are performed by unfolding the detector level jet charge distributions with response matrices constructed using PbPb data minimum

bias samples. The resulting unfolded distributions are observed to be in very good agreement with the nominal results. This can be attributed to the tuning of the HYDJET event generator to model the PbPb data background effects very well. Fig. 89 shows the track multiplicity in random cones of radius  $R = 0.4$  in data and MC, and are observed to be in very good agreement with each other.

Other uncertainties from the unfolding procedure include effects from statistical uncertainty in the MC simulation samples used to populate the response matrix and the uncertainty propagated via bin-to-bin correlations as a result of the regularization process. The systematic uncertainties corresponding to these effects are propagated using the ROOUNFOLD software package. The effects of the bin-to-bin correlations are estimated by building covariance matrices from ROOUNFOLD and propagating the respective systematic errors into the template fitting procedure using the inverse of the covariance matrix.

To assess the effects of the bias vector in the unfolding process, a comprehensive calibration test is performed by generating PYTHIA samples with varying fractions of quark jets (0.4 – 0.8). The varied MC samples are then unfolded and fit using the nominal PYTHIA sample for populating the response matrices and building the jet charge flavor templates. Fig. 87 (left) plots the difference between the extracted quark fractions (from the template fits) and initial generated quark fractions in the modified MC sample versus the initial generated quark fractions. The closures are observed to be consistent with unity within the systematic uncertainties.

### 9.4.3 Jet energy resolution

The uncertainty on the jet energy resolution is 10-15% relative to the nominal resolution due to data/MC differences. To account for the effects arising from the differences in the jet energy resolution between data and MC, additional smearing is applied to the jet  $p_T$ . An absolute 5% additional smearing is applied to the reconstructed jet  $p_T$  in data and the differences in the jet charge measurements in the most central PbPb centrality bin are shown in Fig. 87 (right), and the differences from the nominal results are included as systematic uncertainties. The difference in the extracted quark and gluon fractions from fitting the smeared jet charge distributions compared to the nominal values are included as systematic uncertainties to the fitting results, shown in Fig. 92 and Fig. 93). The effects of angular resolution on the measured jet axis are observed to be negligible in the jet charge measurements.

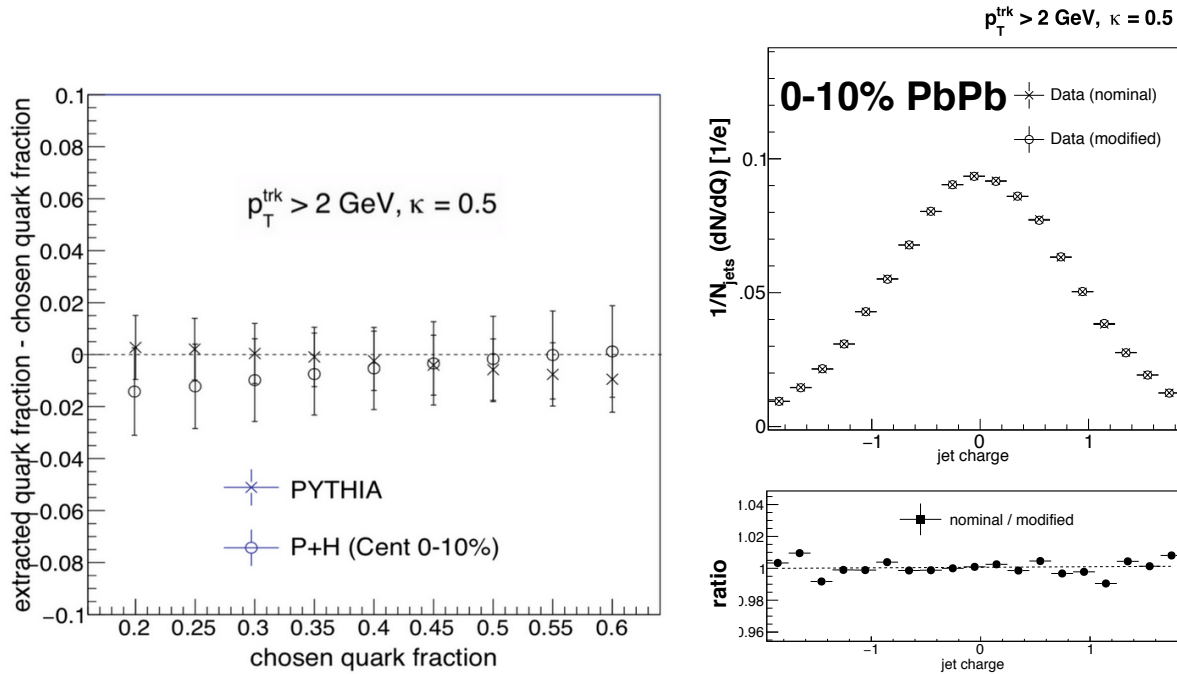


Figure 87. **Left:** Difference of quark jet fractions between generated values from modified MC samples (with quark and gluon fractions varied) and extracted values from unfolding and fitting the modified MC samples with nominal PYTHIA response matrices, bias vectors and templates. **Right:** Jet charge distributions shown for nominal reconstructed jet  $p_T$  and for smeared jet  $p_T$  to assess the effects of jet energy resolution in the most central bin in PbPb data. Figure from Ref. [5].

#### 9.4.4 Zero track jets

Jets with zero tracks above the threshold  $p_T$  are excluded from the jet charge measurements. The fraction of jets with no tracks above a certain track  $p_T$  inside the jet cone is shown in Fig. 79 for data and MC as a function of the lower threshold of the track  $p_T$ . The difference in this fraction of jets between pp and peripheral PbPb collisions in MC is observed to be arising from the tracking efficiency differences between them as shown in Fig. 85. This is cross-checked in Fig. 79 by simulating PbPb tracking efficiency conditions for pp MC and verifying that the fraction of jets with 0 tracks in modified pp (shown in dashed red lines) is in agreement with the peripheral PbPb bin.

It is also observed that this fraction of jets is higher in data compared to MC and this difference increases with increasing track  $p_T$  threshold due to observed depletion of high  $p_T$  tracks in the jet cone in central PbPb collisions [2]. The fraction of jets with zero tracks is cross-checked using Particle-Flow jets instead of Calorimeter jets and the ratio of jets with zero tracks above the

threshold track  $p_T$  in the two types of jets is shown in Fig. 88 and is observed to be in agreement between data and MC.

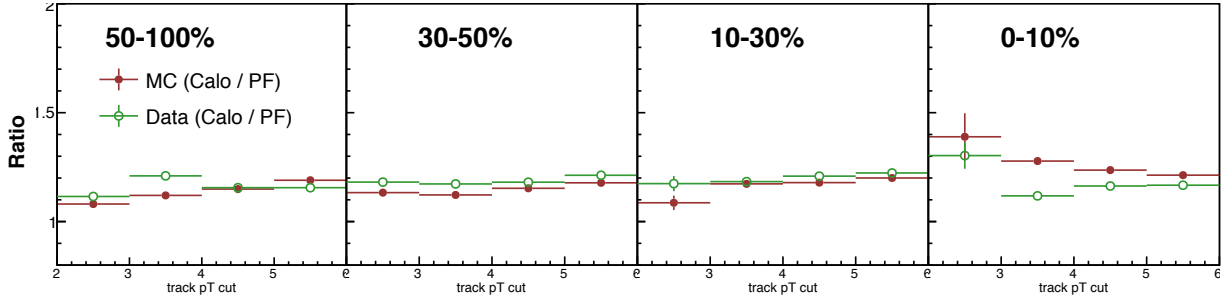


Figure 88. Ratio of fraction of jets in the inclusive jet sample with no tracks above the threshold  $p_T$  between two types of jets (Particle Flow jets and Calorimeter jets) in data and MC for pp and PbPb collisions. Figure from Ref. [5].

The contribution from jets with zero tracks in the jet cone to the quark/gluon jet fractions is assigned from MC (Fig. 78). The difference in the fraction of such jets between data and MC (Fig. 79) is included as a source of uncertainty as shown in Fig. 92 and Fig. 93).

#### 9.4.5 Background fluctuations

In PbPb data, there is an additional jet reconstruction bias toward selecting jets that sit on upward fluctuations in the background (since the jet spectrum is steeply falling, more jets on upward fluctuations are included in the sample than jets on downward fluctuations excluded). As these effects are expected to be included in the jet charge templates as well, the magnitude of the difference in this effect between data and MC is assigned as a source of systematic uncertainty. To quantify the difference in this effect between data and MC, the multiplicity of particles in random jet cones in the kinematic region of interest is shown in Fig. 89 as a comparison between minimum bias PbPb data and MC (HYDJET).

To estimate and assign the uncertainty from the contribution of the excess yield due to background fluctuation bias in jet reconstruction, we consider the jet charge measured in the nominal PYTHIA+HYDJET sample and compare it with measurements from a modified PYTHIA+HYDJET sample, generated with a fluctuated background. The background is fluctuated by 4%, corresponding to the difference in the data/MC random cone multiplicities as shown in Fig. 89, and the resulting variations in the jet charge measurements are shown in Fig. 90, and is observed to be negligible.

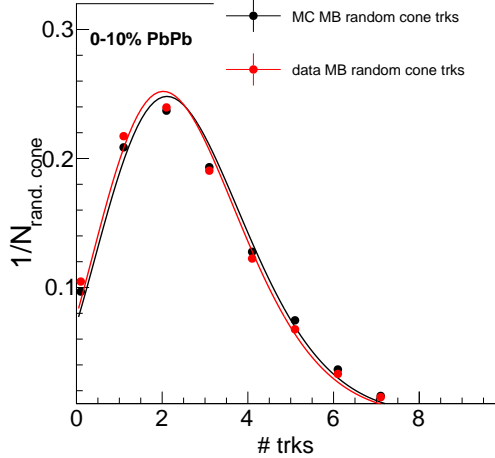


Figure 89. Track multiplicity comparison between minimum bias PbPb data and MC(HYDJET) in random cones of radius 0.4 shown for the most central bin 0-10%. Figure from Ref. [5].

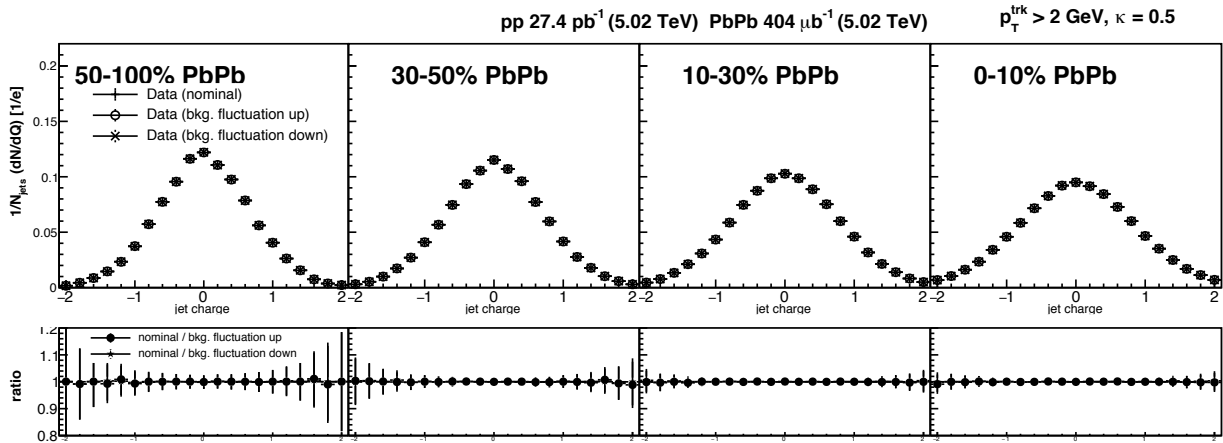


Figure 90. **Top panel:** Jet charge measurements using background fluctuations to estimate the effect of the bias in jet reconstruction. **Bottom panel:** The ratio of the nominal jet charge measurements to those made with fluctuated backgrounds. Figure from Ref. [5].

#### 9.4.6 Statistical uncertainty in MC simulations

To propagate the effects of the statistical uncertainties from the MC templates on the final fitting results, we perform a large number of pseudo-experiments (1000) by generating smeared jet charge templates according to its statistical uncertainty and repeatedly fitting the data measurements using the smeared templates. The bin value from the original template is used as a mean and the statistical uncertainty as the sigma to smear each bin in the template according to a gaussian and

these generated MC templates are used to fit the data jet charge measurements. The spread in the extracted gluon jet fractions, shown in Fig. 91 for a sample bin, from the fits in the pseudo-experiments is assigned as a systematic uncertainty due to limited MC statistics. The relative uncertainties in the extracted gluon jet fraction are shown in Fig. 92 and Fig. 93 and is of the order 2 – 3%.

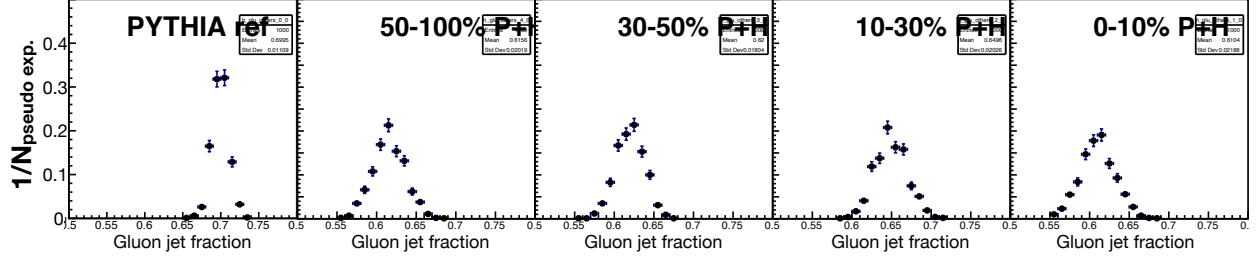


Figure 91. Fitting results for the gluon jet fractions from pseudo-experiments performed to assess the effects of the limited statistics in MC on the final results. The MC templates are smeared according to their statistical uncertainties and the results of fitting the data jet charge measurements with the generated smeared templates, shown for a sample bin of track  $p_T > 2$  GeV and  $\kappa = 0.5$ . Figure from Ref. [5].

#### 9.4.7 “Other” quark templates

Finally, the effect of fixing the “other” quark jets, comprising c (2.9%), s (4.7%) and b (1.7%) (anti)quarks in the fitting procedure is analyzed. The fraction of each of the “other” quark jets are independently varied by its full amount and the effects of this on the fit results are observed to be small compared to other systematic uncertainties.

#### 9.4.8 Summary of systematic uncertainties

The systematic uncertainties from all sources are added in quadrature. Table VI and Table VII list the ranges of the estimated systematic uncertainties from the individual sources and Fig. 92 and Fig. 93 show the dominant individual sources of systematic uncertainty for track  $p_T$  thresholds and  $\kappa$  values used in the measurements, respectively. When an uncertainty range is given, the range of the values is the maximum variation in the fractions for different selections on  $\kappa$  and track  $p_T$  threshold values.

Source	PbPb centrality intervals				pp
	0–10%	10–30%	30–50%	50–100%	
Response matrix modeling	5–6.5	5–6.5	5–6.5	5–6.5	3.5–4
Monte Carlo statistics	3	3	3	3	1.5
Jet energy resolution	2	2	2	2	1
Tracking efficiency (data/MC)	2	2	2	2	1
Tracking efficiency (positive/negative)	0.5–1	0.5–1	1	1	0.5
Zero track jets	0.5–4.5	0.4–3	0.4–2	0.2–1	0.1
Background modeling and fluctuation	1	1	0.5	0.5	NA
“Other” flavor jets	1	1	1	1	1
Total	7–9	7–8	7–8	7–8	4–5

TABLE VI. Relative systematic uncertainties in percentage for the measurements of gluon jet fractions in PbPb and pp events. The range of the values in the uncertainties are for different track  $p_T$  threshold selections.

Source	PbPb centrality intervals				pp
	0–10%	10–30%	30–50%	50–100%	
Response matrix modeling	5–7.5	5–7.5	5–7.5	5–7.5	4–6
Jet energy resolution	2–3	2–3	2	2	1–1.5
Monte Carlo statistics	3	3	3	3	1.5
Tracking efficiency (data/MC)	2	2	2	2	1
Tracking efficiency (positive/negative)	1–1.5	1–1.5	1–2	1–2	0.5–1
Background modeling and fluctuation	1	1	0.5	0.5	NA
“Other” flavor jets	1	1	1	1	1
Zero track jets	0.4	0.4	0.4	0.2	0.1
Total	7–9	7–9	8–9	9–11	4–7

TABLE VII. Relative systematic uncertainties in percentage for the measurements of gluon jet fractions in PbPb and pp events. The range of the values in the uncertainties are for different  $\kappa$  selections.

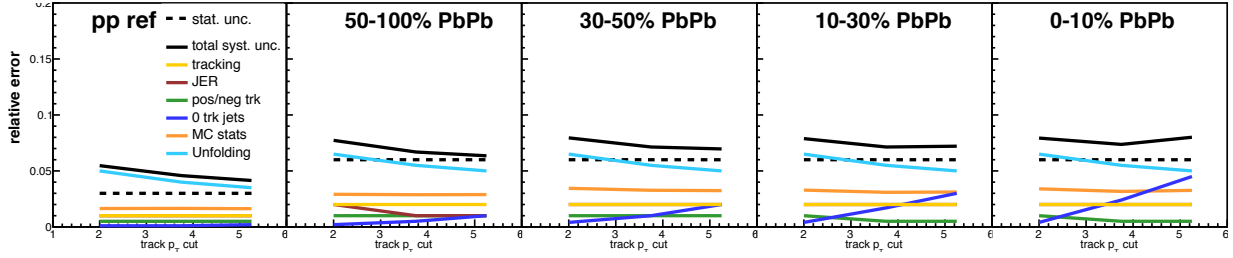


Figure 92. Consolidated relative systematic uncertainties on the extracted fractions of gluon jets from various sources shown for different values of track  $p_T$  thresholds. Figure from Ref. [5].

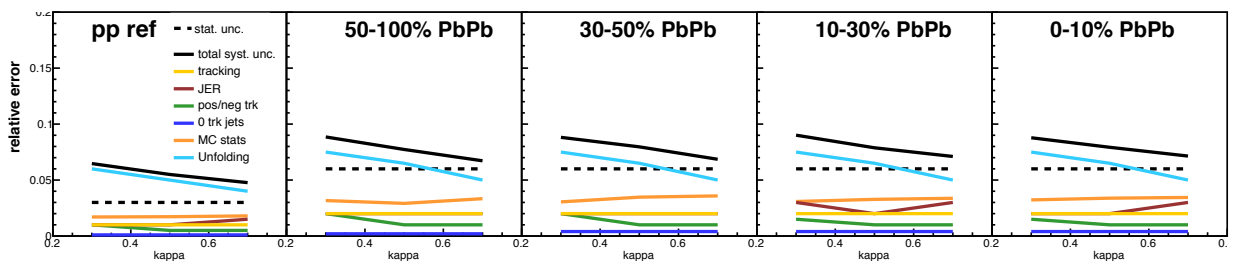


Figure 93. Consolidated relative systematic uncertainties on the extracted fractions of gluon jets from various sources shown for different values of  $\kappa$ . Figure from Ref. [5].

## 9.5 Results

The unfolded jet charge measurements are shown in the upper panels of Figs. 94, 95, and 96 with solid black points for various selections of minimum track  $p_T$  thresholds and  $\kappa$  values. The results are normalized to the total number of jets in the sample ( $N_{\text{jets}}$ ) and are shown for pp and different PbPb event centrality bins. The extracted fractions of quark and gluon-initiated jets from the fitting procedure are displayed as a set of stacked histograms in these figures. The ratios between the jet charge measurements and template fit results are shown in the bottom panels of Figs. 94, 95, and 96. No significant deviation from unity is observed for the ratios in the entire fitting range. An increased presence of valence down quarks is expected in lead collisions (126 neutrons and 82 protons in each nucleus) compared to proton collisions. This results in significantly different fractions of up and down quarks in PbPb collisions compared to pp and this is evident from the figures.

The widths (standard deviations) of the unfolded data jet charge distributions are shown in Fig. 97. The results are shown in different PbPb event centrality bins and in pp, with various track  $p_T$  thresholds and  $\kappa$  values. The pp and PbPb data results are shown as a function of the track- $p_T$  threshold for  $\kappa = 0.3, 0.5$ , and  $0.7$ , with blue squares, red crosses, and green diamonds, respectively. The same are shown for the generator-level predictions from PYTHIA for  $\kappa = 0.3, 0.5$ , and  $0.7$ , with blue solid lines, red dashed lines, and green dotted lines, respectively. The measured standard deviations are observed to increase slightly as a function of the minimum track  $p_T$  threshold and decrease significantly with increasing  $\kappa$  value.

A decreased fraction of gluon jets in the sample is predicted in PbPb collisions compared to pp by theoretical models incorporating color-charge dependence into jet energy loss calculations as discussed in Sec. 4.3 and in detail in Ref. [103]. The gluon jet charge distribution is consistently predicted by various MC simulation models to be centered about zero, and that for quarks to be offset from zero, as shown in Fig. 73. Together with predictions of a decreased gluon jet fraction in central PbPb collisions, this is expected to result in an increase in the width of the jet charge distributions compared to unquenched results. However, from Fig. 97, it is evident that the widths of the unfolded jet charge distributions in both pp and PbPb collisions are consistently well-described by generator-level PYTHIA predictions, without accounting for any quenching effects. This is observed to hold true for detector-level jet charge distributions for all studied track  $p_T$  selections

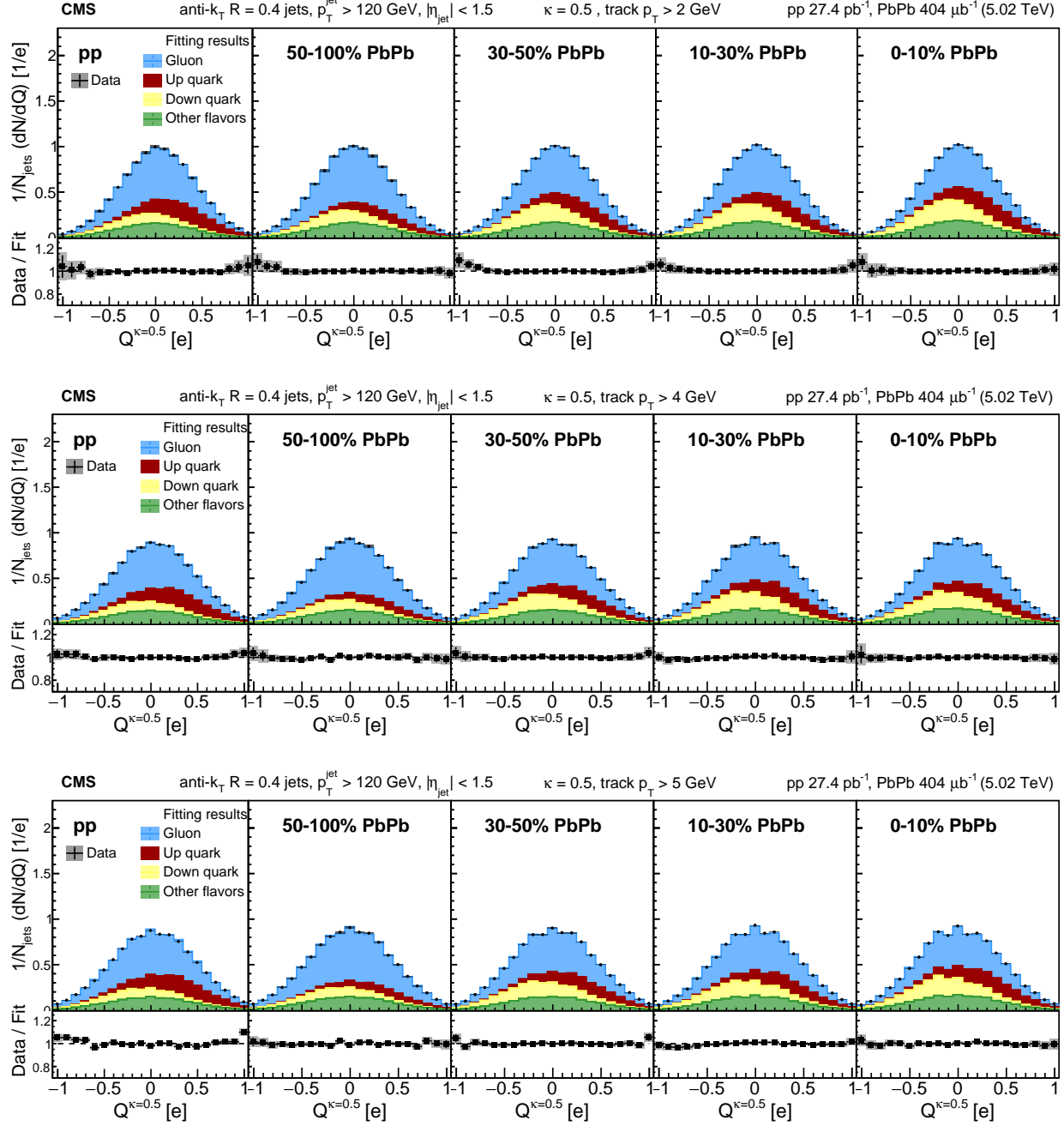


**Figure 94. Upper row of each figure:** Unfolded jet charge measurements shown for inclusive jets in data along with the extracted fractions of up, and down quark jets, gluon jets, and the “other flavor” jets. The systematic and statistical uncertainties in the distributions are shown by the shaded regions and vertical bars, respectively. The jet charge measurements shown here are for  $\kappa = 0.5$  and a minimum track  $p_T$  of 2, 4, and 5 GeV (top, middle, and bottom, respectively). **Lower row of each figure:** Ratio of the jet charge measurements to the results of template fits. Figures from Ref. [1].

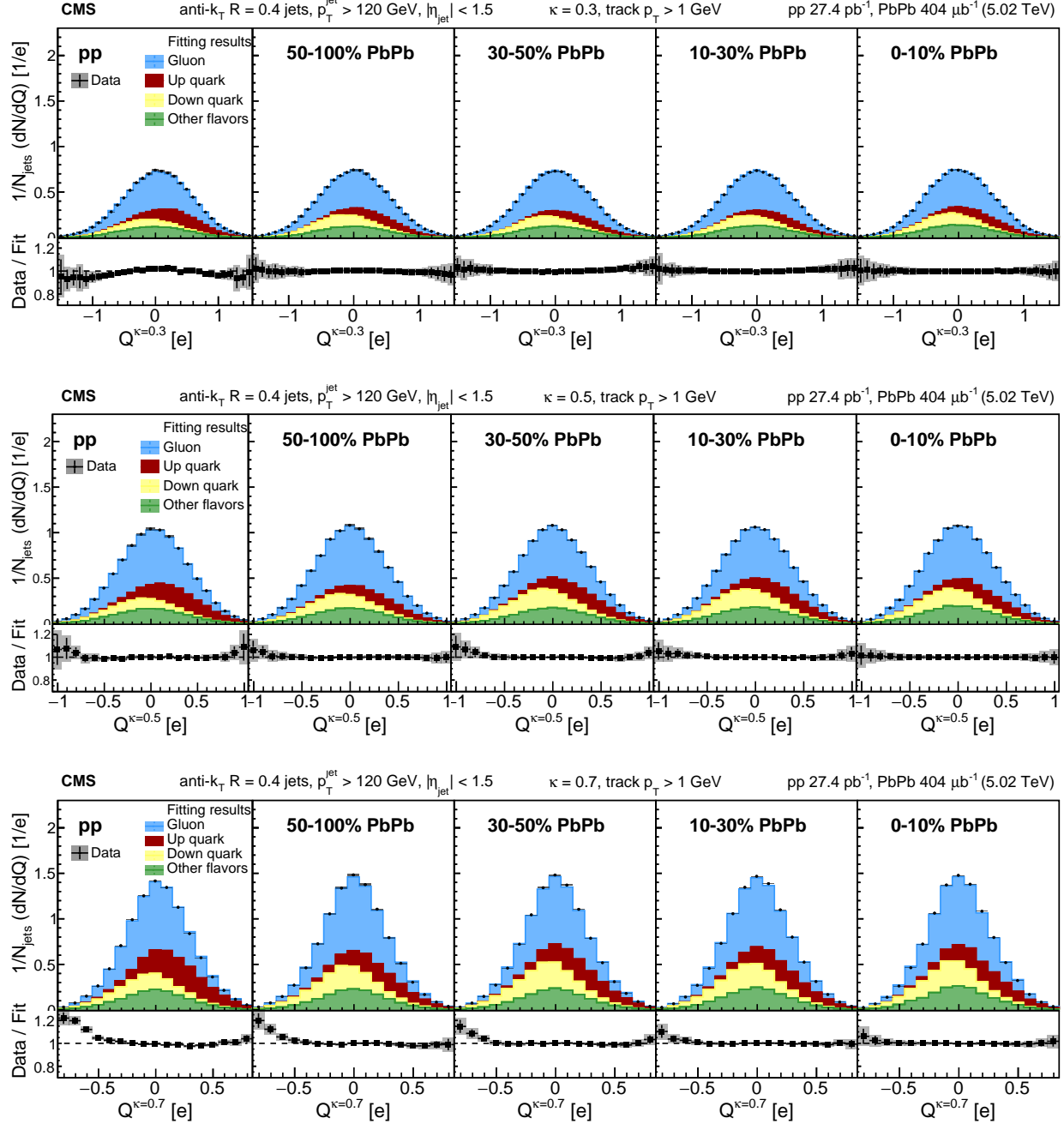


**Figure 95. Upper row of each figure:** Unfolded jet charge measurements shown for inclusive jets in data along with the extracted fractions of up, and down quark jets, gluon jets, and the “other flavor” jets. The systematic and statistical uncertainties in the distributions are shown by the shaded regions and vertical bars, respectively. The jet charge measurements shown here are for a minimum track  $p_T$  of 1 GeV and a  $\kappa$  value of 0.3, 0.5, and 0.7 (top, middle, and bottom, respectively). **Lower row of each figure:** Ratio of the jet charge measurements to the results of template fits. Figures from Ref. [1].

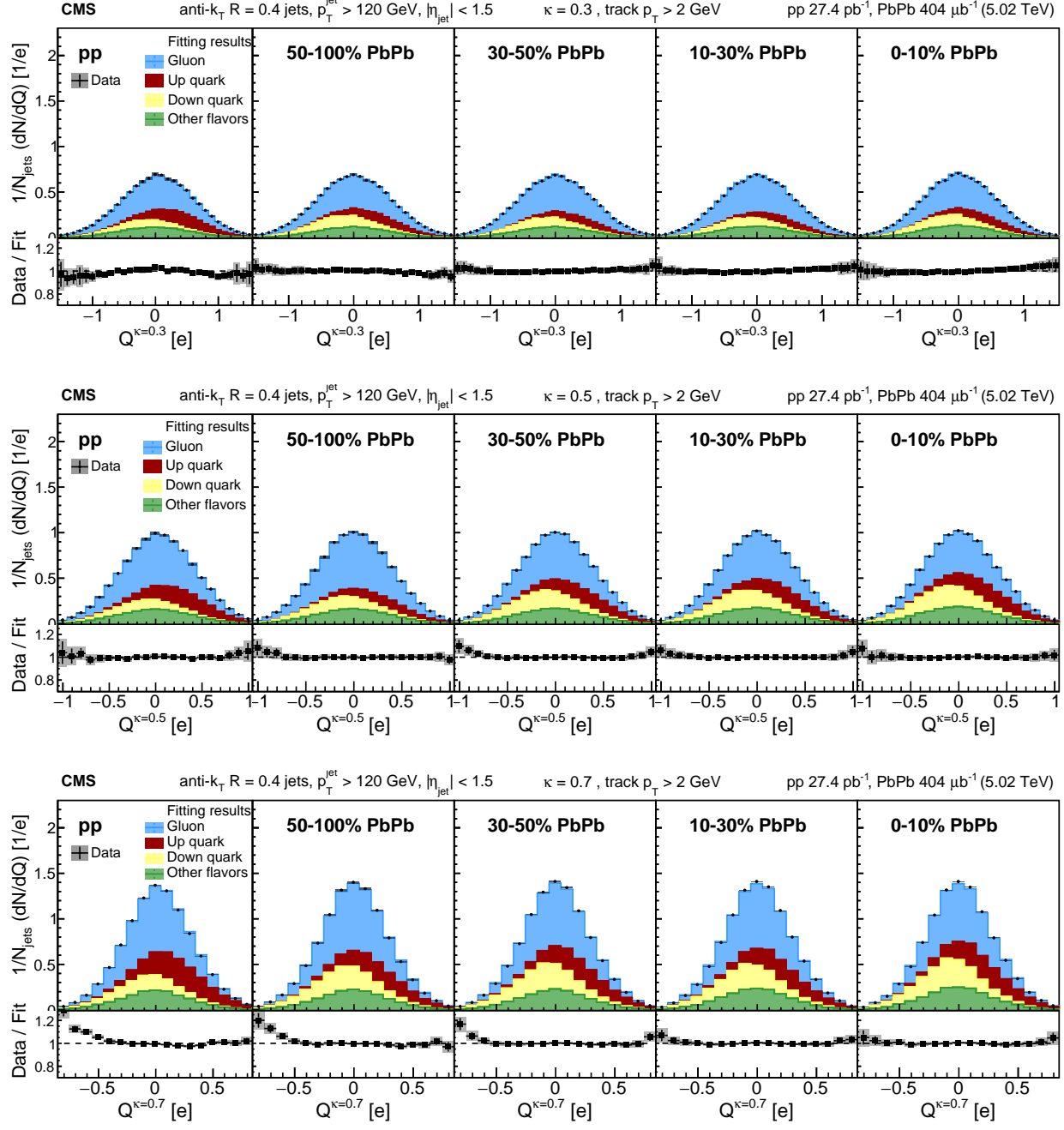


Figure 96. **Upper row of each figure** Unfolded jet charge measurements shown for inclusive jets in data along with the extracted fractions of up, and down quark jets, gluon jets, and the “other flavor” jets. The systematic and statistical uncertainties in the distributions are shown by the shaded regions and vertical bars, respectively. The jet charge measurements shown here are for a minimum track  $p_T$  of 2 GeV and a  $\kappa$  value of 0.3, 0.5, and 0.7 (top, middle, and bottom, respectively). **Lower row of each figure** Ratio of the jet charge measurements to the results of template fits. Figures from Ref. [1].

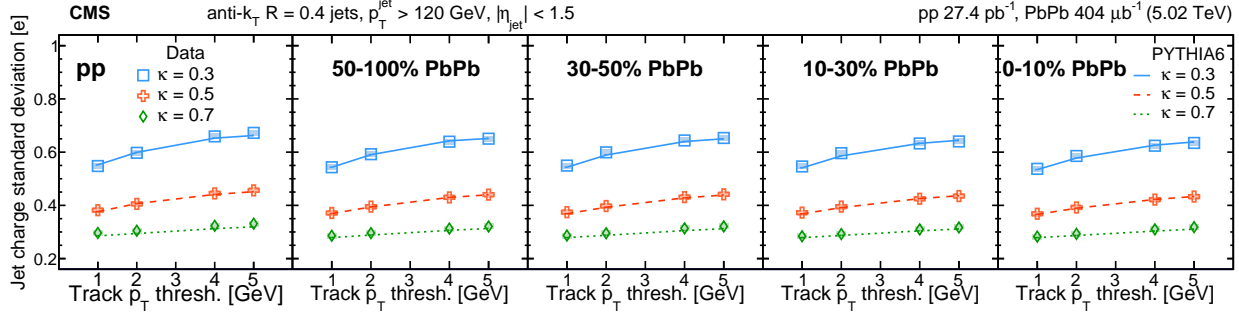


Figure 97. The standard deviation of the jet charge distributions with different track  $p_T$  thresholds and  $\kappa$  values for pp collisions and in the various event centrality bins for PbPb collisions compared with the PYTHIA6 prediction. The systematic and statistical uncertainties in the standard deviation measurements are shown by the shaded regions and vertical bars, respectively. Figure from Ref. [1].

and  $\kappa$  values in both pp and PbPb collisions. The widths of the jet charge measurements are also observed to be unmodified between various event centrality bins in PbPb collisions. Due to the different initial contributions of up and down valence quarks in pp and PbPb collisions, a comparison between the widths of the two collision systems is not discussed here. However, PYTHIA predictions adjusted for the isospin effects in PbPb collisions reproduce the widths of unfolded jet charge distributions in all PbPb collision centralities.

Results from PYQUEN event generator [91], which models the jet quenching in the QGP via collisional and radiational energy loss mechanisms according to the weak coupling model, are shown in Fig. 98. Both settings of PYQUEN predict an enhanced fraction of quark jets in a sample of central PbPb collisions compared to results from PYTHIA, due to the stronger quenching predicted for gluon jets as discussed in Sec. 4.3. The predictions for the width of the jet charge distributions with quenching effects as modeled in PYQUEN are shown in Fig. 98 (right) for the 0 – 10% most central bin in PbPb collisions. The predictions are shown for both collisional and radiational energy loss settings in PYQUEN, in comparison with data measurement for  $\kappa$  value of 0.5. It is observed that both settings of PYQUEN overestimate the width of the jet charge measurements measured in central PbPb collisions, which is instead very well described by PYTHIA. The broadening of the jet charge predicted in PYQUEN for 0 – 10% PbPb collisions is due to a decreased gluon jet fraction in the sample from its stronger quenching and medium-induced parton shower modifications.

The results for the gluon jet fractions extracted from the fitting procedure are shown in Fig. 99 for pp and various centrality bins in PbPb collisions as a function of the track  $p_T$  threshold

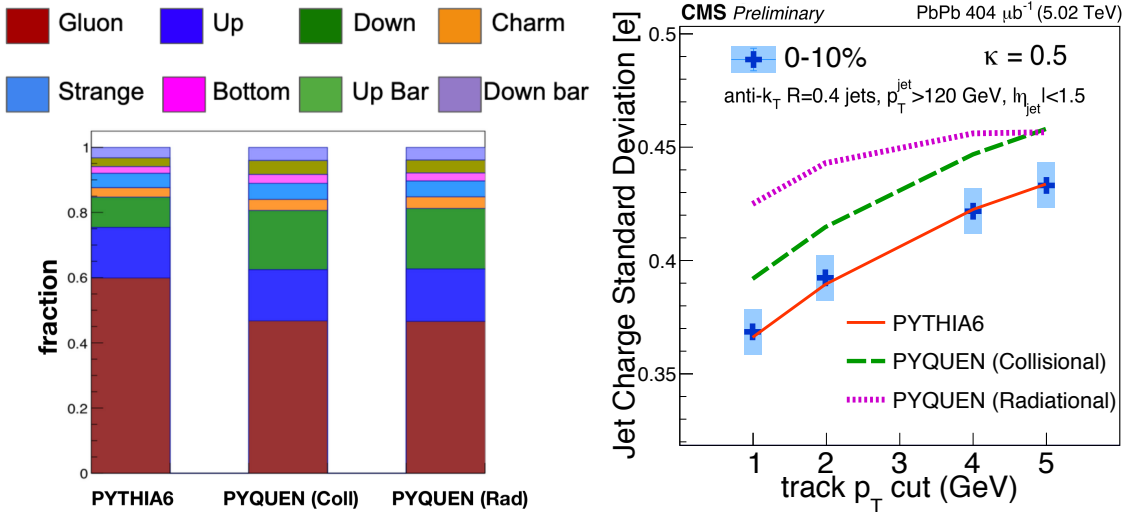


Figure 98. **Left:** Jet flavor composition predictions from PYTHIA and two settings of PYQUEN event generators. **Right:** The standard deviation of jet charge distributions in the  $0 - 10\%$  centrality bin for PbPb collisions, PYTHIA+HYDJET and PYQUEN with a track  $p_T$  threshold of 2 GeV and for  $\kappa = 0.5$ . Figures from Refs. [5, 1].

used in the jet charge measurement. The fitting results are also shown in Figure 100 as a function of the  $\kappa$  used in the measurement for track  $p_T > 1$  and  $> 2$  GeV, shown with red circles and blue crosses, respectively. It should be noted that the quark jet fractions extracted from the fitting procedure is the extracted gluon jet fraction subtracted from unity. The systematic uncertainties on the fit results are shown in shaded regions and the fit uncertainties are shown in vertical bars.

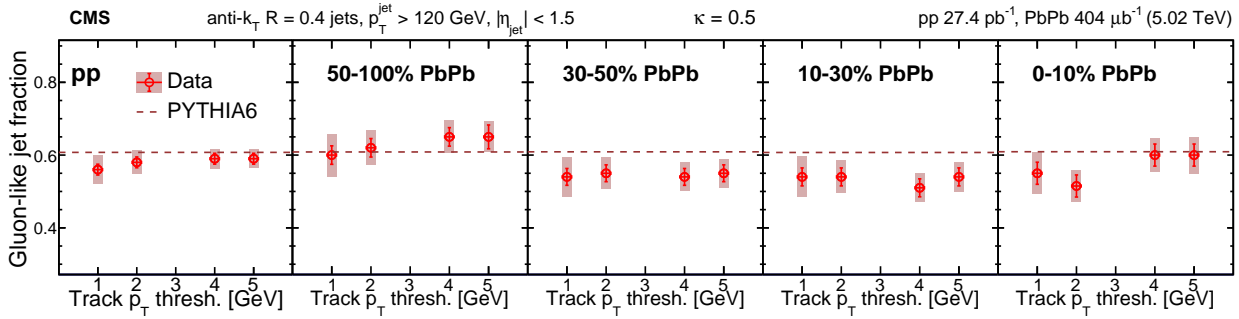


Figure 99. Fitting results for the extraction of gluon jet fractions in pp and PbPb data shown for different track  $p_T$  threshold values and event centrality bins in PbPb collisions. The systematic and statistical uncertainties are represented by the shaded regions and vertical bars, respectively. The predictions for the gluon jet fractions from PYTHIA6 are shown in dashed red lines. Figures from Ref. [1].

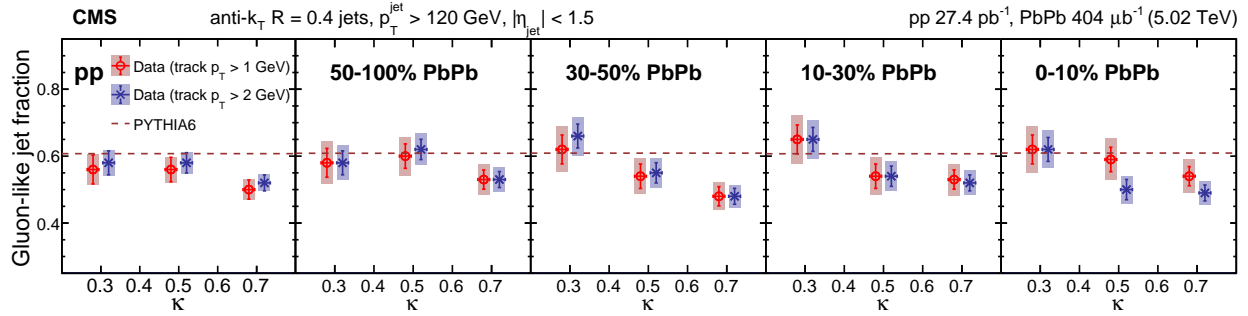


Figure 100. Fitting results for the extraction of gluon jet fractions in pp and PbPb data shown for  $p_T$ -weighting factor  $\kappa$  values of 0.3, 0.5, and 0.7 in different event centrality bins in PbPb. The markers for track  $p_T > 1$  and  $> 2$  GeV have been separated horizontally for clarity. The systematic and statistical uncertainties are represented by the shaded regions and vertical bars, respectively. The predictions for the gluon jet fractions from PYTHIA6 are shown in dashed red lines. Figures from Ref. [1].

No significant modifications are observed in the relative fractions of the quark and gluon jets in central PbPb collisions compared to peripheral PbPb and pp collisions from Figs. 99 and 100. The fitting results are shown for a range of track- $p_T$  threshold and  $\kappa$  values and no significant deviation of the gluon jet fractions is observed in PbPb collisions compared to pp results and unquenched PYTHIA expectations.

The jet charge distributions in PbPb collisions are expected to be shifted compared to pp collisions before accounting for any QGP effects due to different contributions of up and down quarks in the two collision systems. This is observed in the jet charge distributions shown in Figs. 94, 95 and 96. Secondly, a stronger quenching of gluon jets in the QGP medium is predicted by theoretical models compared to quark jets due to their different color charges. The extent of the differential quenching is predicted to be much higher in the weak coupling calculations compared to the strong coupling scenario as discussed in Sec. 4.3. The two scenarios are expected to result in different magnitudes of modification to the jet charge in central PbPb collisions compared to peripheral results. From these measurements, no significant modifications are observed in the quark and gluon jet fractions in central PbPb collisions compared to peripheral PbPb and pp collisions (Figs. 99 and 100). Finally, a medium-induced modification of parton fragmentation functions results in a strong excess of low- $p_T$  tracks relative to the jet axis in PbPb collisions with respect to pp collisions. The proposed descriptions of the low- $p_T$  excess in heavy-ion collisions include in-medium gluon

radiation and a wake-like response of the QGP as elaborated in Sec. 4.2.3, either of which is not expected to considerably affect the jet charge distributions.

The jet charge distributions in PbPb collisions are observed to be well-described by PYTHIA, without accounting for any quenching effects. Furthermore, no significant modifications are observed in the quark- and gluon-initiated jet fractions, as extracted from the jet charge fitting procedure, between pp and the various event centrality bins of PbPb collisions. These measurements provide a challenge to our current understanding of the nature of interactions between energetic partons and the QGP. The jet charge results can also help discriminate between the strong and weak coupling limits of the parton energy loss mechanisms in the QGP and analyze their relative contributions. A more comprehensive study and measurement of jet charge with increased statistics, along with its jet  $p_T$  dependence, can constrain the rich dynamics of the hot QGP medium even further.

## 10 JET SHAPES FEASIBILITY STUDIES FOR IDENTIFIED HADRONS

*Portions of the material in this chapter, which is my own work, were published in Ref. [173]*

Jet shapes have been measured in pp and PbPb collisions for inclusive, photon-tagged, and heavy-flavor jets [2, 63, 105]. A significant redistribution of the jet energy to softer particles and to large relative distances from the jet axis is observed in central PbPb collisions relative to pp results. The exact mechanism of the energy redistribution in QGP is still unclear, and two distinct scenarios are hypothesized for this phenomena as discussed in Sec. 4.2.3. Measuring jet shapes in heavy-ion collisions for individual particle species up to large angular distances can provide valuable insight into this puzzle and provide a key breakthrough in understanding the thermalization process of particles in the QGP.

Currently, no experimental measurements of jet shapes to large relative distances for distinct particle species exist, but CMS has the unique potential of performing this measurement with the addition of a proposed MIP timing detector (MTD) [174, 173]. Jet shapes feasibility measurements for this purpose are performed as a part of this thesis work using Monte-Carlo samples by simulating the process of identifying particle species associated with jets via the MIP Timing Detector. The studies are performed using QCD dijet samples generated with PYTHIA for pp collisions and PYTHIA embedded in HYDJET for PbPb collisions, at a center-of-mass collision energy of 5.5 TeV per nucleon pair.

### 10.1 Particle Identification with MIP timing detector

The proposed MIP timing detector at CMS is based on the difference of time-of-flight of particles with different masses and consequently the velocity for a given particle with momentum  $p$  as shown in Eq. 26,

$$\Delta t = \frac{L}{c} \left( \frac{1}{\beta_1} - \frac{1}{\beta_2} \right), \quad (26)$$

where  $L$  is the particle flight distance, and  $\beta_1$  and  $\beta_2$  are the velocities of the two particles under consideration. In the procedure of particle velocity measurement, the MTD is treated as an extra layer of the silicon tracker subdetector system, and the hits in MTD are matched to the tracker information. The MTD-tracker matching efficiency is observed to be high ( $\sim 85 - 90\%$ ) over wide

$p_T$  and  $\eta$  ranges. Following the MTD-tracker matching, the timing information at the MTD ( $t_0^{\text{MTD}}$ ) and the event information ( $t_0^{\text{evt}}$ ) are used along with the track length  $L$  to calculate the particle velocity as shown in Eq. 27:

$$\frac{1}{\beta} = \frac{c(t_0^{\text{MTD}} - t_0^{\text{evt}})}{L}. \quad (27)$$

The particle identification performance by MTD at CMS is shown in Fig. 101 for barrel and endcap regions via 2D distributions of  $1/\beta$  vs. particle momentum  $p$ . The different velocities of pions, kaons, and protons based on their distinct masses is evident from the bands of the respective species with a Gaussian resolution. The particle identification performance and parameters are expected to change as a function of the rapidity, and this is taken into consideration while performing these studies. From Fig. 101, a reasonable resolution is expected for proton identification up to  $\sim 5$  GeV and for kaons up to  $\sim 3$  GeV.

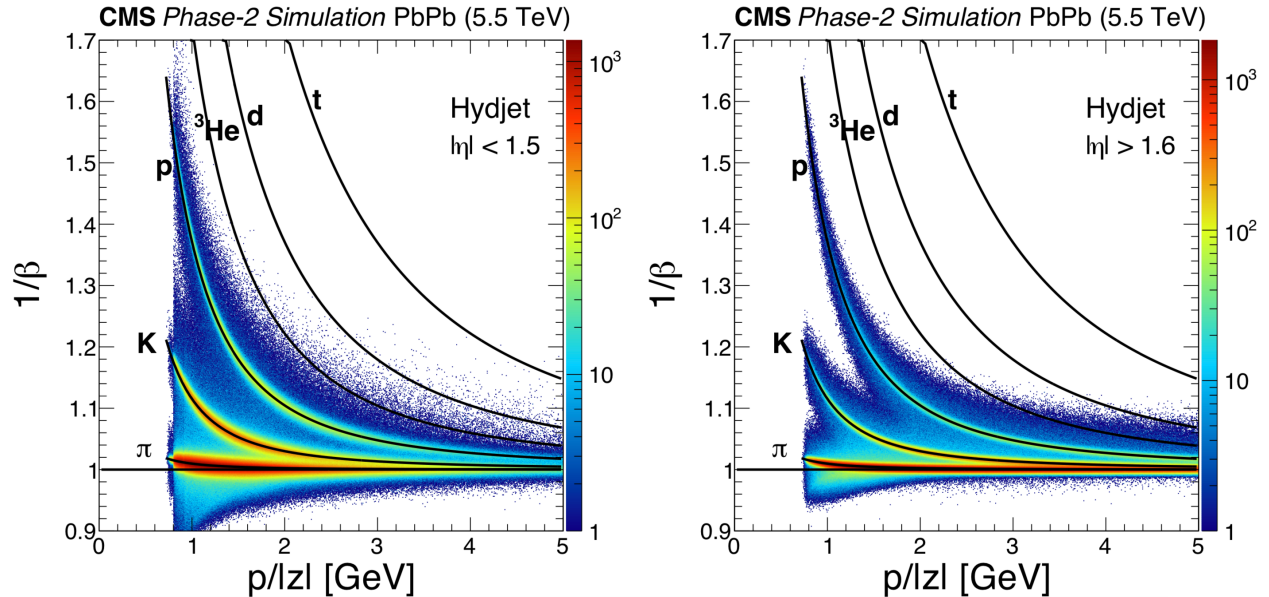


Figure 101. The inverse velocity ( $1/\beta$ ) as a function of total momentum ( $p$ ) for barrel ( $|\eta| < 1.5$ ) and endcap ( $|\eta| > 1.6$ ) regions in HYDJET simulation studies. Figure from Ref. [173].

## 10.2 Jet-track angular correlations

Measurements of jet shapes are performed using simulation samples by constructing correlations of high- $p_T$  jets and tracks, separately for identified pions and protons, in pp and PbPb collision simulations. Jets are selected with the criteria that they have  $p_T > 120$  GeV, and are found

within the pseudorapidity interval  $|\eta| < 3$ . The jet finding region is expanded in this study owing to the expected enhancement in the jet reconstruction capabilities of CMS detector in the forward regions during the upcoming years [175]. In this inclusive jet selection, multiple jets can be selected from the same event, provided that each satisfies the jet selection criteria.

Charged tracks in the event with  $p_T$  above 0.7 GeV are used to construct a two-dimensional relative pseudorapidity ( $\Delta\eta = \eta_{\text{jet}} - \eta_{\text{track}}$ ), relative-azimuth ( $\Delta\phi = \phi_{\text{jet}} - \phi_{\text{track}}$ ) correlation with respect to the measured jet axis. Correlations are constructed separately for identified pions and protons in the following bins in transverse momentum:  $0.7 < p_T < 1$  GeV,  $1 < p_T < 2$  GeV,  $2 < p_T < 3$  GeV and  $3 < p_T < 4$  GeV. The 2D correlations consisting of the  $\Delta\eta$ - $\Delta\phi$  distribution of charged particles about the jet axis, binned in track- $p_T$ , are normalized by the number of jets in the sample. For the momentum distribution measurements, correlations are weighted by track transverse momentum on a per-track basis, producing in this case per-jet average  $\Delta\eta$ - $\Delta\phi$  distribution of charged-particle transverse momentum about the jet axis, binned in track- $p_T$ .

### 10.2.1 Analysis procedure

The initial two-dimensional correlations are constructed as described above, and are shown in Fig. 102 for a sample track  $p_T$  bin for PbPb collisions. The remaining analysis procedure for measuring jet shapes with jets and tracks consists of the following steps:

- A pair-acceptance correction, derived by the "mixed event" method [2];
- Background subtraction, using large- $\eta$  sideband region [2];
- Residual Jet Fragmentation Function corrections [2];
- Background fluctuation bias corrections for PbPb collisions [2].

### 10.2.2 Pair-acceptance correction

While constructing jet-track correlations, many tracks within  $|\Delta\eta| < 2.5$  of a jet lie outside the limited track acceptance of  $|\eta_{\text{track}}| < 3$ , leading to a steeply falling correlation with increasing  $\Delta\eta$ . A pair-acceptance correction is applied to account for this effect using a mixed-event distribution, constructed by correlating jets from the jet-triggered event sample with tracks from a sample of

matched minimum-bias events. The matching is preformed by requiring the minimum-bias event to have a vertex position within 1 cm and collision centrality within 2.5% of the jet-triggered event [2]. The pair-acceptance correction is applied as shown in Eq. 28, where  $N_{\text{jets}}$  denotes the number of inclusive jets selected as described in a given data sample. The per-jet associated yield, weighted per-track by  $p_T^{\text{trk}}$  is defined in Eq. 28 as:

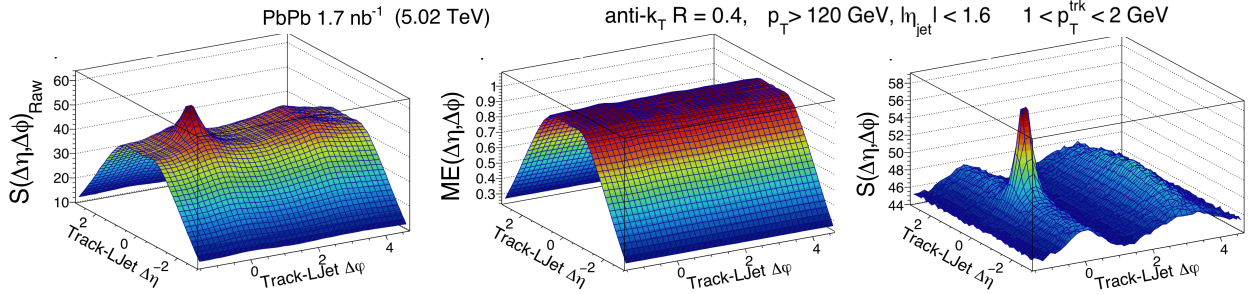


Figure 102. Illustration of the pair-acceptance correction procedure: **Left:** Raw signal correlation  $S(\Delta\eta, \Delta\phi)$ , and **Middle:** Mixed-event correlation  $S(\Delta\eta, \Delta\phi)$ . **Right:** The raw signal correlation is divided by the normalized mixed-event correlation to produce the corrected per-jet correlated yield distribution shown in the right panel. Figure from Ref. [3].

$$\frac{1}{N_{\text{jets}}} \frac{d^2 N}{d\Delta\eta d\Delta\phi} = \frac{ME(0, 0)}{ME(\Delta\eta, \Delta\phi)} \times S(\Delta\eta, \Delta\phi). \quad (28)$$

The signal pair distribution,  $S(\Delta\eta, \Delta\phi)$  (Eq. 29), represents the yield of jet-track pairs normalized by  $N_{\text{jets}}$  from the same jet-triggered event, as shown for a sample track  $p_T$  bin in Fig. 102:

$$S(\Delta\eta, \Delta\phi) = \frac{1}{N_{\text{jets}}} \frac{d^2 N^{\text{same}}}{d\Delta\eta d\Delta\phi}. \quad (29)$$

The mixed-event pair distribution,  $ME(\Delta\eta, \Delta\phi)$  (Eq. 30), is constructed separately for pion and proton correlations to account for pair-acceptance effects, with  $N^{\text{mix}}$  denoting the number of mixed-event jet-track pairs, as shown for a sample track  $p_T$  bin in Fig 102:

$$ME(\Delta\eta, \Delta\phi) = \frac{1}{N_{\text{jets}}} \frac{d^2 N^{\text{mix}}}{d\Delta\eta d\Delta\phi}. \quad (30)$$

. Tracking efficiencies are accounted for on a per-track basis using corrections derived from simulation studies in both signal and mixed event correlations. The pair-acceptance correction is normalized

by taking the ratio  $ME(0,0)/ME(\Delta\eta, \Delta\phi)$ , where  $ME(0,0)$  represents the mixed-event associated yield for jet-track pairs going in the same direction and thus having full pair acceptance.

### 10.2.3 Background subtraction

After mixed event correction, the resulting correlations consist of a Gaussian-like peak around the jet axis confined to the region  $|\Delta\eta| < 1.5$  (or narrower), sitting on a large combinatorial and long range-correlated background (Fig.102). To study the track contributions only coming from the fragmentation of the jet, the underlying event and long-range correlations due to flow effects is treated as background and needs to be subtracted from the 2D correlations. From Fig. 103 and studies in Refs. [176, 177], it is noted that the long range correlations are independent of  $\Delta\eta$  at distances larger than  $\Delta\eta = 1.5$  from the jet. Regions at large  $\Delta\eta$  distances ( $1.5 < \Delta\eta < 2.5$ ), referred to as "sidebands", are therefore used in estimating and subtracting the background contribution in the correlations.

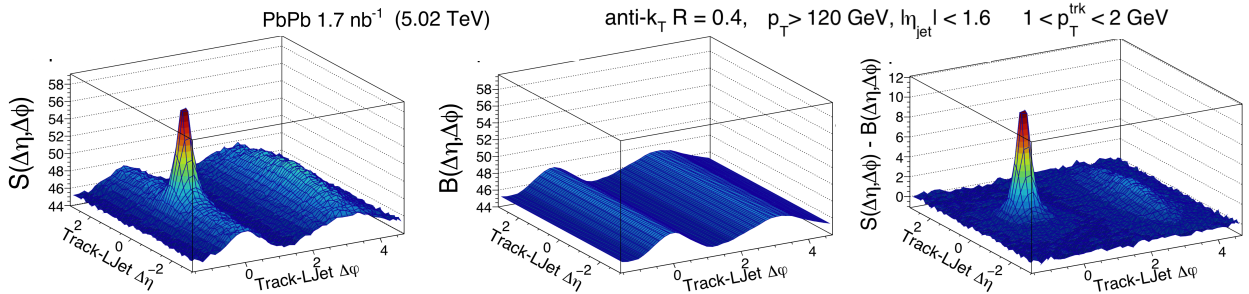


Figure 103. Illustration of the background subtraction procedure: **Left:** Acceptance-corrected signal correlation  $S(\Delta\eta, \Delta\phi)$ , and **Middle:** Combinatorial and long-range correlated background correlation  $B(\Delta\eta, \Delta\phi)$ . **Right:** The background correlation is subtracted from the signal correlation to produce the final per-jet correlated yield distribution shown in the right panel. Figure from Ref. [3].

The long range correlations, as modeled from the sidebands, depend only on  $\Delta\Phi$  and are projected onto the  $\Delta\Phi$  axis of the correlations to average out the local fluctuations in the background. The background is then smoothed and repropagated back into the  $\Delta\eta - \Delta\Phi$  phase space as shown in the middle panel of Fig. 103, and is subsequently subtracted from the acceptance-corrected signal correlations. The background effects in the correlations are observed to be larger in lower track  $p_T$  bins and more central PbPb collisions as expected.

#### 10.2.4 Residual jet fragmentation function corrections

The non-linear response of the calorimeters in the CMS detector results in a bias of preferentially reconstructing jets with harder fragmentation. This bias leads to selecting jets with fewer associated tracks in both pp and PbPb collisions for all studied track- $p_T$  bins. This bias is substantially reduced by the jet fragmentation function-dependent jet energy corrections described in Sec. 8.3. The residual effects are accounted for by applying a simulation-based correction, referred to as residual jet fragmentation function (JFF) corrections [2]. Corrections are derived for this bias by comparing per-jet correlated particle yields for detector- and generator-level jets from simulations. These corrections are determined using jets and generator-level tracks in PYTHIA for pp collisions and using jets and only generator-level tracks arising from the hard scattering in PYTHIA+HYDJET for PbPb collisions. The fragmentation dependent corrections derived in Sec. 8.3 reduces this correction by roughly half its value, thereby leading to a significant decrease in the corresponding systematic uncertainties.

#### 10.2.5 Corrections for bias from background fluctuations

In heavy-ion collisions, there is an additional jet reconstruction bias toward selecting jets that sit on upward fluctuations in the background. Since the jet spectrum is steeply falling, more jets on upward fluctuations are included in the sample than jets on downward fluctuations are excluded. Simulation based corrections are applied only to PbPb collisions to estimate and subtract the contribution of the background fluctuations in the measurement of jet shapes [2]. These corrections are derived by comparing per-jet correlated particle yields in PYTHIA+HYDJET between detector- and generator-level jets, but using only the HYDJET (UE) component of the correlated tracks. A smoothening is applied to these corrections via a gaussian fitting procedure in  $\Delta\eta$  and  $\Delta\phi$  to avoid propagating statistical fluctuations to data. The final signal correlations in different track  $p_T$  bins, corrected for all the above effects, are used in the measurement of per jet yields and jet shapes  $\rho(\Delta r)$ , as discussed in the following section.

### 10.3 Feasibility results of jet shapes

Jet shapes  $\rho(\Delta r)$ , defined in Eq. 31, help constrain mechanisms of redistribution of jet energy to softer particles and large distances from the jet axis in heavy-ion collisions (Sec. 3.4). Measurements of jet shapes (Fig. 14) as a function of the angular distance from the jet axis ( $\Delta r$ ) aid us in comparing widths of jet peaks in differential track  $p_T$  regions between pp and PbPb collisions.

$$\rho(\Delta r) = \frac{1}{\delta r} \frac{\sum_{\text{jets}} \sum_{\text{tracks} \in \delta r} p_T^{\text{trk}}}{\sum_{\text{jets}} \sum_{\text{tracks}} p_T^{\text{trk}}}, \quad (31)$$

The track  $p_T$ -weighted jet-track correlations constructed according to the procedure described in the previous section can be used in the calculation of jet shapes. This study employs generator-level jets and detector-level tracks in constructing jet track correlations and measuring jet shapes and therefore requires only pair-acceptance correction and background subtraction steps. In this work,  $\rho(\Delta r)$  is measured separately for different particle species, identified using information from the simulated MTD detector up to  $p_T < 4$  GeV. The measured jet shapes are shown in Fig. 104 in annular rings of width  $\Delta r = 0.05$  and up to  $\Delta r < 1$  for identified pions and protons in differential track  $p_T$  bins. The results are shown at  $\sqrt{s_{\text{NN}}} = 5.5$  TeV and extrapolated to an integrated luminosity of  $3 \text{ nb}^{-1}$ , corresponding to one year of data taking at the HL-LHC.

The bottom panel in Fig. 104 shows the ratio of the jet shapes for the identified particle species up to  $\Delta r < 1$ . A narrower jet shape is observed for pions compared to protons from PYTHIA, and a general rising trend is observed in the ratio of jet shapes between identified protons and pions. It should be noted that all the results are shown without taking into consideration any quenching effects in these simulation studies.

The ratios of integrated particle yields between protons and pions, correlated with the jet axis, are shown in Fig. 105. The ratio plots are shown as a function of the track  $p_T$  in Fig. 105 for two different regions, i.e., within the jet cone ( $\Delta r < 0.4$ ) and outside of the jet cone ( $0.4 < \Delta r < 1$ ). In comparison, similar measurements of the baryon to meson ratio from ALICE is also shown for the 0 – 10% most central PbPb collisions as a function of  $p_T$ . These MC measurements are also shown for regions inside the jet cone in jet-triggered events and for bulk particles from minimum-bias events in Fig. 105.

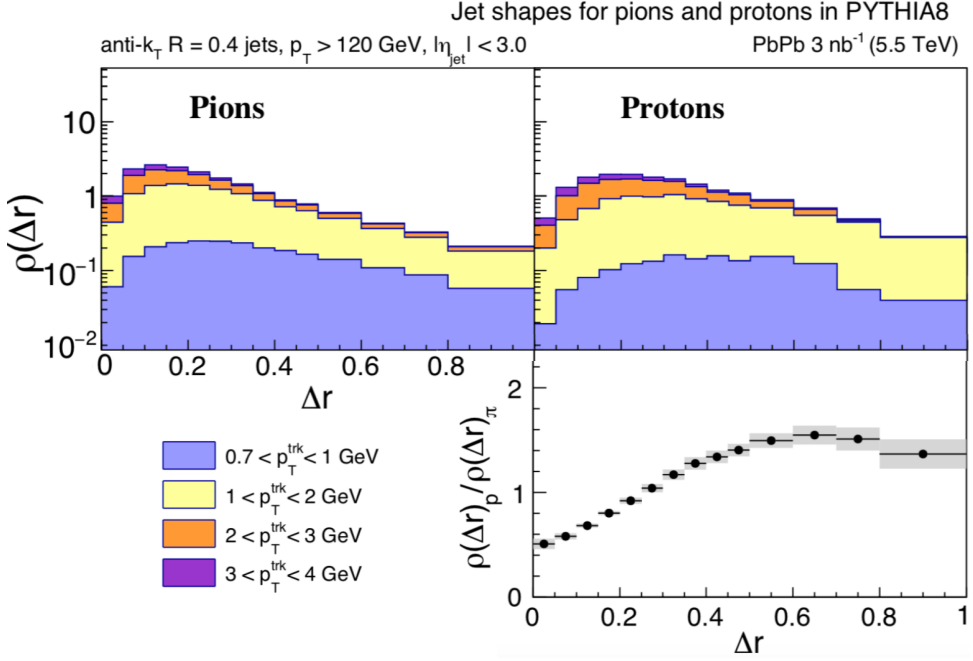


Figure 104. **Top panel:** Jet shapes  $\rho(\Delta r)$  for identified pions (top left) and protons (top right) in PYTHIA for different track  $p_T$  regions at  $\sqrt{s_{\text{NN}}} = 5.5 \text{ TeV}$ . **Bottom panel:** Ratio between proton and pion jet shapes for the inclusive track  $p_T$  range. The shaded band in the ratio plots shows the projected uncertainties.

As discussed in Sec. 4.2.3, the jet shapes for identified protons and pions can help distinguish between distinct hadronization scenarios occurring in the QGP. From Fig. 105 (left), an excess yield of pions is observed compared to protons within the jet cone, in the vacuum fragmentation scenario modeled by PYTHIA. However, outside of the jet cone, a larger proton yield is observed to be correlated to the jet axis compared to pions for  $p_T > 1 \text{ GeV}$ . Similar ratio plots for different centrality PbPb collisions produced with information from the MTD can provide a key breakthrough in understanding the QGP hadronization processes.

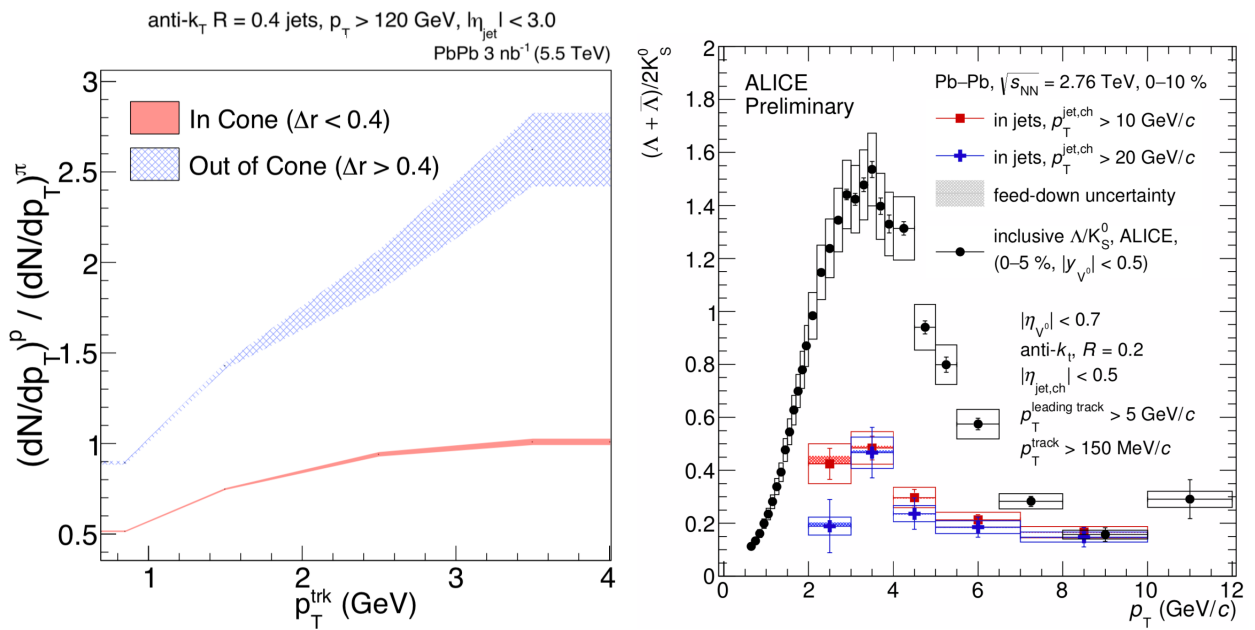


Figure 105. **Left:** Integrated particle yields of identified protons and pions correlated to the jet axis as a function of  $p_T$  from PYTHIA at  $\sqrt{s_{NN}} = 5.5$ , shown for inside and outside the jet cone regions. **Right:** Measurements of baryon-to-meson ( $\Lambda$  to  $K_S^0$ ) particle yields ratio as a function of  $p_T$  in 0-10% central PbPb collisions, for bulk particles (black) and for those inside the jet cone (colored). Figure from Ref. [108].

## 11 CONCLUSIONS

This work presents studies of the rich properties and dynamics of Quark-Gluon plasma via different jet observables in heavy-ion collisions in comparison with the pp (vacuum) reference. The first jet charge distributions in heavy-ion collisions are presented in this work along with pp results, fully unfolded for detector and background effects. The jet charge is measured for jets having  $p_T > 120$  GeV and pseudorapidity  $|\eta| < 1.5$ , and using charged particles with transverse momentum  $p_T > 1$  GeV within the jet cone. The jet charge studies use lead-lead (PbPb) and proton-proton (pp) collision data collected with the CMS detector at a nucleon-nucleon center-of-mass energy of 5.02 TeV.

The pp and PbPb unfolded jet charge distributions are presented for a range of minimum track  $p_T$  threshold and  $\kappa$  values used in the measurements, and for different event centrality bins in PbPb collisions. The unfolded distributions in both pp and PbPb (all centralities) are well-described by PYTHIA Monte-Carlo, generated with the appropriate initial nPDFs and without accounting for any quenching effects. The widths of the jet charge distributions are also presented for various track  $p_T$  threshold and  $\kappa$  values. They are observed to be in good agreement with unquenched PYTHIA predictions in both pp and all event centrality bins in PbPb collisions. However, predictions from PYQUEN, an event generator which models quenching effects, overestimate the widths of the jet charge distributions as compared to those measured in 0 – 10% PbPb data. The increase in the width of the jet charge predicted by PYQUEN, and not observed in central PbPb collisions, is driven by a stronger quenching of gluon jets expected from weak coupling calculations, and medium-induced parton shower modifications.

The sensitivity of the jet charge to fundamental differences in the electric charges of quarks and gluons is leveraged to extract quark- and gluon-jet fractions from pp and PbPb collision data. Jet charge distributions from PYTHIA for the different flavor jets are used as templates in a fitting procedure to estimate the quark and gluon-initiated jets in pp and different event centrality bins in PbPb collisions. The fractions of the quark and gluon jets extracted using the template-fitting method indicate no significant modification in the relative fractions of different flavors in PbPb collisions, compared to pp and predictions from PYTHIA. These measurements

are the first attempt to exploit the electric charge of the initiating parton to discriminate between quark- and gluon-initiated jets.

Contrary to theory expectations in the weak coupling regime from parton-medium interaction models, no evidence is seen for a significant change in the quark/gluon jet fractions in a quenched sample of PbPb collision events having  $p_T > 120$  GeV, compared to pp results. These results provide valuable input to studying the parton flavor dependence of jet quenching in the QGP and the extent of strong/weak coupling between them. These measurements are not in agreement with recent interpretations of other results in heavy-ion collisions which are based on color-charge dependent quenching models [178, 179].

Another part of the work explores the feasibility of future measurements of correlations between high- $p_T$  jets and identified particle species (pions and protons) using information from the proposed MTD detector at CMS. The measurements from PYTHIA simulations are performed with jets having  $p_T > 120$  GeV and within  $|\eta| < 3$ , and charged tracks with  $p_T > 0.7$  GeV. Predictions of jet shapes are shown without any quenching effects for identified protons and pions along with their ratio and a narrower distribution is observed for pion jet shapes compared to that of protons. The ratio of integrated yields of pions and protons correlated with the jet axis is also shown as a function of the  $p_T$  inside and outside the jet cone regions. Similar measurements in PbPb collision data as a function of the event centrality will provide key breakthroughs in understanding the hadronization mechanisms in the QGP.

The jet charge measurements presented in this thesis contribute significantly to exploring the full phase space and understanding the mechanisms of parton-medium interactions in the QGP. The LHC Run 2 era has provided access to unprecedented luminosities of heavy-ion collision data containing in-situ energetic probes reconstructed as jets. A host of new jet observables are expected to be accessible with planned upgrades to the CMS detector including improved jet reconstruction and particle identification capabilities. Along with novel analysis techniques and improved computing power, future measurements in the hard probes sector are expected to greatly enhance our understanding of the dynamically rich deconfined QCD matter.

## REFERENCES

- [1] **CMS** Collaboration, A. M. Sirunyan *et al.*, “Measurement of quark- and gluon-like jet fractions using jet charge in PbPb and pp collisions at 5.02 TeV,” [arXiv:2004.00602 \[hep-ex\]](https://arxiv.org/abs/2004.00602).
- [2] **CMS** Collaboration, A. M. Sirunyan *et al.*, “Jet properties in PbPb and pp collisions at  $\sqrt{s_{NN}} = 5.02$  TeV,” *JHEP* **05** (2018) 006, [arXiv:1803.00042 \[nucl-ex\]](https://arxiv.org/abs/1803.00042).
- [3] **CMS** Collaboration, “Jet properties in PbPb and pp collisions at  $\sqrt{s_{NN}} = 5.02$  TeV.” 2016.
- [4] **CMS** Collaboration, “Jet energy corrections for inclusive jets in PbPb and pp collisions at  $\sqrt{s_{NN}} = 5.02$  TeV.” 2017.
- [5] **CMS** Collaboration, “Study of quark and gluon initiated jet fractions using jet charge in PbPb and pp collisions at  $\sqrt{s_{NN}} = 5.02$  TeV.” 2017.
- [6] **CMS** Collaboration, “Jet performance in 2018 PbPb heavy ion run.” 2019.
- [7] Y. Tachibana, N.-B. Chang, and G.-Y. Qin, “Full jet in quark-gluon plasma with hydrodynamic medium response,” *Phys. Rev. C* **95** (2017) 044909, [arXiv:1701.07951 \[nucl-th\]](https://arxiv.org/abs/1701.07951).
- [8] H. Politzer, “Reliable Perturbative Results for Strong Interactions?,” *Phys. Rev. Lett.* **30** (1973) 1346–1349.
- [9] **Particle Data Group** Collaboration, M. Tanabashi *et al.*, “Review of Particle Physics,” *Phys. Rev. D* **98** (2018) 030001.
- [10] J. Bjorken, “Highly Relativistic Nucleus-Nucleus Collisions: The Central Rapidity Region,” *Phys. Rev. D* **27** (1983) 140–151.
- [11] J. Rafelski and B. Muller, “Strangeness Production in the Quark - Gluon Plasma,” *Phys. Rev. Lett.* **48** (1982) 1066. [Erratum: Phys.Rev.Lett. 56, 2334 (1986)].
- [12] L. D. McLerran and T. Toimela, “Photon and Dilepton Emission from the Quark - Gluon Plasma: Some General Considerations,” *Phys. Rev. D* **31** (1985) 545.

- [13] **NA60** Collaboration, A. Colla, “Study of the J/psi production and suppression in In-In collisions at the CERN SPS,” *J. Phys. G* **31** (2005) S317–S323.
- [14] U. W. Heinz and M. Jacob, “Evidence for a new state of matter: An Assessment of the results from the CERN lead beam program,” [arXiv:nucl-th/0002042](https://arxiv.org/abs/nucl-th/0002042).
- [15] M. Gyulassy, “The QGP discovered at RHIC,” in *NATO Advanced Study Institute: Structure and Dynamics of Elementary Matter*, pp. 159–182. 3, 2004. [arXiv:nucl-th/0403032](https://arxiv.org/abs/nucl-th/0403032).
- [16] **BRAHMS** Collaboration, I. Arsene *et al.*, “Quark gluon plasma and color glass condensate at RHIC? The Perspective from the BRAHMS experiment,” *Nucl. Phys. A* **757** (2005) 1–27, [arXiv:nucl-ex/0410020](https://arxiv.org/abs/nucl-ex/0410020).
- [17] **PHENIX** Collaboration, K. Adcox *et al.*, “Formation of dense partonic matter in relativistic nucleus-nucleus collisions at RHIC: Experimental evaluation by the PHENIX collaboration,” *Nucl. Phys. A* **757** (2005) 184–283, [arXiv:nucl-ex/0410003](https://arxiv.org/abs/nucl-ex/0410003).
- [18] B. Back *et al.*, “The PHOBOS perspective on discoveries at RHIC,” *Nucl. Phys. A* **757** (2005) 28–101, [arXiv:nucl-ex/0410022](https://arxiv.org/abs/nucl-ex/0410022).
- [19] **STAR** Collaboration, J. Adams *et al.*, “Experimental and theoretical challenges in the search for the quark gluon plasma: The STAR Collaboration’s critical assessment of the evidence from RHIC collisions,” *Nucl. Phys. A* **757** (2005) 102–183, [arXiv:nucl-ex/0501009](https://arxiv.org/abs/nucl-ex/0501009).
- [20] P. Foka and M. g. A. Janik, “An overview of experimental results from ultra-relativistic heavy-ion collisions at the CERN LHC: Hard probes,” *Rev. Phys.* **1** (2016) 172–194, [arXiv:1702.07231 \[hep-ex\]](https://arxiv.org/abs/1702.07231).
- [21] **HotQCD** Collaboration, A. Bazavov *et al.*, “Equation of state in ( 2+1 )-flavor QCD,” *Phys. Rev. D* **90** (2014) 094503, [arXiv:1407.6387 \[hep-lat\]](https://arxiv.org/abs/1407.6387).
- [22] A. Aprahamian *et al.*, “Reaching for the horizon: The 2015 long range plan for nuclear science.”.

- [23] M. A. Stephanov, K. Rajagopal, and E. V. Shuryak, “Event-by-event fluctuations in heavy ion collisions and the QCD critical point,” *Phys. Rev. D* **60** (1999) 114028, [arXiv:hep-ph/9903292](https://arxiv.org/abs/hep-ph/9903292).
- [24] **STAR** Collaboration, G. Odyniec, “Beam Energy Scan Program at RHIC (BES I and BES II) – Probing QCD Phase Diagram with Heavy-Ion Collisions,” *PoS CORFU2018* (2019) 151.
- [25] S. Sarkar, H. Satz, and B. Sinha, eds., *The physics of the quark-gluon plasma*, vol. 785. 2010.
- [26] “LHC animation.” <http://web.mit.edu/mithig/movies/LHCanimation.mov>.
- [27] U. W. Heinz, “Thermalization at RHIC,” *AIP Conf. Proc.* **739** no. 1, (2004) 163–180, [arXiv:nucl-th/0407067](https://arxiv.org/abs/nucl-th/0407067).
- [28] S. Ryu, J. F. Paquet, C. Shen, G. Denicol, B. Schenke, S. Jeon, and C. Gale, “Importance of the Bulk Viscosity of QCD in Ultrarelativistic Heavy-Ion Collisions,” *Phys. Rev. Lett.* **115** no. 13, (2015) 132301, [arXiv:1502.01675 \[nucl-th\]](https://arxiv.org/abs/1502.01675).
- [29] U. Heinz, C. Shen, and H. Song, “The viscosity of quark-gluon plasma at RHIC and the LHC,” *AIP Conf. Proc.* **1441** (2012) 766–770, [arXiv:1108.5323 \[nucl-th\]](https://arxiv.org/abs/1108.5323).
- [30] **STAR** Collaboration, L. Adamczyk *et al.*, “Bulk Properties of the Medium Produced in Relativistic Heavy-Ion Collisions from the Beam Energy Scan Program,” *Phys. Rev. C* **96** no. 4, (2017) 044904, [arXiv:1701.07065 \[nucl-ex\]](https://arxiv.org/abs/1701.07065).
- [31] **ALICE** Collaboration, B. Abelev *et al.*, “Centrality dependence of  $\pi$ , K, p production in Pb-Pb collisions at  $\sqrt{s_{NN}} = 2.76$  TeV,” *Phys. Rev. C* **88** (2013) 044910, [arXiv:1303.0737 \[hep-ex\]](https://arxiv.org/abs/1303.0737).
- [32] “Jets, kinematics, and other variables.”  
[http://www.physics.umd.edu/hep/drew/Baden\\_jets\\_kinematics\\_dec\\_2008.pdf](http://www.physics.umd.edu/hep/drew/Baden_jets_kinematics_dec_2008.pdf).
- [33] “Pseudorapidity.” <http://en.wikipedia.org/wiki/Pseudorapidity>.
- [34] C. Loizides, J. Nagle, and P. Steinberg, “Improved version of the PHOBOS Glauber Monte Carlo,” [arXiv:1408.2549 \[nucl-ex\]](https://arxiv.org/abs/1408.2549). [SoftwareX1-2,13(2015)].

- [35] M. L. Miller, K. Reygers, S. J. Sanders, and P. Steinberg, “Glauber modeling in high energy nuclear collisions,” *Ann. Rev. Nucl. Part. Sci.* **57** (2007) 205–243, [arXiv:nucl-ex/0701025](#).
- [36] S. A. Voloshin, A. M. Poskanzer, and R. Snellings, *Collective phenomena in non-central nuclear collisions*, vol. 23, pp. 293–333. 2010. [arXiv:0809.2949 \[nucl-ex\]](#).
- [37] W. Busza, K. Rajagopal, and W. van der Schee, “Heavy Ion Collisions: The Big Picture, and the Big Questions,” *Ann. Rev. Nucl. Part. Sci.* **68** (2018) 339–376, [arXiv:1802.04801 \[hep-ph\]](#).
- [38] CMS Collaboration, V. Khachatryan *et al.*, “Observation of Long-Range Near-Side Angular Correlations in Proton-Proton Collisions at the LHC,” *JHEP* **09** (2010) 091, [arXiv:1009.4122 \[hep-ex\]](#).
- [39] CMS Collaboration, S. Chatrchyan *et al.*, “Multiplicity and Transverse Momentum Dependence of Two- and Four-Particle Correlations in pPb and PbPb Collisions,” *Phys. Lett. B* **724** (2013) 213–240, [arXiv:1305.0609 \[nucl-ex\]](#).
- [40] H. Niemi, K. J. Eskola, and R. Paatelainen, “Event-by-event fluctuations in a perturbative QCD + saturation + hydrodynamics model: Determining QCD matter shear viscosity in ultrarelativistic heavy-ion collisions,” *Phys. Rev. C* **93** (2016) 024907, [arXiv:1505.02677 \[hep-ph\]](#).
- [41] M. Strickland, “Small system studies: A theory overview,” *Nucl. Phys. A* **982** (2019) 92–98, [arXiv:1807.07191 \[nucl-th\]](#).
- [42] A. Badea, A. Baty, P. Chang, G. M. Innocenti, M. Maggi, C. McGinn, M. Peters, T.-A. Sheng, J. Thaler, and Y.-J. Lee, “Measurements of two-particle correlations in  $e^+e^-$  collisions at 91 GeV with ALEPH archived data,” *Phys. Rev. Lett.* **123** (2019) 212002, [arXiv:1906.00489 \[hep-ex\]](#).
- [43] G. Altarelli and G. Parisi, “Asymptotic Freedom in Parton Language,” *Nucl. Phys. B* **126** (1977) 298–318.

- [44] Y. L. Dokshitzer, “Calculation of the Structure Functions for Deep Inelastic Scattering and e+ e- Annihilation by Perturbation Theory in Quantum Chromodynamics.,” *Sov. Phys. JETP* **46** (1977) 641–653.
- [45] V. Gribov and L. Lipatov, “Deep inelastic e p scattering in perturbation theory,” *Sov. J. Nucl. Phys.* **15** (1972) 438–450.
- [46] J. Bjorken, “Energy Loss of Energetic Partons in Quark - Gluon Plasma: Possible Extinction of High  $p(t)$  Jets in Hadron - Hadron Collisions.”.
- [47] D. d’Enterria, “Jet quenching,” *Landolt-Bornstein* **23** (2010) 471, [arXiv:0902.2011 \[nucl-ex\]](#).
- [48] G.-Y. Qin and X.-N. Wang, *Jet quenching in high-energy heavy-ion collisions*, vol. 24, p. 1530014. 10, 2015. [arXiv:1511.00790 \[hep-ph\]](#).
- [49] **STAR** Collaboration, C. Adler *et al.*, “Disappearance of back-to-back high  $p_T$  hadron correlations in central Au+Au collisions at  $\sqrt{s_{NN}} = 200\text{-GeV}$ ,” *Phys. Rev. Lett.* **90** (2003) 082302, [arXiv:nucl-ex/0210033](#).
- [50] **CMS** Collaboration, V. Khachatryan *et al.*, “Charged-particle nuclear modification factors in PbPb and pPb collisions at  $\sqrt{s_{NN}} = 5.02\text{ TeV}$ ,” *JHEP* **04** (2017) 039, [arXiv:1611.01664 \[nucl-ex\]](#).
- [51] **ALICE** Collaboration, K. Aamodt *et al.*, “Suppression of Charged Particle Production at Large Transverse Momentum in Central Pb-Pb Collisions at  $\sqrt{s_{NN}} = 2.76\text{ TeV}$ ,” *Phys. Lett. B* **696** (2011) 30–39, [arXiv:1012.1004 \[nucl-ex\]](#).
- [52] A. Majumder and M. Van Leeuwen, “The Theory and Phenomenology of Perturbative QCD Based Jet Quenching,” *Prog. Part. Nucl. Phys.* **66** (2011) 41–92, [arXiv:1002.2206 \[hep-ph\]](#).
- [53] **CMS** Collaboration, S. Chatrchyan *et al.*, “Observation and studies of jet quenching in PbPb collisions at nucleon-nucleon center-of-mass energy = 2.76 TeV,” *Phys. Rev. C* **84** (2011) 024906, [arXiv:1102.1957 \[nucl-ex\]](#).

- [54] **ATLAS** Collaboration, M. Aaboud *et al.*, “Measurement of the nuclear modification factor for inclusive jets in Pb+Pb collisions at  $\sqrt{s_{NN}} = 5.02$  TeV with the ATLAS detector,” *Phys. Lett. B* **790** (2019) 108–128, [arXiv:1805.05635 \[nucl-ex\]](#).
- [55] **CMS** Collaboration, V. Khachatryan *et al.*, “Measurement of inclusive jet cross sections in pp and PbPb collisions at  $\sqrt{s_{NN}} = 2.76$  TeV,” *Phys. Rev. C* **96** (2017) 015202, [arXiv:1609.05383 \[nucl-ex\]](#).
- [56] **ATLAS** Collaboration, G. Aad *et al.*, “Observation of a Centrality-Dependent Dijet Asymmetry in Lead-Lead Collisions at  $\sqrt{s_{NN}} = 2.77$  TeV with the ATLAS Detector at the LHC,” *Phys. Rev. Lett.* **105** (2010) 252303, [arXiv:1011.6182 \[hep-ex\]](#).
- [57] T. Sjostrand, S. Mrenna, and P. Z. Skands, “PYTHIA 6.4 Physics and Manual,” *JHEP* **05** (2006) 026, [arXiv:hep-ph/0603175](#).
- [58] I. Lokhtin and A. Snigirev, “A Model of jet quenching in ultrarelativistic heavy ion collisions and high-p(T) hadron spectra at RHIC,” *Eur. Phys. J. C* **45** (2006) 211–217, [arXiv:hep-ph/0506189](#).
- [59] **CMS** Collaboration, V. Khachatryan *et al.*, “Measurement of transverse momentum relative to dijet systems in PbPb and pp collisions at  $\sqrt{s_{NN}} = 2.76$  TeV,” *JHEP* **01** (2016) 006, [arXiv:1509.09029 \[nucl-ex\]](#).
- [60] **CMS** Collaboration, S. Chatrchyan *et al.*, “Measurement of Jet Fragmentation in PbPb and pp Collisions at  $\sqrt{s_{NN}} = 2.76$  TeV,” *Phys. Rev. C* **90** (2014) 024908, [arXiv:1406.0932 \[nucl-ex\]](#).
- [61] **CMS** Collaboration, S. Chatrchyan *et al.*, “Modification of Jet Shapes in PbPb Collisions at  $\sqrt{s_{NN}} = 2.76$  TeV,” *Phys. Lett. B* **730** (2014) 243–263, [arXiv:1310.0878 \[nucl-ex\]](#).
- [62] **CMS** Collaboration, A. M. Sirunyan *et al.*, “Observation of Medium-Induced Modifications of Jet Fragmentation in Pb-Pb Collisions at  $\sqrt{s_{NN}} = 5.02$  TeV Using Isolated Photon-Tagged Jets,” *Phys. Rev. Lett.* **121** (2018) 242301, [arXiv:1801.04895 \[hep-ex\]](#).

- [63] **CMS** Collaboration, A. M. Sirunyan *et al.*, “Jet Shapes of Isolated Photon-Tagged Jets in Pb-Pb and pp Collisions at  $\sqrt{s_{\text{NN}}} = 5.02$  TeV,” *Phys. Rev. Lett.* **122** (2019) 152001, [arXiv:1809.08602 \[hep-ex\]](https://arxiv.org/abs/1809.08602).
- [64] R. Field and R. Feynman, “A Parametrization of the Properties of Quark Jets,” *Nucl. Phys. B* **136** (1978) 1.
- [65] **CMS** Collaboration, A. M. Sirunyan *et al.*, “Measurements of jet charge with dijet events in pp collisions at  $\sqrt{s} = 8$  TeV,” *JHEP* **10** (2017) 131, [arXiv:1706.05868 \[hep-ex\]](https://arxiv.org/abs/1706.05868).
- [66] **ATLAS** Collaboration, G. Aad *et al.*, “Measurement of jet charge in dijet events from  $\sqrt{s}=8$  TeV pp collisions with the ATLAS detector,” *Phys. Rev. D* **93** (2016) 052003, [arXiv:1509.05190 \[hep-ex\]](https://arxiv.org/abs/1509.05190).
- [67] **PHENIX** Collaboration, A. Adare *et al.*, “Inclusive cross-section and double helicity asymmetry for  $\pi^0$  production in  $p + p$  collisions at  $\sqrt{s} = 200$  GeV: Implications for the polarized gluon distribution in the proton,” *Phys. Rev. D* **76** (2007) 051106, [arXiv:0704.3599 \[hep-ex\]](https://arxiv.org/abs/0704.3599).
- [68] **STAR** Collaboration, B. Abelev *et al.*, “Longitudinal double-spin asymmetry and cross section for inclusive jet production in polarized proton collisions at  $s^{**}(1/2) = 200$ -GeV,” *Phys. Rev. Lett.* **97** (2006) 252001, [arXiv:hep-ex/0608030](https://arxiv.org/abs/hep-ex/0608030).
- [69] **ATLAS** Collaboration, M. Aaboud *et al.*, “Measurement of the inclusive jet cross-sections in proton-proton collisions at  $\sqrt{s} = 8$  TeV with the ATLAS detector,” *JHEP* **09** (2017) 020, [arXiv:1706.03192 \[hep-ex\]](https://arxiv.org/abs/1706.03192).
- [70] S. Cao and X.-N. Wang, “Jet quenching and medium response in high-energy heavy-ion collisions: a review,” [arXiv:2002.04028 \[hep-ph\]](https://arxiv.org/abs/2002.04028).
- [71] R. Thomas, B. Kampfer, and G. Soff, “Gluon emission of heavy quarks: Dead cone effect,” *Acta Phys. Hung. A* **22** (2005) 83–91, [arXiv:hep-ph/0405189](https://arxiv.org/abs/hep-ph/0405189).
- [72] J. Casalderrey-Solana, D. Gulhan, G. Milhano, D. Pablos, and K. Rajagopal, “Angular Structure of Jet Quenching Within a Hybrid Strong/Weak Coupling Model,” *JHEP* **03** (2017) 135, [arXiv:1609.05842 \[hep-ph\]](https://arxiv.org/abs/1609.05842).

- [73] R. Baier, Y. L. Dokshitzer, A. H. Mueller, S. Peigne, and D. Schiff, “Radiative energy loss of high-energy quarks and gluons in a finite volume quark - gluon plasma,” *Nucl. Phys. B* **483** (1997) 291–320, [arXiv:hep-ph/9607355](#).
- [74] R. Baier, Y. L. Dokshitzer, A. H. Mueller, S. Peigne, and D. Schiff, “Radiative energy loss and p(T) broadening of high-energy partons in nuclei,” *Nucl. Phys. B* **484** (1997) 265–282, [arXiv:hep-ph/9608322](#).
- [75] R. Baier, Y. L. Dokshitzer, A. H. Mueller, and D. Schiff, “Quenching of hadron spectra in media,” *JHEP* **09** (2001) 033, [arXiv:hep-ph/0106347](#).
- [76] M. Gyulassy, P. Levai, and I. Vitev, “Jet quenching in thin quark gluon plasmas. 1. Formalism,” *Nucl. Phys. B* **571** (2000) 197–233, [arXiv:hep-ph/9907461](#).
- [77] M. Gyulassy, P. Levai, and I. Vitev, “NonAbelian energy loss at finite opacity,” *Phys. Rev. Lett.* **85** (2000) 5535–5538, [arXiv:nucl-th/0005032](#).
- [78] M. Djordjevic and U. W. Heinz, “Radiative energy loss in a finite dynamical QCD medium,” *Phys. Rev. Lett.* **101** (2008) 022302, [arXiv:0802.1230 \[nucl-th\]](#).
- [79] X.-f. Guo and X.-N. Wang, “Multiple scattering, parton energy loss and modified fragmentation functions in deeply inelastic e A scattering,” *Phys. Rev. Lett.* **85** (2000) 3591–3594, [arXiv:hep-ph/0005044](#).
- [80] X.-N. Wang and X.-f. Guo, “Multiple parton scattering in nuclei: Parton energy loss,” *Nucl. Phys. A* **696** (2001) 788–832, [arXiv:hep-ph/0102230](#).
- [81] A. Majumder, “Hard collinear gluon radiation and multiple scattering in a medium,” *Phys. Rev. D* **85** (2012) 014023, [arXiv:0912.2987 \[nucl-th\]](#).
- [82] P. B. Arnold, G. D. Moore, and L. G. Yaffe, “Photon emission from ultrarelativistic plasmas,” *JHEP* **11** (2001) 057, [arXiv:hep-ph/0109064](#).
- [83] P. B. Arnold, G. D. Moore, and L. G. Yaffe, “Photon and gluon emission in relativistic plasmas,” *JHEP* **06** (2002) 030, [arXiv:hep-ph/0204343](#).

- [84] C. W. Bauer, D. Pirjol, and I. W. Stewart, “Soft collinear factorization in effective field theory,” *Phys. Rev. D* **65** (2002) 054022, [arXiv:hep-ph/0109045](#).
- [85] A. Idilbi and A. Majumder, “Extending Soft-Collinear-Effective-Theory to describe hard jets in dense QCD media,” *Phys. Rev. D* **80** (2009) 054022, [arXiv:0808.1087 \[hep-ph\]](#).
- [86] Z.-B. Kang, R. Lashof-Regas, G. Ovanesyan, P. Saad, and I. Vitev, “Jet quenching phenomenology from soft-collinear effective theory with Glauber gluons,” *Phys. Rev. Lett.* **114** (2015) 092002, [arXiv:1405.2612 \[hep-ph\]](#).
- [87] H. Li, F. Liu, G.-l. Ma, X.-N. Wang, and Y. Zhu, “Mach cone induced by  $\gamma$ -triggered jets in high-energy heavy-ion collisions,” *Phys. Rev. Lett.* **106** (2011) 012301, [arXiv:1006.2893 \[nucl-th\]](#).
- [88] Y. He, T. Luo, X.-N. Wang, and Y. Zhu, “Linear Boltzmann Transport for Jet Propagation in the Quark-Gluon Plasma: Elastic Processes and Medium Recoil,” *Phys. Rev. C* **91** (2015) 054908, [arXiv:1503.03313 \[nucl-th\]](#). [Erratum: Phys.Rev.C 97, 019902 (2018)].
- [89] H. Liu, K. Rajagopal, and U. A. Wiedemann, “Calculating the jet quenching parameter from AdS/CFT,” *Phys. Rev. Lett.* **97** (2006) 182301, [arXiv:hep-ph/0605178](#).
- [90] J. Casalderrey-Solana, D. C. Gulhan, J. G. Milhano, D. Pablos, and K. Rajagopal, “A Hybrid Strong/Weak Coupling Approach to Jet Quenching,” *JHEP* **10** (2014) 019, [arXiv:1405.3864 \[hep-ph\]](#). [Erratum: JHEP 09, 175 (2015)].
- [91] I. Lokhtin, A. Belyaev, and A. Snigirev, “Jet quenching pattern at LHC in PYQUEN model,” *Eur. Phys. J. C* **71** (2011) 1650, [arXiv:1103.1853 \[hep-ph\]](#).
- [92] B. Schenke, C. Gale, and S. Jeon, “MARTINI: An Event generator for relativistic heavy-ion collisions,” *Phys. Rev. C* **80** (2009) 054913, [arXiv:0909.2037 \[hep-ph\]](#).
- [93] S. Cao and A. Majumder, “Nuclear modification of leading hadrons and jets within a virtuality ordered parton shower,” *Phys. Rev. C* **101** (2020) 024903, [arXiv:1712.10055 \[nucl-th\]](#).

- [94] K. C. Zapp, F. Krauss, and U. A. Wiedemann, “A perturbative framework for jet quenching,” *JHEP* **03** (2013) 080, [arXiv:1212.1599 \[hep-ph\]](#).
- [95] T. Renk, “YaJEM: a Monte Carlo code for in-medium shower evolution,” *Int. J. Mod. Phys. E* **20** (2011) 1594–1599, [arXiv:1009.3740 \[hep-ph\]](#).
- [96] A. Buzzatti and M. Gyulassy, “A running coupling explanation of the surprising transparency of the QGP at LHC,” *Nucl. Phys. A* **904-905** (2013) 779c–782c, [arXiv:1210.6417 \[hep-ph\]](#).
- [97] N. Armesto, L. Cunqueiro, and C. A. Salgado, “Q-PYTHIA: A Medium-modified implementation of final state radiation,” *Eur. Phys. J. C* **63** (2009) 679–690, [arXiv:0907.1014 \[hep-ph\]](#).
- [98] J. Putschke *et al.*, “The JETSCAPE framework,” [arXiv:1903.07706 \[nucl-th\]](#).
- [99] **JET** Collaboration, K. M. Burke *et al.*, “Extracting the jet transport coefficient from jet quenching in high-energy heavy-ion collisions,” *Phys. Rev. C* **90** (2014) 014909, [arXiv:1312.5003 \[nucl-th\]](#).
- [100] A. Majumder, B. Muller, and X.-N. Wang, “Small shear viscosity of a quark-gluon plasma implies strong jet quenching,” *Phys. Rev. Lett.* **99** (2007) 192301, [arXiv:hep-ph/0703082](#).
- [101] K. Kovarik *et al.*, “nCTEQ15 - Global analysis of nuclear parton distributions with uncertainties in the CTEQ framework,” *Phys. Rev. D* **93** (2016) 085037, [arXiv:1509.00792 \[hep-ph\]](#).
- [102] K. J. Eskola, P. Paakkinen, H. Paukkunen, and C. A. Salgado, “EPPS16: Nuclear parton distributions with LHC data,” *Eur. Phys. J. C* **77** (2017) 163, [arXiv:1612.05741 \[hep-ph\]](#).
- [103] S.-Y. Chen, B.-W. Zhang, and E.-K. Wang, “Jet charge in high energy nuclear collisions,” *Chin. Phys. C* **44** (2020) 024103, [arXiv:1908.01518 \[nucl-th\]](#).
- [104] **CMS Collaboration** Collaboration, “Measurement of Jet Nuclear Modification Factor in PbPb Collisions at  $\sqrt{s_{NN}} = 5.02$  TeV with CMS,” Tech. Rep. CMS-PAS-HIN-18-014, CERN, 2019. <http://cds.cern.ch/record/2698506>.

- [105] CMS Collaboration, “Measurement of b jet shapes in pp collisions at  $\sqrt{s} = 5.02$  TeV,” Tech. Rep. CMS-PAS-HIN-18-020, CERN, 2019. <http://cds.cern.ch/record/2698321>.
- [106] R. Kunnavalkam Elayavalli and K. C. Zapp, “Medium response in JEWEL and its impact on jet shape observables in heavy ion collisions,” *JHEP* **07** (2017) 141, [arXiv:1707.01539 \[hep-ph\]](https://arxiv.org/abs/1707.01539).
- [107] Y.-T. Chien and I. Vitev, “Towards the understanding of jet shapes and cross sections in heavy ion collisions using soft-collinear effective theory,” *JHEP* **05** (2016) 023, [arXiv:1509.07257 \[hep-ph\]](https://arxiv.org/abs/1509.07257).
- [108] ALICE Collaboration, V. Kučera, “Production of strange particles in charged jets in Pb–Pb and p–Pb collisions measured with ALICE,” *Nucl. Part. Phys. Proc.* **276-278** (2016) 181–184, [arXiv:1511.02766 \[hep-ex\]](https://arxiv.org/abs/1511.02766).
- [109] ALICE Collaboration, S. Acharya *et al.*, “Production of charged pions, kaons and (anti-)protons in Pb–Pb and inelastic pp collisions at  $\sqrt{s_{\text{NN}}} = 5.02$  TeV,” *Phys. Rev. C* **101** (2020) 044907, [arXiv:1910.07678 \[nucl-ex\]](https://arxiv.org/abs/1910.07678).
- [110] S. Wicks, W. Horowitz, M. Djordjević, and M. Gyulassy, “Elastic, inelastic, and path length fluctuations in jet tomography,” *Nucl. Phys. A* **784** (2007) 426–442, [arXiv:nucl-th/0512076](https://arxiv.org/abs/nucl-th/0512076).
- [111] S. Cao, T. Luo, G.-Y. Qin, and X.-N. Wang, “Heavy and light flavor jet quenching at RHIC and LHC energies,” *Phys. Lett. B* **777** (2018) 255–259, [arXiv:1703.00822 \[nucl-th\]](https://arxiv.org/abs/1703.00822).
- [112] H. T. Li and I. Vitev, “Jet charge modification in dense QCD matter,” *Phys. Rev. D* **101** (2020) 076020, [arXiv:1908.06979 \[hep-ph\]](https://arxiv.org/abs/1908.06979).
- [113] W. Liu, C. Ko, and B. Zhang, “Jet conversions in a quark-gluon plasma,” *Phys. Rev. C* **75** (2007) 051901, [arXiv:nucl-th/0607047](https://arxiv.org/abs/nucl-th/0607047).
- [114] X. Chen, H. Zhang, B.-W. Zhang, and E. Wang, “A Study on the anomaly of p over pi ratios in Au+Au collisions with jet quenching,” *J. Phys.* **37** (2010) 015004, [arXiv:0806.0556 \[hep-ph\]](https://arxiv.org/abs/0806.0556).

- [115] L. Apolinário, J. Barata, and G. Milhano, “On the breaking of Casimir scaling in jet quenching,” [arXiv:2003.02893 \[hep-ph\]](https://arxiv.org/abs/2003.02893).
- [116] Y. Mehtar-Tani and S. Schlichting, “Universal quark to gluon ratio in medium-induced parton cascade,” *JHEP* **09** (2018) 144, [arXiv:1807.06181 \[hep-ph\]](https://arxiv.org/abs/1807.06181).
- [117] A. Banfi, G. P. Salam, and G. Zanderighi, “Infrared safe definition of jet flavor,” *Eur. Phys. J. C* **47** (2006) 113–124, [arXiv:hep-ph/0601139](https://arxiv.org/abs/hep-ph/0601139).
- [118] J. Gallicchio and M. D. Schwartz, “Quark and Gluon Tagging at the LHC,” *Phys. Rev. Lett.* **107** (2011) 172001, [arXiv:1106.3076 \[hep-ph\]](https://arxiv.org/abs/1106.3076).
- [119] CMS Collaboration, S. Chatrchyan *et al.*, “Search for a Higgs boson in the decay channel  $H \rightarrow ZZ^(*)$  to  $q\bar{q} \ell^-\ell^+$  in  $pp$  collisions at  $\sqrt{s} = 7$  TeV,” *JHEP* **04** (2012) 036, [arXiv:1202.1416 \[hep-ex\]](https://arxiv.org/abs/1202.1416).
- [120] D. Krohn, M. D. Schwartz, T. Lin, and W. J. Waalewijn, “Jet Charge at the LHC,” *Phys. Rev. Lett.* **110** (2013) 212001, [arXiv:1209.2421 \[hep-ph\]](https://arxiv.org/abs/1209.2421).
- [121] J. Gallicchio and M. D. Schwartz, “Quark and Gluon Jet Substructure,” *JHEP* **04** (2013) 090, [arXiv:1211.7038 \[hep-ph\]](https://arxiv.org/abs/1211.7038).
- [122] A. J. Larkoski, G. P. Salam, and J. Thaler, “Energy Correlation Functions for Jet Substructure,” *JHEP* **06** (2013) 108, [arXiv:1305.0007 \[hep-ph\]](https://arxiv.org/abs/1305.0007).
- [123] Y.-T. Chien and R. Kunnawalkam Elayavalli, “Probing heavy ion collisions using quark and gluon jet substructure,” [arXiv:1803.03589 \[hep-ph\]](https://arxiv.org/abs/1803.03589).
- [124] Fermilab-Serpukhov-Moscow-Michigan Collaboration, J. Berge *et al.*, “Net Charge in Deep Inelastic Antineutrino - Nucleon Scattering,” *Phys. Lett. B* **91** (1980) 311–313.
- [125] OPAL Collaboration, R. Akers *et al.*, “Measurement of the time dependence of  $B(d)0 \rightarrow \bar{d}$  anti- $B(d)0$  mixing using a jet charge technique,” *Phys. Lett. B* **327** (1994) 411–424.
- [126] OPAL Collaboration, G. Abbiendi *et al.*, “Measurement of triple gauge boson couplings from  $W^+W^-$  production at LEP energies up to 189-GeV,” *Eur. Phys. J. C* **19** (2001) 1–14, [arXiv:hep-ex/0009022](https://arxiv.org/abs/hep-ex/0009022).

- [127] **D0** Collaboration, V. Abazov *et al.*, “Experimental discrimination between charge 2e/3 top quark and charge 4e/3 exotic quark production scenarios,” *Phys. Rev. Lett.* **98** (2007) 041801, [arXiv:hep-ex/0608044](https://arxiv.org/abs/hep-ex/0608044).
- [128] **ATLAS** Collaboration, G. Aad *et al.*, “Measurement of the top quark charge in  $pp$  collisions at  $\sqrt{s} = 7$  TeV with the ATLAS detector,” *JHEP* **11** (2013) 031, [arXiv:1307.4568 \[hep-ex\]](https://arxiv.org/abs/1307.4568).
- [129] O. S. Brüning, P. Collier, P. Lebrun, S. Myers, R. Ostojic, J. Poole, and P. Proudlock, *LHC Design Report*. CERN Yellow Reports: Monographs. CERN, Geneva, 2004.  
<https://cds.cern.ch/record/782076>.
- [130] **CMS** Collaboration, A. M. Sirunyan *et al.*, “Pileup mitigation at CMS in 13 TeV data,” [arXiv:2003.00503 \[hep-ex\]](https://arxiv.org/abs/2003.00503).
- [131] **CMS** Collaboration, S. Chatrchyan *et al.*, “The CMS experiment at the CERN LHC,” *JINST* **3** (2008) S08004.
- [132] **CMS Collaboration** Collaboration, T. Sakuma, “Cutaway diagrams of CMS detector,” .  
<https://cds.cern.ch/record/2665537>.
- [133] **CMS Collaboration** Collaboration, S. R. Davis, “Interactive Slice of the CMS detector,” .  
<https://cds.cern.ch/record/2205172>.
- [134] **CMS** Collaboration, S. Chatrchyan *et al.*, “Description and performance of track and primary-vertex reconstruction with the CMS tracker,” *JINST* **9** (2014) P10009, [arXiv:1405.6569 \[physics.ins-det\]](https://arxiv.org/abs/1405.6569).
- [135] **CMS** Collaboration, V. Khachatryan *et al.*, “Performance of Photon Reconstruction and Identification with the CMS Detector in Proton-Proton Collisions at  $\sqrt{s} = 8$  TeV,” *JINST* **10** (2015) P08010, [arXiv:1502.02702 \[physics.ins-det\]](https://arxiv.org/abs/1502.02702).
- [136] **CMS** Collaboration, V. Khachatryan *et al.*, “Performance of Electron Reconstruction and Selection with the CMS Detector in Proton-Proton Collisions at  $\sqrt{s} = 8$  TeV,” *JINST* **10** (2015) P06005, [arXiv:1502.02701 \[physics.ins-det\]](https://arxiv.org/abs/1502.02701).

- [137] CMS Collaboration, G. L. Bayatian *et al.*, *CMS Physics: Technical Design Report Volume 1: Detector Performance and Software*. Technical Design Report CMS. CERN, 2006.  
<http://cds.cern.ch/record/922757>.
- [138] CMS Collaboration, V. Khachatryan *et al.*, “The CMS trigger system,” *JINST* **12** (2017) P01020, [arXiv:1609.02366 \[physics.ins-det\]](https://arxiv.org/abs/1609.02366).
- [139] T. Sjöstrand, S. Ask, J. R. Christiansen, R. Corke, N. Desai, P. Ilten, S. Mrenna, S. Prestel, C. O. Rasmussen, and P. Z. Skands, “An Introduction to PYTHIA 8.2,” *Comput. Phys. Commun.* **191** (2015) 159–177, [arXiv:1410.3012 \[hep-ph\]](https://arxiv.org/abs/1410.3012).
- [140] J. C. Collins, *Sudakov form-factors*, vol. 5, pp. 573–614. 1989. [arXiv:hep-ph/0312336](https://arxiv.org/abs/hep-ph/0312336).
- [141] B. Andersson, G. Gustafson, G. Ingelman, and T. Sjostrand, “Parton Fragmentation and String Dynamics,” *Phys. Rept.* **97** (1983) 31–145.
- [142] R. Field, “Early LHC Underlying Event Data - Findings and Surprises,” in *21st Hadron Collider Physics Symposium*. 10, 2010. [arXiv:1010.3558 \[hep-ph\]](https://arxiv.org/abs/1010.3558).
- [143] CMS Collaboration, V. Khachatryan *et al.*, “Event generator tunes obtained from underlying event and multiparton scattering measurements,” *Eur. Phys. J. C* **76** no. 3, (2016) 155, [arXiv:1512.00815 \[hep-ex\]](https://arxiv.org/abs/1512.00815).
- [144] GEANT4 Collaboration, S. Agostinelli *et al.*, “GEANT4: A Simulation toolkit,” *Nucl. Instrum. Meth. A* **506** (2003) 250–303.
- [145] C. Collaboration, “Identification and filtering of uncharacteristic noise in the CMS hadron calorimeter,” *JINST* **5** no. 03, (Mar, 2010) T03014.  
<https://doi.org/10.1088%2F1748-0221%2F5%2F03%2Ft03014>.
- [146] CMS Collaboration, S. Chatrchyan *et al.*, “Description and performance of track and primary-vertex reconstruction with the CMS tracker,” *JINST* **9** (2014) P10009, [arXiv:1405.6569 \[physics.ins-det\]](https://arxiv.org/abs/1405.6569).
- [147] R. Fruhwirth, “Application of Kalman filtering to track and vertex fitting,” *Nucl. Instrum. Meth. A* **262** (1987) 444–450.

- [148] P. Billoir, “Progressive track recognition with a Kalman like fitting procedure,” *Comput. Phys. Commun.* **57** (1989) 390–394.
- [149] P. Billoir and S. Qian, “Simultaneous pattern recognition and track fitting by the Kalman filtering method,” *Nucl. Instrum. Meth. A* **294** (1990) 219–228.
- [150] K. Rose, “Deterministic annealing for clustering, compression, classification, regression, and related optimization problems,” *IEEE Proc. 86* no. 11, (1998) 2210–2239.
- [151] S. D. Ellis and D. E. Soper, “Successive combination jet algorithm for hadron collisions,” *Phys. Rev. D* **48** (1993) 3160–3166, [arXiv:hep-ph/9305266](#).
- [152] Y. L. Dokshitzer, G. Leder, S. Moretti, and B. Webber, “Better jet clustering algorithms,” *JHEP* **08** (1997) 001, [arXiv:hep-ph/9707323](#).
- [153] G. P. Salam, “Towards Jetography,” *Eur. Phys. J. C* **67** (2010) 637–686, [arXiv:0906.1833 \[hep-ph\]](#).
- [154] **UA1** Collaboration, G. Arnison *et al.*, “Hadronic Jet Production at the CERN Proton - anti-Proton Collider,” *Phys. Lett. B* **132** (1983) 214.
- [155] S. Catani, Y. L. Dokshitzer, M. Seymour, and B. Webber, “Longitudinally invariant  $K_t$  clustering algorithms for hadron hadron collisions,” *Nucl. Phys. B* **406** (1993) 187–224.
- [156] M. Cacciari, G. P. Salam, and G. Soyez, “The anti- $k_t$  jet clustering algorithm,” *JHEP* **04** (2008) 063, [arXiv:0802.1189 \[hep-ph\]](#).
- [157] **CMS** Collaboration, “A Cambridge-Aachen (C-A) based Jet Algorithm for boosted top-jet tagging.”
- [158] M. Cacciari, G. P. Salam, and G. Soyez, “FastJet User Manual,” *Eur. Phys. J. C* **72** (2012) 1896, [arXiv:1111.6097 \[hep-ph\]](#).
- [159] **CMS** Collaboration, A. Sirunyan *et al.*, “Particle-flow reconstruction and global event description with the CMS detector,” *JINST* **12** (2017) P10003, [arXiv:1706.04965 \[physics.ins-det\]](#).

- [160] O. Kodolova, I. Vardanian, A. Nikitenko, and A. Oulianov, “The performance of the jet identification and reconstruction in heavy ions collisions with CMS detector,” *Eur. Phys. J. C* **50** (2007) 117.
- [161] CMS Collaboration, A. M. Sirunyan *et al.*, “Measurement of the Splitting Function in  $pp$  and Pb-Pb Collisions at  $\sqrt{s_{\text{NN}}} = 5.02$  TeV,” *Phys. Rev. Lett.* **120** (2018) 142302, [arXiv:1708.09429 \[nucl-ex\]](https://arxiv.org/abs/1708.09429).
- [162] CMS Collaboration, A. M. Sirunyan *et al.*, “Measurement of the groomed jet mass in PbPb and pp collisions at  $\sqrt{s_{\text{NN}}} = 5.02$  TeV,” *JHEP* **10** (2018) 161, [arXiv:1805.05145 \[hep-ex\]](https://arxiv.org/abs/1805.05145).
- [163] P. Berta, M. Spousta, D. W. Miller, and R. Leitner, “Particle-level pileup subtraction for jets and jet shapes,” *JHEP* **06** (2014) 092, [arXiv:1403.3108 \[hep-ex\]](https://arxiv.org/abs/1403.3108).
- [164] CMS Collaboration Collaboration, “Updates to Constituent Subtraction in Heavy Ions at CMS,” <https://cds.cern.ch/record/2621977>.
- [165] Y. Mehtar-Tani, A. Soto-Ontoso, and M. Verweij, “Background estimator for jet studies in  $p + p$  and  $A + A$  collisions,” *Phys. Rev. D* **100** (2019) 114023, [arXiv:1904.12815 \[hep-ph\]](https://arxiv.org/abs/1904.12815).
- [166] CMS Collaboration, V. Khachatryan *et al.*, “Jet energy scale and resolution in the CMS experiment in pp collisions at 8 TeV,” *JINST* **12** (2017) P02014, [arXiv:1607.03663 \[hep-ex\]](https://arxiv.org/abs/1607.03663).
- [167] W. J. Waalewijn, “Calculating the Charge of a Jet,” *Phys. Rev. D* **86** (2012) 094030, [arXiv:1209.3019 \[hep-ph\]](https://arxiv.org/abs/1209.3019).
- [168] G. D’Agostini, “A multidimensional unfolding method based on Bayes’ theorem,” *Nucl. Instrum. Meth. A* **362** (1995) 487.
- [169] W. H. Richardson, “Bayesian-based iterative method of image restoration,” *Opt. Soc. Am.* **62** (1972) 55.
- [170] L. B. Lucy, “An iterative technique for the rectification of observed distributions,” *Astron. J.* **79** (1974) 745.

- [171] T. Adye, “Unfolding algorithms and tests using RooUnfold,” in *Proceedings of the PHYSTAT 2011 Workshop, CERN, Geneva, Switzerland, January 2011*, CERN-2011-006, p. 313. 2011. [arXiv:1105.1160 \[physics.data-an\]](https://arxiv.org/abs/1105.1160).  
<https://inspirehep.net/record/898599/files/arXiv:1105.1160.pdf>.
- [172] CMS Collaboration, “Measurement of tracking efficiency,” *CMS Physics Analysis Summary CMS-PAS-TRK-10-002* (2010) .
- [173] CMS Collaboration, “A MIP Timing Detector for the CMS Phase-2 Upgrade,” Tech. Rep. CERN-LHCC-2019-003. CMS-TDR-020, CERN, Mar, 2019.  
<https://cds.cern.ch/record/2667167>.
- [174] CMS Collaboration, “Technical Proposal for a MIP Timing Detector in the CMS Experiment Phase 2 Upgrade,” Tech. Rep. CERN-LHCC-2017-027. LHCC-P-009, CERN, Dec, 2017. <https://cds.cern.ch/record/2296612>.
- [175] CMS Collaboration, A. Martelli, “The CMS HGCAL detector for HL-LHC upgrade,” in *5th Large Hadron Collider Physics Conference*. 8, 2017. [arXiv:1708.08234 \[physics.ins-det\]](https://arxiv.org/abs/1708.08234).
- [176] CMS Collaboration, S. Chatrchyan *et al.*, “Centrality dependence of dihadron correlations and azimuthal anisotropy harmonics in PbPb collisions at  $\sqrt{s_{NN}} = 2.76$  TeV,” *Eur. Phys. J. C* **72** (2012) 2012, [arXiv:1201.3158 \[nucl-ex\]](https://arxiv.org/abs/1201.3158).
- [177] CMS Collaboration, S. Chatrchyan *et al.*, “Azimuthal anisotropy of charged particles at high transverse momenta in PbPb collisions at  $\sqrt{s_{NN}} = 2.76$  TeV,” *Phys. Rev. Lett.* **109** (2012) 022301, [arXiv:1204.1850 \[nucl-ex\]](https://arxiv.org/abs/1204.1850).
- [178] M. Spousta and B. Cole, “Interpreting single jet measurements in Pb + Pb collisions at the LHC,” *Eur. Phys. J. C* **76** no. 2, (2016) 50, [arXiv:1504.05169 \[hep-ph\]](https://arxiv.org/abs/1504.05169).
- [179] ALICE Collaboration, S. Acharya *et al.*, “Exploration of jet substructure using iterative declustering in pp and Pb–Pb collisions at LHC energies,” *Phys. Lett. B* **802** (2020) 135227, [arXiv:1905.02512 \[nucl-ex\]](https://arxiv.org/abs/1905.02512).

## APPENDICES

### A Open access statements for material adapted from previous publications



Regular Article - Experimental Physics | [Open Access](#) | Published: 02 May 2018

### Jet properties in PbPb and pp collisions at $\sqrt{s_N} = 5.02 \text{ TeV}$

[The CMS collaboration, A. M. Sirunyan, \[...\] N. Woods](#)

[Journal of High Energy Physics](#) 2018, Article number: 6 (2018) | [Cite this article](#)

524 Accesses | 7 Citations | 1 Altmetric | [Metrics](#)

First issued by the Director-General – 16.10.2014  
Amended by the Director-General – 27.04.2017

### Open Access Policy for CERN Publications

CERN is committed to Open Access, as it reflects values that have been enshrined in our Convention for more than sixty years and is becoming increasingly important for the Member States, the European Commission and other institutional partners across the world. For over twenty years, most of CERN's physics publications have been made immediately and openly accessible online, in the form of CERN preprints, before publication in journals. This is generally known as "Green" Open Access.

## VITA

NAME	:	Dhanush Anil Hangal
EDUCATION	:	Ph.D., Physics, University of Illinois at Chicago, 2020  M.S., Physics, University of Illinois at Chicago, 2017  Integrated MSc., Physics, Indian Institute of Technology Roorkee, India, 2015
HONORS	:	Indian Academy of Sciences (IAS) Fellowship, Department of Science and Technology, Government of India, 2012  Innovation in Science Pursuit for Inspired Research (INSPIRE) Scholarship, Department of Science and Technology, Government of India, 2010-2015
TEACHING	:	Physics 106 and 108 at University of Illinois at Chicago, TA for lab and discussion sections for Mechanics (Fall 2015) and Electrodynamics (Spring 2016)  Physics 481 at University of Illinois at Chicago, TA for lab course “Modern Experimental Physics” (Fall 2016)  Physics 241 at University of Illinois at Chicago, TA for lab course “Experiments in Modern Physics” (Spring 2017)  Physics 215 at University of Illinois at Chicago, TA for lab sections of “Computational and Mathematical Methods for the Physical Sciences” (Fall 2018)
PUBLICATIONS	:	CMS Collaboration, Sirunyan, A.M. et al.: Measurement of quark- and gluon-like jet fractions using jet charge in PbPb and pp collisions at 5.02 TeV. arXiv:2004.00602 [hep-ex]  CMS Collaboration, Sirunyan, A.M. et al.: Jet properties in PbPb and pp collisions at $\sqrt{s_{NN}} = 5.02$ TeV. JHEP 05 (2018) 006  D.A. Hangal on behalf of the CMS collaboration: Probing properties of the QCD Medium using jet substructure techniques in pp and PbPb collisions at 5.02 TeV at CMS. PoS (HardProbes2018) 007

PRESENTATIONS : “Studies of quark and gluon contributions to jets using jet charge measurements in pp and PbPb collisions,” at Hard Probes X, Austin, TX, June 2020

“Probing the quark-gluon plasma with jets,” at Lawrence Livermore National Laboratory, Livermore, CA, February 2020

“Studies of quark and gluon contributions to jets using jet charge measurements in pp and PbPb collisions,” at Quark Matter XVIII, Wuhan, China, November 2019

“Probing properties of the QCD Medium using jet substructure techniques in pp and PbPb collisions at 5.02 TeV at CMS,” plenary speaker at Hard Probes IX, Aix-les-Bains, France, November 2018